AD-A190 961 THE ROLE OF VORTEX STRUCTURE IN TROPICAL CYCLONE MOTION 1/4
(U) NAVAL POSTGRADUATE SCHOOL MONTEREY CA M FIORINO
DEC 87

UNCLASSIFIED FFG 4/2 NL

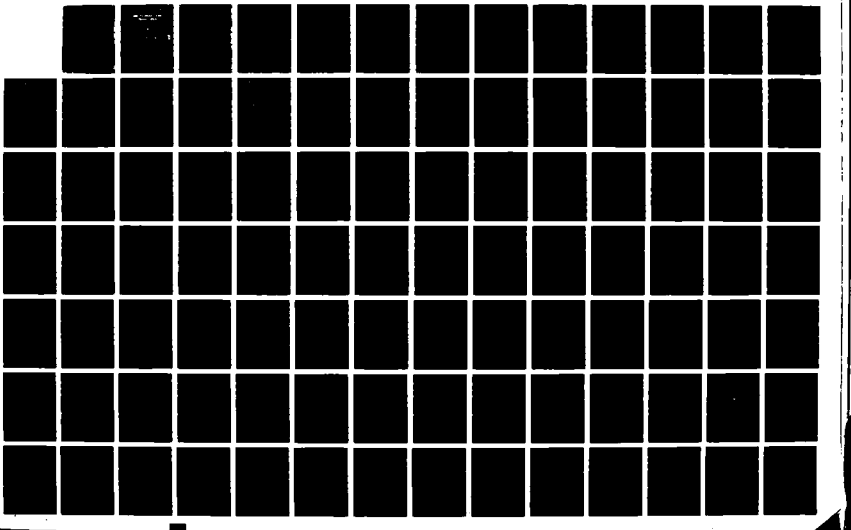

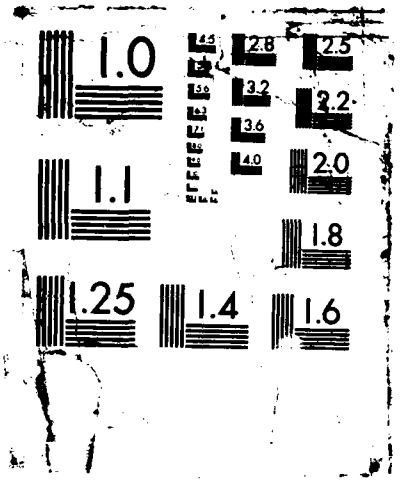
1.0
1.1
1.25
1.4
1.6
1.8
2.0
2.2
2.5
2.8
3.2
3.6
4.0

NAVAL POSTGRADUATE SCHOOL
Monterey, California

DISSERTATION

THE ROLE OF VORTEX STRUCTURE
IN TROPICAL CYCLONE MOTION

by

Michael Fiorino

December 1987

Dissertation Supervisor: R.L. Elsberry

SECURITY CLASSIFICATION OF THIS PAGE

REPORT DOCUMENTATION PAGE

1a. REPORT SECURITY CLASSIFICATION UNCLASSIFIED	1b RESTRICTIVE MARKINGS
2a. SECURITY CLASSIFICATION AUTHORITY	3. DISTRIBUTION / AVAILABILITY OF REPORT Approved for public release; distribution is unlimited.
2b. DECLASSIFICATION / DOWNGRADING SCHEDULE	
4. PERFORMING ORGANIZATION REPORT NUMBER(S)	5. MONITORING ORGANIZATION REPORT NUMBER(S)
6a. NAME OF PERFORMING ORGANIZATION Naval Postgraduate School 6b. OFFICE SYMBOL (If applicable) 63	7a. NAME OF MONITORING ORGANIZATION Naval Postgraduate School
6c. ADDRESS (City, State, and ZIP Code) Monterey, California 93943-5000	7b. ADDRESS (City, State, and ZIP Code) Monterey, California 93943-5000
8a. NAME OF FUNDING / SPONSORING ORGANIZATION 8b. OFFICE SYMBOL (If applicable)	9. PROCUREMENT INSTRUMENT IDENTIFICATION NUMBER
8c. ADDRESS (City, State, and ZIP Code)	10. SOURCE OF FUNDING NUMBERS PROGRAM ELEMENT NO. / PROJECT NO. / TASK NO. / WORK UNIT ACCESSION NO.

11. TITLE (Include Security Classification)
The Role of Vortex Structure in Tropical Cyclone Motion

12. PERSONAL AUTHOR(S)
Fiorino, Michael

13a. TYPE OF REPORT	13b. TIME COVERED	14. DATE OF REPORT (Year, Month, Day)	15. PAGE COUNT
Ph.D. Dissertation	FROM _____ TO _____	1987 December	371

16. SUPPLEMENTARY NOTATION

17. COSATI CODES			18. SUBJECT TERMS (Continue on reverse if necessary and identify by block number)
FIELD	GROUP	SUB-GROUP	Tropical cyclone motion, Barotropic model, Tropical cyclones, Circulation analysis, Beta drift

19. ABSTRACT (Continue on reverse if necessary and identify by block number)

The role of vortex structure in tropical cyclone motion is studied using a moving-grid, nondivergent barotropic model on a beta plane in a no-flow environment. Initial condition sensitivity tests reveal that the northwestward "beta" drift of the vortex is controlled by the symmetric circulation in the r = 300 - 800 km "critical" annulus. Enhanced cyclonic or anticyclonic flow in this critical annulus leads to long-term cyclonic or anticyclonic turning motions. The dynamics of the motion process is examined in terms of the symmetric and asymmetric circulations. When the vortex is moving in a quasi-steady manner, the asymmetric flow appears as a pair of large-scale, counter-rotating gyres with a broad "ventilation" flow through the vortex center. A second much smaller pair ~~of gyres~~ is ~~also~~ found near the center. ~~It is~~ the interaction between these two sets of gyres and the symmetric flow ~~that~~ governs the motion process as revealed by a streamfunction tendency-

20. DISTRIBUTION / AVAILABILITY OF ABSTRACT ☒ UNCLASSIFIED/UNLIMITED ☐ SAME AS RPT. ☐ DTIC USERS	21. ABSTRACT SECURITY CLASSIFICATION UNCLASSIFIED
22a. NAME OF RESPONSIBLE INDIVIDUAL R.L. Elsberry	22b. TELEPHONE (Include Area Code) (408)-646-2373 22c. OFFICE SYMBOL 63 Es

DD FORM 1473, 84 MAR 83 APR edition may be used until exhausted. All other editions are obsolete

SECURITY CLASSIFICATION OF THIS PAGE

19. cont.

analysis and dynamical sensitivity tests in which the model equation is modified during the integration. Beta drift can be described as a balancing process between linear Rossby dispersion which generates the asymmetric gyres and nonlinear advection that moves the vortex to limit gyre development. Vortex structure is the key to this balance as it determines both the linear generation of the asymmetric forcing and the nonlinear interaction between the symmetric and asymmetric circulations.

Approved for public release; distribution is unlimited

The Role of Vortex Structure in Tropical Cyclone Motion

by

Michael Fiorino
B.S., Pennsylvania State University, 1975
M.S., Pennsylvania State University, 1978

Submitted in partial fulfillment of the requirements for the degree of

DOCTOR OF PHILOSOPHY IN METEOROLOGY

from the

NAVAL POSTGRADUATE SCHOOL
December 1987

Author: Michael Fiorino
Michael Fiorino

Approved by:

C.-P. Chang
Professor of Meteorology

R. Franke
Professor of Mathematics

P. Jacobs
Professor of Operations Research

R.T. Williams
Professor of Meteorology

R.L. Elsberry
Professor of Meteorology
Dissertation Supervisor

Approved by: R.J. Renard, Chairman, Department of Meteorology

Approved by: Kneale T. Marshall, Acting Academic Dean

ABSTRACT

The role of vortex structure in tropical cyclone motion is studied using a moving-grid, nondivergent barotropic model on a β plane in a no-flow environment. Initial condition sensitivity tests reveal that the northwestward "beta" drift of the vortex is controlled by the symmetric circulation in the r = 300 - 800 km "critical" annulus. Enhanced cyclonic or anticyclonic flow in this critical annulus leads to long-term cyclonic or anticyclonic turning motions. The dynamics of the motion process is examined in terms of the symmetric and asymmetric circulations. When the vortex is moving in a quasi-steady manner, the asymmetric flow appears as a pair of large-scale, counter-rotating gyres with a broad "ventilation" flow through the vortex center. A second much smaller pair of gyres is also found near the center. It is the interaction between these two sets of gyres and the symmetric flow that governs the motion process as revealed by a streamfunction tendency analysis and dynamical sensitivity tests in which the model equation is modified during the integration. Beta drift can be described as a balancing process between linear Rossby dispersion which generates the asymmetric gyres and nonlinear advection that moves the vortex to limit gyre development. Vortex structure is the key to this balance as it determines both the linear generation of the asymmetric forcing and the nonlinear interaction between the symmetric and asymmetric circulations.

TABLE OF CONTENTS

LIST OF TABLES

LIST OF FIGURES

ACKNOWLEDGMENTS

This research effort was not funded through normal R&D channels. However, the project was not unsupported and would have been impossible without the generous computational, technical and administrative resources of Fleet Numerical Oceanography Center. I would also like to acknowledge my former employer, the Naval Environmental Prediction Research Facility, who fully backed my Ph.D. program and continued to provide assistance throughout the research.

Although the FNOC computational resources were a necessary condition, the high level of science only occurred through the boundless energy, enthusiasm and insistence on excellence of my thesis advisor, Professor R.L. Elsberry who made my efforts an outstanding learning experience. I also wish to thank the other members of my committee: Professor R.T. Williams who provided excellent guidance and insight into the dynamics of my problem; Professor C.-P. Chang for his comments and expeditious handling of the final stages; Professor R. Franke for making my passage through the mathematics minor an almost painless experience; and Professor P. Jacobs for her interest and her role as the "outsider" giving larger context to the work.

A special note of thanks goes to my family and especially to my fiancée Sue Hill. Their constant love and support kept me afloat during the seemingly never-ending toil.

This dissertation is dedicated to my grandfather John Fiorino. He immigrated to this country as a penniless orphan from Bari, Italy and taught himself to read and write in both Italian and English. His life-long love of learning and strongly-held belief that education was the key to improving our family's position in America have been a constant inspiration for my academic pursuits.

I. INTRODUCTION

The dominant concept in the theory and forecasting of tropical cyclone motion is "steering." The essential nature of the steering process can be represented by the motion of a "leaf on a flowing stream;" i.e., the leaf is bodily carried along without interaction with the stream's steering current. This analogy has been applied to the motion of tropical cyclones with surprisingly (considering the complex physics in these cyclones) good success. The studies of George and Gray (1976) and Brand et al. (1981) clearly show the existence of a statistically significant relationship between the mean (over many storm cases) tropical cyclone motion vector and the much larger scale, mean flow vector. As pointed out by Chang and Madala (1982), the standard deviation of the difference between the storm motion and the large-scale flow vector is much greater than the average of this difference. This implies that on a storm-by-storm basis the mean relationship is not strong, and that large deviations of the storm motion vector from the surrounding larger-scale flow are possible (Bell, 1979).

The real-data analysis of Jones (1970) is a good illustration of how this discrepancy can occur. In his study, the flows "inside" and "outside" a hyphothesized interaction radius were compared to the storm motion. Large discrepancies were found, particularly between the motion and the inside flow, which suggests a radial dependence on the motion-steering flow relationship. Jones (1977) studied the vortex motion in a numerical model and showed a similar radial dependence between the motion vector and the environmental flow.

There are two explanations for the large standard deviations and motion discrepancies noted above. Either the steering flow and the storm motion are poorly defined and/or inadequately measured, or the implied simple point steering relationship is not as reasonable as the mean statistics suggest. Both sources of "error" are probably contributing to the large standard deviations. Neumann (1979) illustrates the difficulties in defining both the horizontal steering current and at what level the steering process is operating. Certainly the lack of observations is a significant contributor to the uncertainties in the tropical cyclone-steering relationship. However, tropical cyclone motion is more complex than a simple relationship to some mean flow at a single (or integrated) level.

First, the separation of the tropical cyclone scale of motion from that of the "environment" is not as simple and clear-cut as steering theory would imply. More importantly, the tropical cyclone is not a "solid" vortex being "pushed" along by some "steering" stream. In reality, the storm interacts with its environment in many ways. Therefore, the fundamental physical problem is how this interaction occurs. The particular goal of this study is to understand how the structure of the tropical cyclone contributes to the motion.

A. CURRENT UNDERSTANDING

Observational studies of the dependence of motion on structure have mainly been based on composite studies. The most notable is Chan (1982). Although his results are mixed, it can be seen (i.e., Table 4, Chan, 1982) that the variations in the differences between the steering flow vector and the storm motion vector as a function of cyclone size (e.g., radius of 30 kt winds) and intensity (e.g., maximum wind speed) are greater than for other stratifications (e.g., speed of motion).

In contrast to the limited observational evidence, the motion problem has received considerable theoretical attention and these theories invariably involve some dependence on tropical cyclone structure. The earliest motion theories assumed very simple models for the tropical cyclone structure. The poleward drift of a symmetric, cyclonic vortex in solid body rotation was first deduced by Ferrel (1859), although this discovery has been attributed incorrectly to Rossby (1948). Other examples of this type of vortex model include Yeh (1950) and Kuo (1969).

Significant improvements in tropical cyclone motion theories occurred in the 1950's, as highlighted by the work of Kasahara (1957). Although the motion solutions were derived from a physically more realistic basis, the vortex necessarily was kept simple. In fact, the only dependency on storm structure was represented by a size parameter and the vortex (as well as the environment) was assumed to be barotropic. Extensions of these barotropic, analytical theories to a baroclinic atmosphere (Kasahara, 1960) did not address the role of structure in the motion process.

Recent developments have expanded and clarified the problem. Holland (1983) and Chan (1982) analytically solved the barotropic vorticity equation with a vortex profile that more explicitly demonstrated how cyclone size influences motion under simple environmental flow conditions. DeMaria (1985) examined the same problem with a numerical barotropic spectral model. The advantage of DeMaria's spectral approach was that the arbitrary scale separation (large-scale environment and small-scale vortex) necessary in analytical treatments was avoided, and the inherent aliasing of finite difference models was reduced. While DeMaria's results tended to confirm the findings from the simpler models, he also demonstrated that the impact of storm size

on motion was a function of the base state (large-scale flow) vorticity gradient.

Most recently, Chan and Williams (1987) have examined in more detail the underlying barotropic dynamics of tropical cyclone motion. They have shown that the nonlinear advection terms in the barotropic vorticity equation are required for significant displacement of the vortex center. The primary role of the so-called β term is to force a wavenumber one asymmetric distortion in the initially symmetric vortex by the Rossby wave dispersion effect. The linear β effect does not cause the storm center to move. Rather, the storm is advected by the linearly-induced asymmetric circulation. They also examined how the motion depends on the shape of the initial vortex tangential wind profile and found that larger storms have greater motion or "beta drift."

Experimentation with baroclinic numerical models has been surprisingly limited. Hovermale (1980) does highlight how different structures (again size) can have significant impacts on the track and that the sensitivity depends on the vertical shear of the large-scale flow. Mathur (1987) has extended Hovermale's work using a more sophisticated hurricane model and reported similar sensitivity to cyclone size.

Important findings and areas of needed research may be summarized:

(i) Current theory is primarily barotropic. Dependence of beta drift on storm factors has been demonstrated, but the dynamical reasons behind the response are not well understood;

(ii) The nonlinear effects generate motion in response to asymmetric distorting forces (e.g., β); and

(iii) The dependence of the nonlinear effects on vortex characteristics and the distorting forces is unknown.

From this brief review, it can be seen that many important scientific questions need to be addressed. However, there is more than just academic interest in this problem, as two recent notable failures of two operational dynamical forecast models illustrate.

Supertyphoon Abby of 1983 was the most significant cyclone in recent memory with regard to impact on DOD operations. The forecast errors (mean great circle distance between the forecast and verifying position) of the Joint Typhoon Warning Center (JTWC), Guam were fairly typical, but the track errors (distance from the verifying position to the track) were larger than average and had the effect of placing nearly all of the DOD assets in the western North Pacific on alert. The JTWC forecasts were consistent with the guidance from two dynamical models: (i) the One-way influence Tropical Cyclone Model (OTCM) (Hodur and Burk, 1978); and (ii) the Nested Tropical Cyclone Model (NTCM, version 2.0) (Harrison, 1981). Abby was a very large typhoon and the inability of the two models to properly simulate this size of cyclone was thought to be a partial explanation of the forecast failure. Fiorino (1985a) and Chan (1986) provide a complete discussion of this important storm. The main point is that the structure of Abby was apparently a very significant factor in its track.

Another operationally important case was tropical storm Narda in the eastern North Pacific (Fiorino, 1985a). Narda was a very shallow storm with weak winds and little convection. As Narda approached the Hawaiian islands, the NTCM consistently predicted a turn to the north, even though Narda was tracking with the northeast trades. The NTCM is initialized with a 60 kt bogus and uses a heating field that maintains a deep circulation. The inability of the NTCM to predict such a shallow storm explains part of the model's erroneous prediction. Although Narda was clearly not a

dangerous cyclone, the decision of the National Weather Service to forecast a track over Oahu nearly resulted in an unnecessary evacuation of all Navy ships from Pearl Harbor!

The Abby and Narda cases demonstrated that storm structure needs to be more fully considered in dynamical forecast systems and in operational forecast preparation. This opinion was strongly endorsed in a planning meeting on dynamical tropical cyclone models during January, 1985 (Elsberry and Fiorino, 1985). The operational representatives stated that one of the most important features of an advanced tropical cyclone forecast model is the ability to correctly (realistically from the viewpoint of the forecaster) specify the initial tropical cyclone vortex. This desire is not solely based on theory, but also on forecaster experience (as noted above) that structure can be an important element in track prediction.

However, a different sentiment has been expressed by some forecasters from the National Hurricane Center (NHC), Miami. According to R. Sheets (personal communication) of NHC, "steering is 80% of the problem." Consequently, there have been great efforts at NHC to improve the analysis of the "steering current." While there is no doubt that greater observational density and better analysis methods will be necessary for track prediction advancements, limitations in theoretical understanding of the motion process also could seriously restrict future gains. Research into the role of structure in tropical cyclone motion can help settle the issue, i.e., is steering 80% of the problem, or are storm effects important, and if so when?

B. GOALS OF THE RESEARCH

This research hinges on two basic premises:

(i) It is necessary to more fully understand simple models (dynamics) before studying more complicated effects.

(ii) Tropical cyclone motion is essentially a barotropic process. Baroclinic and physical effects can be thought of as modifying the barotropic motion process by changing the storm and the vertical level at which interaction with the environment occurs.

The literature review has shown that current theory has relied on simple models and has provided insight into the actual dynamics of the motion process. Thus, the first premise is well supported. The validity of the second premise has not been explicitly supported and is really a simplifying assumption. However, many participants at a recent Planning Meeting on the Theory of Tropical Cyclone Motion (Elsberry, 1986) felt that the barotropic model is a good first-order approximation.

Given these two premises, the basic goals of this research are:

(i) To more completely understand the dynamics of the barotropic motion process; and

(ii) To determine which features of the vortex (e.g., maximum wind, size, total relative angular momentum, etc.) have the greatest influence on motion.

The research uses three kinds of tools to meet these goals: 1) a nondivergent barotropic numerical model as the dynamical basis; 2) new analysis procedures to diagnose the motion process from the model solution; and 3) special model adaptations to isolate the nonlinear and linear effects and interactions between the symmetric and asymmetric circulations.

Chapter II describes: (i) the numerical model; (ii) the numerical precision of the solutions; and (iii) a moving grid procedure to permit ultra-long ($t \geq 12$ days) integrations and to simplify solution analysis. The

dynamical limitations of a no-flow environment on a β plane (the beta drift problem) are also addressed in this chapter.

The dependence of beta drift on the symmetric vortex structure is first determined in Chapter III using an initial-condition sensitivity approach in which a series of vortices, which are patterned after typical tropical cyclone structures, are used as initial conditions in the integrations. The tracks show that the structure of the flow beyond r = 300 km determines beta drift.

In Chapter IV, the dynamics of beta drift is examined through a streamfunction tendency analysis of the symmetric and asymmetric circulations. This analysis explicitly demonstrates how the symmetrical circulation induces an asymmetric flow via linear Rossby wave dispersion and how the asymmetric circulation interacts with the symmetric circulation to move the vortex.

In Chapter V, the concepts developed in the tendency analysis (which is a "static" approach) are then extended by directly modifying the dynamical terms in the model equation. In this way, the nonlinear interactions between the symmetric and asymmetric circulations can be controlled during the integration (a form of "dynamical" sensitivity analysis). It is shown that the motion process occurs on two scales. In the inner-core (r < 100 km), the advection of asymmetric vorticity by the symmetric flow is responsible for the motion of the center. The advection of symmetric vorticity by the asymmetric flow, which appears as a steering-type process, moves the larger components of the vortex (100 km < r < 600 km). These two motion processes have varying contributions to the overall motion of the vortex depending on the strength of the vortex flow in the inner regions (r < 300 km).

The longest integrations of a barotropic model of this type in previous studies has been 96 h (Kitade, 1981).

Extended integrations presented in Chapter VI (made possible by the moving grid procedure) indicate that when Rossby dispersion acts for "ultra-long" periods (~ 12 days), a common or "universal" profile tends to develop in the outer regions ($r > 300$ km). The concept of a "β-neutral" profile is developed and the possible application to real cyclones is addressed.

The initial-condition sensitivity experiments in Chapter III, together with the dynamical understanding developed in Chapters IV and V, are re-examined in Chapter VII from a Fourier series viewpoint. In this viewpoint, the initial vortex is represented as a sum of wave components using a generalized 2-D Fourier transform. Then scale groups (e.g., small, medium and large) are either deleted or retained in the initial specification of the vortex structure. Model integrations with these Fourier filtered initial conditions demonstrate that the largest scales ($\lambda \geq 1500$ km) control the speed of motion and that the medium scales (500 km $< \lambda <$ 1500 km) determine turning motions.

Finally, a summary and conclusions is provided in Chapter VIII where the implication of these results to future theoretical studies and tropical cyclone forecast models is addressed. The fundamental result of this study is that the dynamics of tropical cyclone motion are a highly nonlinear process and that the initial (and evolving) vortex structure can be a large factor in the motion process. Thus, it is recommended that greater emphasis be given to vortex specification (including both the initial cyclone and the insertion procedure) in future dynamical tropical cyclone forecast models.

II. THE MODEL AND NUMERICAL PROCEDURES

The dynamical basis of this study is the conservation of absolute vorticity, which is mathematically expressed by the nondivergent barotropic vorticity equation. This model contains the two most fundamental dynamical processes involved in vortex motion: 1) nonlinear interaction (advection); and 2) linear wave dispersion due to the gradient of absolute vorticity (e.g., the β effect). Both processes are critical to motion as shown by Chan and Williams (1987). Observational support for this model was given by Chan (1984). The following development is patterned after Tupaz (1977) and Chan and Williams (1987).

A. ANALYTICAL FORMULATION

The conservation of absolute vorticity is simply

$$\frac{d\zeta_a}{dt} = 0 \quad , \tag{2.1}$$

where ζ_a is the absolute vorticity. Expanding the total derivative into the local or Eulerian derivatives, (2.1) becomes

$$\frac{\partial \zeta}{\partial t} + \vec{V} \cdot \nabla\zeta + \frac{\partial f}{\partial y} v = 0 \quad , \tag{2.2}$$

where ζ is the relative vorticity and the other variables have their usual meaning. Assuming that the latitudinal variation of the Coriolis parameter ($\beta = \partial f/\partial y$) is a constant (the β-plane approximation), the governing equation becomes

$$\frac{\partial \zeta}{\partial t} + \vec{V} \cdot \nabla\zeta + \beta v = 0 \quad . \tag{2.3}$$

In this study, β is set to a value valid at 15° N. The initial assumption that absolute vorticity is conserved implies that the flow is nondivergent. Thus, a streamfunction (ψ) can be defined to represent the wind components. That is,

$$\nabla^2\psi = \zeta \quad , \tag{2.4}$$

and

$$\vec{V} = \hat{k} \cdot \nabla\times\psi \quad , \quad \text{or} \quad u = -\frac{\partial\psi}{\partial y} \, , \quad v = \frac{\partial\psi}{\partial x} \quad . \tag{2.5}$$

In comparison to more complex and physically more complete models, it is important to note that the nondivergent, barotropic model does not permit mass-momentum adjustments (gravity waves and geostrophic adjustment) and does not allow for inertial instability (e.g., Alaka, 1962). Although barotropic instability is possible, it is not readily apparent in the vortex motion solutions. In summary, the model is dynamically conservative and can only represent the presumed dominant effects of vorticity advection and Rossby wave dispersion.

Applying the streamfunction representation to (2.3) and rearranging the order of differentiation, the analytical form of the model to be solved numerically is

$$\nabla^2 \frac{\partial\psi}{\partial t} + J(\psi,\nabla^2\psi) + \beta \frac{\partial\psi}{\partial x} = 0 \quad , \tag{2.6}$$

where J is the Jacobian defined as

$$\begin{aligned} J(\psi,\nabla^2\psi) &= \frac{\partial\psi}{\partial x}\frac{\partial\zeta}{\partial y} - \frac{\partial\psi}{\partial y}\frac{\partial\zeta}{\partial x} \\ &= v\frac{\partial\zeta}{\partial y} + u\frac{\partial\zeta}{\partial x} \quad . \end{aligned} \tag{2.7}$$

Thus, changes in ψ are due to both nonlinear ($J(\psi,\nabla^2\psi)$) and linear ($\beta\partial\psi/\partial x$) effects. Setting the Jacobian term to zero produces the linear vorticity equation describing pure Rossby wave dispersion (Rossby, 1939) since the Jacobian term contains the nonlinear effects of vorticity advection.

B. NUMERICAL FORMULATION

Solutions to the full model equation are obtained numerically using the same methods as employed by Tupaz (1977). Only highlights are given here, as the detailed description can be found in Tupaz (1977) or Tupaz et al. (1978).

The model equation (2.6) is solved on a rectangular, Cartesian grid with uniform grid spacing. A typical configuration is 101 x 101 points in the north-south and east-west directions with a horizontal grid increment, Δx, of 40 km. The Jacobian term is estimated using the Arakawa (1966) form, which ensures conservation of energy and enstrophy, and the linear β term is calculated using centered differences. Given the forcing function on the right side of (2.6), the Helmholtz equation for the streamfunction tendency is solved using a direct or matrix inversion method (Sweet, 1971; Rosmond and Faulkner, 1976). The boundary conditions for the Helmholtz tendency equation (for the Jacobian) are the same as used during the model integration (described in next section). The time integration is then made using centered-in-time differencing and a time step, Δt, determined by the Courant-Friedrichs-Lewy (CFL) linear stability requirement (e.g., Haltiner and Williams, 1980)

$$c\,\frac{\Delta t}{\Delta x} \leq \frac{1}{2^{1/2}} \quad , \tag{2.7}$$

where c is the phase speed of the fastest moving wave (the advecting velocity in this model). These numerical

procedures are fairly standard and produce smooth and stable results.

1. Boundary Conditions

The lateral boundary conditions used in this version of the model are somewhat simpler than in Tupaz (1977), who specified a zero vorticity gradient at the penultimate row and $\psi = 0$ at the north and south boundaries. In this version of the model, no slip or a zero gradient of ψ is assumed, so that ψ on the north and south boundaries are the same as at the first adjacent interior rows. As in Chan and Williams (1987), cyclic continuity or periodicity is assumed in the east-west direction. These boundary conditions are mathematically stable and allow for the shifting of the grid during the integration.

It should also be pointed out that the north and south boundary conditions will affect the linear Rossby wave dispersion. Thus, changes in boundary conditions and domain size will affect the linear dispersion characteristics of the model.

2. Moving Grid

A moving vortex in a geographically-fixed grid complicates calculation of the dynamical quantities relative to the moving center. Even with a relatively large domain of 4000x4000 km, a 72-h translation of 1000 km would put the vortex within 1000 km of a boundary (assuming an initial position at the center of the domain). The non-uniform distribution of the model solution relative to the center would prevent a meaningful analysis beyond 1000 km. Thus, the model grid is shifted to keep the vortex near the center of the domain, which avoids any boundary contamination of the solution within 2000 km of the center. Another important advantage of the moving grid is that extremely long integrations (e.g., 12 days in Chapter VI) are possible without the necessity of extremely large domains.

Since the model lateral boundary conditions are specified in terms of the adjacent interior values, the entire grid can be shifted one grid point without losing any information. Furthermore, the β-plane assumption implies that the earth's vorticity gradient is not a function of position, so a shift in the grid does not change the external forcing relative to a geographically fixed grid.

When the vortex center moves one grid interval away from the grid center, the indices of the solution are shifted one value in the opposite direction. For example, if the vortex center moved eastward from I = 51 to I = 50, then the I = 2 (I = 101) value on unshifted grid becomes the I = 1 (I = 100) value on the shifted grid and the storm would again located at I = 51 (2 --> 1 and 51 --> 50). The cyclic ψ boundary conditions at I=1 and I=101 are then applied (2 --> 101 and 100 --> 1) to specify the solution on the trailing edge. A record of the grid shifts is stored to permit reconstruction of the track of the vortex relative to a fixed grid.

Experiments with moving and stationary grids showed very little difference (less than 1%) in the tracks. The moving grid procedure apparently does not affect vortex motion and allows for a simplified analysis of the solutions.

3. Vortex Center Definition

The center of the vortex may be specified as either the location of maximum relative vorticity or of minimum streamfunction. Both of the ψ and ζ centers are calculated each hour during the integration. To interpolate for a center between grid points, the ψ or ζ is represented by an analytical function. The center location algorithm locates the greatest extrema on the grid as a first guess of the vortex position. This estimated position is then refined using Stirling's polynomial interpolation function (e.g.,

Gerald and Wheatley, 1984) in the Fleet Numerical Oceanography Center (FNOC) routine "MINMAX." This routine finds where the derivative of the function goes to zero in an area within one grid point around the first guess.

4. Summary

The numerical procedures used to solve the nonlinear model equation are straightforward and well behaved. The model has been optimized to run on the CYBER 205 supercomputer at FNOC using vector coding. However, vector size limitations and the direct solver make the model somewhat expensive for large domains with small grid intervals (a 201x201 grid with Δx = 20 km requires almost 1000 CP sec for a 72 h integration). More advanced elliptical equation solvers, and perhaps nesting of a fine grid within the domain, would improve the efficiency of the model. Nevertheless, the current model yields satisfactory solutions for the purposes of this study.

C. NUMERICAL PRECISION

It is very important to establish the numerical precision of the model solution procedures to assure that numerical effects are not misinterpreted as physical processes. The key numerical issues are the appropriate grid spacing and the domain size for a tropical cyclone application, as the accuracy of the numerical methods for the same type of model has been established from previous studies (e.g., Chan and Williams, 1987; Tupaz et al., 1978).

For tropical cyclone-scale vortices, the radius of maximum wind (RMW) is on the order of r = 40 km (Weatherford, 1985) and a grid spacing of 10-15 km would be required to resolve the inner core with 6-10 points for reasonable accuracy (Haltiner and Williams, 1980). If a RMW larger than 40 km could be used, there would be a considerable savings in computational resources. These savings would not only reduce execution time, but would also

allow for physically larger domains without resorting to nested grids (e.g., Harrison, 1973). Experiments by DeMaria (1985) and Chan and Williams (1987) have shown that the motion of a vortex on a β plane does not depend on the intensity of the inner core. Thus, it would be reasonable to expect little dependence of vortex motion on the RMW (scale of the inner core). Therefore, it is important to perform numerical sensitivity tests with a series of vortices in which only the radius of maximum wind is changed.

Domain size restricts the development of large-scale features through the lateral boundary conditions. If such features are important to the simulation of β drift effects, then it would be desirable to use large grids. The array (vector) size on the FNOC CYBER 205 is limited to 64K words for high-speed vector operations. For a square domain, this vector size limitation is equivalent to 256x256 grid points. Therefore, the maximum domain size for a non-nested grid becomes a function of grid spacing if advantage is to be taken of the much faster vector processing.

The first numerical tests determine the role of the inner core (in the vicinity of r = RMW) in controlling vortex motion by varying the radius of maximum winds while holding all other parts of the vortex fixed. Once the maximum RMW is determined, then the grid spacing is varied to determine resolution effects. Finally, the domain size is varied to show how boundary conditions modify the large-scale features and change the motion of the cyclone.

1. Radius of Maximum Wind Test

The tangential wind profile of the "basic vortex" is shown in Fig. 2-1. This vortex represents a typical tropical cyclone with a maximum wind speed of 35 m/s (weak typhoon intensity) and the radius of 30 kt (15 m/s) winds is 300 km (Williams, 1986). Although the RMW = 100 km is

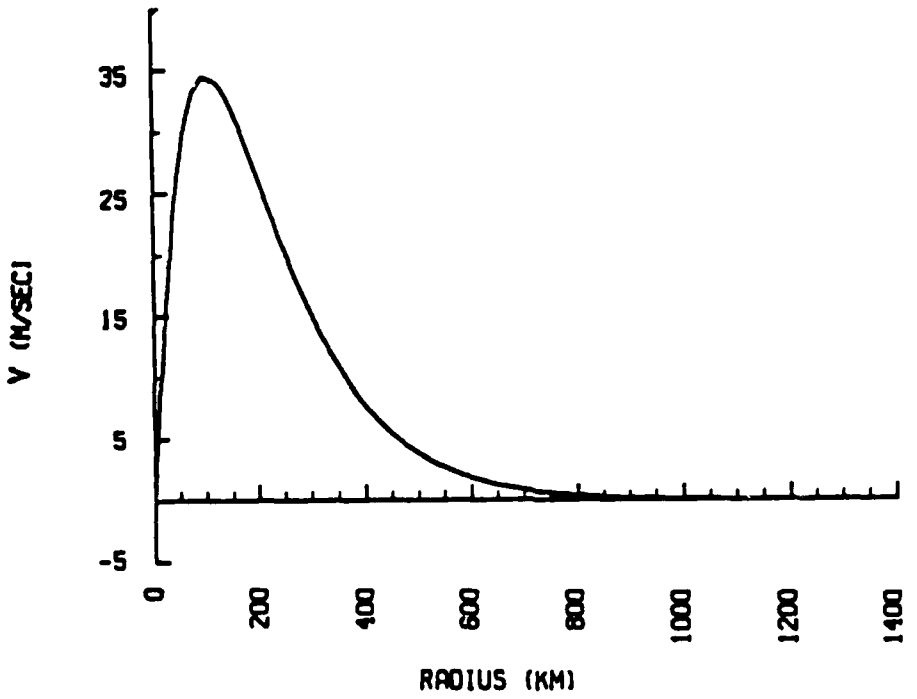

Fig. 2-1. The tangential wind profile of the "basic" vortex.

larger than typically observed, the inner strength, or the area-averaged tangential wind in the r = 100-300 km annulus, is still reasonable (Merrill, 1982; Weatherford, 1987). Using the vortex specification procedure to be described in Chapter III, this basic vortex is first modified (Fig. 2-2) to shift the RMW inward to r = 50 km, which is a more representative value. This modified vortex is nearly identical to the basic vortex in terms of inner strength and size. However, there are small differences within r < 200 km.

The initial model configuration used in the RMW test has 101x101 points in the east-west and north-south directions and a grid spacing of 40 km. The moving grid option is used for all the runs to simplify solution analysis. The 72-h tracks for the two RMW specifications are shown in Fig. 2-3. Except for the short-term, small-scale oscillations in the RMW = 50 km case, the tracks are nearly identical, especially at 72 h. As demonstrated in the next section, the oscillations are caused by numerical errors. However, the basic conclusion is that when the vortex structure is fixed outside of r = 150 - 200 km (the inner core), the RMW has no bearing on the vortex track. It is interesting to note that the maximum wind and the strength of the flow in the r = 100 - 300 km annulus are not well correlated in real tropical cyclones (Weatherford, 1985). This is similar to lack of a motion dependence on intensity.

2. Horizontal Resolution Effects

Some researchers (e.g., Chan and Williams, 1987; Kitade, 1981) have speculated that the small-scale oscillations, which have been observed in comparable nondivergent barotropic models models initialized with similar vortices, may be a physical effect. The physical realism of the oscillations is determined by decreasing the

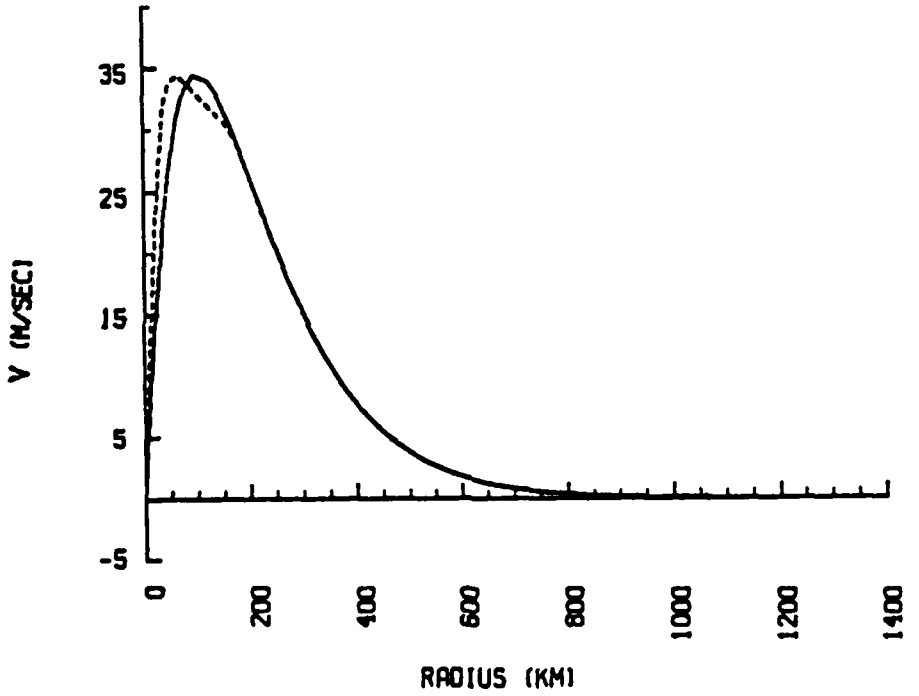

Fig. 2-2. Basic (solid) and modified (dashed) tangential wind profiles used in the radius of maximum wind test.

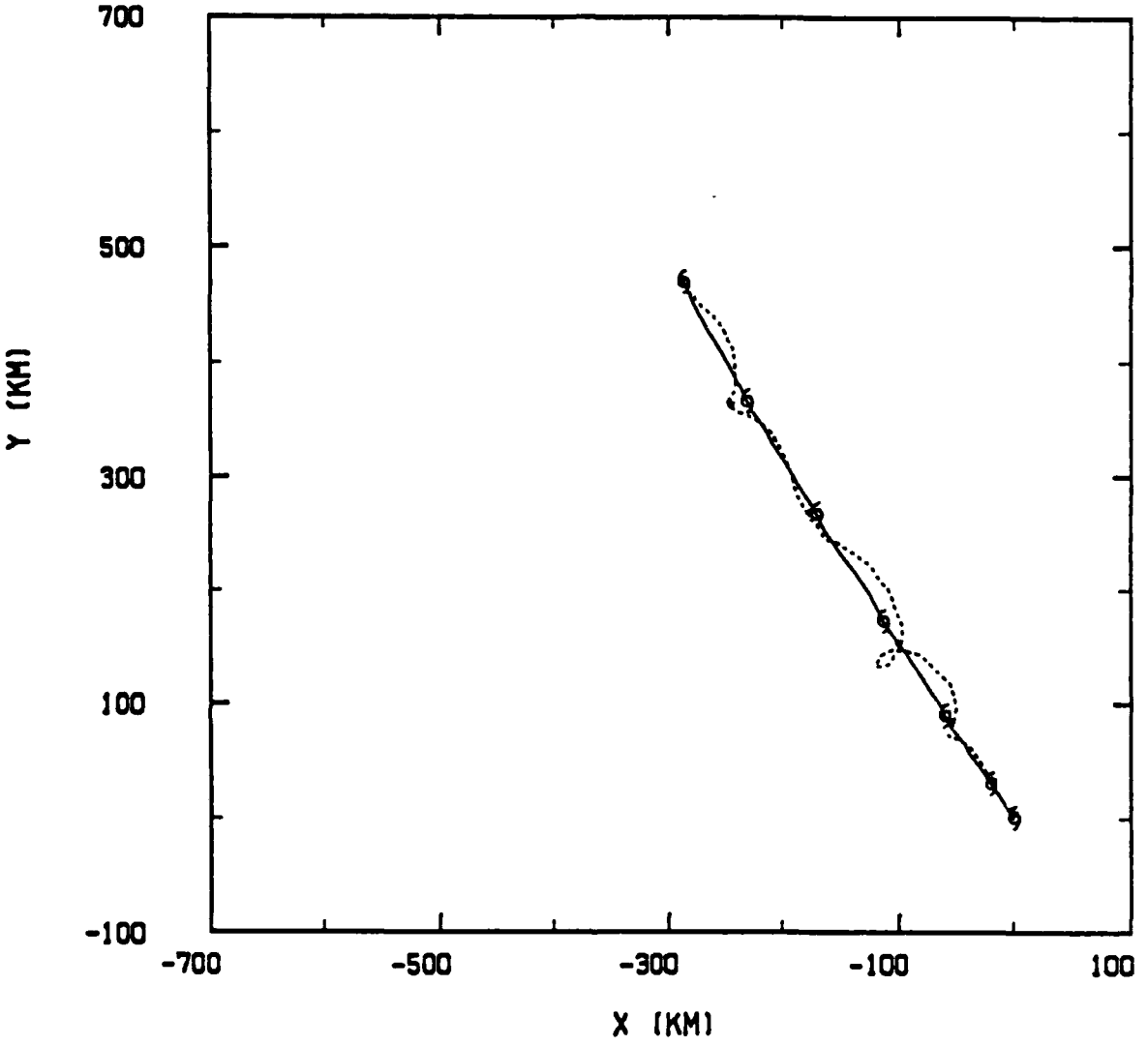

Fig. 2-3. The 72-h track of the basic vortex with RMW = 100 km (solid) and RMW = 50 km (dashed). The 12-hourly positions are denoted with an asterisk (RMW = 50 km) and a hurricane symbol (RMW = 100 km). The model is configured with 101x101 points and Δx = 40 km. The 72-h positions are highlighted.

grid spacing by one half while holding the domain size fixed, i.e., using a configuration of 201x201 points with Δx = 20 km vice the domain with 101x101 and Δx = 40 km. The track forecasts from the higher-resolution model for the same vortices are given in Fig. 2-4. The track fluctuations in the RMW = 50 km vortex have been reduced, but the 72-h positions have not changed. This implies that the oscillation depends on the resolution and thus must be numerically related. Runs (not shown) with even higher resolution (Δx = 10 km) confirmed that the oscillations are strictly a numerical artifact.

As a further test of resolution effects, the domain size is fixed and the resolution is degraded by increasing Δx from 40 to 80 km. A grid spacing on the order of 80 km is typical of operational, uniform-grid tropical cyclone track forecast models (e.g., the Navy's NORAPS model (Hodur, 1987) and the National Meteorological Center's Movable Fine Mesh (MFM) model (Fiorino et al., 1982). The model is run with the basic vortex (RMW = 100 km) and the tracks are given in Fig. 2-5. Compared to Fig. 2-4, the tracks for Δx = 20 and 40 km are nearly identical, but the numerically generated track noise and a slight northward deviation are found when the grid spacing is increased to 80 km. The approximately 40 km difference at 72 h with Δx = 80 km implies that the simulation of the larger scale circulations is degraded and that this degradation affects the long-term motion.

Several conclusions regarding resolution can be made from these experiments. The small-scale (10-20 km) and short-term (12-24 h) oscillations in the simulated track are not physical and depend on grid resolution relative to the RMW (representative of the smallest scale in the tropical cyclone). That is, as the number of points in the high-resolution core (twice the RMW) is decreased, the amplitude

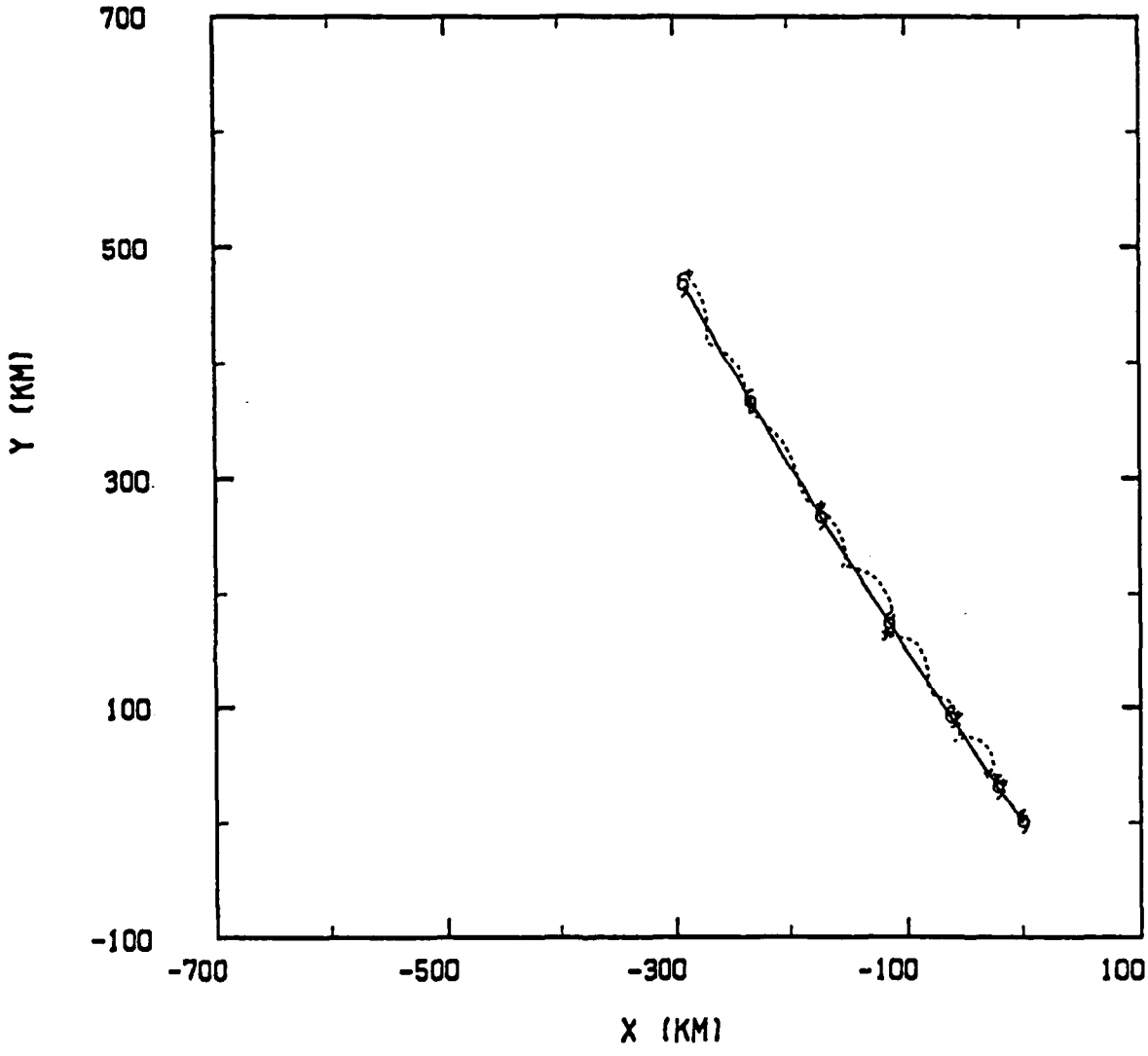

Fig. 2-4. As in Fig. 2-3, except with a model configuration of 201x201 points and Δx = 20 km.

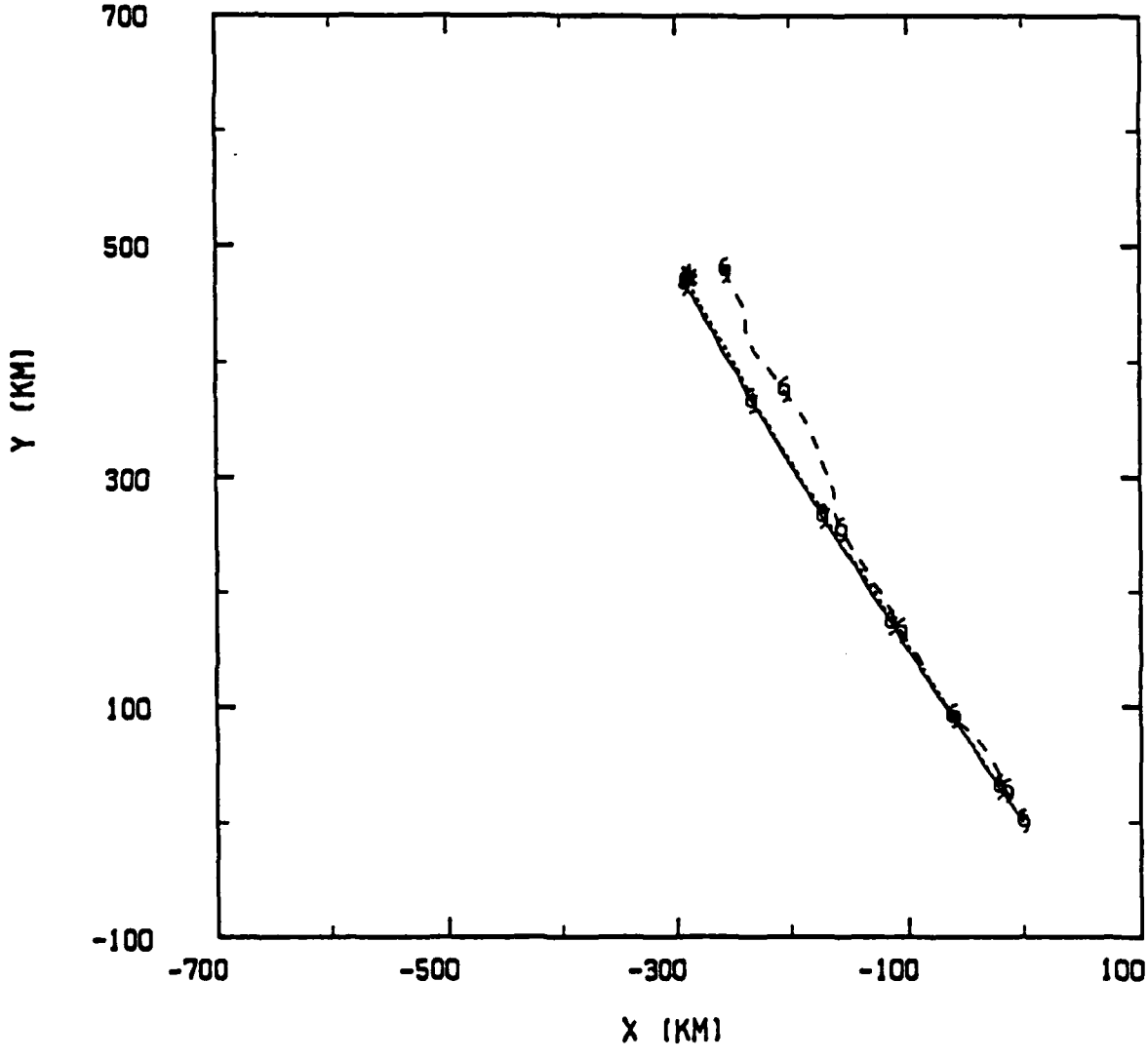

Fig. 2-5. Track forecast to 72 h for the basic vortex using model configurations with 201x201 points, Δx = 20 km (solid), with 101x101 points, Δx = 40 km (short-dashed) and with 51x51 points, Δx = 80 km (long-dashed). The 72-h positions are highlighted.

of the track noise increases (compare the RMW = 50 km, Δx = 40 km track to the RMW = 100 km, Δx = 80 km solution). Therefore, the smallest scales in the initial vortex should be forced to match the model resolution to avoid track noise. This track noise is not necessarily damped in the first 24 h of the forecast and can lead to long-term deviations from the numerically more precise simulation.

These conclusions are strictly applicable only to a nondivergent, barotropic model. Assuming the motion process in the more complex baroclinic models is primarily due to advection processes, several implications for the coarse grid (Δx = 60 - 100 km) operational models may be suggested. No attempt should be made to initialize a coarse-grid model with a realistic inner core (e.g., RMW = 40 km) structure. On the positive side, the fairly successful (relative to the most precise numerical solution) simulation with Δx = 80 km suggests that coarse-resolution models may have reasonable track prediction skill and that higher resolution may not lead to a significant improvement (Fiorino, 1985b). That is, the skill of coarse-resolution models may not be necessarily compromised by horizontal resolution limitations.

Unless otherwise stated, all tracks will be smoothed to remove numerical track noise and thus to avoid misrepresentation of the simulated motion. The procedure involves the application of a smoother-desmoother operator (Shuman, 1957) to the hourly (x,y) vortex positions prior to plotting or motion calculations. An example of the smoothing is given in Fig. 2-6 for the same experiments as in Fig. 2-5. Notice how the smoothing has eliminated some of the longer time scale (24-36 h) fluctuations as well as the shorter time scales. It is doubtful that these longer term fluctuations are realistic.

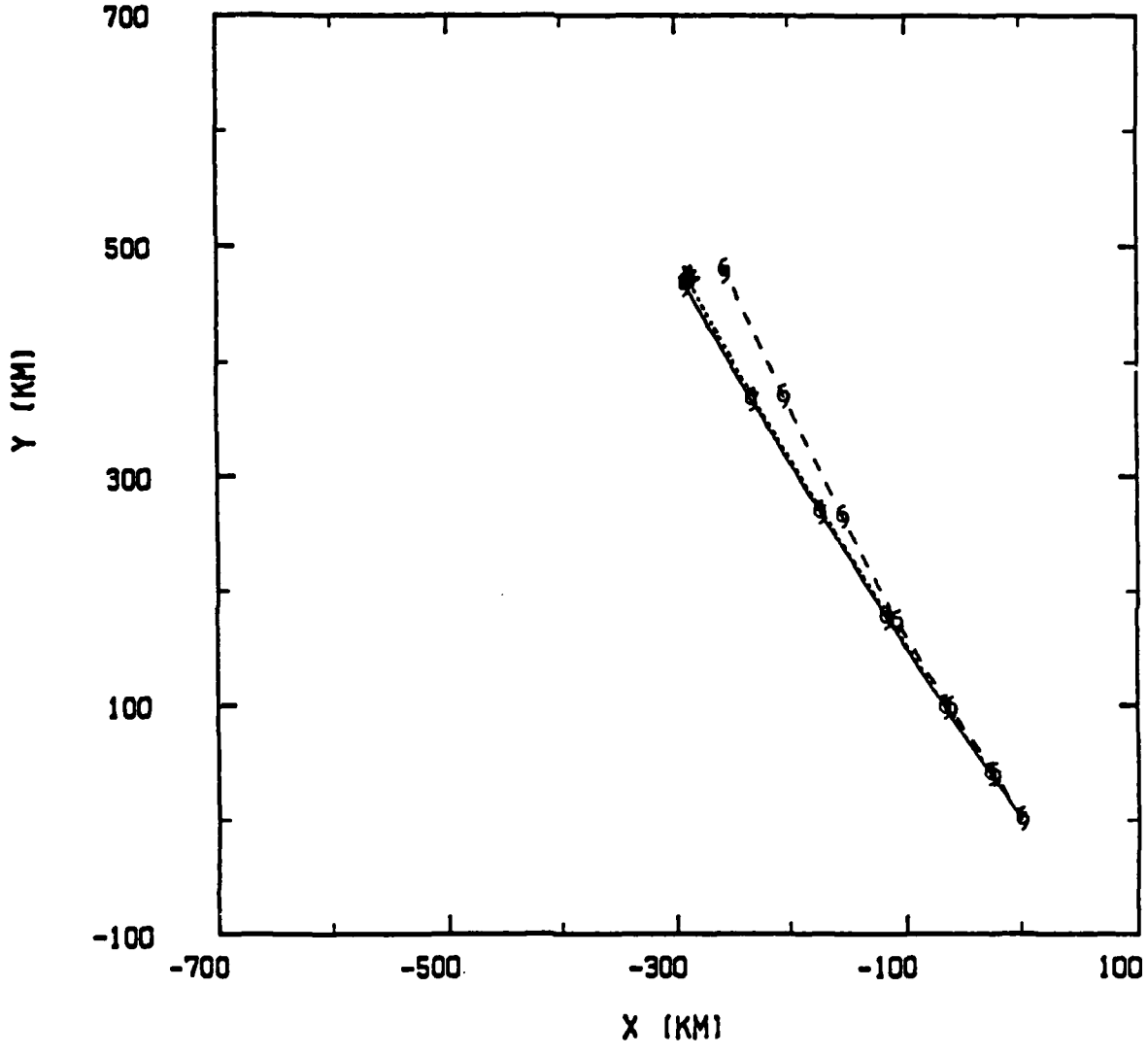

Fig. 2-6. As in Fig. 2-5, except with smoothing of the track.

3. Domain Size Effects

The RMW and resolution sensitivity tests establish a "standard" model configuration of 101x101 points with Δx = 40 km. Tests with larger grids (e.g., 201x201 points and Δx = 40 km) showed only small differences in the track (< 2%). However, reducing the domain size did have a significant effect, as shown in Fig. 2-7, which compares the track of the basic vortex in the standard model to a grid 51x51 points and Δx = 40 km. Reduction of the domain size from 4000 km to 2000 km on a side results in a westward motion as the smaller domain has affected the larger scales in the environment of the tropical cyclone. A similar result was obtained by DeMaria (1987) with a comparable model using real data. He suggested that increasing the domain size of the operational models might correct a common slow bias problem (Fiorino, 1985b). These results may also provide a clue as to why the nested-grid operational models (Harrison and Fiorino, 1982; Ookochi, 1978; and Iwasaki et al., 1987) have an especially severe slow bias. Although these models are far more complicated than the one in this research, the evaluation of the nesting techniques used even simpler approaches. Thus, a starting point for determining the source of the nested-grid model speed bias may be in the first-order barotropic dynamics that all such models contain.

The two-way interactive nesting procedure (Harrison, 1973) is supposed to provide uninhibited communication between the grids. A disruption in this communication may result in an "effective" domain size that is smaller than the largest grid and thus would cause slower motion as in Fig. 2-7. Such a reduced domain could slow the motion on average, especially if the effective domain size is that of the finest grid (e.g., 1200x1200 km in the NTCM). This concept is also supported by the domain-size experiments of

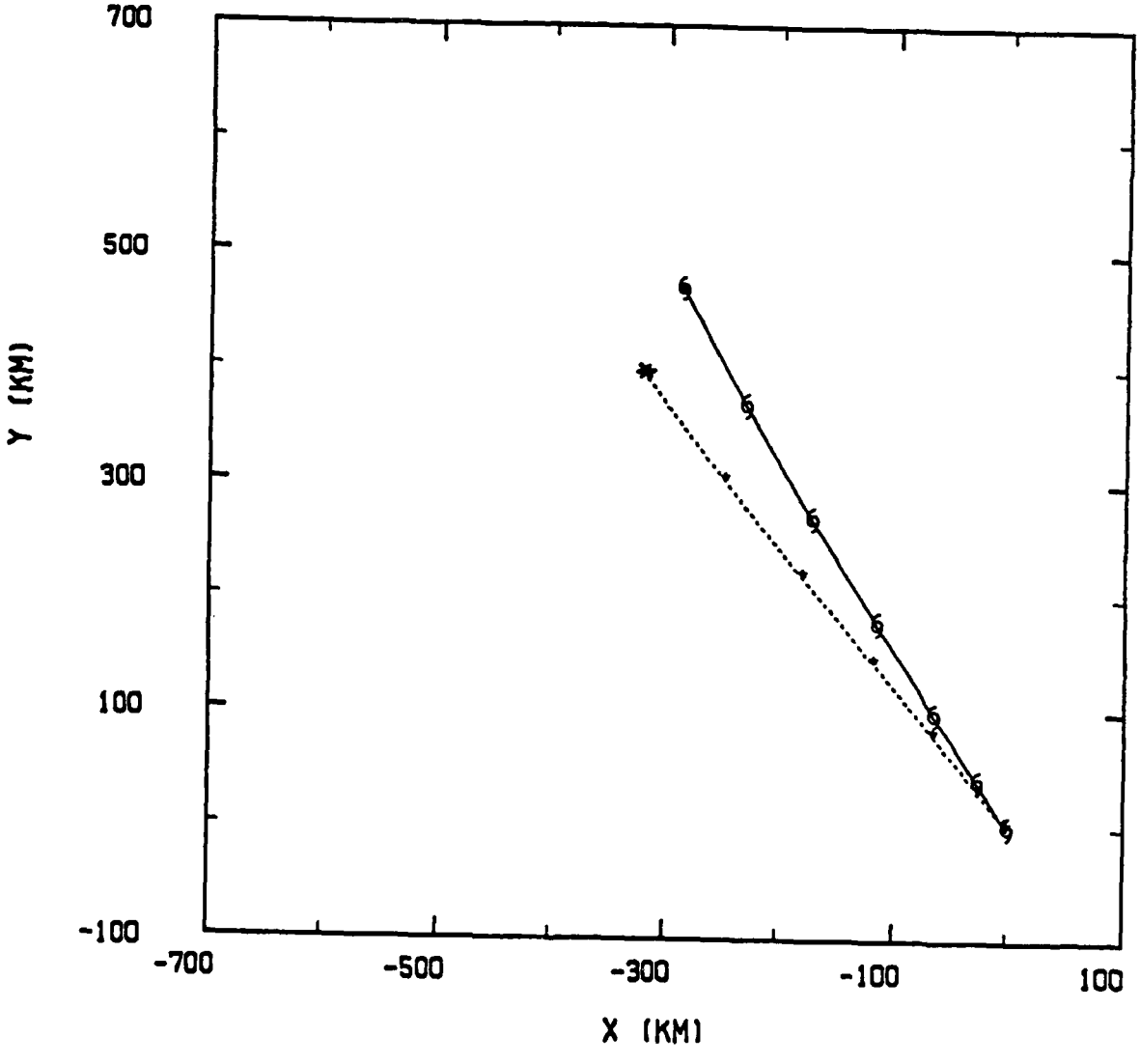

Fig. 2-7. Track to 72 h of the basic vortex using the standard model configuration of 101x101 points and Δx = 40 km (solid) and with 51x51 point and Δx = 40 km (dashed). The 72-h positions are highlighted.

DeMaria (1987) for a real-data barotropic forecast model. He finds the smaller domain sizes result in reduced motion and suggests that the slow bias may be related to the limited size of the operational models.

D. SUMMARY

The dynamical framework used in this study is the nondivergent barotropic vorticity equation on a β plane in a no-flow environment. Despite the simplicity of this system, the model does account for the two dominant dynamical processes in tropical cyclone motion: (i) nonlinear advection; and (ii) linear Rossby wave dispersion.

Numerical procedures to solve the model equation are fairly standard. However, a moving grid procedure that takes advantage of the free-slip north-south, and cyclical east-west lateral boundary conditions, has been developed to facilitate solution analysis and to allow for extremely long integrations of a moving vortex.

The numerical fidelity of the model, relative to the smallest scales in the vortex, has been established through a series of sensitivity tests with a vortex representative of typical tropical cyclone. The first test involves the radius of maximum wind. The vortex structure inward of r = 100 km has no bearing on the motion provided the vortex structure outside r = 150-200 km is fixed. The advantages of using a larger RMW (r = 100 km) than that typically observed are reduced computational resources and, more importantly, the potential for larger domain sizes to minimize possible lateral boundary contamination.

A fixed domain size of 4000x4000 km has been used to assess the impact of varying the grid spacing. A grid spacing that provides five to six points in the inner core (e.g., Δx = 40 km for RMW = 100 km) produces a smooth track. When the number of points is reduced by decreasing the scale of inner core (RMW = 50 km and Δx = 40 km), small-scale (10-

20 km) and short-term (12-24 h) oscillations are generated. It had been suggested in previous studies with comparable models that these track fluctuations may be physical, but these resolution experiments demonstrate that the oscillations are strictly numerical. A track smoothing operator is employed to remove the numerically-induced track noise.

A coarse resolution model of Δx = 80 km in the RMW = 100 km vortex yields nearly identical results as the higher-resolution model configurations, except for a small, but significant (around 40 km) difference in the 72-h forecast position. These resolution experiments suggest that high resolution may not be a necessary condition for motion prediction in operational dynamical forecast models and that the scales in the initial vortex should match the scales well simulated by the model. Discrepancies between the model and the vortex could lead to persistent and significant oscillations.

Domain sizes less than 4000x4000 km cause the basic vortex to move relatively slower, which implies a dependence on the large scales (> 2000 km) in the simulation . The numerical accuracy of the model is primarily dependent on domain size, provided that there is adequate resolution for the smallest scales of the vortex. In summary, the strategy used here is to sacrifice the representation of the vortex inner core (which does not affect the tropical cyclone track) by using a coarser grid spacing and thereby larger domains.

III. DEPENDENCE OF VORTEX MOTION ON THE INITIAL SYMMETRIC FLOW

The numerical sensitivity tests described in Sec. II-C indicated that the details of the inner core ($r < 100$ km) structure of the vortex do not affect cyclone motion on a beta plane ("beta drift"). By contrast, the very large scales ($r > 2000$ km) are a significant factor in the longer term forecasts, as they are influenced by lateral boundary conditions. In this chapter, the dependence of motion on the symmetric structure of the vortex is further refined through a series of initial-condition sensitivity tests. It will be shown that beta drift is very sensitive to the tangential wind profile in the "critical" $r = 300 - 800$ km annulus. Small profile changes (1-2 m/s) in this critical annulus can lead to large differences in path. Furthermore, speed of motion is nearly proportional to "outer" strength (area-averaged tangential wind in the $r = 300$-1000 km).

The relevant vortex parameters are first defined and a description is then given of the experiment design. The track results not only establish the basic dependence of motion on the symmetric vortex structure, but also establish the critical scientific issues that must be addressed to more fully understand the dynamics of vortex motion.

A. VORTEX STRUCTURE

Prior to specifying the primary structure parameters, some general terms to describe vortex regions are defined. "Inner core" refers to the inner-most part of the vortex in the vicinity of RMW, so that in this study the inner core is within $r = 100$ km. The "inner region" pertains to the zone that contains the greatest cyclonic flow ($r = 0 - 300$ km). The region beyond the inner portion of the vortex ($r > 300$

km) is defined as the "outer region." These regions are defined based on many experiments with a wide variety of vortices with different intensities and radii of 15 m/s winds.

The key structural parameters of the vortex tangential wind profiles, v, are illustrated in Fig. 3-1. In addition to the three parameters (intensity, strength and size) discussed by the Colorado State University (CSU) tropical cyclone research group (e.g., Merrill, 1982), a second strength parameter related to the average flow away from the inner region of the cyclone is introduced. This second strength parameter will be called "outer" strength to distinguish it from the CSU "strength" parameter, which will here be referred to as "inner" strength. The vortex parameters are defined in Table 3-1.

TABLE 3-1. Definition of the primary vortex parameters. A complete description of how these parameters are calculated from the model solution is given in Appendix A.

INTENSITY - Maximum tangential wind speed V_{max}

INNER STRENGTH - Area-averaged tangential wind in the r = 100 - 300 km annulus

$$V_{si} = \frac{\int_{100\ km}^{300\ km} rv\ dr}{\int_{100\ km}^{300\ km} r\ dr} \qquad (3.1)$$

OUTER STRENGTH - Square root of the area-average of the square of the tangential wind speed in the r = 300-1000 km annulus

$$V_{so} = \left\{ \frac{\int_{300\ km}^{1000\ km} rv^2\ dr}{\int_{300\ km}^{1000\ km} r\ dr} \right\}^{1/2} \qquad (3.2)$$

SIZE - Radius of 15 m/s (30 kt) winds, r_{15}

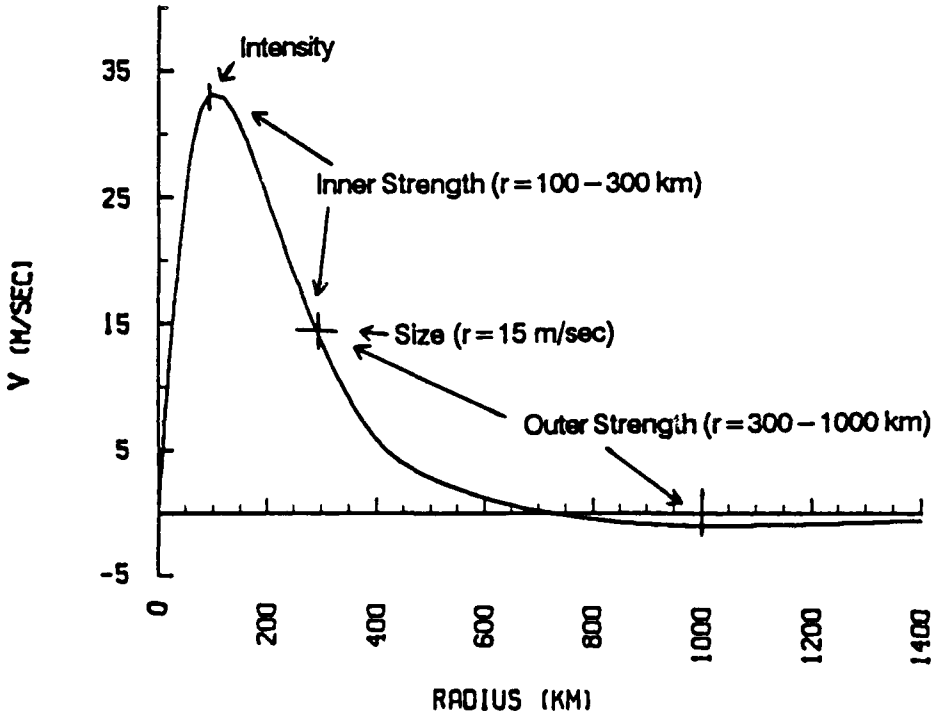

Fig. 3-1. Definitions of the four primary symmetric structure parameters.

The main reason for using the intensity, inner strength and size parameters is that they have been observed operationally via aircraft reconnaissance (Weatherford, 1985). The outer strength parameter was developed after consideration of model sensitivity tests. The square of v is used to represent wind speed because the tangential component tends to change sign in this region. Experiments with other definitions for outer strength (e.g., area-averaged | v |) were not as well related to the vortex motion. Although outer strength is difficult to measure operationally, future satellite observing systems such as microwave radiometers may be able to provide acceptable estimates of the surface wind speeds and outer strength in this region.

B. SPECIFYING THE INITIAL SYMMETRIC VORTEX

The initial symmetric wind profile is based on the analytical tangential wind profile of Chan and Williams (1987)

$$v(r) = V_{max} \left[\frac{r}{r_{max}} \right] \exp \left\{ \frac{1}{b} \left[1 - \left[\frac{r}{r_{max}} \right]^b \right] \right\}, \quad (3.3)$$

where v(r) is the tangential wind, V_{max} is the maximum wind (intensity), r_{max} is the radius of maximum wind and b is an exponential factor that together with r_{max} governs the shape of the profile outside $r = r_{max}$. The profile can be fitted to the observed size and intensity values by calculating the b factor that leads to a smooth profile passing through two specified v values at $r = r_{max}$ and at some r_1 outside $r = r_{max}$. Given (V_{max}, R_{max}) and the outer pair (v_1, r_1), the solution for b is,

$$\ln \left[\frac{v_1}{V_{max}} \cdot \frac{r_{max}}{r_1} \right] = \frac{1}{b} \left[1 - \left[\frac{r_1}{r_{max}} \right]^b \right] . \quad (3.4)$$

This equation is solved numerically by finding the root of

$$f(b) = 1 - R^b + bA \quad , \tag{3.5}$$

where,

$$R = \frac{r_1}{r_{max}} \quad , \quad \text{and} \quad A = \ln \left[\frac{v_1}{V_{max}} \cdot \frac{r_{max}}{r_1} \right] \quad ,$$

using modified linear interpolation (Gerald and Wheatley, 1984). For example, b is equal to 0.96 for typical values of V_{max} = 35 m/s, R_{max} = 100 km, v_1 = 15 m/s and r_1= 300 km. The profile using this numerically determined b comes within 0.01 m/s of v_1 at r_1. The initial streamfunction on the model Cartesian grid is found by solving (2.4). The forcing function (vorticity or ζ) of this Poisson equation is found by finite differencing the tangential wind profile interpolated to the model grid points. Details on this procedure are given in Appendix B.

The v profiles used in previous studies (DeMaria, 1985; Chan and Williams, 1987) are very similar to the one in (3.1) in that the entire profile is specified with one or two parameters. The disadvantage to this simple approach is that a change in one structure parameter results in changes to several aspects of the structure. For instance, changing b in (3.4) changes both the inner and outer strength and the size, which makes it difficult to isolate which parameter would be dominant in the resulting track (e.g., Chan and Williams, 1987). Thus, a capability to modify the analytical profile is needed to vary the symmetric structure parameters independently.

1. Combining Two Profiles

The first modification procedure combines two individual profiles through a linear combination around a "match" point (Fig. 3-2). The two profiles cross at the

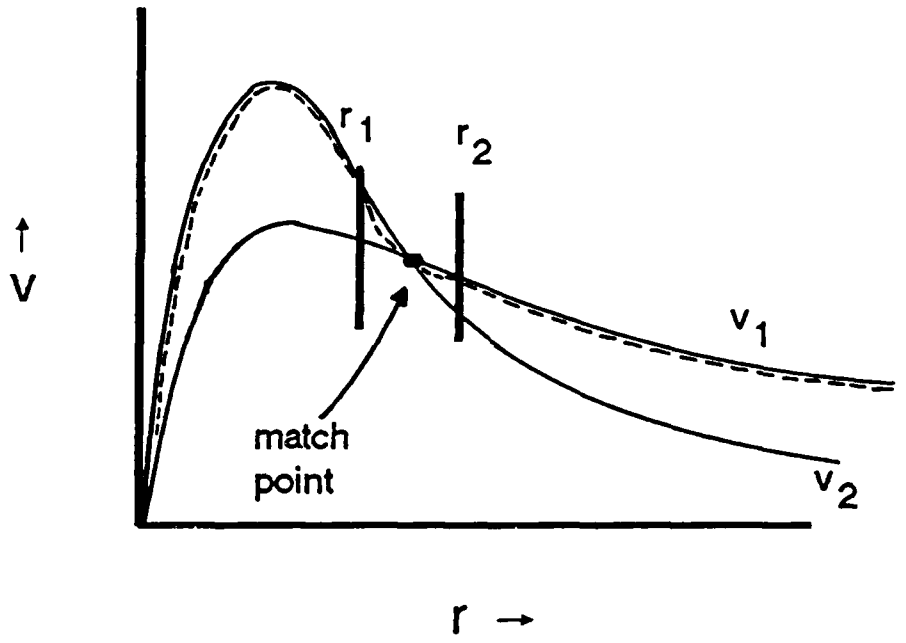

Fig. 3-2. Illustration of combining two tangential wind profiles within the region between r_1 and r_2. The combined profile (dashed) is a combination of the v_1 profile (thin, solid) and the v_2 profile (heavy, solid).

size radius of 300 km ($r = r_{15} = R_{match}$) and are blended together in the interval $r_1 \leq r \leq r_2$ via:

$$v_c = \begin{cases} v_2 & r \leq r_1 \\ av_2+(1-a)v_1 \ ; \ a=(r_2-r)/(r_2-r_1) & r_1<r<r_2, \\ v_1 & r \geq r_2 \end{cases} \quad (3.6)$$

where v_c is the combined profile. This procedure allows a specification of the inner and outer flow and thereby both the inner and outer strength. It is also possible to expand and contract the size radius while holding the inner strength fixed.

A potential problem with combining two profiles is that the first derivatives will not be continuous at the ends of the blending interval. Smoothing the combined profile using the Shuman (1957) procedure prior to the model initialization, or specifying the endpoints of the blending interval between model grid points will insure smooth variations of the derivatives. Also notice that large changes in the curvature are posible in the blend zone. Such changes have been observed in the inner region of a hurricane (Riehl, 1962).

2. Forcing a Zero in a Profile

A second type of modification to a single profile is to force a zero at some radius within an interval of r. Two possible options (Fig. 3-3) are employed:

(i) Force v to linearly approach zero at the end of the interval; or

(ii) Force a zero at the midpoint of the interval and cause the profile to become negative.

The first modification is typically used to force the profile to vanish at a distance several size radii away from the center. At this radius, the distinction between the vortex and the environmental flow is blurred and this

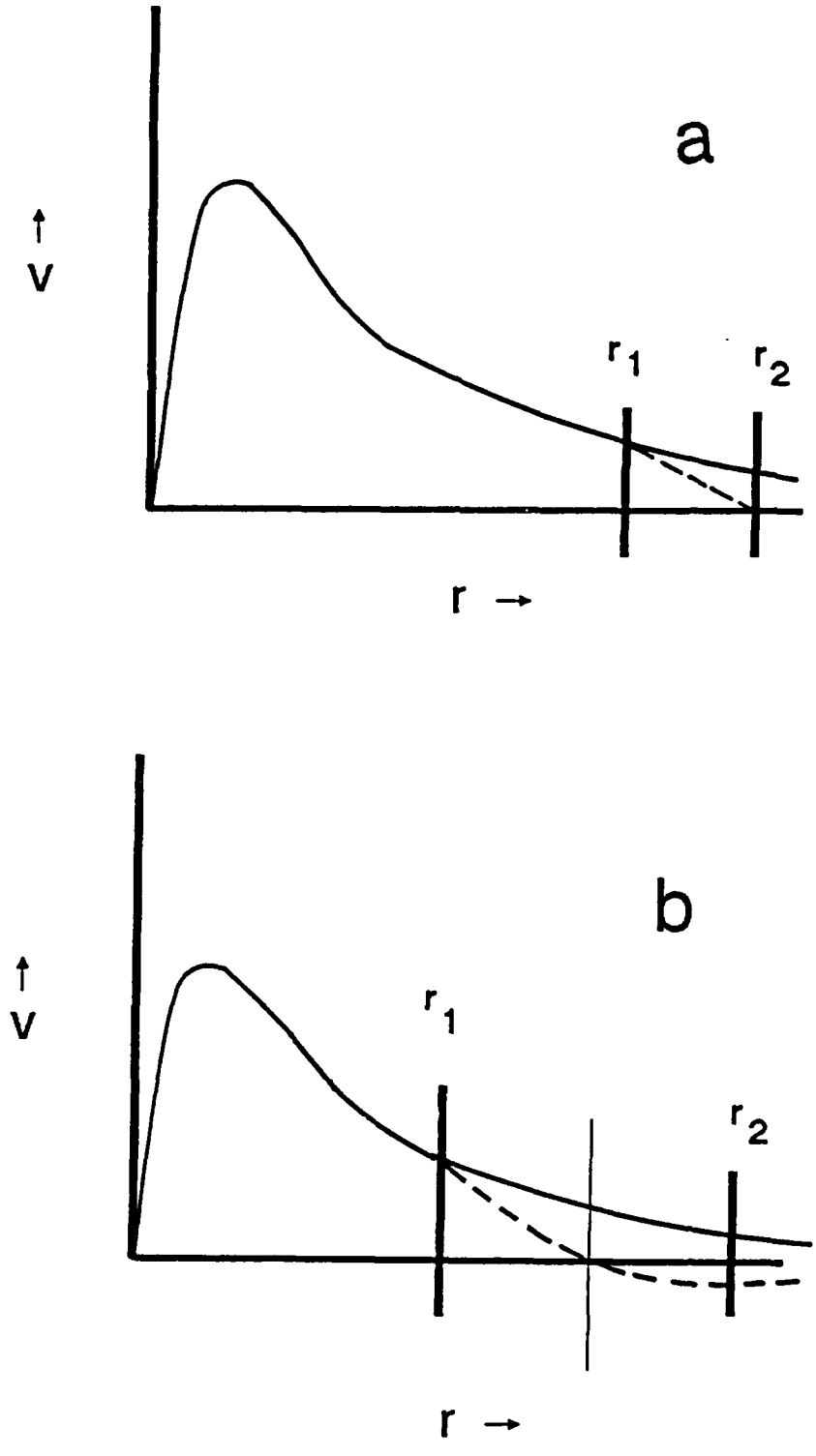

Fig. 3-3. Schematic of forcing (a) a zero at $r = r_2$ in a tangential wind profile, (b) modifying a profile between r_1 and r_2.

procedure terminates the vortex. By contrast, a small b in the (3.3) profile normally retains a significant v (1 m/s) at r = 1000 - 1500 km.

The integrated relative angular momentum (RAM)

$$RAM = \frac{\int_{r_1}^{r_2} r(rv)dr}{\int_{r_1}^{r_2} rdr} , \qquad (3.7)$$

for $r_1 = 0$ to $r_2 = \infty$ is always positive for the analytical profile in (3.3). As stated earlier, there is evidence that both RAM (Willoughby, 1987) and area-integrated tangential wind (DeMaria and Biak, 1987) are related to beta drift. Thus, it is desirable to vary RAM by forcing the analytical profile to become negative at some radius, which is accomplished by modifying the profile through

$$v_c = av_1 , \quad a = \begin{cases} +1 & r \le r_1 \\ \dfrac{2r - (r_2 + r_1)}{r_1 - r_2} & r_1 < r < r_2 \\ -1 & r \ge r_2 \end{cases} . \qquad (3.7)$$

An example of the procedure is shown in Fig. 3-3b. Notice that these single profile modifications can be made prior to the combination procedure.

C. EXPERIMENT DESIGN

The basic vortex in the numerical tests of Sec. II-C was based on typical values of intensity, size and strength for the tropical cyclone, i.e., average for all cyclones of both tropical storm and typhoon intensity. In the following initial-vortex sensitivity tests, these three structure

parameters and outer strength are varied in an independent manner. An example would be to hold the inner strength fixed while changing the outer strength. The capability to vary separately the initial vortex parameters is a unique aspect of this research. In other studies (e.g., De Maria, 1985; Chan and Williams, 1987), inner and outer strength were varied simultaneously as the intensity and RMW were changed, because the profile beyond RMW was controlled by a single parameter (e.g., b).

D. TRACK RESULTS WITH THE BASIC PROFILES

The first set of experiments involves three vortices (Fig. 3-4) with a variety of intensities and strengths in the analytical profile in (3.3). The RMW is fixed at 100 km, and the maximum wind is varied from a weak tropical storm (20 m/s) to a fairly intense typhoon (50 m/s). The shape parameter b, which controls the vortex flow beyond the RMW in the analytical profile, was specified to keep the size radius constant at 300 km. This size is typical of tropical cyclones in the western North Pacific (Williams, 1986). Notice that a change in intensity varies both the inner and the outer strength in the profiles in Fig. 3-4. As the RMW wind is always 100 km, the value of intensity also controls the inner strength. As stated above, the inner core ($r < 100$ km) intensity is not a factor in the beta drift. Thus, intensity in the CSU context is not addressed.

The primary vortex parameters for these basic profiles, and the rest of the profiles used in the initial vortex sensitivity test, are provided in Table 3-2. Consider first the basic ("B") profile cases. Although the inner strength is almost doubled between the weak-intensity (B3) and strong-intensity cyclone (B2), the outer strength is almost cut in half. Thus, these profiles provide a significant variation in the inner and outer strength parameters.

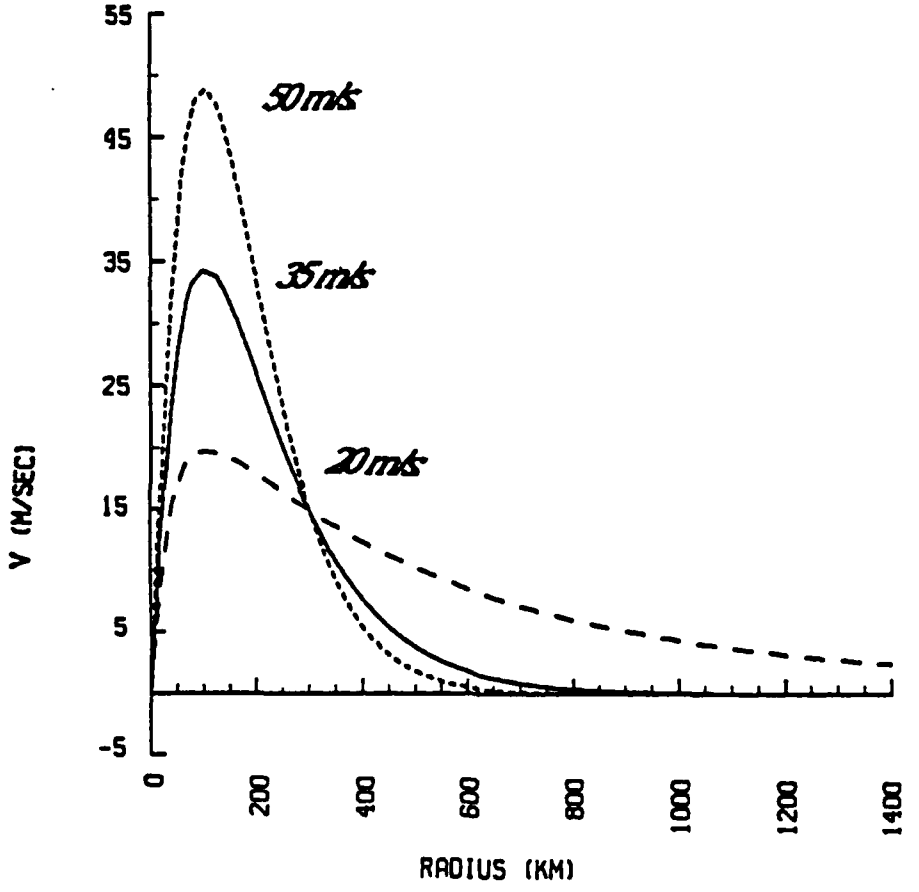

Fig. 3-4. Tangential wind profiles of the three basic vortices, with intensities of 50 m/s (short-dashed), 35 m/s (solid) and 20 m/s (long-dashed) and a size radius of 300 km.

TABLE 3-2. Primary vortex parameters at t = 0 h and the model-produced steady-state speed of motion for all the vortices in the initial profile sensitivity tests. The RMW is 100 km and the size radius is 300 km for all cases

Exp. No.		Intensity (m/s)	Inner Strength (m/s)	Outer Strength (m/s)	Speed of Motion (m/s)
"B"	B1	35	23.9	3.7	2.65
	B2	50	30.2	3.0	2.80
	B3	20	17.3	8.0	4.40
"I"	I4	50	30.2	3.7	2.70
	I5	20	17.3	3.7	2.80
"O"	O6	35	23.9	3.0	2.70
	O7	35	23.9	8.0	4.90
"S"	S8	35	23.9	4.5	3.10
	S9	35	23.9	3.3	1.80
"F"	F10	20	17.3	8.0	4.40
	F11	20	17.3	7.2	4.00

Key:

"B" - Basic vortices
"I" - Inner strength change experiments
"O" - Outer strength change experiments
"S" - Symmetric perturbation experiments
"F" - Modify flow outside the critical annulus (r>800 km)

F10 - Linearly reduce flow to 0.0 from r = 1000 - 1200 km in the B3 profile.
F11 - Linearly reduce flow to 0.0 from r = 800 - 1000 km in the B3 profile.

The 72-h tracks for the basic profiles are shown in Fig. 3-5. These tracks (and the others below) have been smoothed to eliminate numerical track noise as discussed in Sec. II-C. In all cases, the vortex moves toward the NW with a speed of motion of around 3 m/s. A similar result had been obtained in previous studies using comparable models (e.g., Kitade, 1981; DeMaria, 1985; Chan and Williams, 1987). The most distinctive feature of the tracks is the greater speed of motion and more westward translation as outer strength

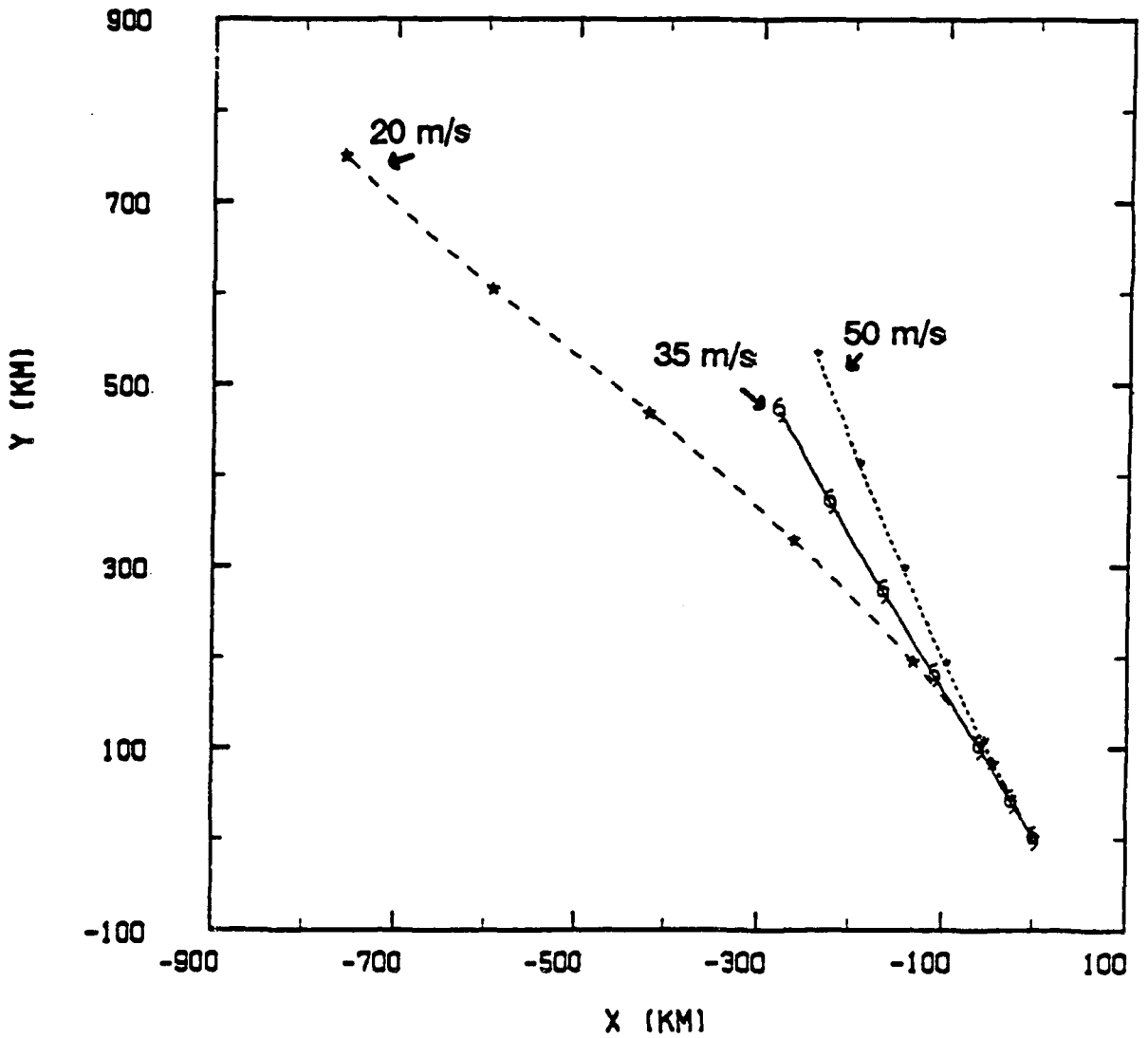

Fig. 3-5. Tracks to 72-h for the basic profiles in Fig. 3-4 and a maximum intensity of 50 m/s (short-dashed), 35 m/s (solid) and 20 m/s (long-dashed). The symbols along the tracks indicate 12-h positions and the line pattern corresponds to that in Fig. 3-4.

increases (B3 versus B1). It also appears that greater inner strength causes somewhat greater northward motion when the outer strength is approximately the same (B2 versus B1).

E. INNER-OUTER STRENGTH CHANGE PROFILES

To more clearly isolate the role of inner and outer strength, the basic profiles are modified to hold constant one type of strength while adjusting the other. In the "inner-change" case, the profile beyond r = 300 km is fixed and the inner strength is changed (Fig. 3-6a). The modification is made by combining two profiles as in (3.6) (see Fig. 3-2). By contrast, in the "outer-strength" case, the profile inward of r = 300 km is fixed and the outer strength varied (Fig. 3-7a). The choice of a common size radius of r = 300 km, and the linear blending in a zone about this "matching" radius, insures a smooth transition between the profile segments.

Slightly greater northwestward displacements occur when the inner strength is increased in the inner-change experiments (Fig. 3-6b). An increased northward drift is also found in the outer-change experiments by comparing the tracks labeled with 50 m/s in Fig. 3-7b and Fig. 3-5. The only difference between these two cases is greater inner strength in Fig. 3-5, and an additional northward displacement is observed. However, the greater motion is only on the order of 5% in both cases.

The 72-h tracks for the outer change experiments (Fig. 3-7b) clearly show that the path variations in the basic profile experiments (Fig. 3-5) are a function of the flow outside the size radius (r = 300 km). Thus, the key vortex structure factor in the dynamics of tropical cyclone motion is in this outer flow.

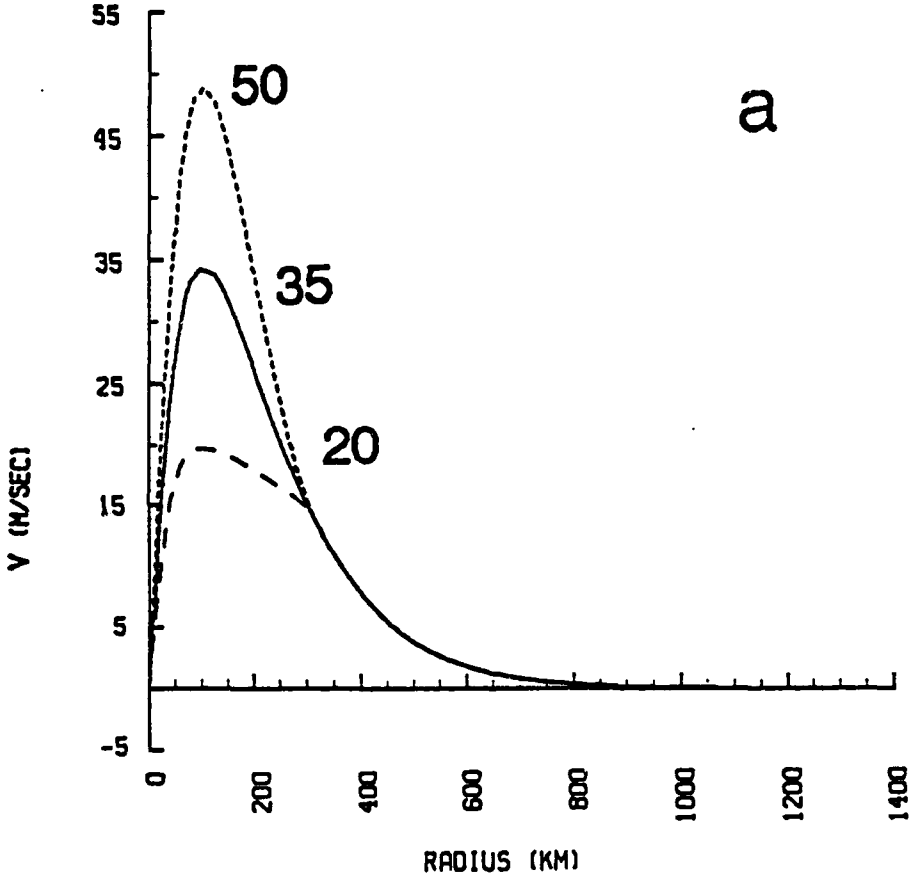

Fig. 3-6. (a) Tangential wind profiles with identical outer profiles and maximum intensity of 50 m/s (short-dashed), 35 m/s (solid) and 20 m/s (long-dashed) and (b) corresponding tracks to 72 h with the same line pattern as used in (a).

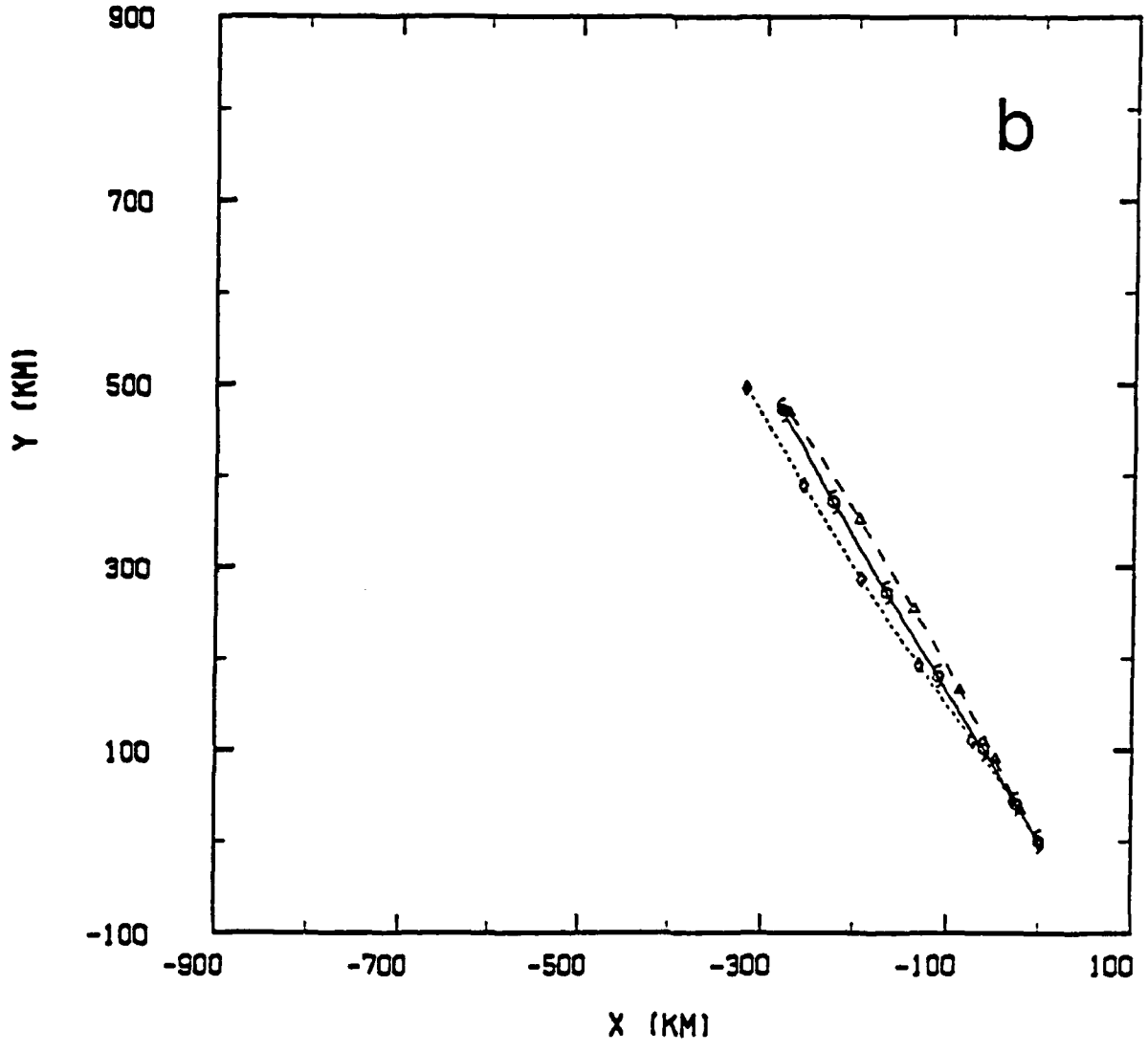

Fig. 3-6. (Continued)

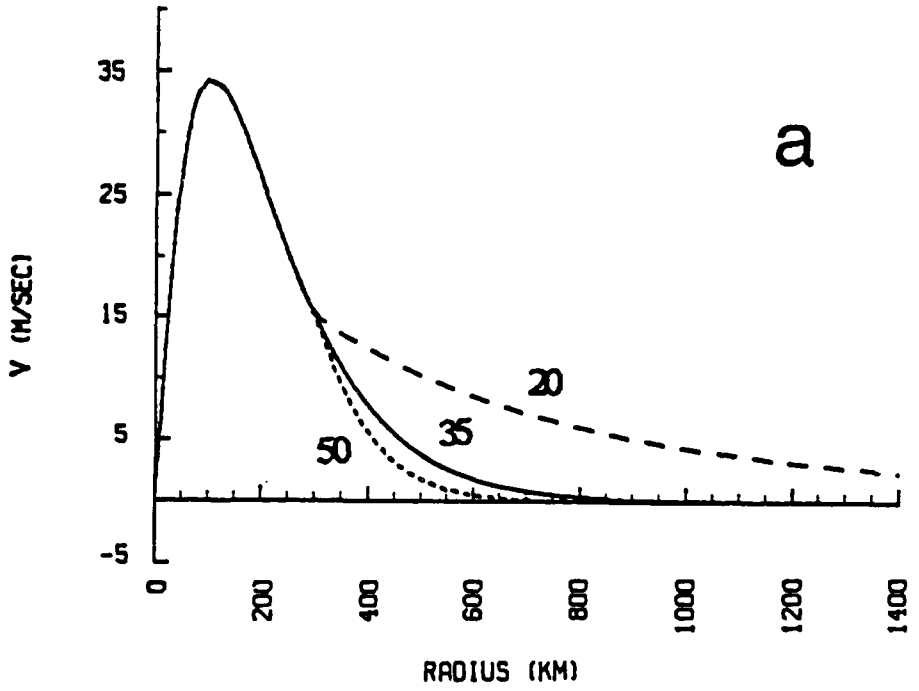

Fig. 3-7. As in Fig. 3-6, except for identical inner profiles and outer profiles corresponding to those in Fig. 3-4.

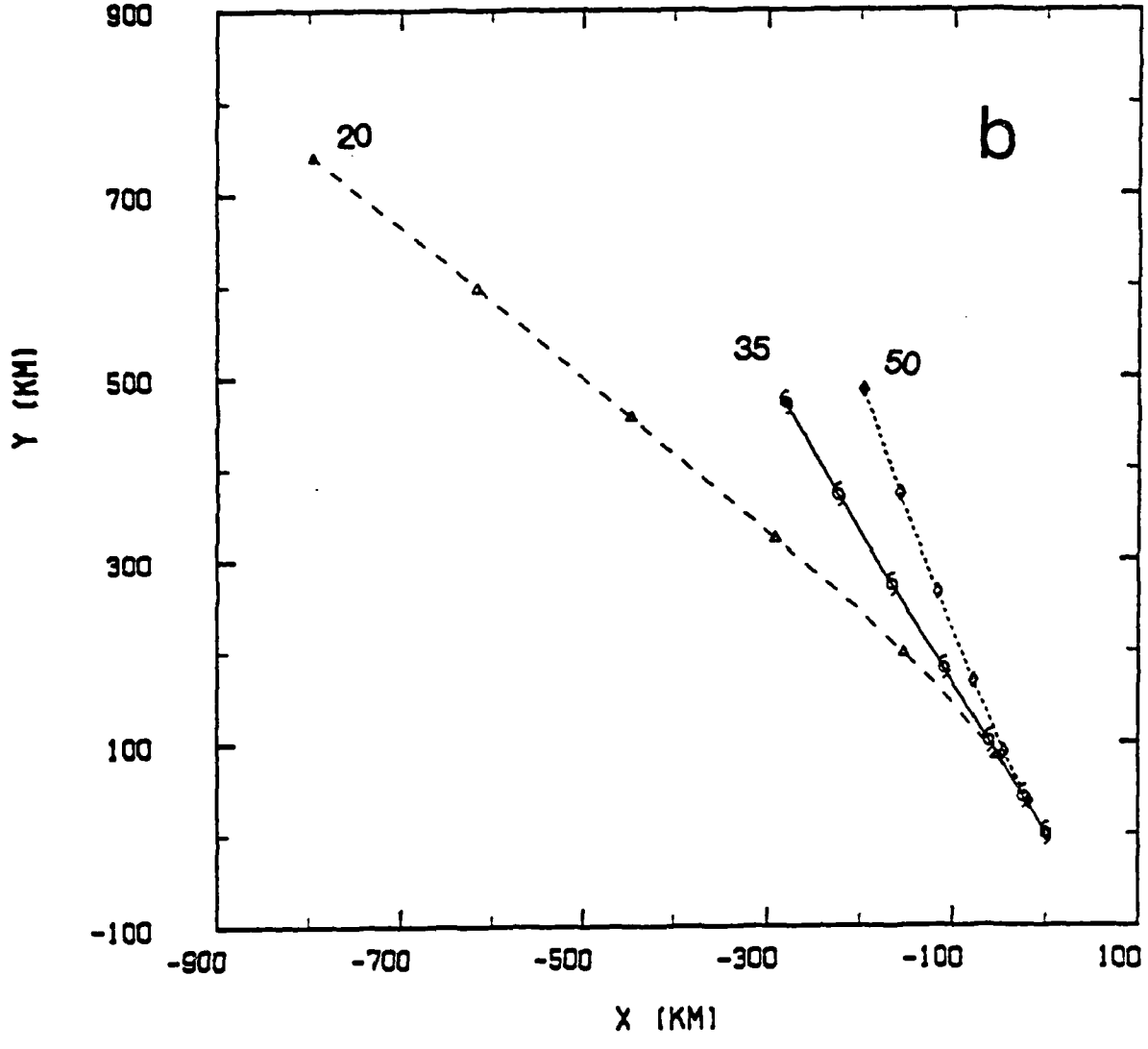

Fig. 3-7 (Continued)

F. SYMMETRIC PERTURBATIONS

The inner-outer strength experiments demonstrate that the vortex flow beyond r = 300 km controls the "beta drift" of an isolated vortex in a no-flow environment on a beta plane. To better understand how the flow in this region influences track, the basic vortex (B1 in Table 3-2) is perturbed in a cyclonic (positive v) and anticyclonic (negative v) sense as illustrated in Fig. 3-8a. Such perturbations may occur in tropical cyclones, although the magnitude of changes may be difficult to observe over the data-sparse tropical oceans. The main purposes of these experiments are to demonstrate how the symmetric flow beyond r = 300 km would change the beta drift, and to indicate the importance of specifying the outer portion of the vortex in tropical cyclone prediction models and in future theoretical motion studies.

The anticyclonic perturbation experiment is designed to determine the role of the "outer anticyclone" that is a common feature of many tropical cyclone model studies (see Anthes, 1982, for a review). Furthermore, the quasi-linear, analytical motion study of Willoughby (1987) suggested that the motion of an isolated, barotropic tropical cyclone on a beta plane would be zero if the integrated RAM was zero. The outer anticyclone must exist if the integrated RAM in the r = 0-2000 km region is to approach zero or become negative. The Willoughby result is in agreement with the earlier study of Tojo (1953), who demonstrated that a moving vortex must have the outer anticyclone to satisfy conservation of absolute vorticity. Another purpose of the anticyclonic perturbation experiment is to verify Willoughby's theory in a nonlinear model. Finally, this anticyclonic profile is similar to one used by DeMaria and Biak (1987). The anticyclonic profile (S9 in Table 3-2) is

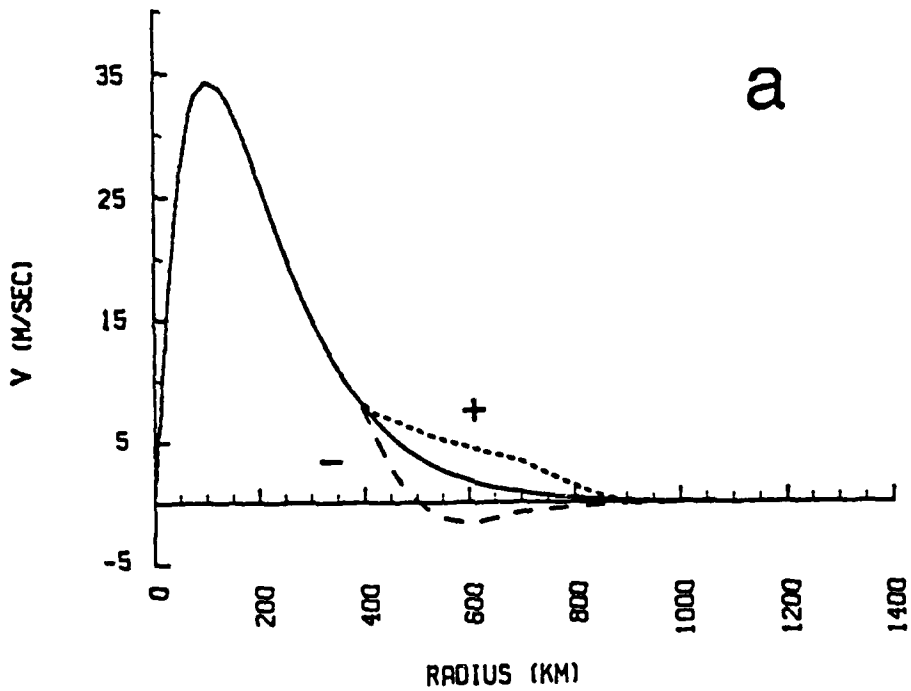

Fig. 3-8. As in Fig. 3-6, except for cyclonic (short-dashed) and anticyclonic (long-dashed) perturbations added to the basic symmetric vortex (solid) in the 300 - 800 km annulus.

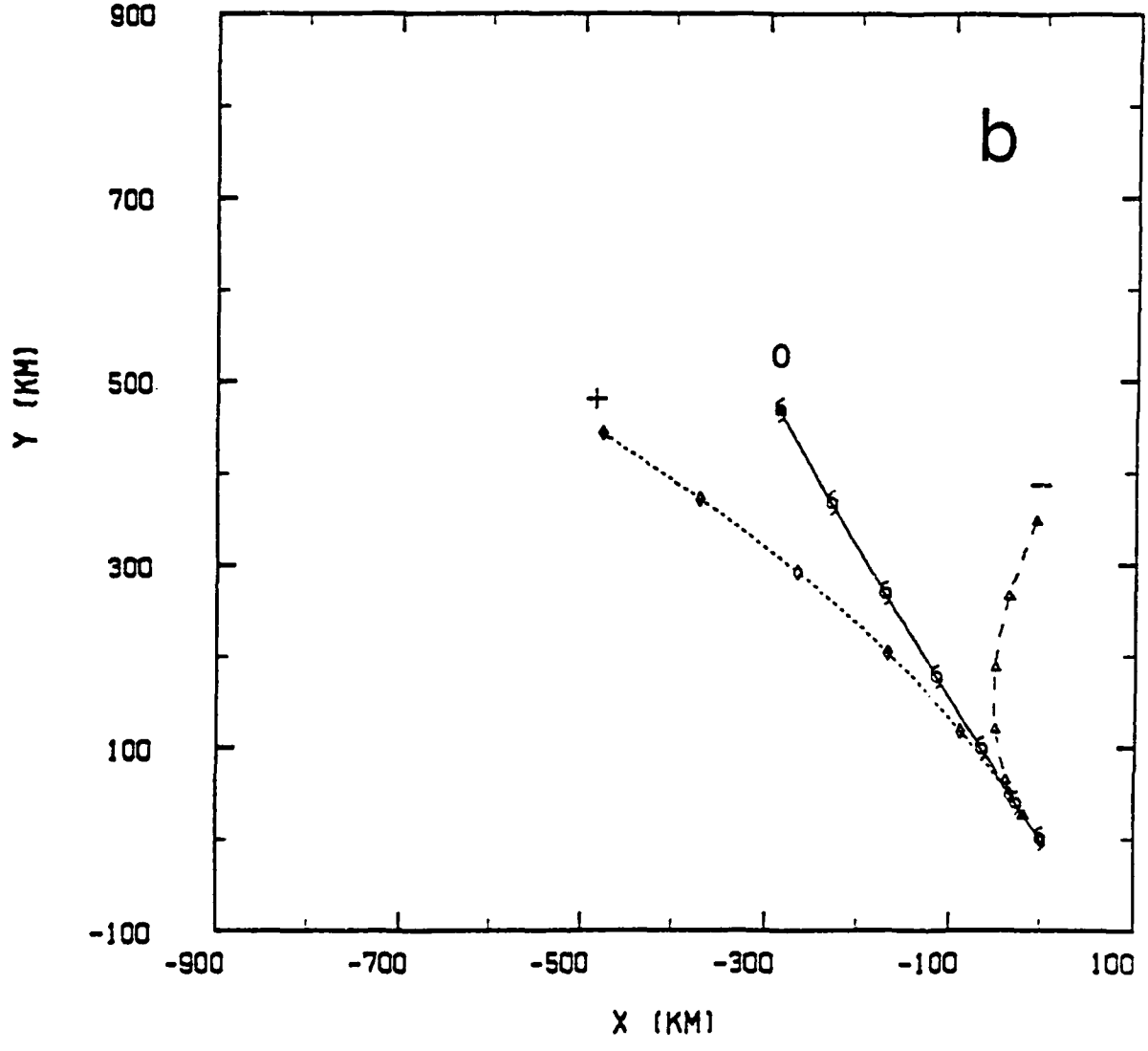

Fig. 3-8. (Continued)

created by forcing a zero in the B1 profile at midpoint in the r = 400-600 km interval (see Fig. 3.3b).

The cyclonic perturbation profile (S8 in Table 3-2) is formed by combining the B1 profile with a second profile with a maximum wind of 15 m/s and a b parameter of 0.56. The two profiles have a common matching point at r = 400 km. After the combination, the profile is then linearly forced to zero from r = 650 - 900 km (Option 1 in Fig. 3-3). These adjustments have the net effect of increasing the tangential wind speed in the r = 400 - 900 km annulus.

The 72-h track forecasts (Fig. 3-8b) indicate that the perturbations have caused long-term (t > 72 h) turning motions in the same rotational sense as the flow changes in the r = 300 - 800 km annulus. For example, if the flow in the annulus is made more cyclonic, then the vortex track will turn cyclonically and move toward the west in the Northern Hemisphere. The speed of motion also increases as the flow in this "critical" annulus increases in a cyclonic sense (S8 versus S9). This point will be amplified in Section H below.

G. FAR OUTER FLOW

The tangential wind in a composite western North Pacific typhoon includes low-level cyclonic flow beyond r = 1400 km (see Fig. 8.7 in Gray, 1981). However, the significant tangential wind (v ~ 3.5 m/s) at r = 1400 km in the weak-large vortex (B3 in Table 3-2) profile (see Fig. 3-4) may be too large. Recall that the model lateral boundary conditions require that the flow approaches zero near the boundaries. Thus, a set of experiments is performed to test the sensitivity to the flow beyond the critical annulus (Fig. 3-9). The B3 profile is linearly forced to zero from r = 1000 - 1400 km in case F10 and from r = 800-1200 km in case F11. The forecast tracks (Fig. 3-9b) have a small, but significant, effect on the speed of translation,

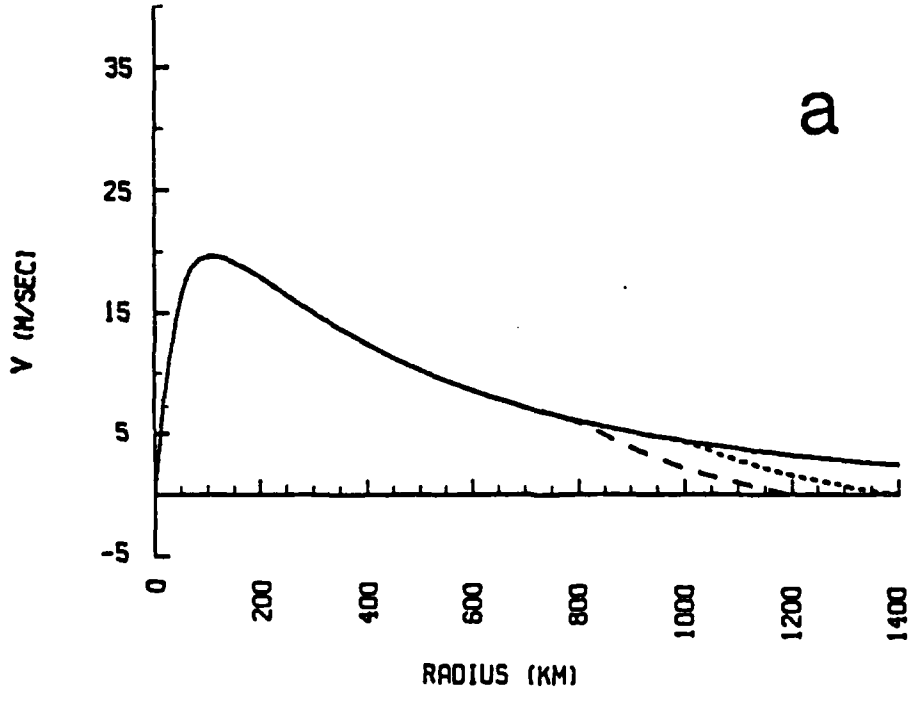

Fig. 3-9. As in Fig. 3-6, except for modifications to the weak-large profile (solid) in Fig. 3-4 to reduce the flow to zero at the 1400 km (short-dashed) or at 1200 km (long-dashed).

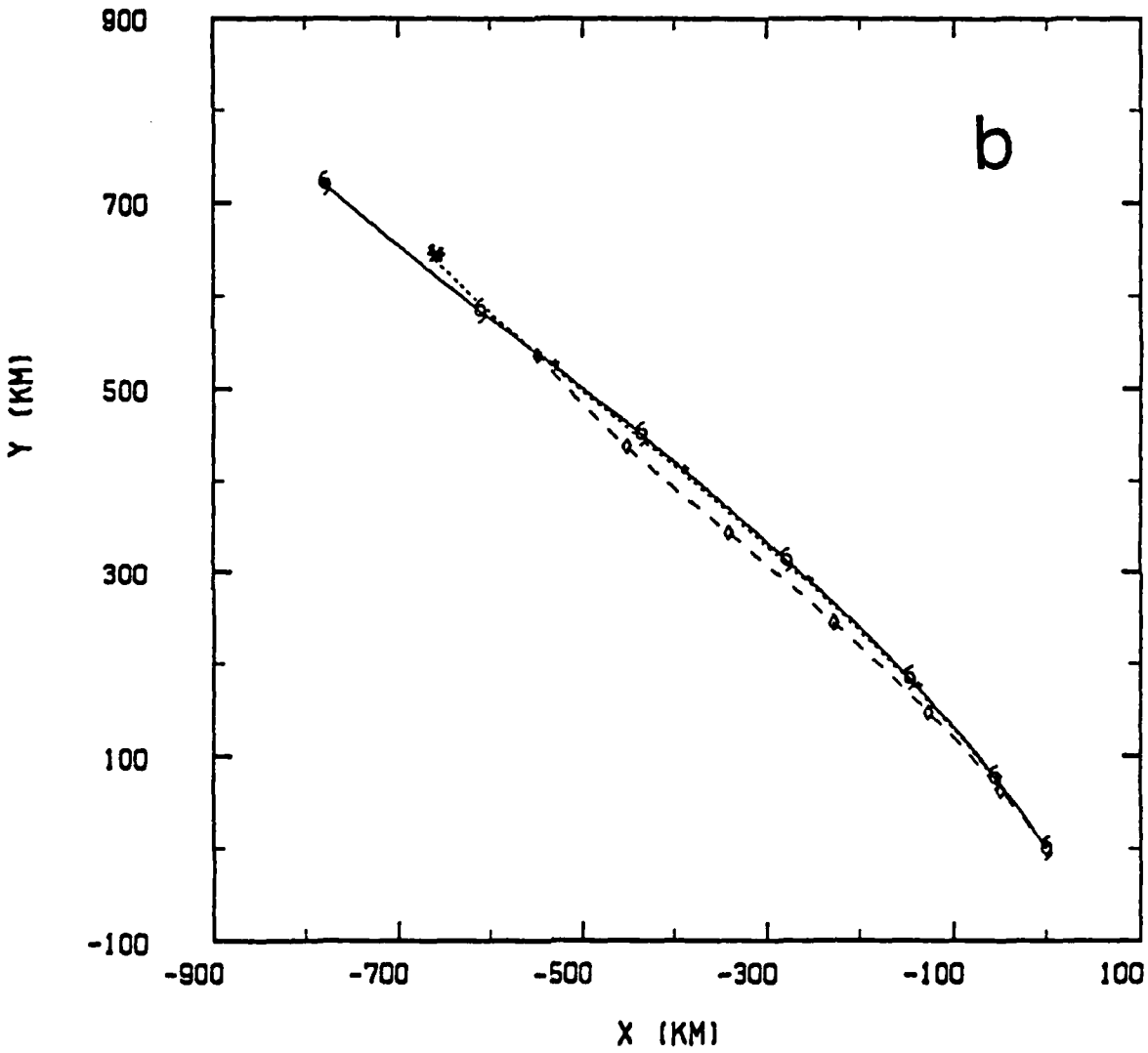

Fig. 3-9. (Continued)

particularly when the flow beyond 800 km is modified (F11). In contrast, the path is virtually unaffected.

The flow in the far-outer zone is related to the largest scale features of the vortex. In Chapter VII, a Fourier decomposition procedure will be used to understand how these largest scales influence the motion. The important result of these experiments is the dominance of the large scales (r > 300 km) in the motion process.

H. SPEED OF MOTION AS A FUNCTION OF STRENGTH

The initial-condition sensitivity experiments in this chapter have demonstrated that the vortex flow beyond r = 300 km controls beta drift both in terms of speed and direction of motion. Specifically, the cyclonic/anticyclonic sense of the tangential wind is related to long-term curving in the track (Fig. 3-8). The relationship between the speed of motion and the outer strength (see values in Table 3-2) is shown in Fig. 3-10 for the various profiles tested. Although the speed of motion is nearly proportional to the initial outer strength of the vortex, the relationship is not perfect, especially for smaller values of outer strength.

I. SUMMARY AND DISCUSSION

The above initial-condition sensitivity tests have shown that the flow in the critical r = 300 - 800 km annulus controls the direction and speed of beta drift. Only a small (less that 5%) increase in northward motion occurs as the inner strength is increased. Changes in the flow beyond r = 1000 km only affect the speed of motion, but the differences are greater and on the order of 10%.

Speed of motion during the slowly-varying state is nearly proportional to initial outer strength, whereas the direction of motion is influenced by the magnitude and the sense (i.e., cyclonic or anticyclonic) of the tangential

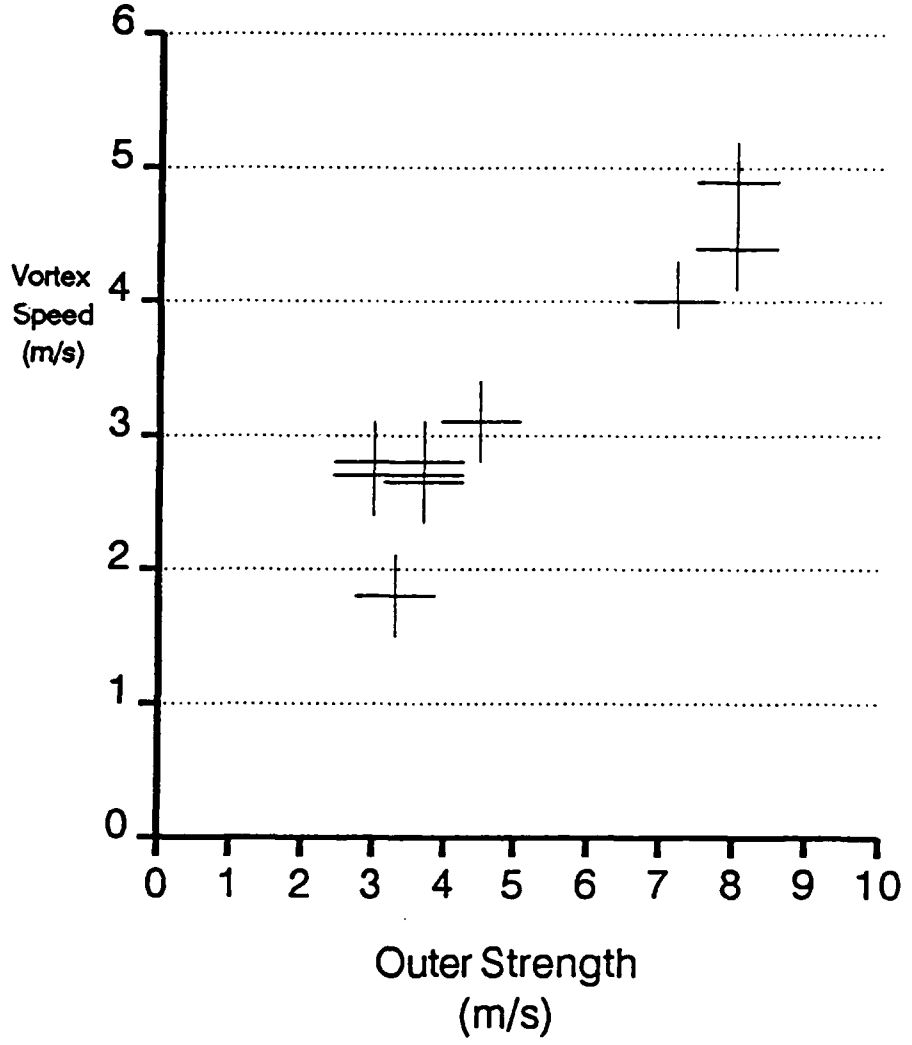

Fig. 3-10. Steady-state speed of motion (m/s) versus outer strength (m/s) for all initial-vortex sensitivity experiments in Table 3-2.

flow. Thus, apparently subtle changes in the vortex structure can lead to significant track changes.

The model used in this research is extremely simple. However, the underlying nonlinear dynamics permits a large variety of track responses as the vortex structure is changed. The applicability of these results to more realistic tropical cyclone track forecast models is limited to the degree that the barotropic motion process dominates other effects in the more complete models. It can be argued that non-barotropic effects simply modify the barotropic effects directly by changing the vortex and indirectly by changing the level of barotropic "steering."

Nonetheless, the magnitude of beta drift is on the order of 500 km over a 72-h period. While this displacement is significant, what is more important is the differences in beta drift as the flow in the critical annulus is varied. Forecast errors at t = 72 h on the order of 500 km or greater would appear to be possible, if the tangential winds in this annulus are not representative of the actual tropical cyclone. A similar result was obtained by Mathur (1987) using a full physics, baroclinic model and a uniform, barotropic environmental flow. In operational forecasting, other factors (e.g., an improper analysis of the large-scale flow) might mask such beta-drift errors.

These experiments also suggest that initializing the initial vortex in a numerical model by specifying a size radius may not be sufficient. The flow in the critical annulus appears to be controlling beta drift irrespective of the radius of 15 m/s winds. Evidently, the vortex flow beyond the size radius should also be carefully specified. This implies that it will be necessary to measure the vortex flow beyond r = 300 km (perhaps out to r = 1000 km). Such measurements would have to be fairly accurate as changes on the order of 1 - 3 m/s have a significant effect on the

track, particularly with regard to direction of motion. Further experiments with other sizes and other flow regimes would be useful. However, as will be argued in the Chapter VII, the track sensitivity is not scaled by vortex size, but is a function of the physical size of the scales in the vortex.

The relative insensitivity to the vortex flow in the inner region implies that a high-resolution model and a precise initialization of the inner portion of the storm may not be necessary to simulate the barotropic component of motion. Unfortunately, most of observational efforts have been directed toward the inner region due to operational "fix" (locating the center) requirements and aircraft range limitations. The inner portions of the vortex are observationally (given aircraft reconnaissance) easier to specify, whereas the dynamically important flow in the critical annulus is very difficult to define.

The remainder of this dissertation is devoted toward explaining the initial-vortex sensitivity and gaining further physical insight into the dynamics of tropical cyclone motion. In Chapter IV, the symmetric/asymmetric circulations within the total vortex will be analyzed to understand how these circulations interact and control the motion. The dynamical processes will then be further refined in Chapter V by using dynamical sensitivity tests. In this type of experiment, the model equation is modified during the integration to control nonlinear/linear and symmetric/asymmetric interactions. The moving grid option allows very long integrations to be performed without an extremely large grid. In Chapter VI, it will be shown that the linear and nonlinear processes force the symmetric circulation to a state that is independent of the initial conditions. Finally, the role of physical scales in the initial vortex, which are defined through a 2-D Fourier

series representation, will be isolated to demonstrate that the "projection" of the vortex onto the most linearly dispersive scales is the key factor in explaining the observed beta drift tracks.

IV. EVOLUTION OF THE SYMMETRIC AND ASYMMETRIC CIRCULATIONS

The dynamical basis for the dependence of vortex motion on the initial structure is examined from the "viewpoints" of: (i) the "total" solution; and (ii) the "symmetric and asymmetric" components. In the total solution viewpoint, the track is displayed and the total ψ solution and diagnostic quantities (e.g., $\mathbf{V} = \hat{k} \cdot \nabla \times \psi$) are plotted. Although this approach is the most commonly used (e.g., Chan and Williams, 1987; DeMaria, 1985), it fails to differentiate the role of individual components of the total vortex system.

By contrast, the symmetric/asymmetric viewpoint is useful in understanding the interaction of the separate flow regimes that make up the total vortex. This viewpoint is based on the observation that tropical cyclones are predominantly axially symmetric in the low and mid troposphere (Gray, 1981) and on theoretical considerations.

The assumption of axial symmetry was crucial to early analytical studies of tropical cyclone motion (e.g., Tojo, 1953; Adem, 1956) as the mathematical treatment of the vortex and the dynamical equations were greatly simplified. More recently, a group of theoretical specialists at an Office of Naval Research planning meeting on the theory of tropical cyclone motion (Elsberry, 1986) recommended that the total flow system be divided into three components:

(i) An axially symmetric circulation representing the vortex;

(ii) An asymmetric circulation that arises from an interaction between the symmetric circulation and the "environment" (the earth's vorticity field and larger-scale flows); and

(iii) A larger-scale "steering" flow representing horizontally uniform flow steering effects.

Even though the symmetric and asymmetric components are relatively simple to define (given the central point), some ambiguity exists regarding the location and what really is the center. For simplicity, and consistency with the model formulation, the center is defined as the point of minimum ψ (see Sec. II-B) rather than the maximum vorticity.

The greatest difficulty with the three-component decomposition is in defining the "steering" flow. If the storm center is defined, and the symmetric and asymmetric circulations have been calculated, then it is fairly clear that the symmetric circulation would represent the "vortex" inwards of the size radius. However, the "vortex" distinction using the symmetric component would be "blurred" at larger radii (say r = 1000 km). Furthermore, the asymmetric flow could contain both steering-like features (large-scale, with little horizontal variation) and smaller-scale circulations near the cyclone center. Thus, it would be impossible to clearly isolate "interactive" and "steering" effects from such an asymmetric field.

Defining the environmental flow will be a difficult problem and the definitions used in each study will have to be clearly stated in order to compare results. The first step in resolving the ambiguity between asymmetric interactive components and the steering flow is to first document that character of the asymmetric field in a no-flow environment, i.e., from a model solution started from an initially symmetric, isolated vortex on a β plane. In this situation, the asymmetric flow is only due to interaction of the vortex with the earth's vorticity field (the Coriolis parameter).

Basic flows will not be considered in this study. Rather, the focus is on the motion of a single vortex on a β plane to understand the earth-vortex interaction. However, there are two aspects of the environmental flow definition

that should be take into consideration (see Holland, 1983, for a similar discussion). In a numerical/analytical model, it is simple to initially specify each of the three components and it is even possible to separately integrate each component to document changes. Taking a total solution from a model or from a real-data analysis and deriving the "basic" flow (total minus the symmetric and asymmetric components) is a considerably more difficult and ambiguous problem.

In this case, it seems appropriate to first define or extract the environmental component by removing it from the total flow, and then perform the symmetric/asymmetric separation. One option for eliminating the vortex and the interaction effects is by filtering either the total flow or a residual formed by removing the symmetric component from the total. In either case, having a clear understanding of the "pure" interactive asymmetric field will be critical for resolving the environmental flow issue.

A. SYMMETRIC/ASYMMETRIC SEPARATION PROCEDURE

Separating a field into symmetric and asymmetric components is trivial in a cylindrical coordinate system. However, the numerical model grid is in Cartesian coordinates. Thus, it is desirable to express all quantities that would be used in diagnostic calculations in terms of the model grid to maximize consistency with the model finite differences. The symmetric/asymmetric decomposition is developed below using both a cylindrical grid and the model Cartesian grid.

The first step in the symmetric/asymmetric separation is to interpolate the solution to a cylindrical grid centered on the storm (point of minimum ψ). The cylindrical grid has a radial increment of 20 km and a azimuthal (θ) increment of eight degrees (45 sectors). A schematic representation of the two grids is given in Fig. 4-1. The cylindrical grid

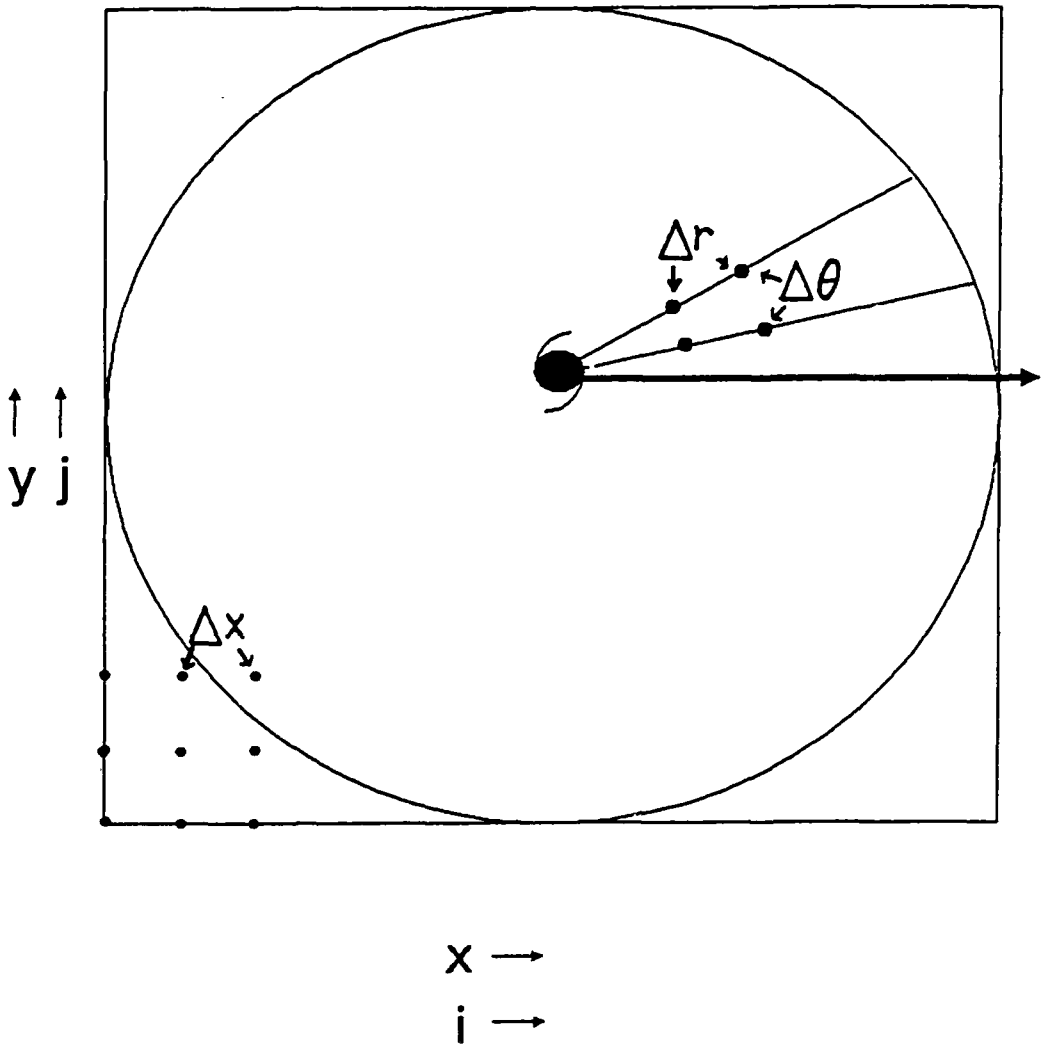

Fig. 4-1. Illustration of the cylindrical grid used in the symmetric/asymmetric decomposition as superposed on the model Cartesian grid. The dots indicate grid points on the grids.

can extend beyond the limits of the Cartesian model grid. In this situation, only field data on the Cartesian grid are used during azimuthal averaging.

Once the cylindrical grid is established, the interpolation from the model grid to the cylindrical grid is performed with a bicubic spline routine from the National Center for Atmospheric Research (NCAR) Scientific Subroutine Package (SSP) using the same boundary conditions as in the model. This routine is exceptionally accurate and has been optimized for rapid execution on the FNOC CYBER 205 supercomputer.

The symmetric component of the field on the cylindrical grid is found by averaging in θ along each radii, which generates a function tabulated at uniform points in r. Although it would be simple to calculate the asymmetric component on the cylindrical grid, it also would be necessary to interpolate back to the model Cartesian grid to perform finite difference operations consistent with the model. Examples of such finite difference operations include calculation of the asymmetric wind from the asymmetric ψ or the calculations of the model vorticity tendency terms. Instead, the symmetric component at each model grid point is specified using the symmetric function in r. This is accomplished by calculating the radial distance of each model grid point from the vortex center and then interpolating from the symmetric component (e.g., $\psi_s(r)$) using a spline under tension (NCAR SSP). The tension factor was adjusted to optimize the numerical recovery of the vortex parameters from an analytically-specified profile. This interpolation yields a function of x and y, or $\psi_s(r) \rightarrow \psi_s(x,y)$. The asymmetric component on the model grid is then found by subtracting the symmetric component from the total (i.e., $\psi_a(x,y) = \psi_t(x,y) - \psi_s(x,y)$).

In the symmetric/asymmetric decomposition routine, the size of the cylindrical grid is limited so that it nearly fits within the model grid because the symmetric/asymmetric components cannot be defined in the corners of the model. Fortunately, the model boundary conditions force the solution to zero at the edges of the grid so that slight grid extensions do not impact the azimuthal averaging. The symmetric and asymmetric components for radii beyond the cylindrical grid are set to the value of the function at edge of the cylindrical grid.

Tests with symmetric/asymmetrical analytical functions specified on the model grid demonstrated that the procedure was able to very accurately recover the true (analytical) symmetric/asymmetric components. This also helped verify the center location algorithm.

To summarize, the inputs to the symmetric/asymmetric procedure are a field on a Cartesian grid $f_t(x,y)$ and a center point (x_0,y_0). The outputs are the symmetric $f_s(x,y)$ and asymmetric $f_a(x,y)$ fields on the input grid and the symmetric component as a function of radius $f_s(r)$. The procedure is applied only to the ψ_t solution. All other quantities are then derived (e.g., ζ_a from ψ_a) using diagnostic relationships to insure maximum consistency with the model solutions.

B. SYMMETRIC WIND PROFILE

The vortex structure parameters described in Chapter III are derived from the function-of-radius form of the symmetric component of the 2-D model ψ_t. Details on the calculation of the tangential wind (v) and the structure parameters are given in Appendix B.

The symmetric/asymmetric circulation analysis is applied to only four of the 11 vortices considered in Table 3-2:

B1 - The basic vortex
B3 - Weak intensity but strong outer strength
S8 - Cyclonic perturbation to B1
S9 - Anticyclonic perturbation to B3

These vortices represent the full range of track types observed in the initial-vortex experiments and thus warrant the most attention in analyzing the motion process and structure effects.

The evolution of the tangential wind profiles is given in Fig. 4-2. Notice that the integration length is 144 h vice 72 h as in Chapter III. The additional integration time helped establish the time scale of the variations. Results from even longer integrations will be discussed in Chapter VI. There are two distinctive features of the profiles: (i) the maximum wind decreases slightly; and (ii) the largest changes occur beyond the inner region. For the weak large vortex (B3), the changes are more dramatic as anticyclonic flow has formed at t = 144 h beyond r = 800 km. The vortex parameters are given in Table 4-1.

TABLE 4-1. Temporal change in the vortex parameters for the four vortices.

Exp. No.	Time (h)	V_{max} (m/s)	Inner Strength (m/s)	Outer Strength (m/s)	RAM_{18} X 10 (m^2/s)
B1	0	34.3	23.9	3.69	6.5
	72	33.7	22.7	3.02	-6.4
	144	32.9	21.5	2.34	4.0
S8	0	34.3	23.9	4.52	9.7
	72	33.7	22.8	3.40	-10.1
	144	33.3	22.2	2.94	-2.6
S9	0	34.3	23.9	3.34	2.4
	72	33.9	23.0	3.07	-2.2
	144	33.6	22.3	2.64	0.8
B3	0	19.7	17.3	7.96	70.2
	72	18.5	15.5	4.82	11.0
	144	18.2	14.4	3.32	-24.9

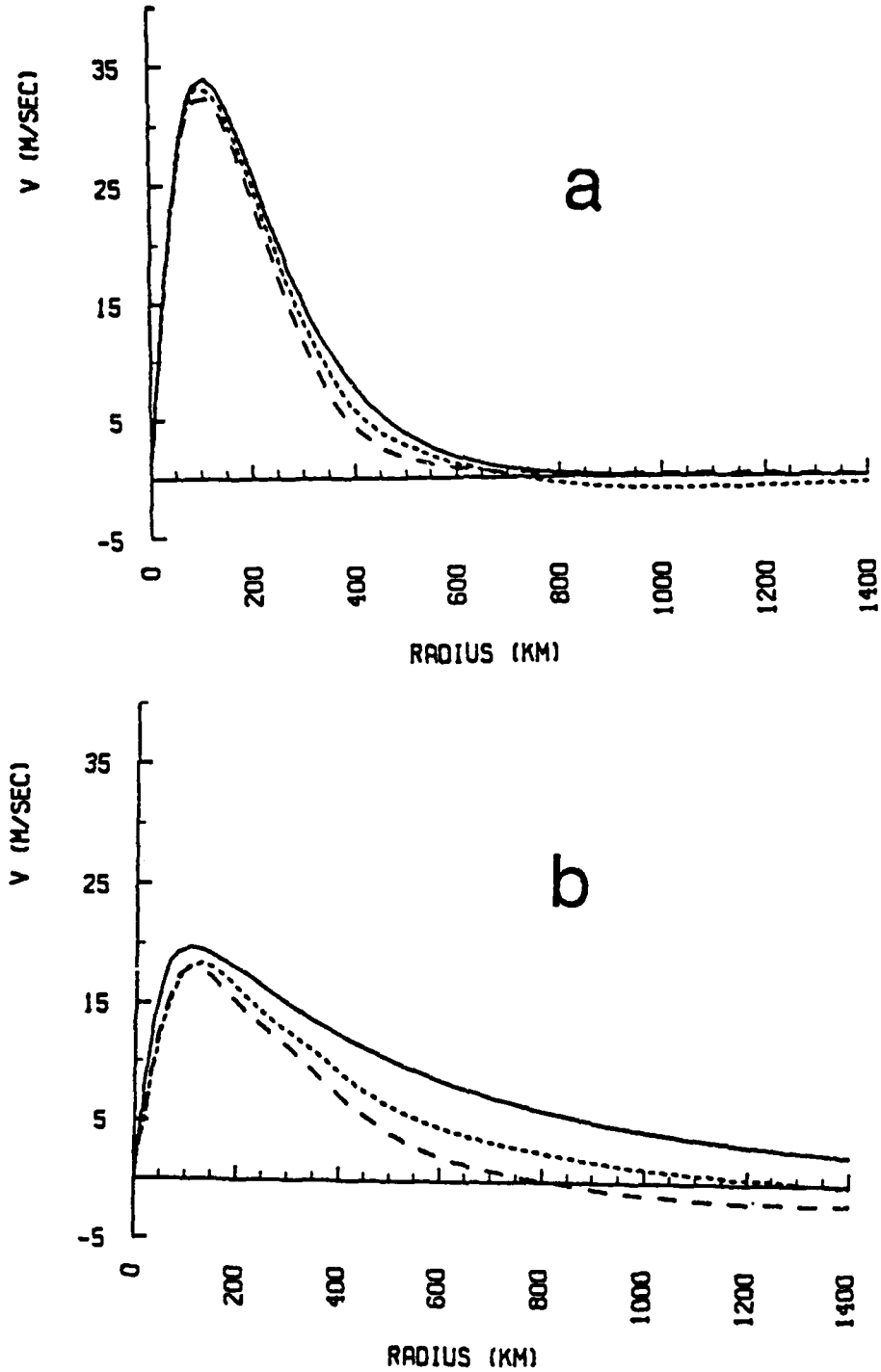

Fig. 4-2. Evolution of the tangential wind profile at t = 0 (solid), 72 h (short-dashed), 144 h (long-dashed) for initial profiles (see Table 3-2) (a) the basic vortex (B1), (b) the weak-large vortex (B3), (c) the cyclonic perturbation and (S8) and (d) the anticyclonic perturbation vortex (S9).

The symmetric perturbation (S8 and S9) cases are derived from the basic profile B1. This similarity is reflected in the temporal changes of the inner region parameters (V_{max} and V_{si}). Thus, it appears that the dynamical processes in this region are similar and may be separated from events in the outer region. Notice also that the outer strength decreases in time and seems to approach a common value. In the weak, large vortex (B3), the changes in the inner and outer strength are much greater.

Willoughby (1987) suggested that the integrated RAM must be less than zero for a cyclone to move northward. Similarly, Tojo (1953) calculated the tangential wind profile for a moving vortex and demonstrated the formation of an outer anticyclone and negative RAM as a consequence of conservation of absolute vorticity. The integrated RAM in the r= 0 - 2000 km annulus (Table 4-1) shows a general decrease in magnitude and an oscillation between positive and negative values in some cases. Thus, it does not appear that negative integrated RAM is a necessary requirement for beta drift. Rather, the results presented here suggest that the RAM tends to be reduced in magnitude and may be either negative or positive.

The decrease in the maximum wind speed, inner and outer strength suggests a transfer of energy from the initial symmetric vortex to the asymmetric circulation. However, a more accurate description is that the changes in the symmetric circulation are a result of the formation of asymmetries. The fact that the largest changes occur in the outer region implies that the asymmetries must be greatest in this zone.

The B3 vortex is weaker than the other three vortices. Thus, the inertial stability ($\Gamma \equiv \{f+\zeta\}\{f+2v/r\}$), which is proportional to the nonlinear term in the model equation, is smaller in the B3 vortex. Therefore, the B3 vortex will

have less resistance to asymmetric forcing than the B1 vortex. As shown by Chan and Williams (1987), the linear term (βv) is the source of the asymmetries in this model. Thus, the largest changes in the symmetric circulation seem to occur when the ratio of the nonlinear to linear term (N2L) is smaller. In other words, it is suggested that there is a balance between nonlinear effects that attempt to keep the vortex symmetrical and the Rossby dispersion that forces the vortex to become asymmetrical. The concept of such a balance had been suggested previously in the study of eddies in the Gulf Stream (e.g., Flierl, 1977). Another consequence of this balance is that changes to the vortex in the outer regions where the N2L is smaller will have a greater potential for affecting motion than in the inner core. In the outer zone, the inertial stability is weaker, which implies that the vortex could be influenced to a greater extent. These ideas are further developed in the next section in which the asymmetrical circulation is analyzed.

C. THE ASYMMETRIC CIRCULATION

In this section, the evolution of the asymmetric circulation is evaluated for the basic vortex B1. From this discussion, the essential properties of the asymmetric flow are derived to provide a basis for the analysis of the the other vortices (S8, S9 and B3). A strong relationship between the formation of a pair of large-scale gyres and the motion of the center will be shown.

A time sequence of asymmetric streamfunction (ψ_a) for the basic vortex experiment is given in Fig. 4-3. The general features of the asymmetric streamfunction are: (i) a dipole-like pattern with an anticyclone to the right of the center and a cyclone to the left; (ii) a "ventilation" flow through the center; (iii) a "buckle" at the center where the gradient of ψ_a goes to zero, and a small region (the

a

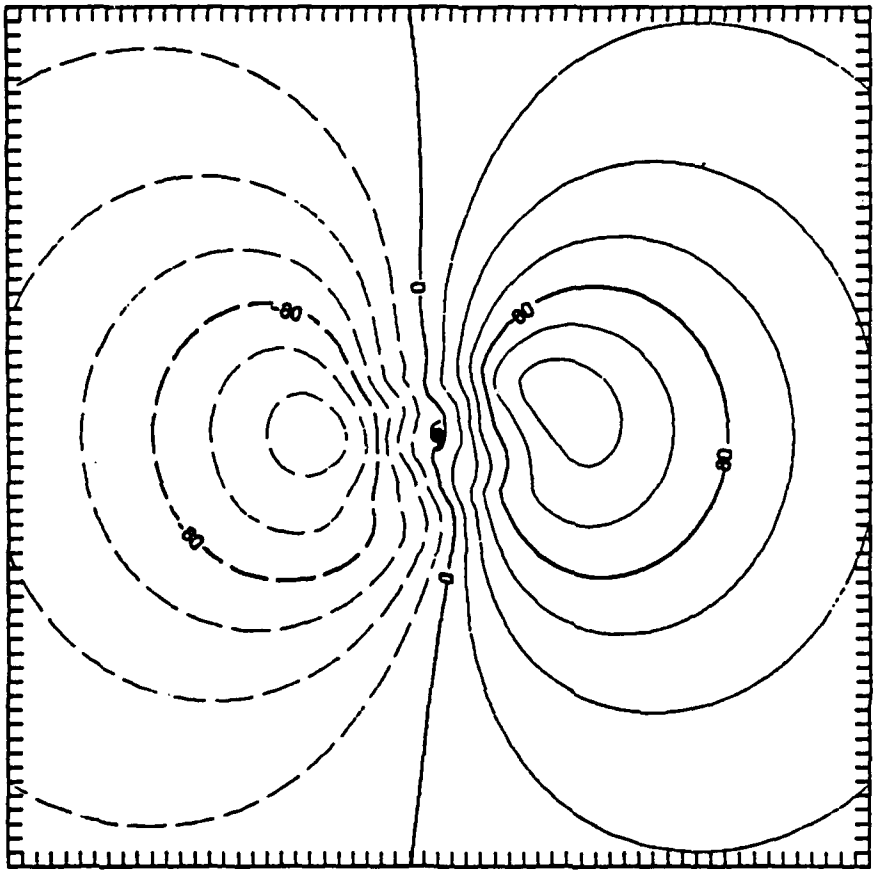

(a) $t = 3$ h, $|\psi_a| \sim 10^5$ m^2/s
contour interval = 20 x 10^3 m^2/s.

Fig. 4-3. Temporal evolution of the asymmetric streamfunction ψ_a (m^2/s). The plot domain is 61x61 points (with $\Delta x \cong 40$ km, 2400x2400 km) centered on the vortex. The tick marks indicate the location of the grid points. This domain size will be used in all subsequent figures in this chapter unless otherwise noted. Positive (negative) values indicate cyclonic (anticyclonic) streamfunctions.

b

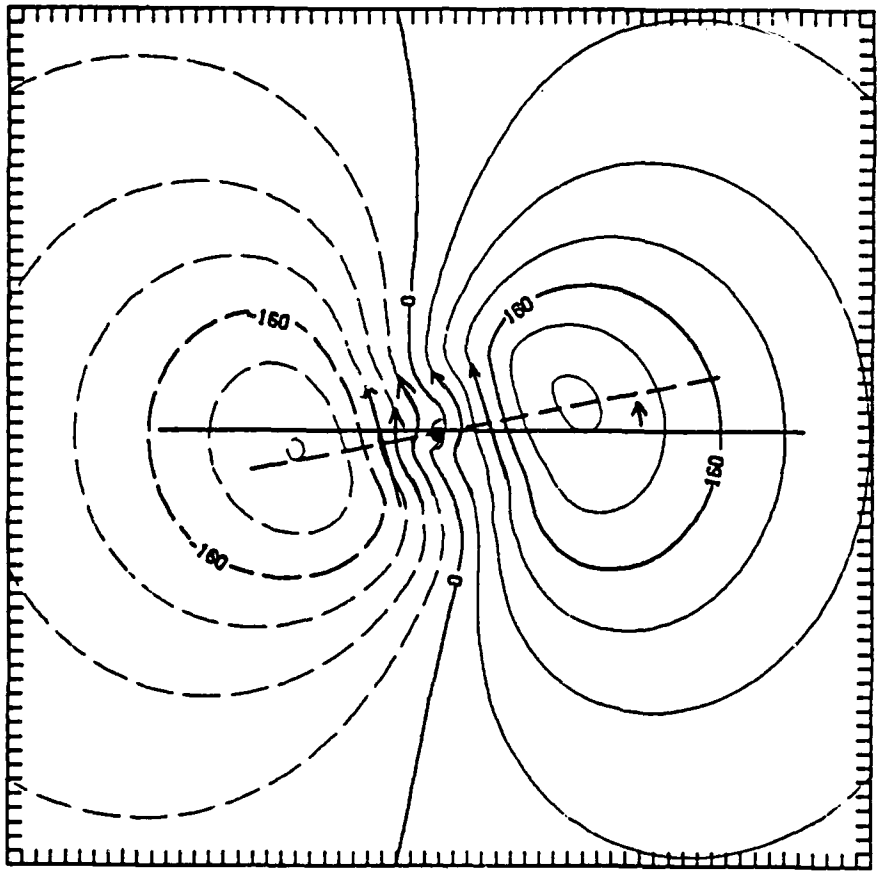

(b) t = 6 h, $|\psi_a|$ ~ 2.5x10^5 m^2/s
contour interval = 40 x 10^3 m^2/s.

Fig. 4-3. (Continued)

C

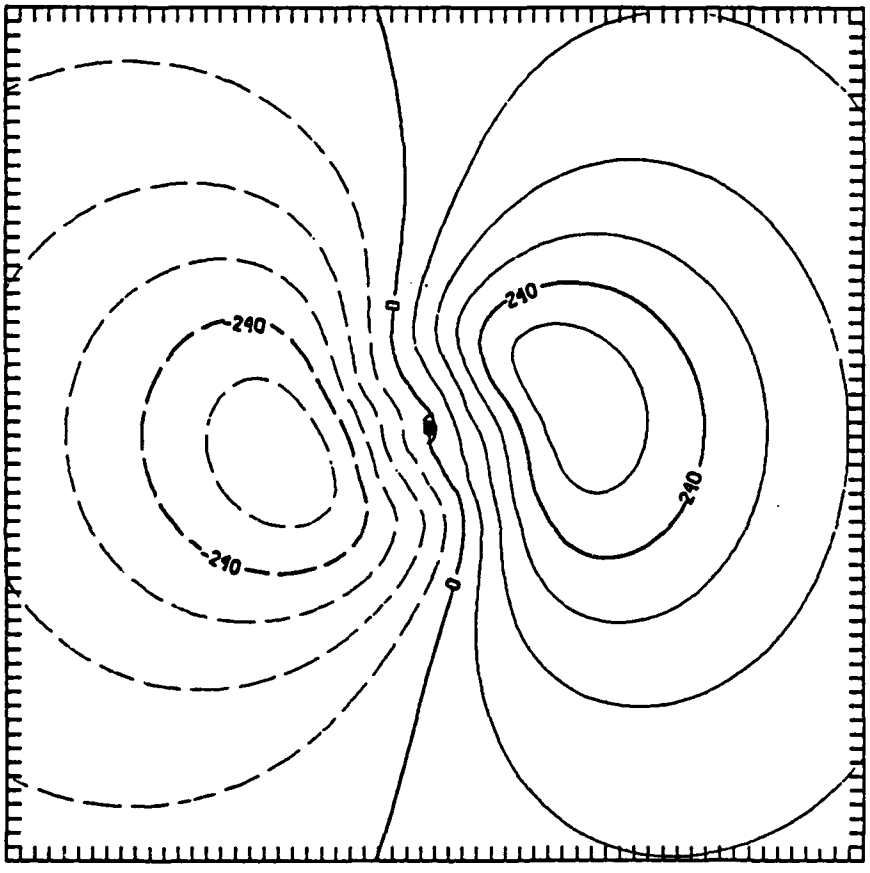

(c) t = 9 h, $|\psi_a|$ ~ 3.0×10^5 m^2/s
contour interval = 60 x 10^3 m^2/s.

Fig. 4-3. (Continued)

d

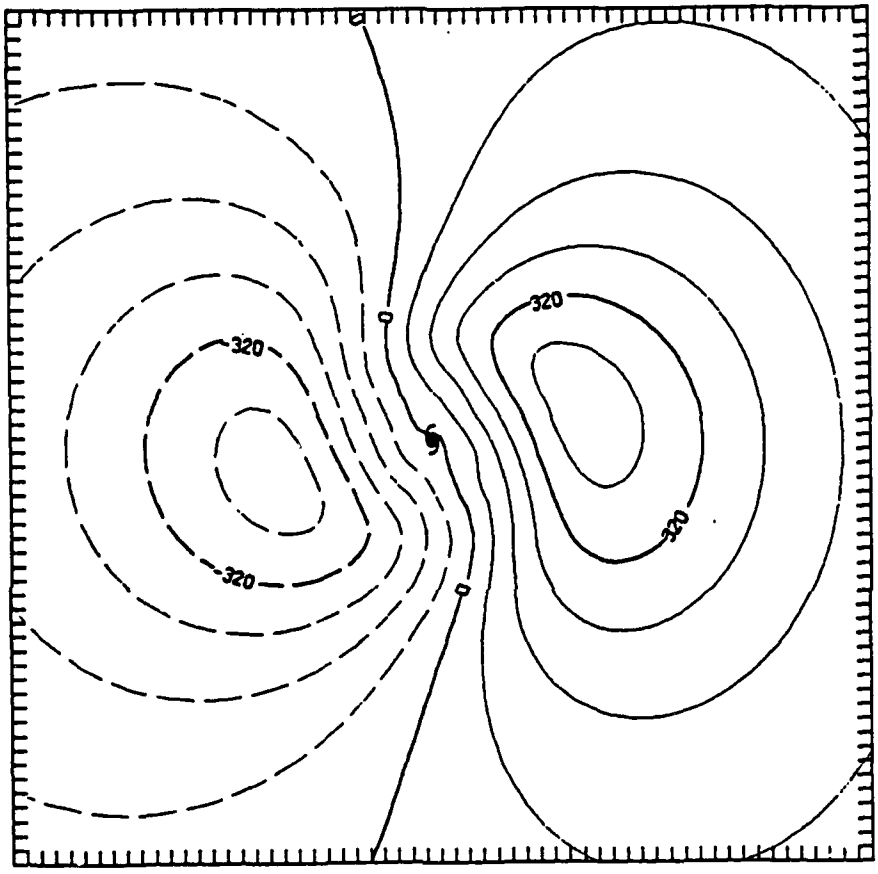

(d) $t = 12$ h, $|\psi_a| \sim 4.0 \times 10^5$ m^2/s
contour interval = 80×10^3 m^2/s.

Fig. 4-3. (Continued)

e

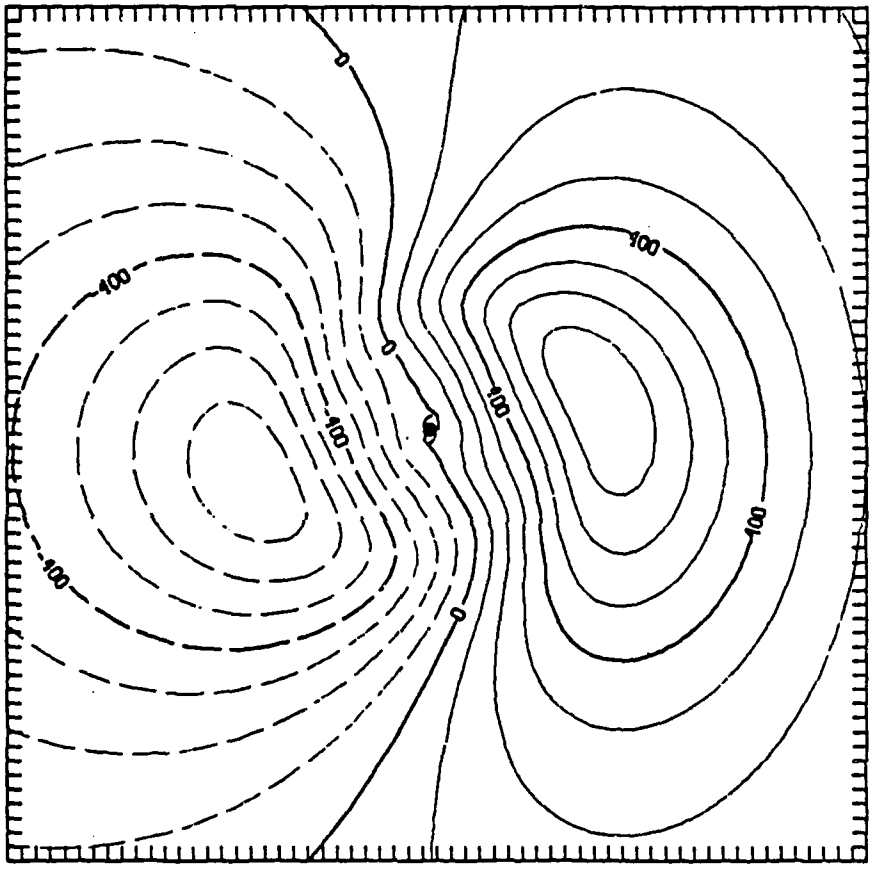

(e) $t = 24\ h$, $|\psi_a| \sim 7.0 \times 10^5\ m^2/s$
contour interval = $100 \times 10^3\ m^2/s$.

Fig. 4-3. (Continued)

f

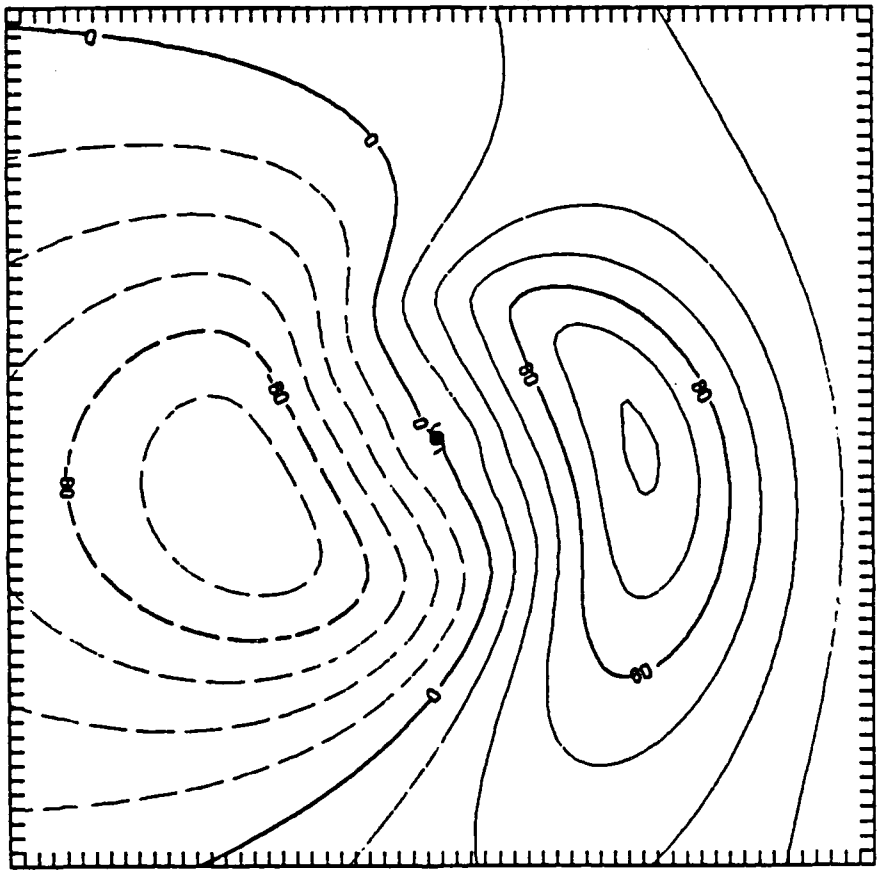

(f) t = 48 h, $|\psi_a|$ ~ 12.0x10^5 m^2/s
contour interval = 20 x 10^4 m^2/s.

Fig. 4-3. (Continued)

g

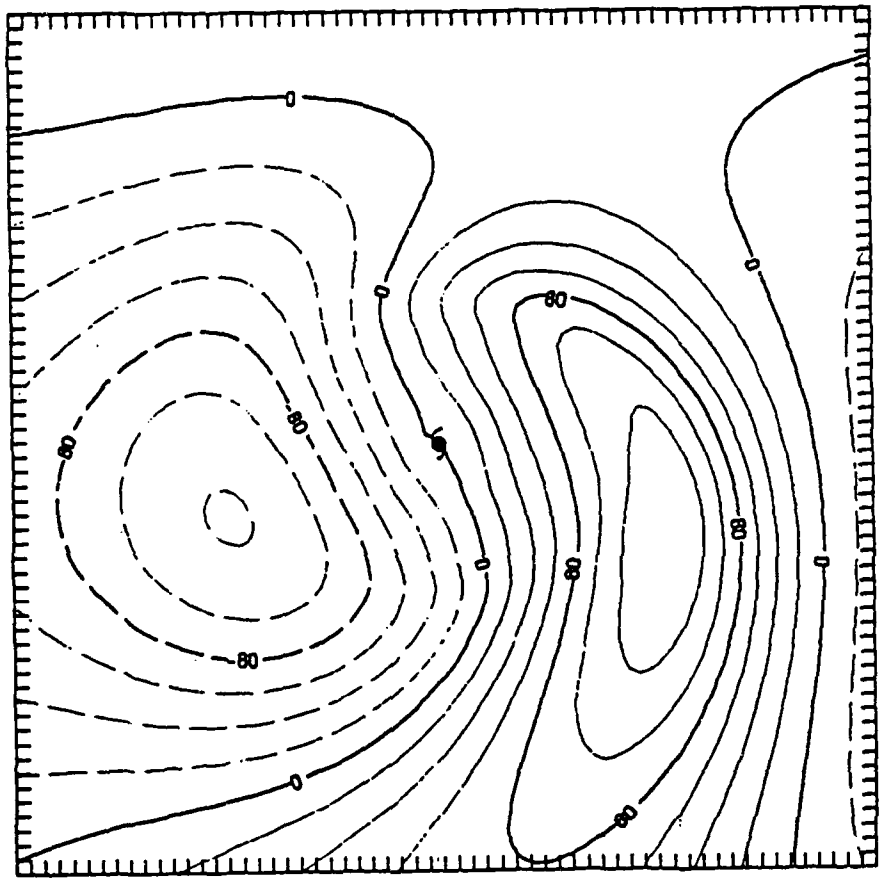

(g) t ≈ 72 h, $|\psi_a|$ ~ 12.0x10^5 m^2/s
contour interval = 20 x 10^4 m^2/s.

Fig. 4-3. (Continued)

inertially stiff core) around which the asymmetric wind flows; and (iv) a cyclonic twisting or rotation of the gyre centers that reorients the ventilation flow from north to the northwest. These four features are highlighted in Fig. 4-3b.

1. Growth of the Asymmetric Gyres

The analysis of the time variations of ψ_a starts by examining the amplitude of the asymmetric gyres as a function of time (Fig. 4-4). Three stages in the gyre development from an initially symmetric vortex are apparent. During the first 12 h of the integration, rapid growth of the gyres quickly establishes the circulation (rapid growth phase). From 12 to 48 h, the gyre amplitude grows linearly (linear growth stage) and a steady state occurs from 48 to 72 h (steady state phase). The translation speed of the vortex (Fig. 4-5) follows a similar development curve compared to the magnitude of ψ_a. In contrast to the time scale for the evolution of the translation speed, the direction of motion stabilizes to within 5° of the steady-state value of 320° within 3 h. This finding is similar to DeMaria (1985), except that the direction of motion in this experiment is more stable, which is possibly due to different definitions of the center.

These changes in Figs. 4-4 and 4-5 are useful in understanding the temporal variation of ψ_a in Fig. 4-3. At t = 3 h, the gyre centers are approximately 400 km from the cyclone center and have already shifted to orient the ventilation flow toward about 320°, which is similar to the storm motion vector. The area of perturbed asymmetric flow is confined to a scale of approximately r = 300 km. Notice how the contours farther away from the perturbed zone are still aligned north-to-south. During the rapid growth phase from t = 3 to 12 h (Figs. 4-3b to 4-3d), the gyres build in intensity and expand outward. Similarly, the region of

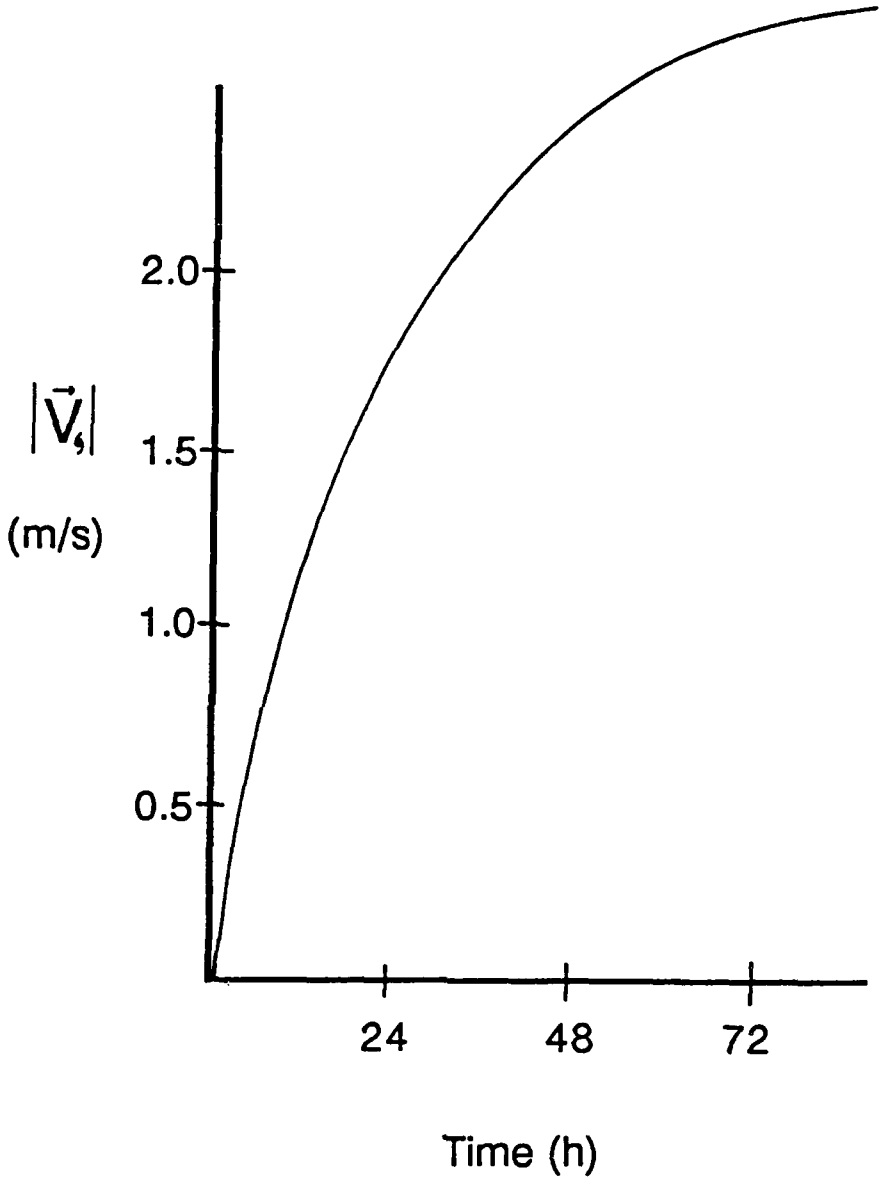

Fig. 4-5. As in Fig. 4-4, except for speed of motion for the center.

AD-A190 961 THE ROLE OF VORTEX STRUCTURE IN TROPICAL CYCLLNE MOTION 2/4
(U) NAVAL POSTGRADUATE SCHOOL MONTEREY CA M FIORINO
DEC 87

UNCLASSIFIED FFG 4/2 NL

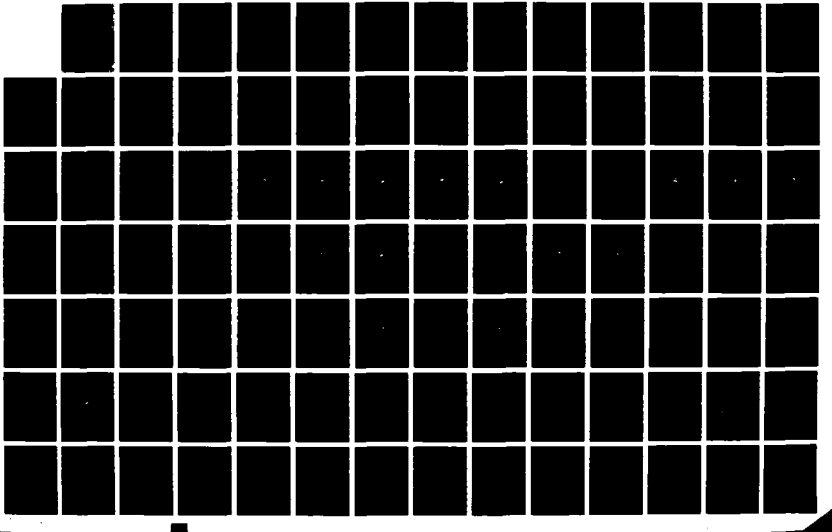

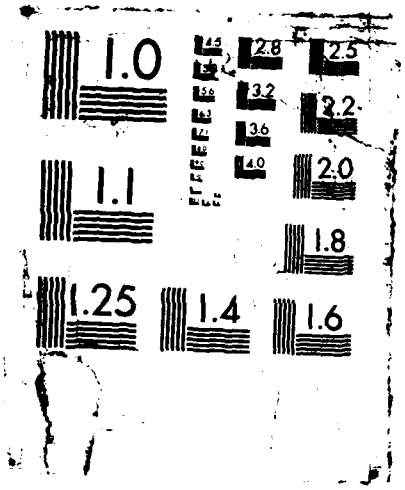
1.0
1.1
1.25
1.4
1.6
1.8
2.0
2.2
2.5
2.8
3.2
3.6
4.0

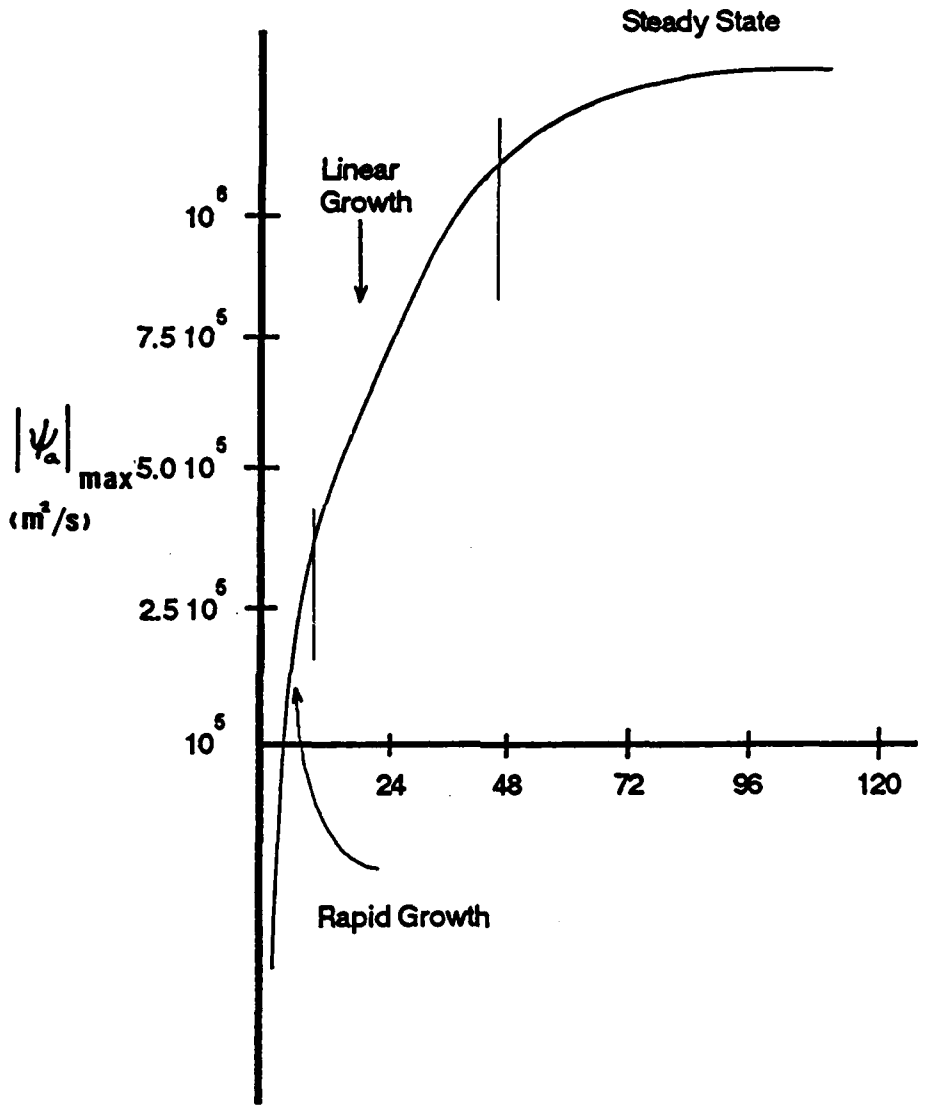

Fig. 4-4. Time variation of the maximum amplitude of the ψ_a gyres of the basic vortex experiment.

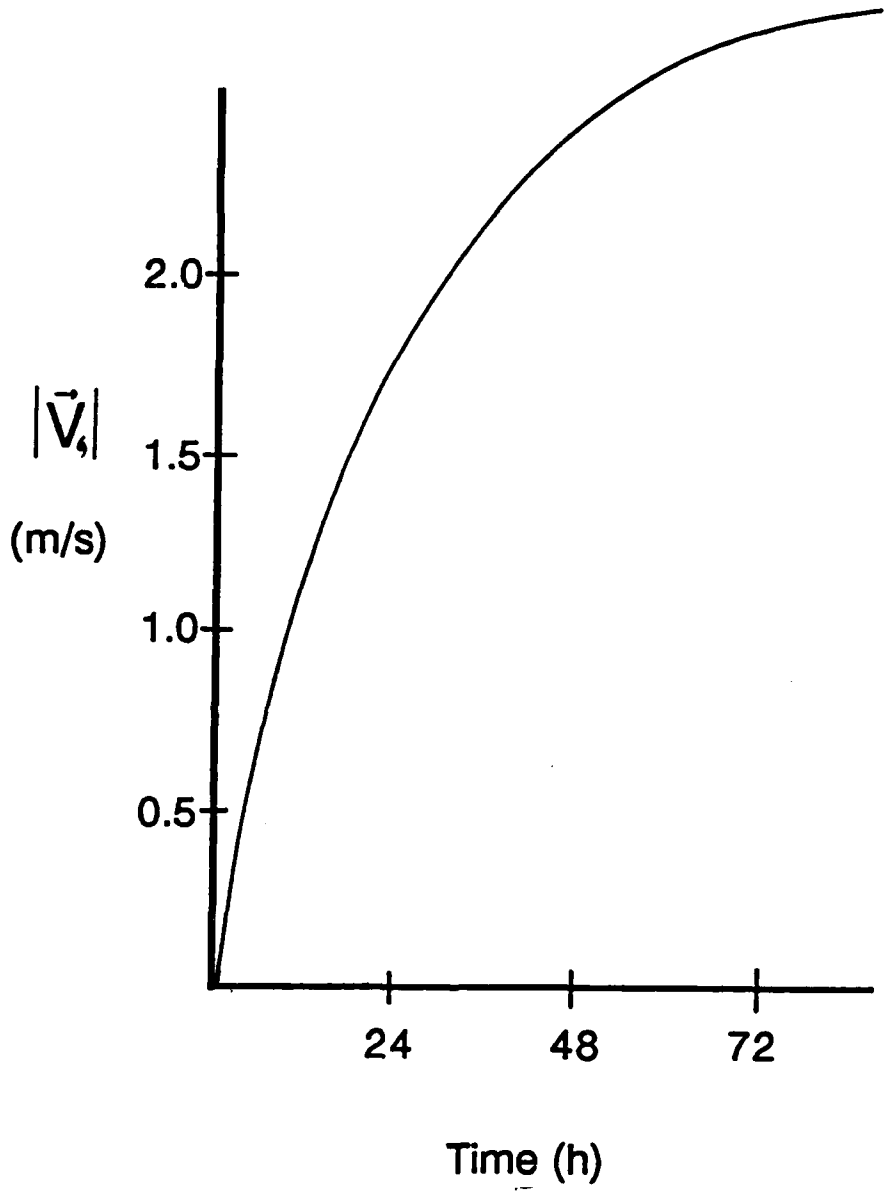

Fig. 4-5. As in Fig. 4-4, except for speed of motion for the center.

rotated flow expands outward and results in a broader ventilation flow. Although this ventilation flow continues to increase from t = 24 to 48 h (Figs. 4-3e and 4-3f), during the linear growth phase, the ψ_a field far from the cyclone center becomes distorted in the east-west direction. At t = 72 h (Fig. 4-3g), the anticyclonic gyre has rotated clockwise, although the center of this gyre appears to be lagging behind the moving center. Nevertheless, the ventilation flow in the inner region maintains the same intensity and horizontal extent. Even though the amplitude of the asymmetric circulation has reached a steady state, the development of east-west distortions suggests the formation of an azimuthally wavenumber two asymmetry. An alternate explanation is that the basic wavenumber one circulation is breaking down in the very weak flow in the outer portions (r > 700 km) of the system.

Longer integrations to t = 144 h (Fig. 4-6) show that the breakdown in the asymmetric flow continues, although the track remains essentially steady from t = 72 - 144 h. The "trailing lobe" of the anticyclonic gyre at t = 72 h splits into a separate circulation feature and then rotates anticyclonically and results in a new anticyclonic center east of the center. During this bifurcation, the ventilation flow remains approximately steady (constant motion).

The fact that the vortex motion continues even with significant changes in the outer asymmetric flow implies that the critical motion dynamics are occurring within the region of "significant" symmetric flow. A measure of the significant symmetric flow is the horizontal scale of the gyres at t = 144 h gyres, which is approximately r = 700 km. This scale coincides with the point at which the symmetric component of vortex reverses from cyclonic to anticyclonic circulation (see Fig. 4-2) at t = 72 h, which is

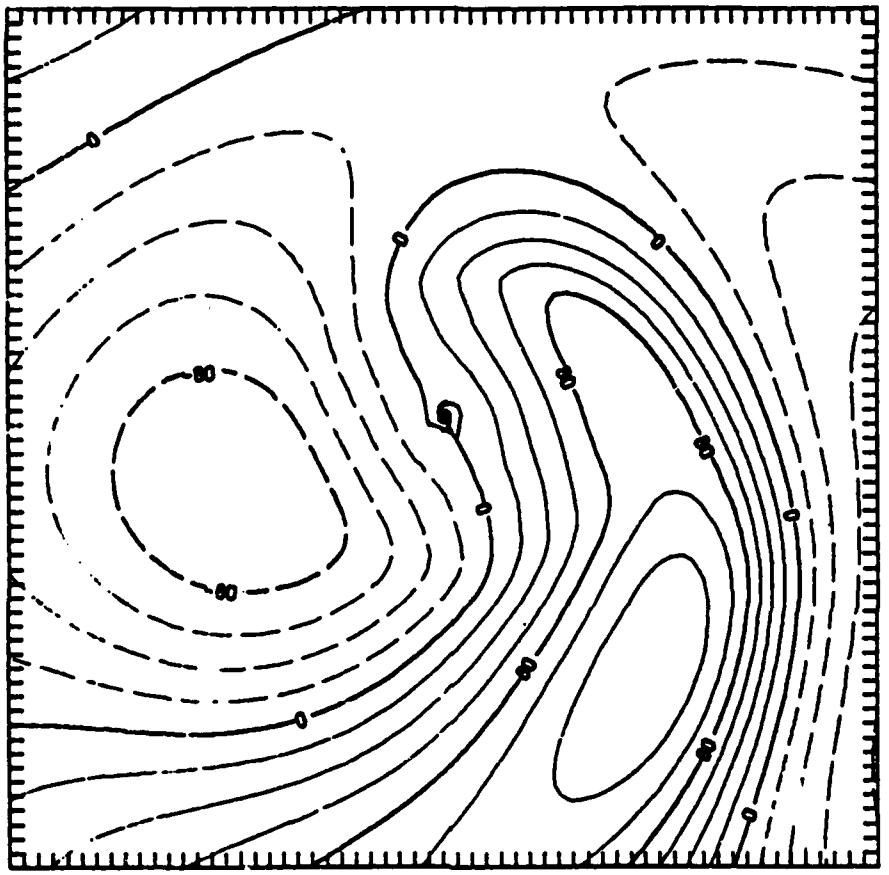

(a) t = 96 h, $|\psi_a| \sim 12.0 \times 10^5$ m²/s
contour interval = 20×10^4 m²/s.

Fig. 4-6. As in Fig. 4-3, except for (a) 96 h, (b) 120 h and (c) 144 h.

b

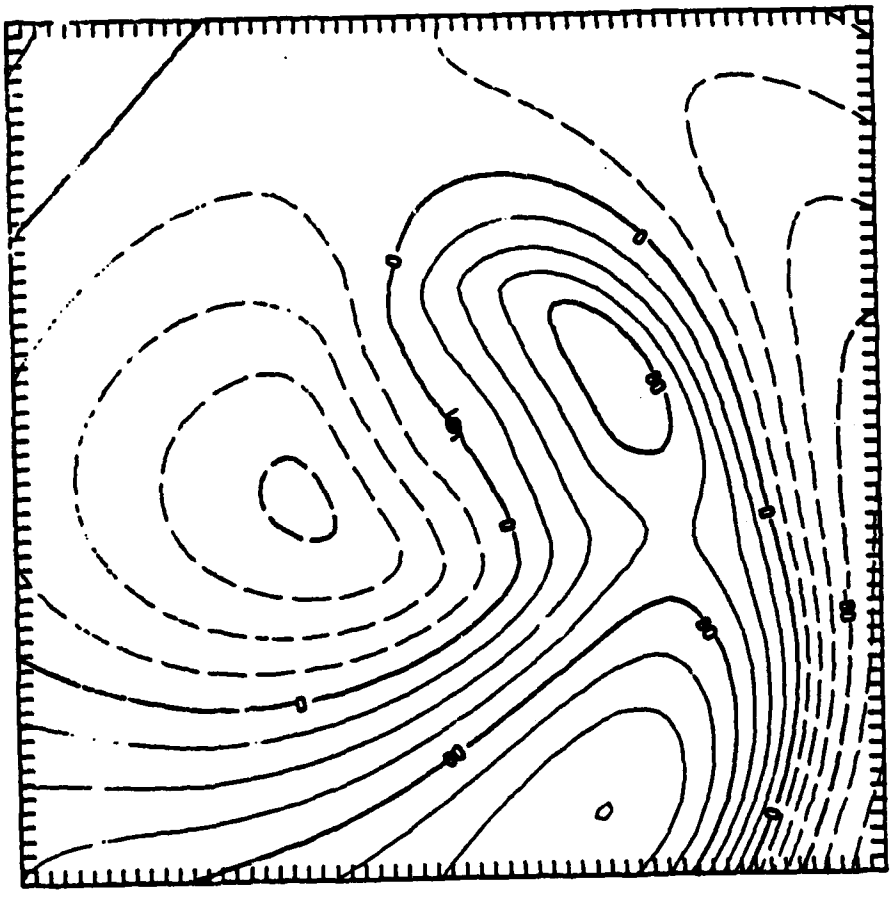

(b) t = 120 h, $|\psi_a|$ ~ 14.0x10^5 m^2/s
contour interval = 20 x 10^4 m^2/s.

Fig. 4-6. (Continued)

C

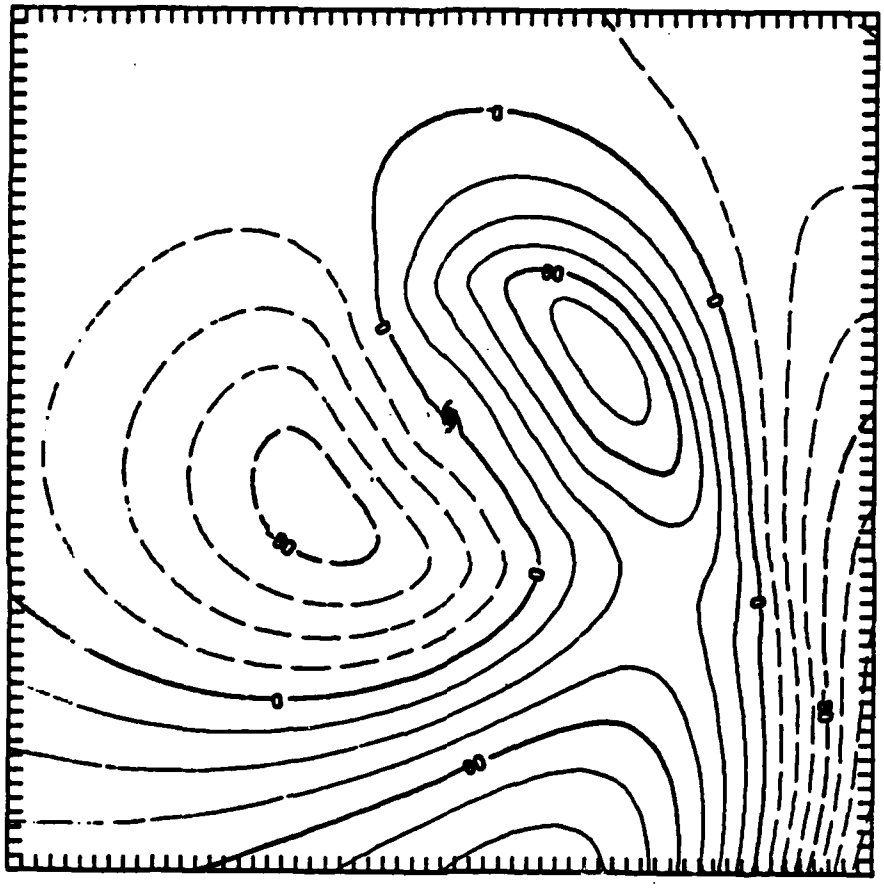

(c) t = 144 h, $|\psi_a|$ ~ 12.0x10^5 m^2/s
contour interval = 20 x 10^4 m^2/s.

Fig. 4-6. (Continued)

representative of the steady-state period. A further supposition is that the balance between linear forcing and nonlinear vorticity advection within this region must stabilize the system.

2. The Asymmetric Flow

To more explicitly relate the motion of the vortex to the asymmetric circulation, the asymmetric flow is derived from ψ_a via

$$u_a = -\frac{\partial \psi_a}{\partial y} \quad \text{and} \quad v_a = \frac{\partial \psi_a}{\partial x} \quad , \qquad (4.1)$$

The asymmetric flow at t = 72 h for the basic vortex are shown in Fig. 4-7 from a large-scale and a smaller-scale view. A strong relationship is evident between the asymmetric flow in the vicinity of the center and the vortex motion vector. This relationship is better illustrated by removing the motion vector from the asymmetric flow to form the "relative" asymmetric flow (Fig. 4-8). Nearly perfect cancellation occurs between the asymmetric flow and the motion vector within the region of the symmetric circulation, except in the high energy core (within the radius of maximum wind). In the inner core, smaller gyres (< 100 km) are found with a "ventilation" flow opposite to the motion of the storm. Model runs with different resolutions demonstrated that the horizontal scale of the inner zone with weak asymmetric flow is independent of the grid spacing, which suggests it is a physical effect.

These inner gyres are nearly identical in pattern to those found by Marks and Houze (1987) in the inner core (r ~ 50 km) of an intense hurricane (Norbert, September 1984 in the eastern North Pacific). Marks and Houze (1987) hypothesized that the gyres resulted from the motion of the vortex based on the theoretical study of Willoughby (1987). While their argument may be valid, an alternate explanation

a

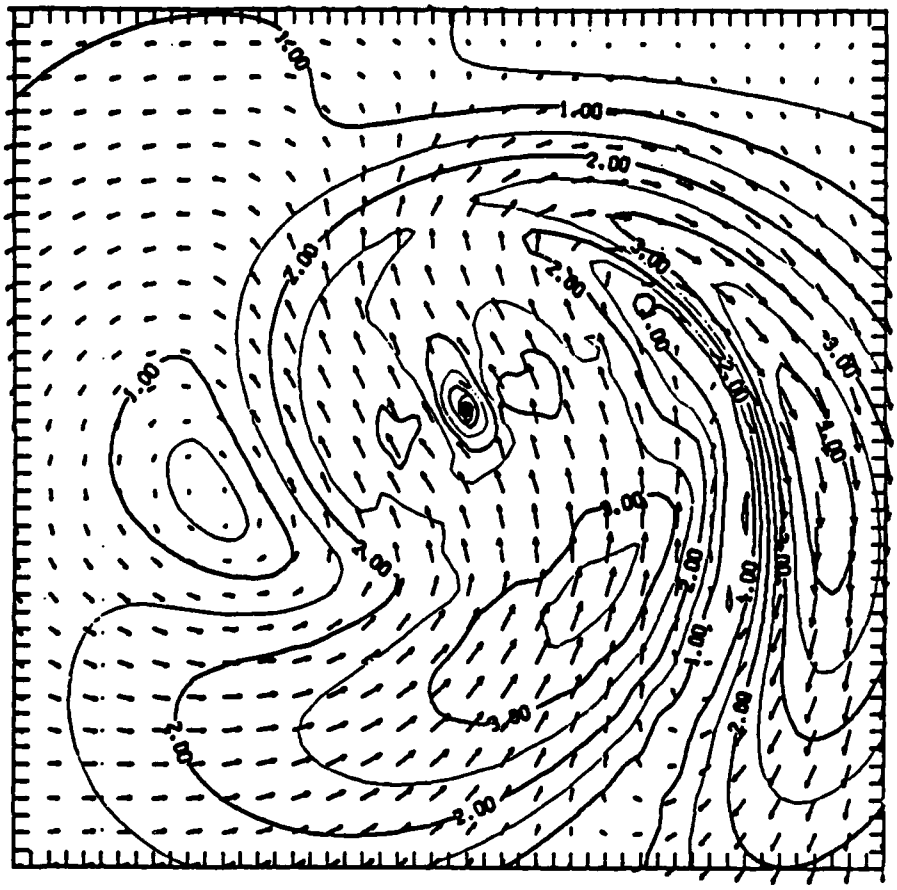

Fig. 4-7. Asymmetric flow at t = 72 h for the basic vortex B1 within a domain of (a) 2000x2000 km and (b) 640x640 km region. The flow speed (m/s) is contoured with an interval of 0.5 m/s in both panels. The maximum vector length corresponding to two grid points (between two tick marks) is 5 m/s.

b

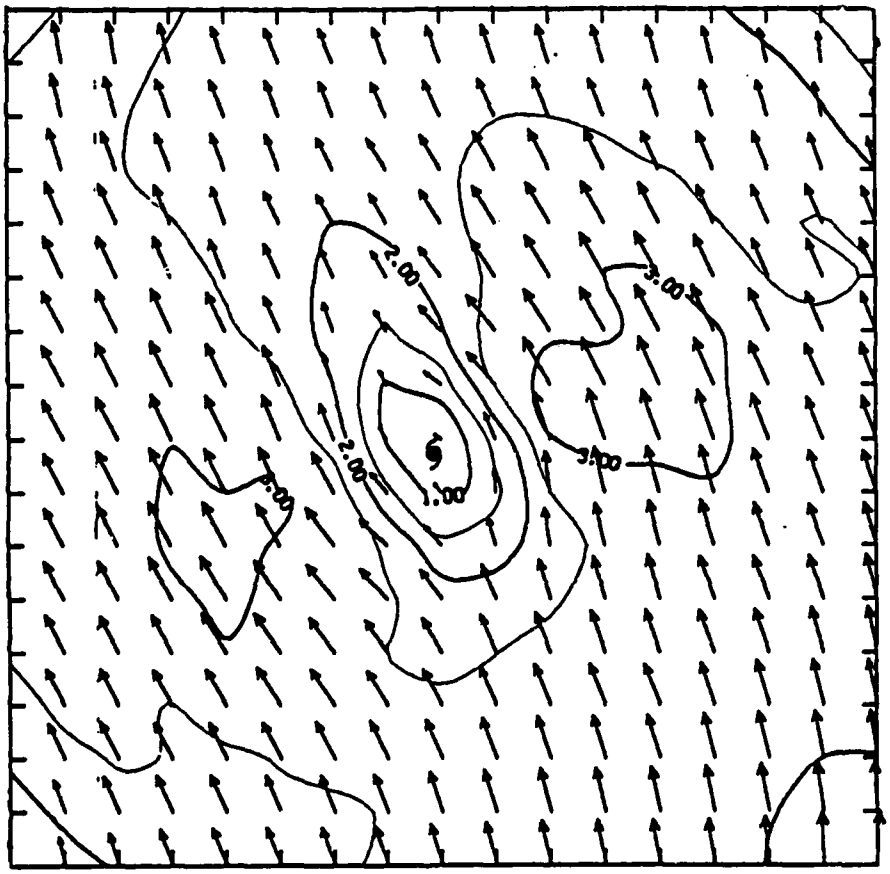

Fig. 4-7. (Continued)

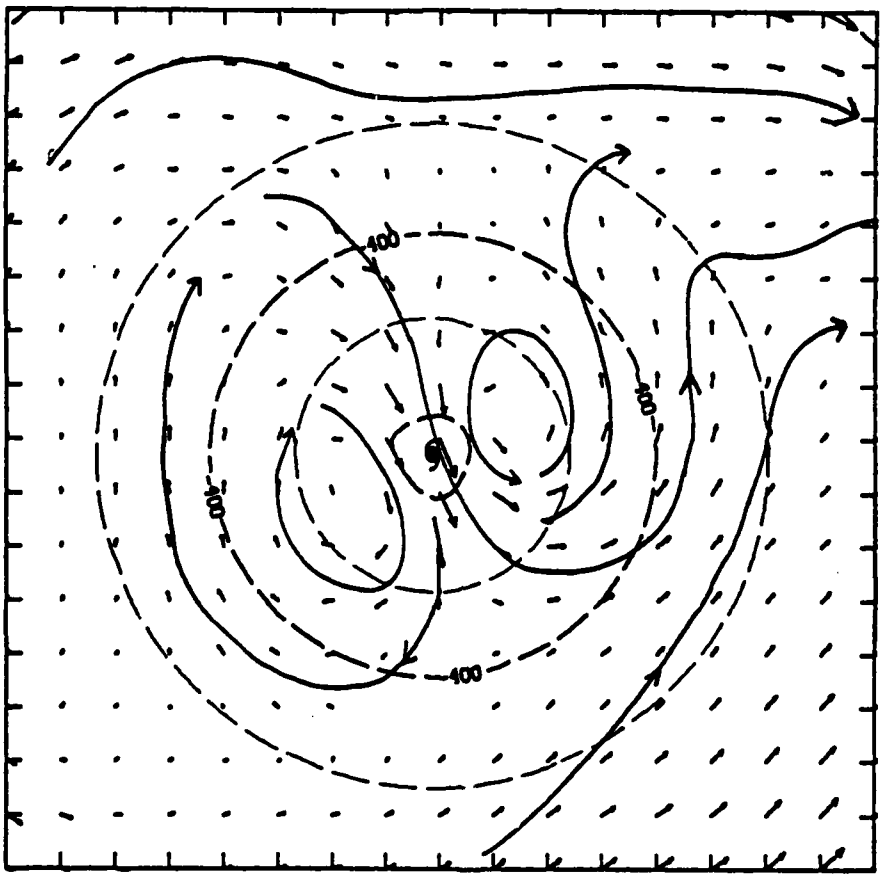

Fig. 4-8. As in Fig. 4-7b, except for relative asymmetric flow (arrows) formed by subtracting the motion vector at 72 h. The maximum arrow length in the upper right corner corresponds to 5.0 m/s. The symmetric streamfunction (contour interval of 200×10^5 m^2/s) depicts the scale of the symmetric vortex circulation.

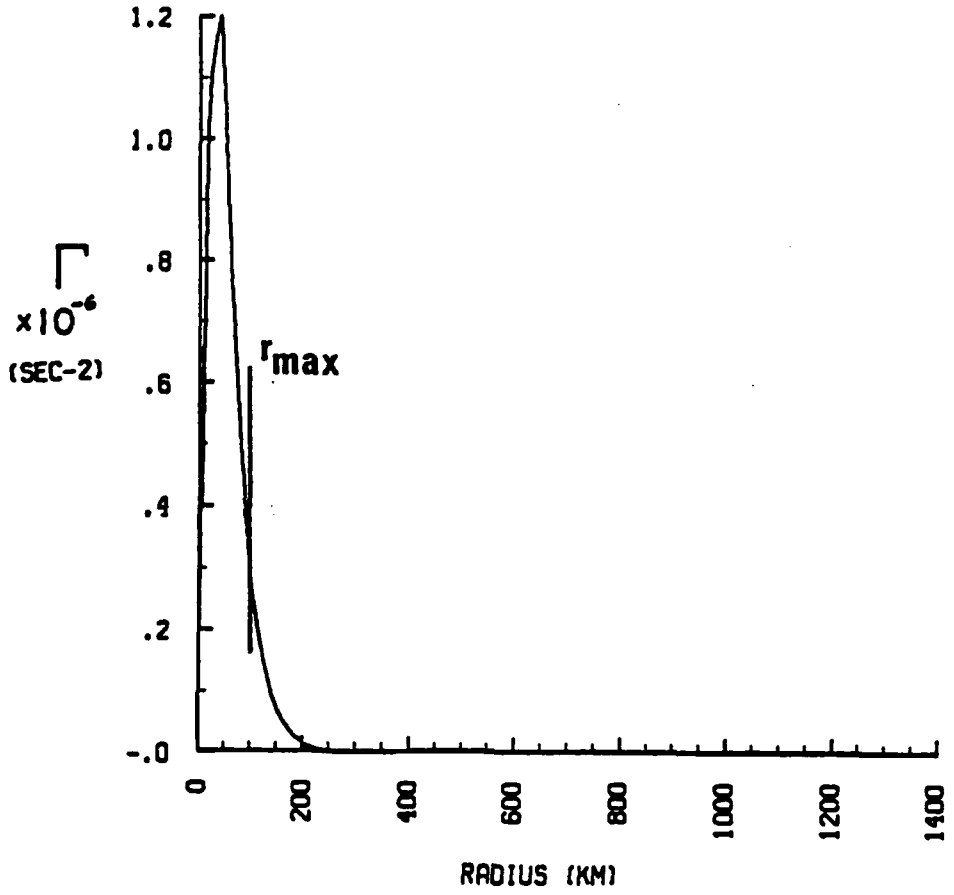

Fig. 4-9. Inertial stability parameter at t = 72 h. The radius of maximum wind is indicated by the heavy vertical line.

is that the inner-gyre pattern is a result of the vortex flow tending to zero at the center.

The scale of the inner gyres in the relative asymmetric flow corresponds closely to the rotational stiffness of the core as represented by the inertial stability parameter (Fig. 4-9) which has been used in other studies (e.g, Holland, 1983). Thus, vorticies of this type have strong rotational stiffness within the radius of maximum wind which resists departures from a symmetrical state. Winds in the eye of tropical cyclones are light and variable, which implies a point where the flow in a fixed framework (Eulerian) goes to zero. Furthermore, a symmetric low pressure system would have a point with zero pressure gradient or no flow at the center. The only effect of an additional environmental pressure field would be a horizontal displacement of the no-flow point from the center of the symmetric vortex. The linear forcing also contributes to the inner-gyre formation. For a perfectly symmetrical vortex βv will go to zero at the center. Thus, the generation of an asymmetric circulation would be limited.

Based on the considerations above, it is argued that the motion of the center is really the motion of a small (50-100 km) stiff core. The scale of this highly stable moving core is on the order of the radius of maximum wind, rather than the "effective" radius of Holland (1983) who proposed a higher value (~ 300 km). Another important point is that the existence of this rotationally stiff core complicates the interpretation of the streamfunction tendency (vorticity budget) used to explain the behavior of the asymmetric circulation later in Sec. IV-D.

D. DESCRIPTION OF THE DYNAMICS OF BETA DRIFT

The apparently strong relationship of the motion of the center to the ventilation flow between the asymmetric

gyres suggests that advection of the symmetric circulation (the vortex) by the asymmetric flow (which arises from the interaction between the vortex and the environment) is responsible for the motion of the center. Even though this idea has been suggested in the past (e.g., Anthes and Hoke, 1975; Holland, 1983), the display in Figs. 4-3, 4-7 and 4-8 explicitly illustrates the spatial relationships. What is less well understood, and of fundamental importance, is the dynamics of the asymmetric gyres.

1. Overview

Rossby dispersion is the source of the large-scale gyres, as is shown in the linear (β only) model runs of Chan and Williams (1987). However, the nonlinear interaction by which the symmetric circulation modifies the asymmetric flow is also important. One aspect of this process is suggested by the cyclonic rotation of the gyres (in the same sense as the symmetric flow) and the expansion of the perturbed (rotated) zone between the gyres as the asymmetric flow rapidly grows (Fig. 4-3). As the asymmetric flow is established, the symmetric forcing through the nonlinear advection term begins to rotate the gyres, and thus the ventilation flow. This rotation effect expands outward as the asymmetric flow develops. Eventually a balance is achieved within the cyclonic portion of the symmetric vortex.

The questions are how and why the symmetric and asymmetric circulations reach a mutually sustaining arrangement that allows the entire system to move uniformly as an entity. To answer these questions, the model tendency equation is examined in great detail. However, an overview of the dynamical processes is given first based on the above analysis.

The symmetric circulation forces a wavenumber one asymmetrical circulation through Rossby (or β) dispersion.

The β term in the model equation tends to produce anticyclonic tendencies when the north-south wind component (v) is positive (east of the center) and cyclonic tendencies when v is negative (west of the center). Recall that the β term appears as a forcing function in the Poisson equation $\nabla^2(\partial\psi/\partial t) = \beta v$, so that the horizontal scale of the tendencies is much larger than the symmetric vortex.

Advection of symmetric vorticity by the asymmetric flow in Fig. 4-3 causes the translation of the symmetric vortex, whereas the cyclonic symmetric circulation advects the asymmetric flow cyclonically (the rotation). If the vortex did not move, the gyres would continue to rotate. Because the asymmetric flow is advecting the symmetric circulation, the β forcing of the asymmetric flow is moving as well. This is a key point, because the translation of the β forcing with the center limits the time for the formation of the asymmetric flow to the east and west of the moving center. Consequently, the asymmetric gyres are not simply aligned in the east-west (location of the maximum v) direction as in arguments with linear forcing relative to a stationary vortex. Furthermore, this alignment is opposed by the advection of the gyres by the symmetric flow. A balance eventually occurs between the asymmetric flow formation by the moving source (the symmetric circulation) and advective twisting by the vortex. In other words, advection tries to rotate the gyres <u>cyclonically</u> (depending on the symmetric flow in the vicinity of the gyres) while the β forcing always tries to keep the gyres aligned east-west (equivalent to an <u>anticyclonic</u> rotation) relative to the position of the moving vortex.

Another way to understand this balance is to consider a situation in which the motion of the symmetric circulation is made independent of the asymmetric flow. Suppose the symmetric circulation could move at a speed

greater the "balanced" or physically correct speed. Then, the symmetric vortex would soon be displaced beyond the asymmetric ventilation flow that sustains the movement. Presumably, this would result in a tendency for the vortex to slow down to allow the asymmetric gyres to reform. Conversely, if the vortex displacement was much smaller than the ventilation flow, the asymmetric flow would continue to grow (linearly) with much stronger southerly (northerly) flow to the west (east) of the center as shown in the linear solutions of Chan and Williams (1987).

The balance then is between the vortex translation and the asymmetric circulation development. This concept is illustrated (Fig. 4-10) by plotting the ventilation flow as a function of speed of movement for linear and nonlinear effects. Rossby dispersion, or the linear component of the model solution, would yield a large asymmetric flow (linear growth of the asymmetric circulation as in Figs. 4-3 and 4-4) if the vortex did not move due to nonlinear advection. Conversely, if the vortex movement was very large, there would be insufficient time to form an asymmetric circulation around the center. The 1:1 relationship between the ventilation flow and the translation of the center implied by the nonlinear advection curve is simply a statement that the motion is directly proportional to the advection by the ventilation flow (i.e., simple steering).

The conceptual plot (Fig. 4-10) shows that there will always be some balance point, although it might vary in time. A priori, the linear Rossby wave effect might be expected to be a stronger function of the vortex structure than the nonlinear advection effect because small changes in the outer flow could lead to significant changes in the large-scale dispersive modes. Although the conceptual diagram and the balance point are plausible, this considers only the steady-state speed. Transients in the motion and

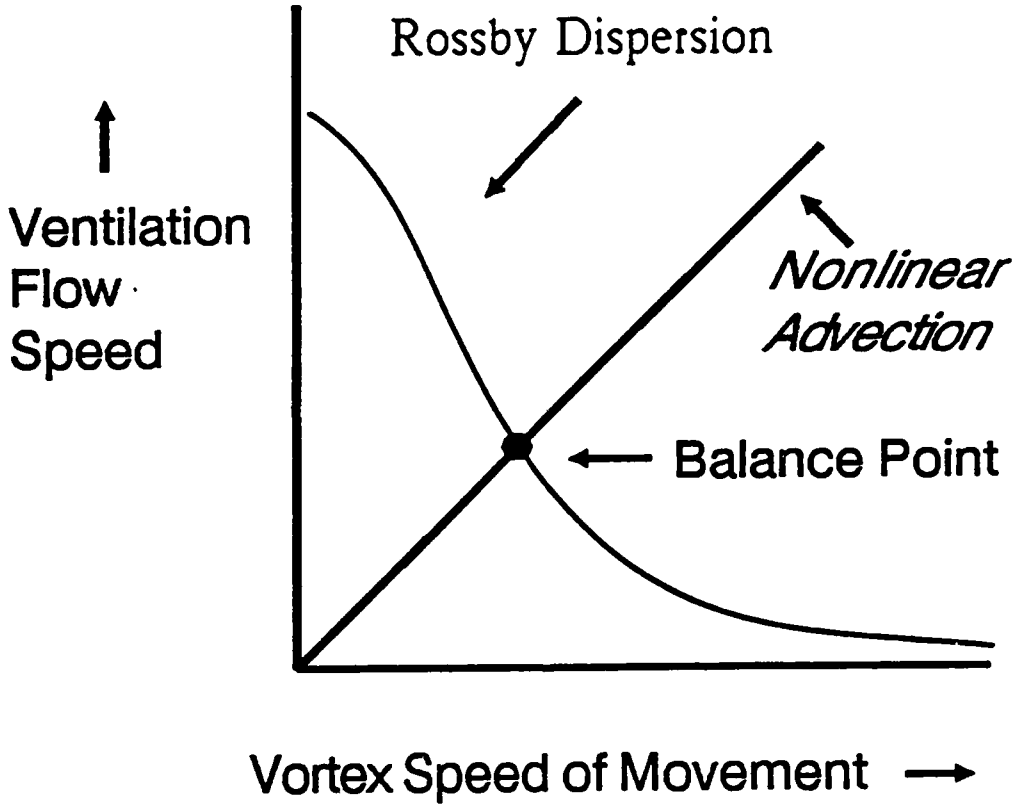

Fig. 4-10. Conceptual plot of the ventilation flow as a function of speed of movement for linear Rossby dispersion and nonlinear advective processes (see description in text).

long time-scale turning motions are likely to be almost exclusively dependent on advective effects as suggested by the symmetric perturbation experiments in Chapter III. The nonlinear advective effects controlling track or path are likely to vary significantly even with seemingly subtle changes in the symmetric vortex. Thus, it is important to focus on the nonlinear effects while keeping in mind that Rossby dispersion is likely to be controlling the basic balance and the translation speed.

The relative asymmetric flow gyres in Fig. 4-8 suggest a role for advection of asymmetric vorticity by the symmetric flow. These inner gyres have a positive vorticity center to the right of the motion vector and a negative center to left (e.g., Fig. 4-11a) opposite to the larger-scale asymmetric gyres). As Marks and Houze (1987) suggested, advection by the symmetric vortex would tend to force a vorticity increase ahead of the center and a decrease to the rear. In terms of streamfunction tendencies, this motion-type pattern would be a dipole (negative in the front/positive in the back) with the centers aligned in the direction of motion. By this reasoning, a "motion-type" tendency pattern very close to the center would be expected in both the symmetric and asymmetric advection terms. This is why the presence of the stiff core will complicate the interpretation of the nonlinear tendency terms. It is also suggested that the motion of symmetric vortex beyond the stiff core (r = 100 - 300 km) may involve different dynamics than that of the center and occur on different time and space scales.

2. Discussion

The concepts developed in the preceding discussion have been based on the B1 vortex and are now evaluated in the other vortices (the symmetric perturbation vortices and the weak-large vortex). The asymmetric streamfunction has

a

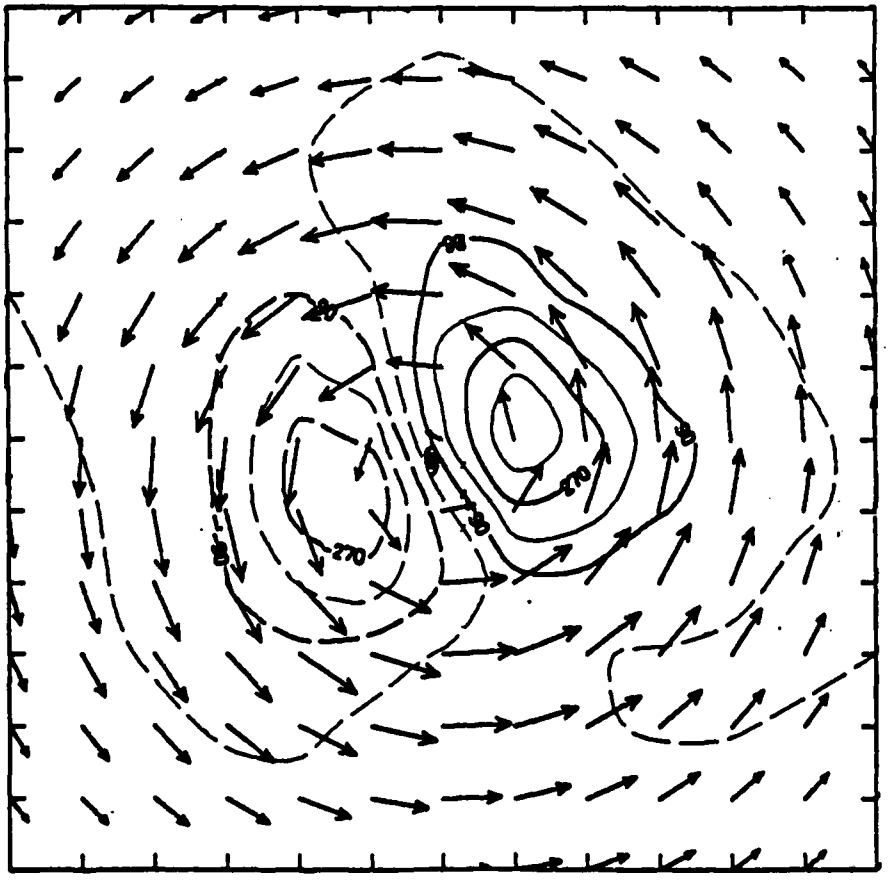

(a) maximum vector length = 33 m/s
contour interval = 90×10^{-7} s^{-1}
minimum contour = -270×10^{-7} s^{-1}
maximum contour = 360×10^{-7} s^{-1}

Fig. 4-11. The symmetric flow (vectors) and the asymmetric vorticity (contoured) at t = 72 h for (a) the basic vortex, (b) the weak-large vortex, (c) the cyclonic perturbation vortex and (d) the anticyclonic perturbation vortex. The domain is 640x640 km and the vectors are plotted at every grid point.

b

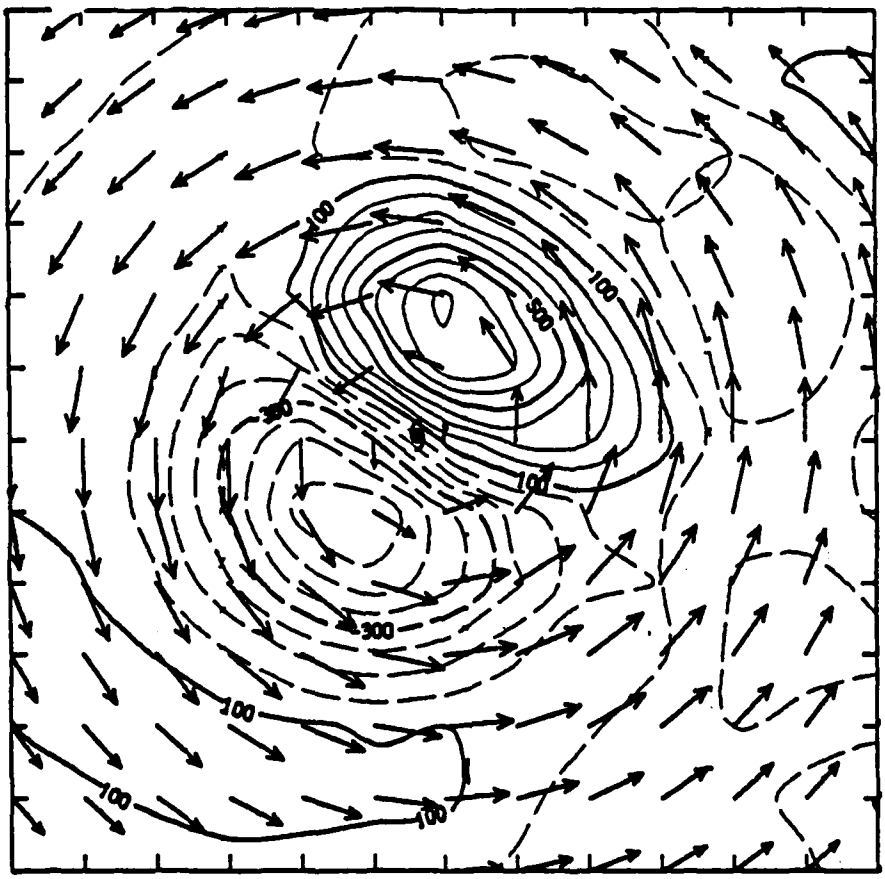

(b) maximum vector length = 18 m/s
contour interval = 100×10^{-7} s^{-1}
minimum contour = -600×10^{-7} s^{-1}
maximum contour = 800×10^{-7} s^{-1}

Fig. 4-11. (Continued)

C

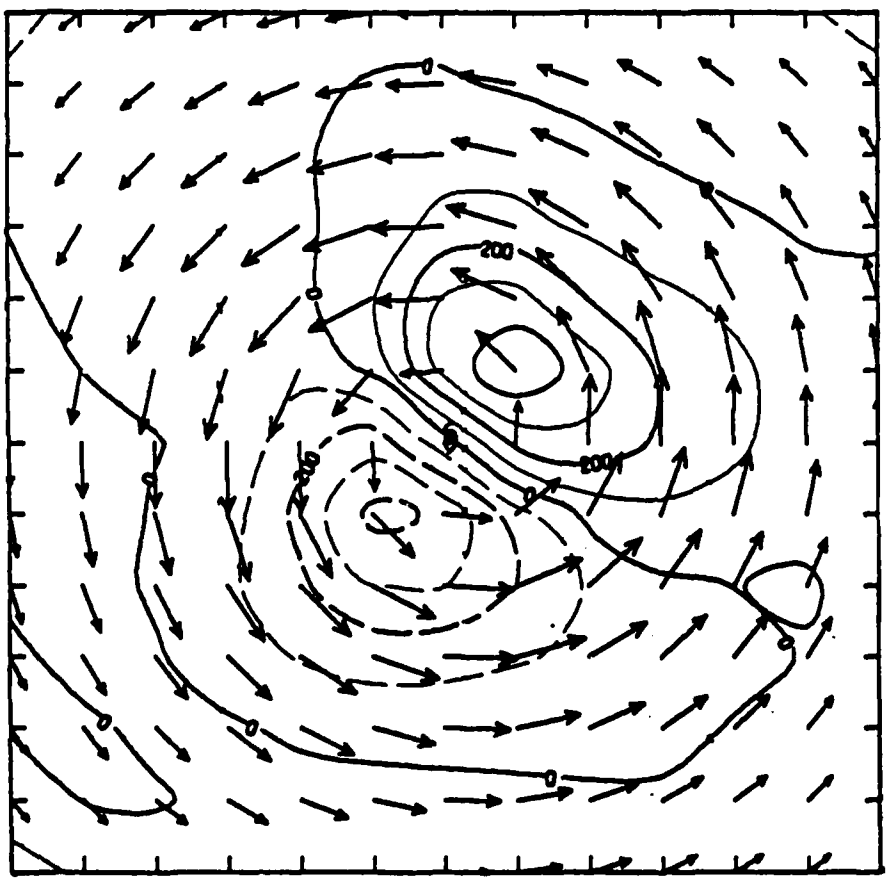

(c) maximum vector length = 33 m/s
contour interval = 100x10^{-7} s^{-1}
minimum contour = -400x10^{-7} s^{-1}
maximum contour = 400x10^{-7} s^{-1}

Fig. 4-11. (Continued)

d

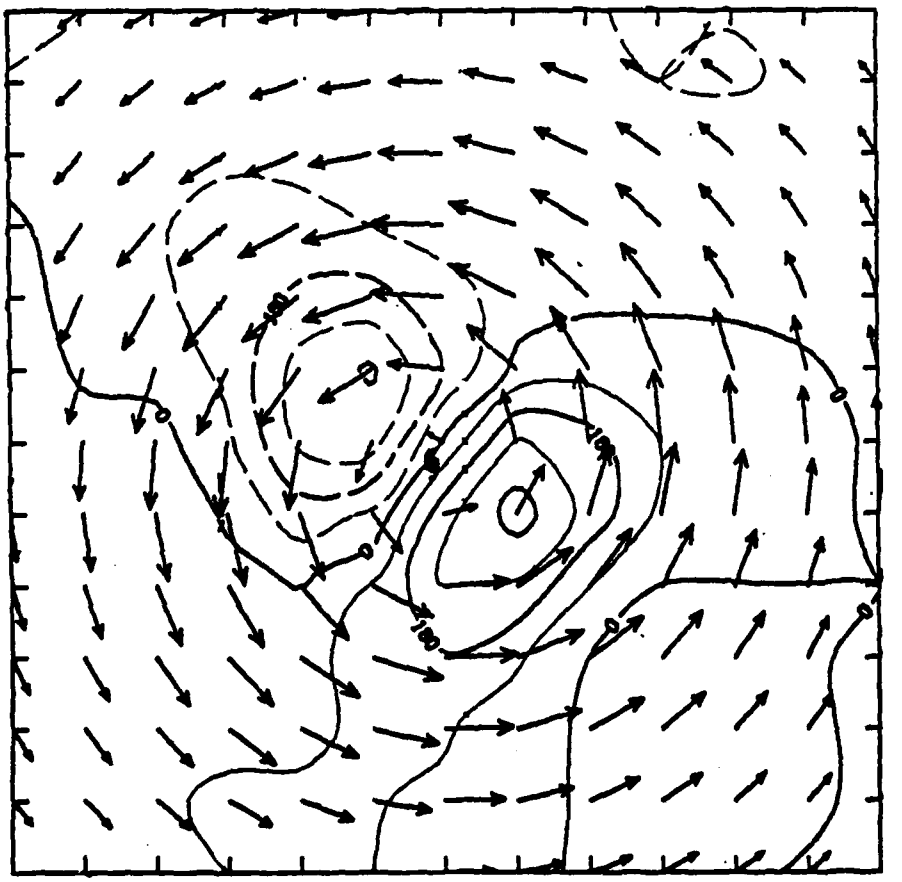

(d) maximum vector length = 33 m/s
contour interval = 90×10^{-7} s^{-1}
minimum contour = -360×10^{-7} s^{-1}
maximum contour = 360×10^{-7} s^{-1}

Fig. 4-11. (Continued)

the same type of relationship to the motion (Fig. 4-12) and undergoes a similar evolution. The size and intensity of the large-scale gyres is proportional to the outer strength (e.g., Fig. 4-12a versus Fig 4-12c). Notice that the ventilation flow in the beginning of the integration and during the development of the gyres, is oriented toward the northwest for all vortices. By 48 h, the tracks (see Figs. 3-5 and 3-8) for these vortices show long-term turning and this is reflected in the orientation of the ventilation flow (Figs. 4-12b, d and e). The differences in the asymmetric streamfunction between t = 6 and 48 h indicate that the gyre rotation is a slower process than the process that moves the center initially. Furthermore, the gyre rotation appears to be a larger-scale effect that gradually influences the motion of the center.

The strong relationship between the asymmetric flow and the motion of the center, except in the inertially stiff core as discussed above, implies that the interaction between the asymmetric and symmetric circulation systems is the key to the motion process. The behavior of the asymmetric flow is described in the next section by use an expanded model tendency equation to understand the dynamics of the asymmetric circulation.

E. STREAMFUNCTION TENDENCY ANALYSIS

To verify the motion hypothesis developed from the analysis of the symmetric and asymmetric circulations, the nonlinear terms in the model tendency equation are examined in detail. The relevant equations from the derivation given in Appendix C are repeated here. First, only the streamfunction tendencies are considered, as opposed to vorticity budgets used in previous studies (e.g., Chan, 1984), because the focus is on the development of the symmetric and asymmetric circulation systems. A vorticity

a

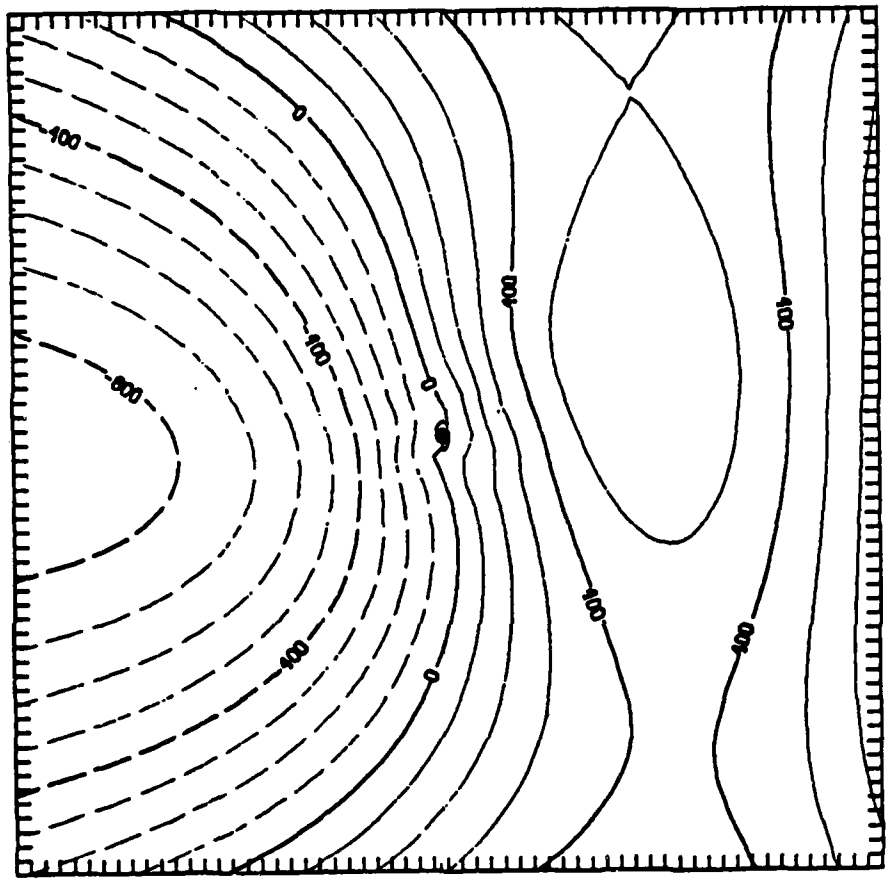

(a) B3 vortex at t = 6 h
contour interval = 100x10³ m²/s
minimum contour = -800x10³ m²/s
maximum contour = 500x10³ m²/s

Fig. 4-12. The asymmetric streamfunction ψ_a (m^2/s) for the weak-large (B3), cyclonic perturbation (S8) and the anticyclonic perturbation vortex (S9). The plot domain is 2400x2400 km (Δx = 40 km, 61x61 grid points). Positive (solid) and negative (long-dashed) contours indicate anticyclonic (cyclonic) streamfunctions.

b

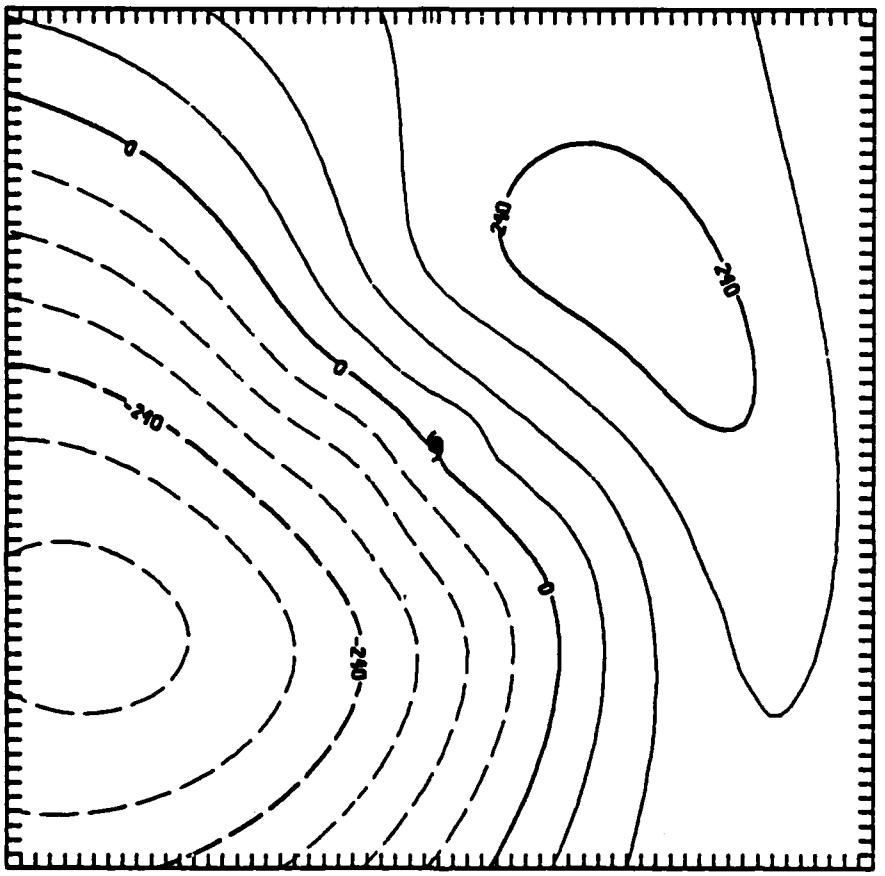

(b) B3 vortex at t = 48 h
contour interval = 60x10⁴ m²/s
minimum contour = -360x10⁴ m²/s
maximum contour = 240x10⁴ m²/s

Fig. 4-12. (Continued)

C

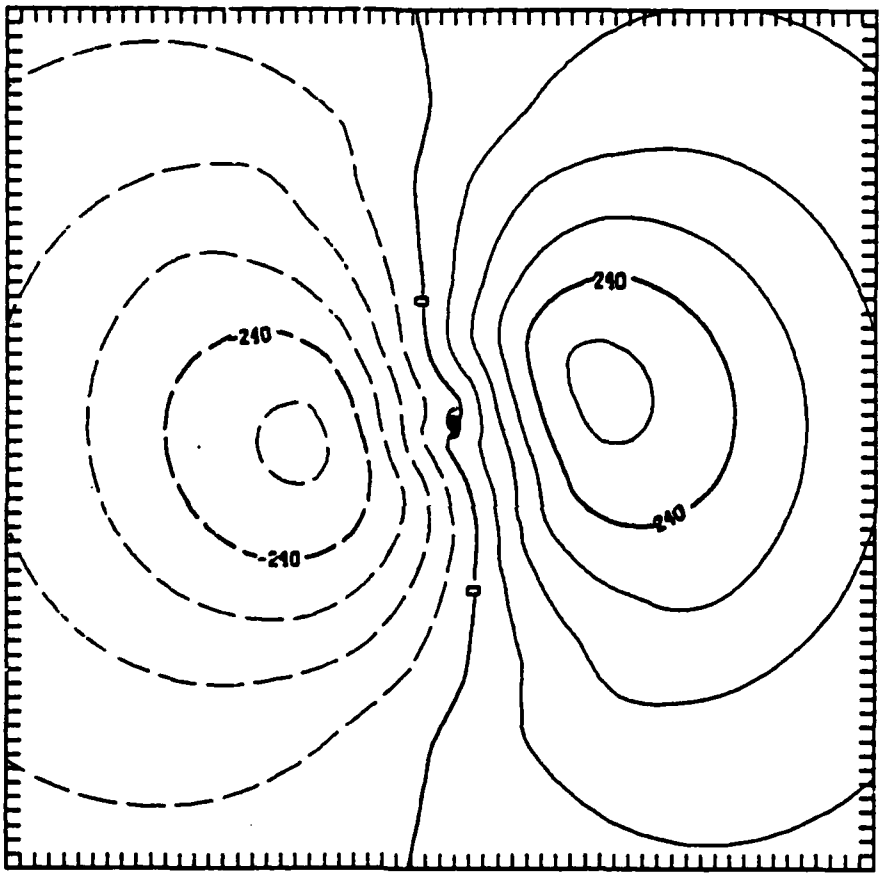

(c) S8 vortex at t = 6 h
contour interval = 60x10³ m²/s
minimum contour = -300x10³ m²/s
maximum contour = 300x10³ m²/s

Fig. 4-12. (Continued)

d

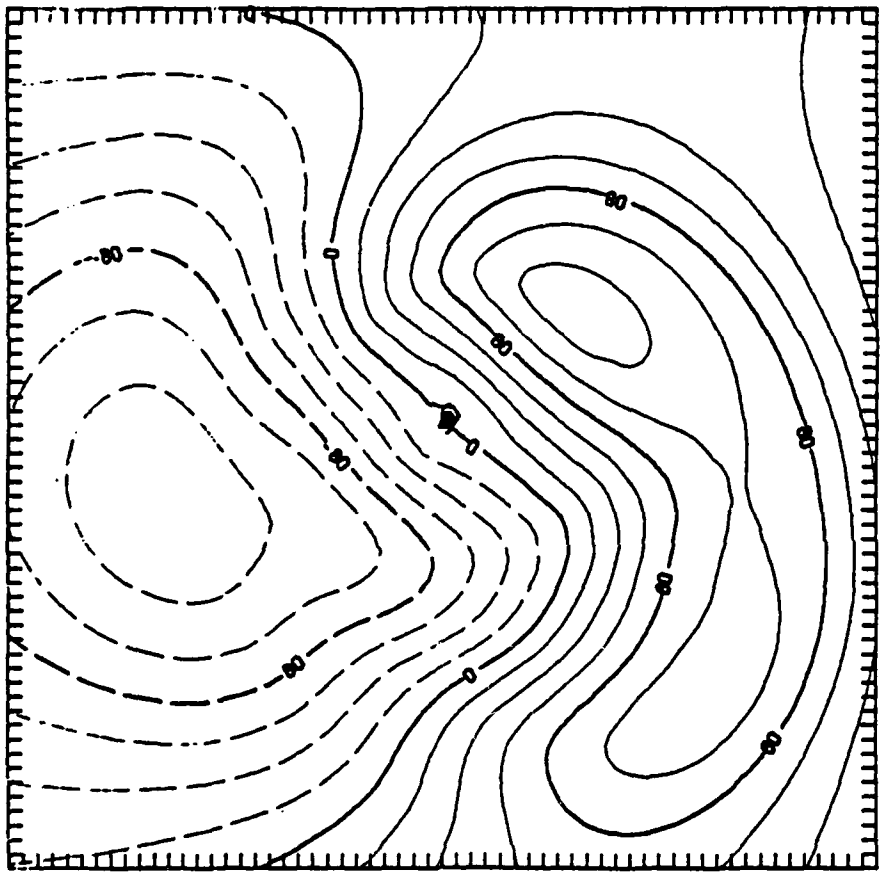

(d) S8 vortex at t = 48 h
contour interval = 20x10⁴ m²/s
minimum contour = -120x10⁴ m²/s
maximum contour = 120x10⁴ m²/s

Fig. 4-12. (Continued)

e

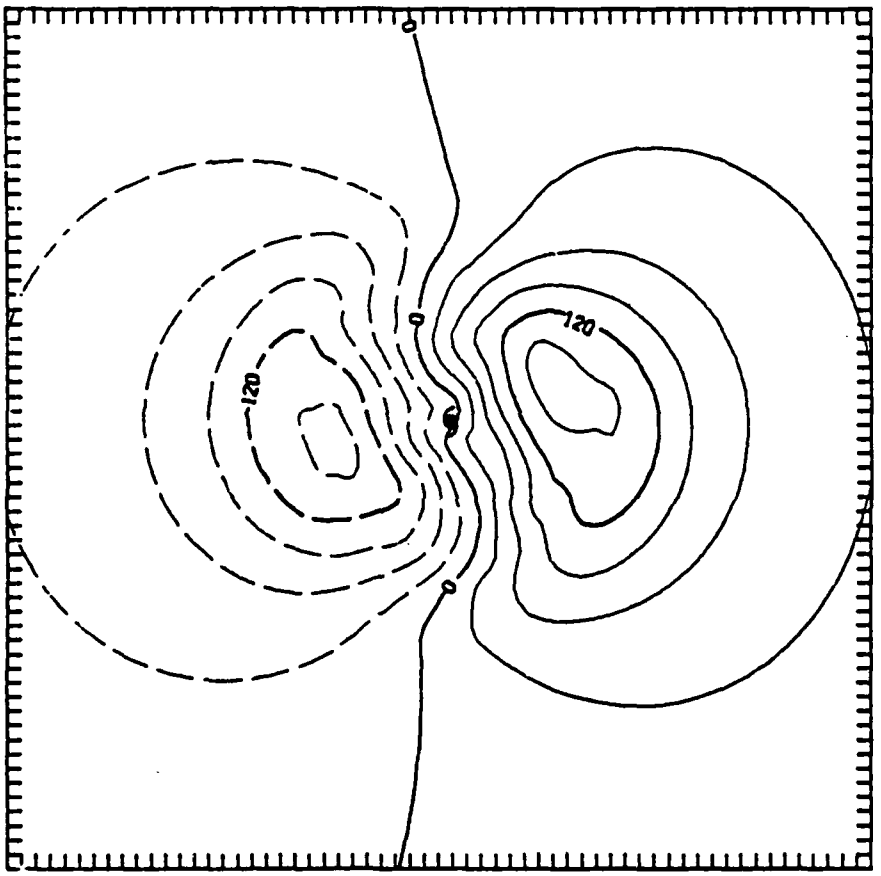

(e) S9 vortex at t = 6 h
contour interval = 30x10^3 m^2/s
minimum contour = -150x10^3 m^2/s
maximum contour = 150x10^3 m^2/s

Fig. 4-12. (Continued)

f

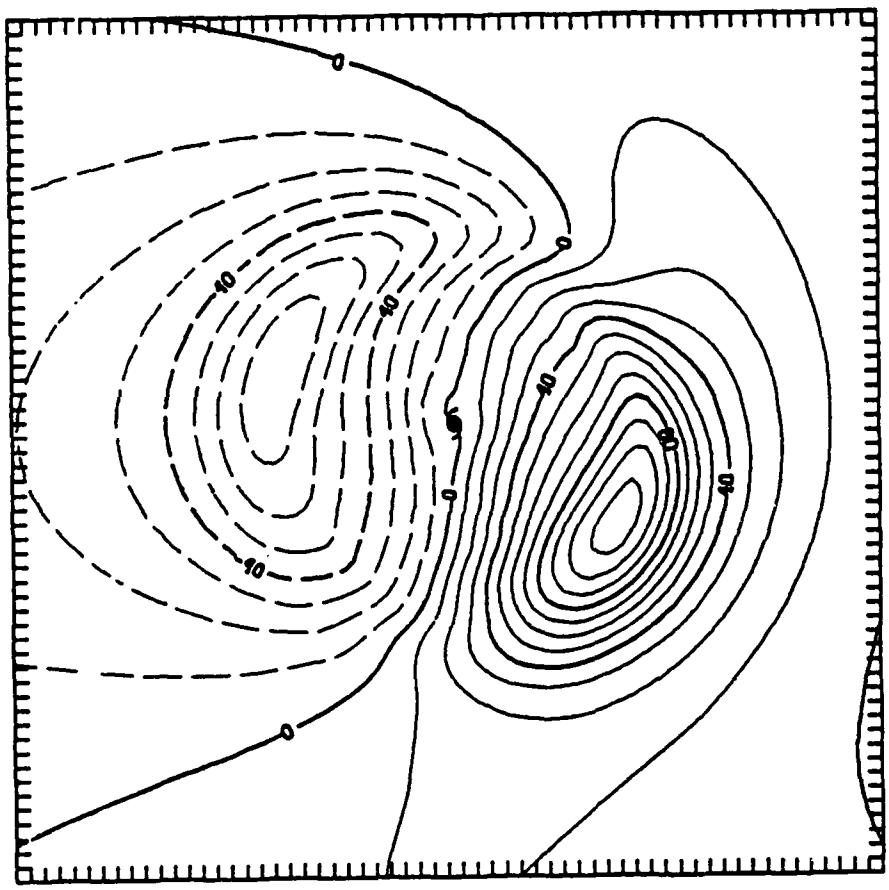

(f) S9 vortex at t = 48 h
contour interval = 10x10⁴ m²/s
minimum contour = -70x10⁴ m²/s
maximum contour = 110x10⁴ m²/s

Fig. 4-12. (Continued)

budget requires a subjective interpretation of the patterns to infer changes in circulation. More importantly, the streamfunction tendency is the model variable by which the model dynamics are best studied.

The model tendency equation for the total streamfunction (ψ_t) can be expressed as

$$\frac{\partial \psi_t}{\partial t} = H^{-1}(-J(\psi_t, \nabla^2 \psi_t) + H^{-1}(\beta v) \quad , \qquad (4.2)$$

where H^{-1} is the inverse operator of $H(f) = \nabla^2 f$.

Splitting the nonlinear advection and beta terms into asymmetric and symmetric components yields

$$\frac{\partial \psi_t}{\partial t} = H^{-1}(-J(\psi_a, \nabla^2 \psi_s) + H^{-1}(-J(\psi_s, \nabla^2 \psi_a)$$

$$\underset{TT}{\qquad} \qquad \underset{ASVA}{\qquad} \qquad \underset{AAVS}{\qquad}$$

$$+ H^{-1}\{ S(\beta v) \} + H^{-1}\{ A(\beta v) \} \quad , \qquad (4.3)$$

$$\underset{SB}{\qquad} \qquad \underset{AB}{\qquad}$$

where

TT	-	Total Tendency
ASVA	-	Advection of symmetric vorticity by the asymmetric flow
AAVS	-	Advection of asymmetric vorticity by the symmetric flow
SB	-	Symmetric component of the beta term that forces the asymmetrical flow
AB	-	Asymmetric component of the beta term that forces the symmetric flow

Additionally, the following tendencies are defined

TA - Total nonlinear advection = ASVA + AAVS

TB - Total beta term = SB + AB

The tendencies in all the following figures have been nondimensionalized (as in the model) with a length scale of 10^6 m and a time scale of 10^5 s. It is emphasized

that the tendencies are calculated on the model grid using the model finite difference operators.

1. Total Tendency Analysis

The total tendency term in each of the three asymmetric development phases are shown in Fig. 4-13. At t = 3 h (Fig. 4-13a), the forcing of the large-scale asymmetric gyres is apparent with positive ψ changes to the east of the center and negative changes to west. However, a smaller-scale tendency dipole also forms near the center. The orientation of this dipole is suggestive of motion toward ψ falls ahead of the center and away from the rises behind. Notice that the orientation is towards the northwest, which is in the same direction as the motion of the center at this time (from the model diagnostics package and not shown). Thus, the beta drift has already been established very early in the integration. By t = 12 h (Fig. 4-13b), the inner dipole tends to dominate the pattern as the contour level is chosen to give a set of approximately 10 contours. Also note that the amplitude of the tendency field has nearly doubled from 3 h to 12 h. The strength of the motion-type dipole pattern continues to grow and a steady state is established by 36-72 h (Figs. 4-13c and d).

Removing the motion component from the pattern will reveal the tendency relative to the moving center. This removal is accomplished by subtracting a "motion" tendency due to the advection of the total vorticity field by a horizontally uniform flow (Fig. 4-14). The uniform flow vector is defined as the average vortex motion in a 6-h period centered around the valid time (see Appendix D for details). Notice that the amplitudes in Fig. 4-14 are nearly identical to total tendency in Fig. 4-13d. Thus, a large fraction of the tendency field during the steady-state

a

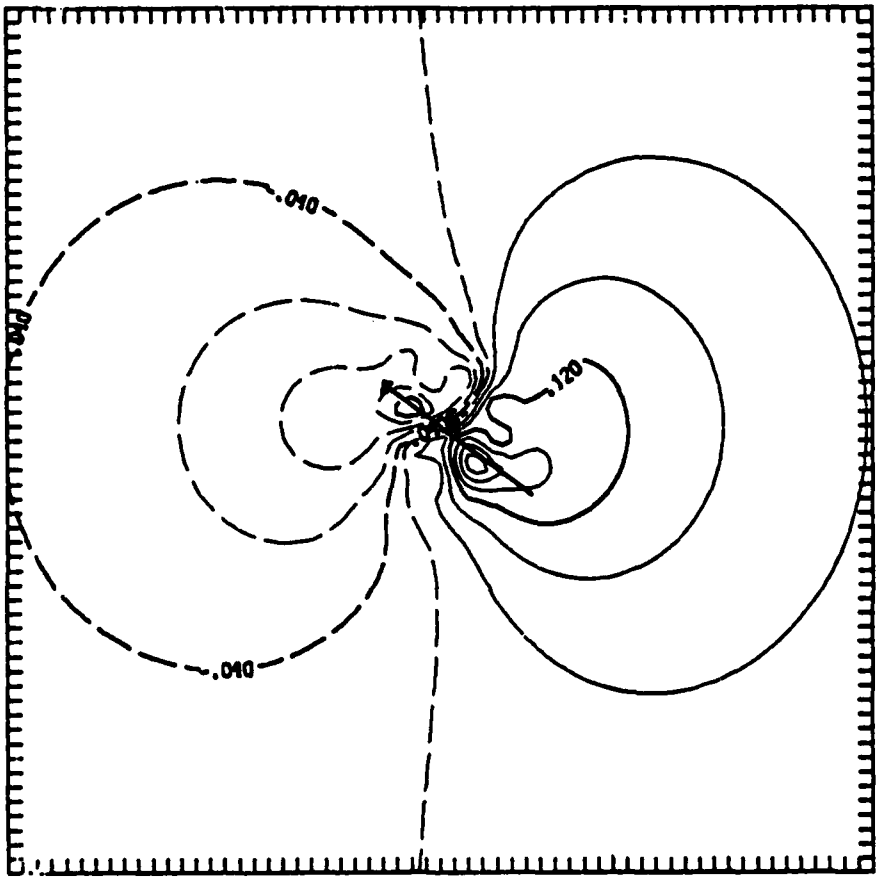

(a) t = 3 h, $|\partial\psi/\partial$ ~ 0.24, contour interval = 0.04

Fig. 4-13. The t al streamfunction tendency, TT (nondimensionalize) at (a) 3h, (b) 12 h, (c) 36 h and (d) 72 h). In all sub equent figures of streamfunction tendencies, positi e (negative) values indicate anticyclonic (cyclonic) changes. The plot domain is the same as in Fig. 4-12.

b

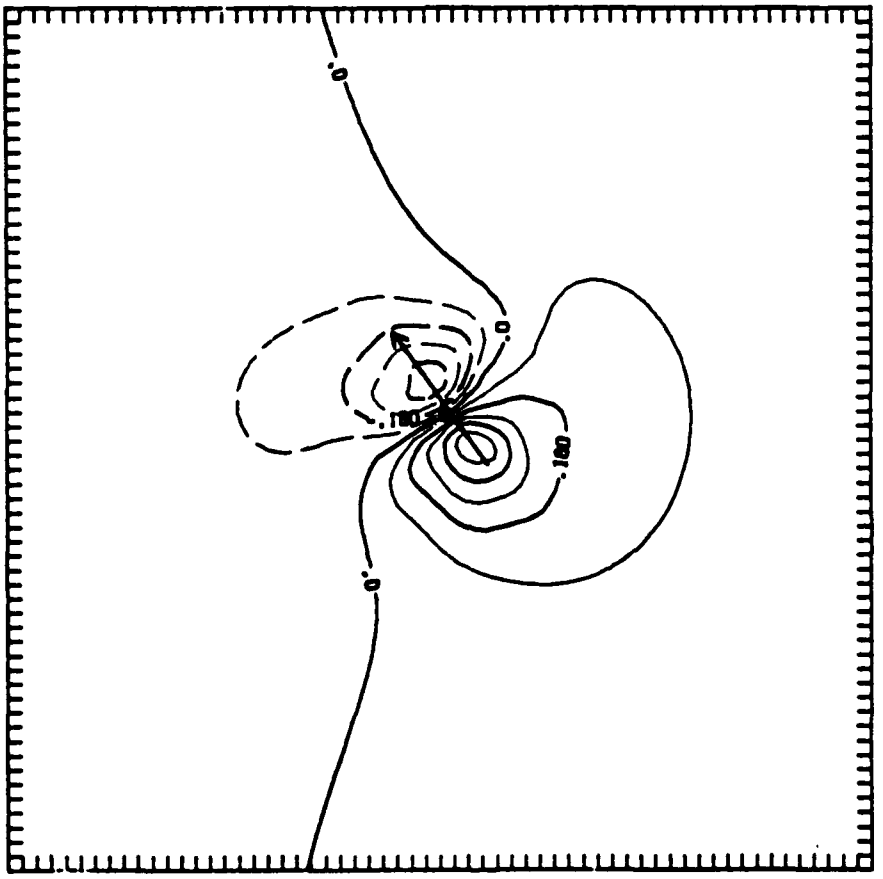

(b) t = 12 h, $|\partial\psi/\partial t|_{max}$ ~ 0.45, contour interval = 0.09

Fig. 4-13. (Continued)

C

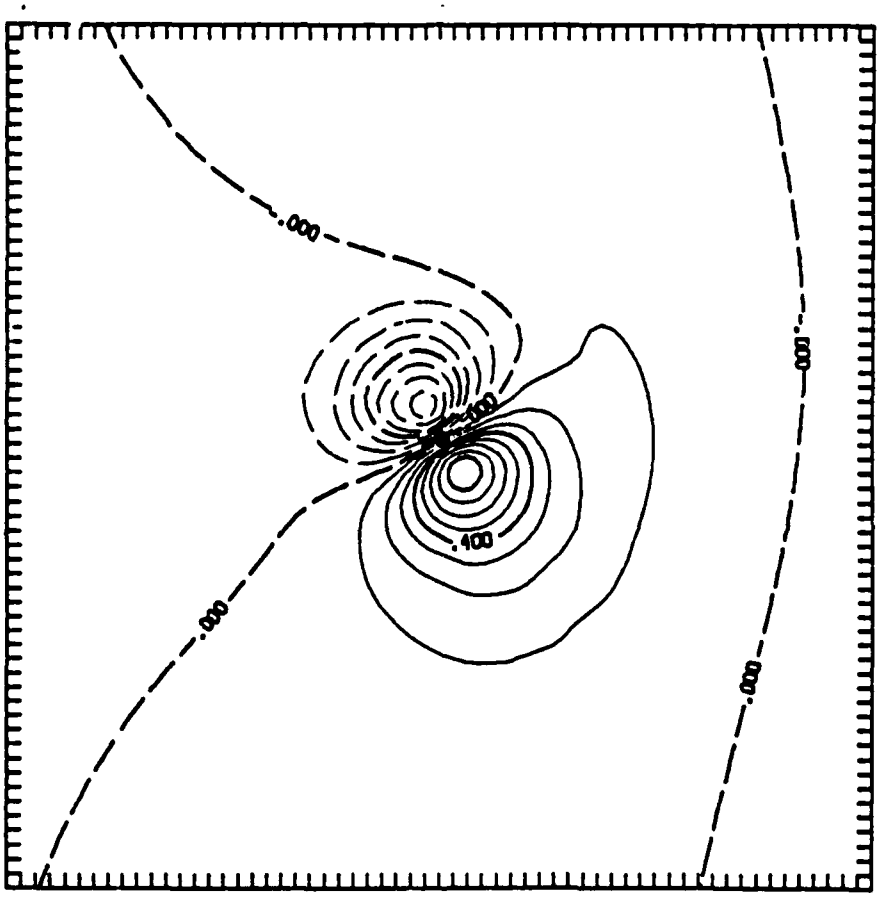

(c) t = 36 h, $|\partial\psi/\partial t|_{max}$ ~ 0.80, contour interval = 0.10

Fig. 4-13. (Continued)

d

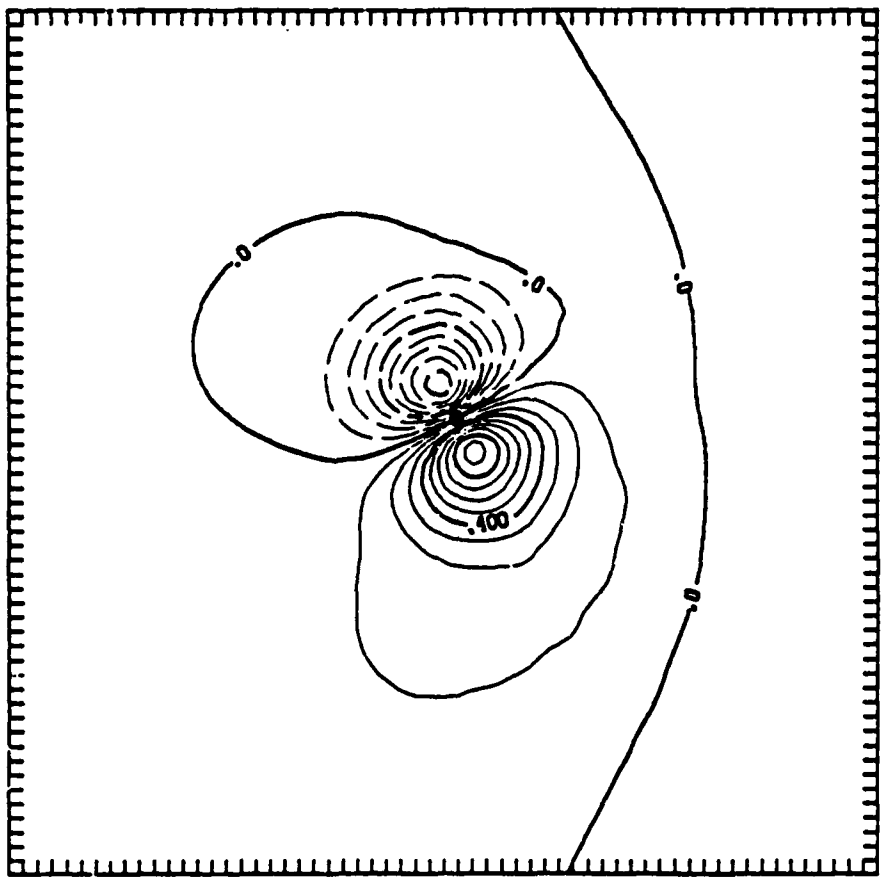

(d) t = 72 h, $|\partial\psi/\partial t|_{max}$ ~ 0.95, contour interval = 0.10

Fig. 4-13. (Continued)

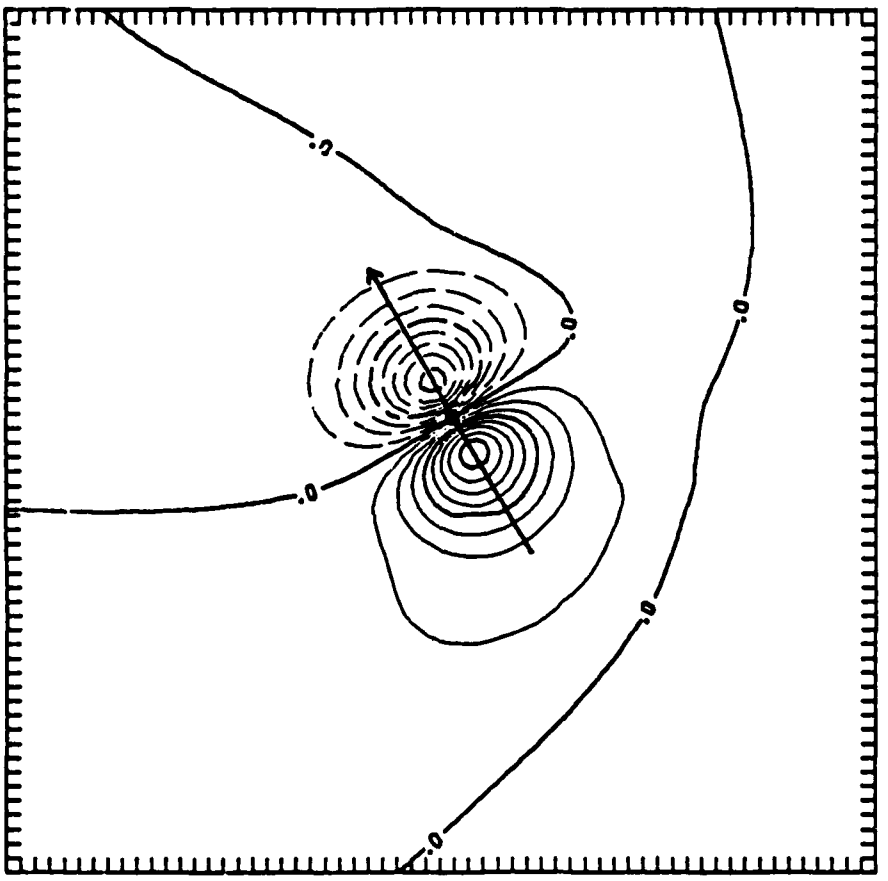

Fig. 4-14. Streamfunction tendency due to the motion of the total vorticity field (nondimensionalized, see text for definition) at t = 72 h ($|\partial\psi/\partial t|_{max}$ ~ 0.80, contour interval = 0.10).

translation period is associated with the motion of the vortex.

The relative total tendency fields are given in Fig. 4-15 for the same times as in Fig. 4-13. The magnitudes are greatest at t = 3 h (Fig. 4-15a) because the large motion tendency at the center dominates the difference in forming the relative tendency. Also notice the relatively (to the center) large values outside r = 100 km indicating the formation of the asymmetric gyres. The positive values 150 - 300 km north of the center are a first indication of the rotation of the asymmetric gyres. By t = 12 h (Fig. 4-15b), most of the relative tendency is associated with an amplification of the large-scale gyres beyond r = 300 km. From t = 36 - 72 h (Figs. 4-15c and d), the rate of development of the asymmetric gyres has slowed. By 72 h, there is very little change in the total vortex except for two features. First, an anticyclonic tendency center has formed far from the center, which also appeared in the ψ_a plots (not shown). The second is the very small dipole near the center that is aligned north-south. This dipole is within the radius of maximum wind and is associated with the inner core gyres discussed in Sec. IV-B. The amplitude is about 15% of the total tendency. Thus, the inner region of the vortex has an additional tendency that contributes to deepening (filling) toward the north (south). Otherwise, there appears to be a fairly good balance between the motion and the linear and nonlinear terms as expected from the model equation. It is also suggested that the motion process of the inner core and of the cyclonic vortex beyond the radius of maximum wind may be different.

To understand how the total tendency field arises, the contributions of the nonlinear and linear terms are examined separately. The beta term produces a large-scale, dipole-type tendency field with a significant magnitude

a

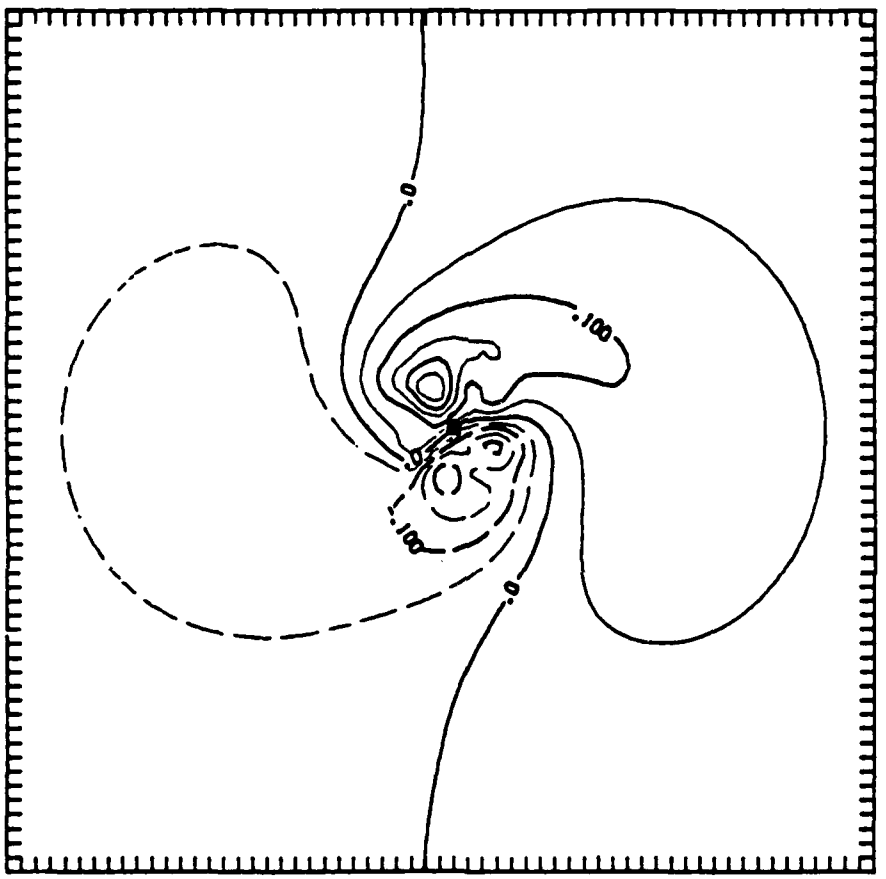

(a) t = 3 h, $|\partial\psi/\partial t|_{max}$ ~ 0.25, contour interval = 0.05

Fig. 4-15. Relative total tendency formed by removing the motion tendency from the total tendency at (a) 3 h, (b) 12 h, (c) 36 h and (d) 72 h.

b

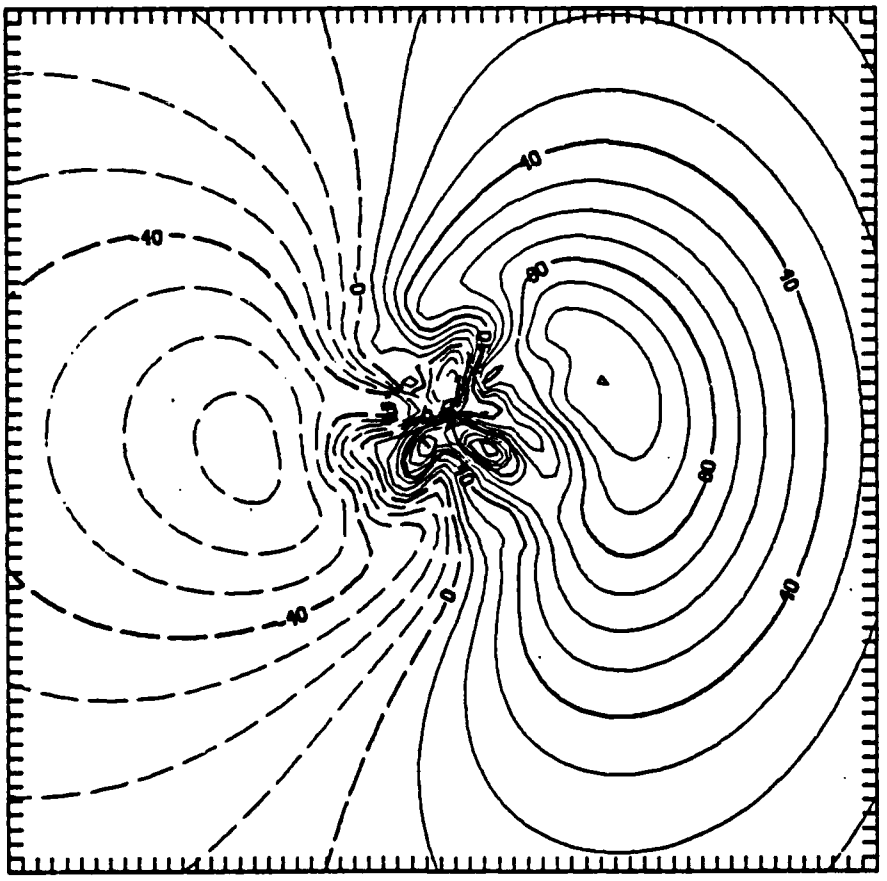

(b) t = 12 h, $|\partial\psi/\partial t|_{max}$ ~ 0.12, contour interval = 10(x10^{-3})

Fig. 4-15. (Continued)

C

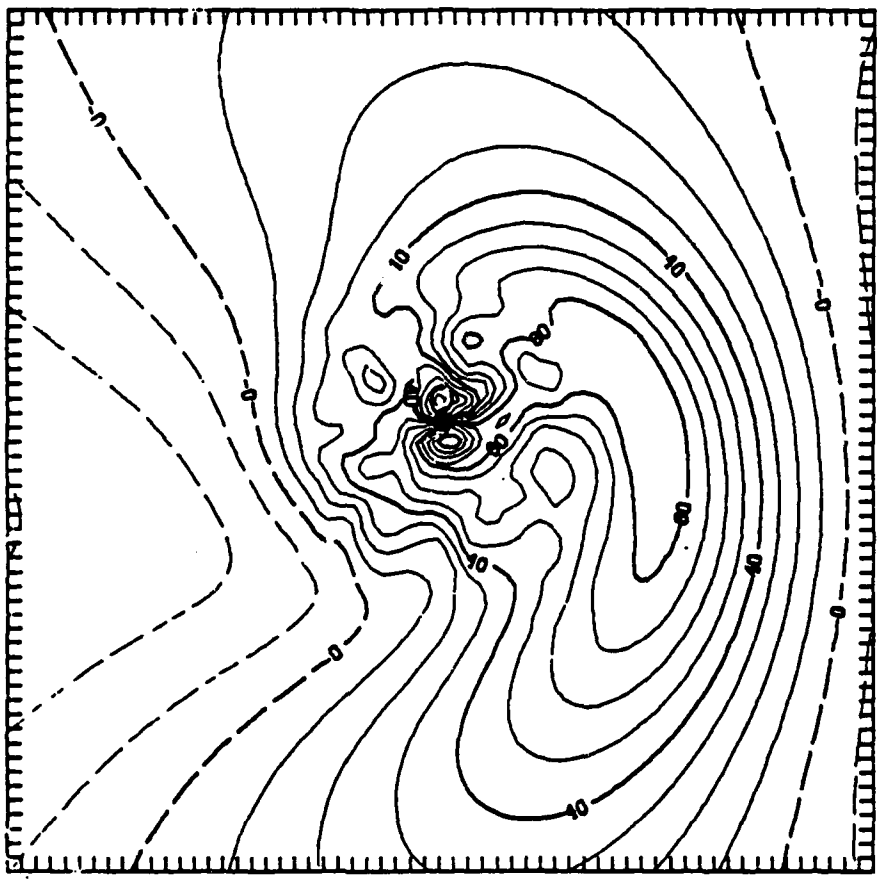

(c) t = 36 h, $|\partial\psi/\partial t|_{max}$ ~ 0.13, contour interval = 10($\times 10^{-3}$)

Fig. 4-15. (Continued)

d

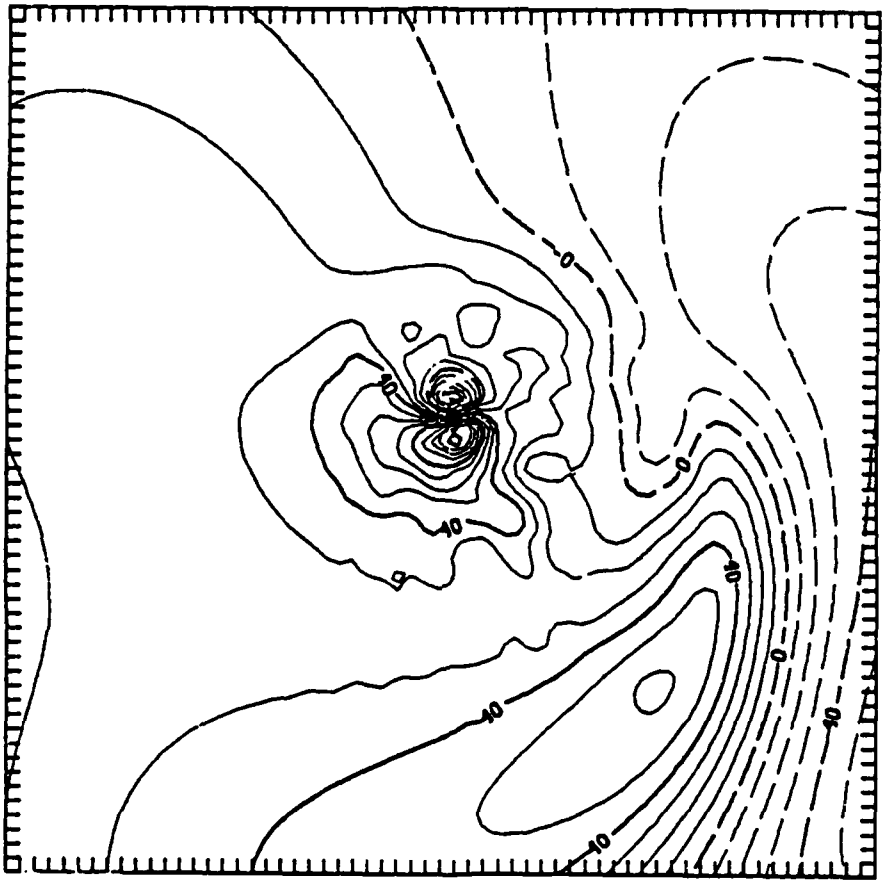

(d) t = 72 h, $|\partial\psi/\partial t|_{max}$ ~ 0.12, contour interval = 10(x10^{-3})

Fig. 4-15. (Continued)

(Fig. 4-16). The maximum/minimum points at all times occur at about r = 250 km. Thus, the beta term results in a circulation because the background field (e.g., see the symmetric streamfunction in Fig. 4-8) is relatively weak compared to the tendency. That is, a small tendency can yield relatively large changes provided the field being modified is weak, whereas a large tendency is required to produce a significant change in a field with a large amplitude. Comparison with the ψ_a pattern in Fig. 4-3 suggests that the beta term is the primary source for the asymmetric flow.

During the rapid growth phase (Fig. 4-16a and b), the zero line in the beta tendency is aligned nearly north-south, which indicates a forcing that is symmetric in the east-west direction. However, a east-west distortion occurs during the linear growth and steady-state phases (Fig. 4-16c and d). Outside of r = 500 km, the positive zone is wrapped around the inner part of the vortex. By t = 72 h, the region of the cyclonic tendencies to the west of the center has been shrunk and a new cyclonic forcing zone has emerged on the far eastern side of the system. This distortion is due to the asymmetric circulation that has formed, but there is still an essentially east-west symmetry in the pattern. To efficiently rotate a wavenumber one asymmetry, the tendency field should also be wavenumber one, but be rotated 90 °. Thus, the beta term can not be directly responsible for the rotation of the large-scale asymmetric gyres (Fig. 4-3) as the forcing is aligned with the asymmetrical circulation.

The most prominent feature in the total nonlinear advection term (Fig. 4-17) is the motion-type dipole pattern, which expands in horizontal scale and amplitude in time. During the early stages of the integration (Fig. 4-17a), only the innermost part of the vortex (r < 150 km) is

a

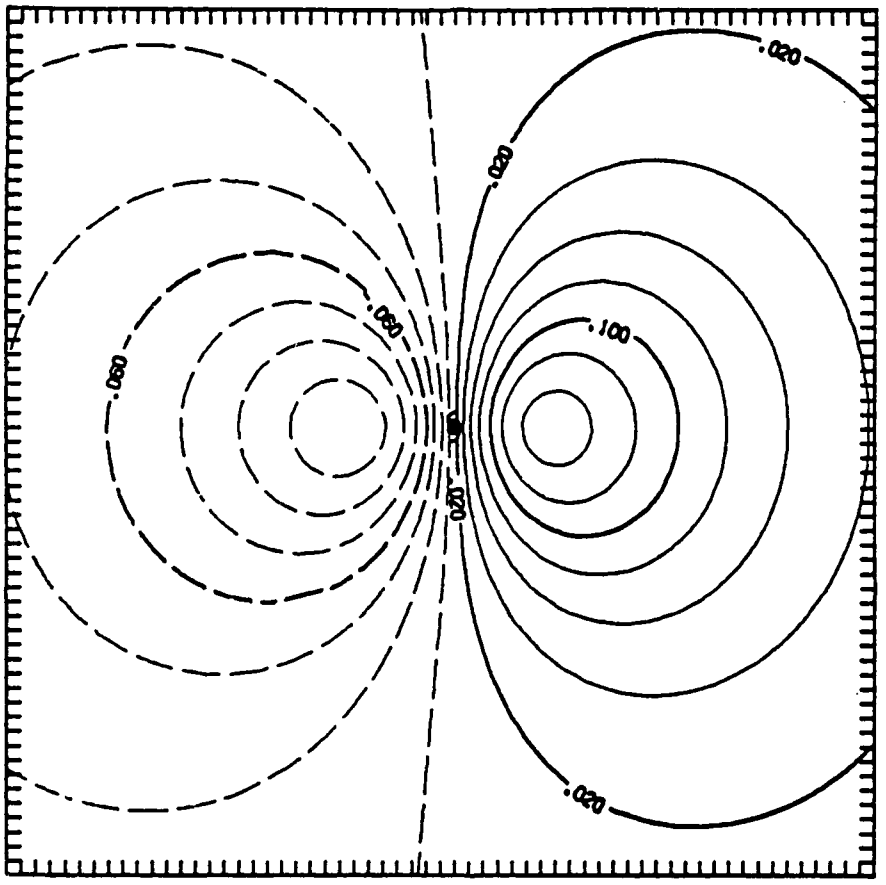

(a) t = 3 h, $|\partial\psi/\partial t|_{max}$ ~ 0.14, contour interval = 0.02

Fig. 4-16. Total linear (βv) tendency at (a) 3 h, (b) 12 h, (c) 36 h) and (d) 72 h.

b

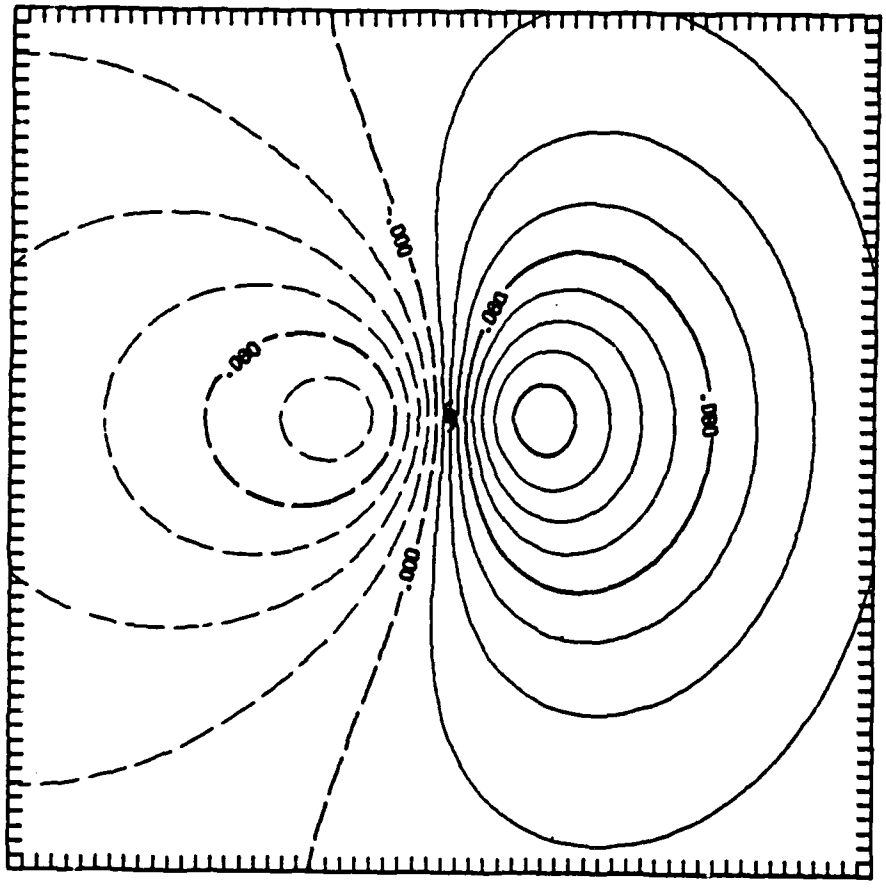

(b) t = 12 h, $|\partial\psi/\partial t|_{max}$ ~ 0.16, contour interval = 0.02

Fig. 4-16. (Continued)

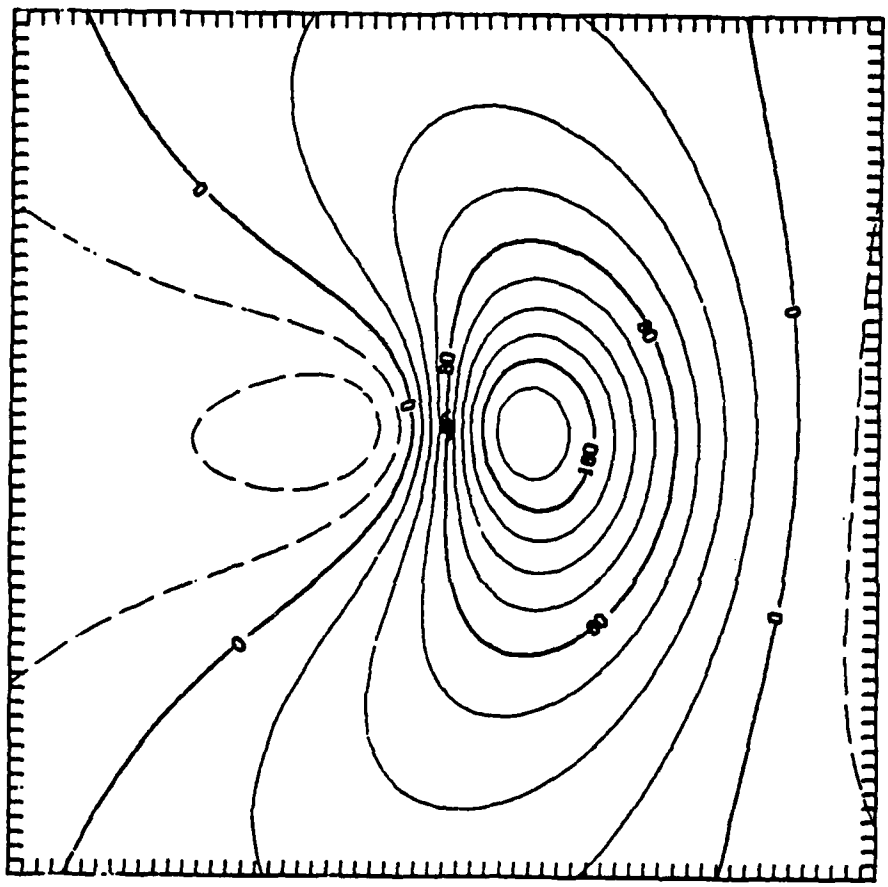

(c) t = 36 h, $|\partial\psi/\partial t|_{max}$ ~ 0.18, contour interval = 20.0(x10^{-3})

Fig. 4-16. (Continued)

d

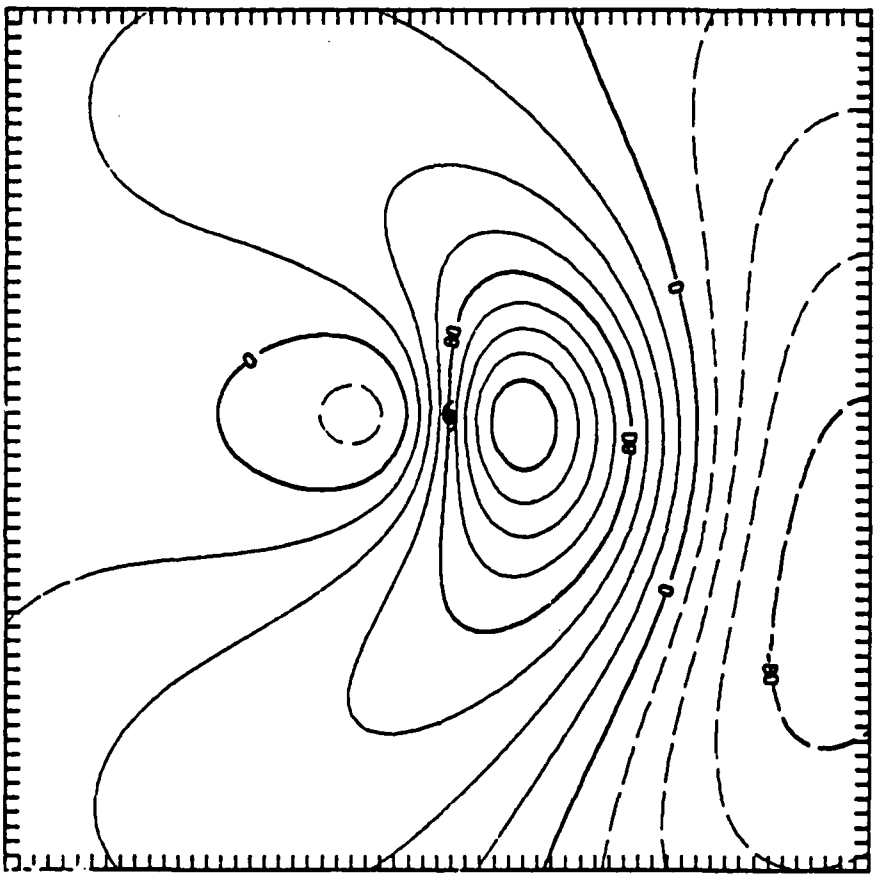

(d) t = 72 h, $|\partial\psi/\partial t|_{max}$ ~ 0.16, contour interval = 20.0($x10^{-3}$)

Fig. 4-16. (Continued)

a

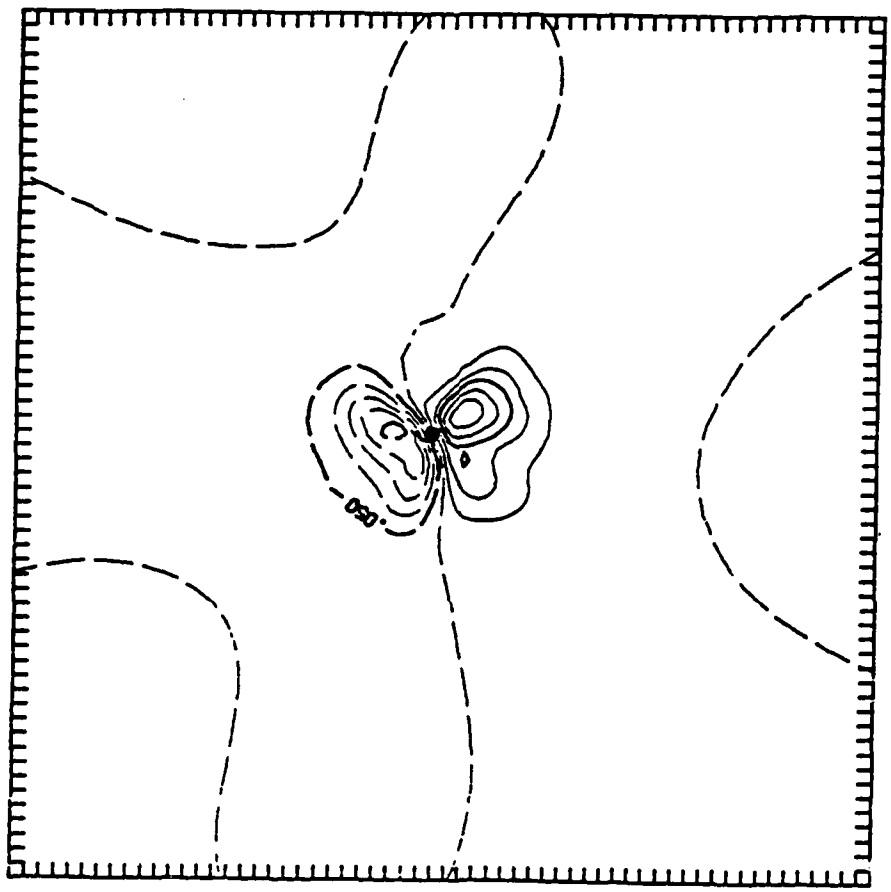

(a) t = 6 h, $|\partial\psi/\partial t|_{max}$ ~ 0.30, contour interval = 0.05

Fig. 4-17. The total nonlinear advection tendency (TA) at (a) 6 h and (b) 48 h.

b

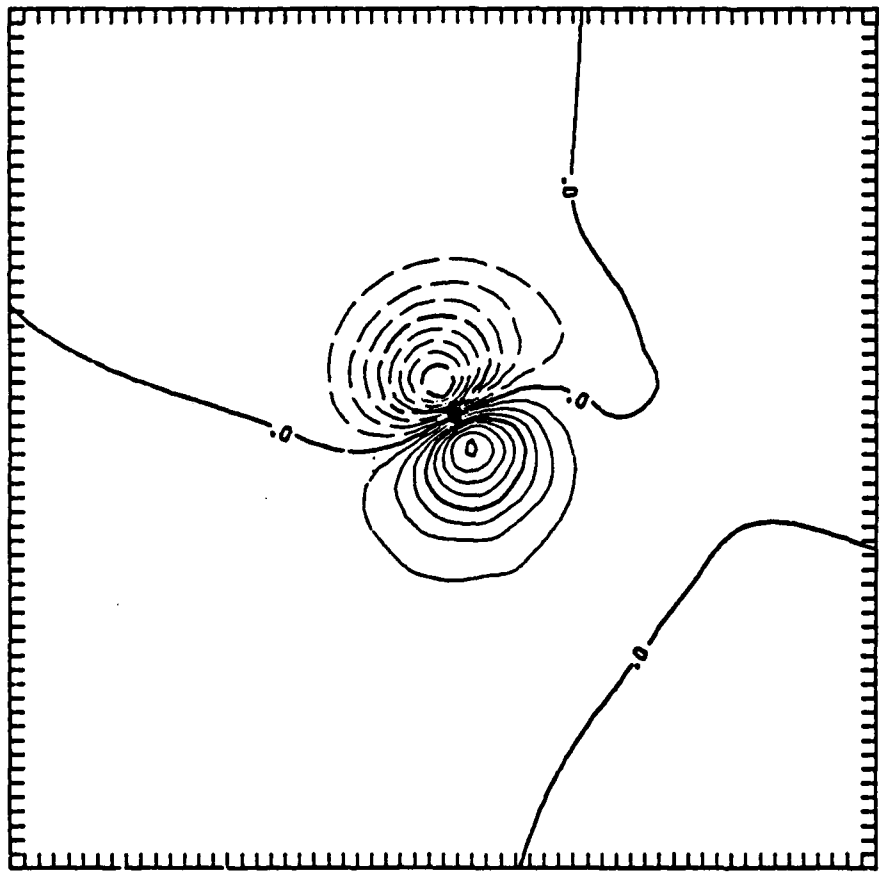

(b) t = 48 h, $|\partial\psi/\partial t|_{max}$ ~ 0.80, contour interval = 0.10

Fig. 4-17. (Continued)

being forced to move. By t = 48 (Fig. 4-17b), the dipole covers the most significant part of the symmetric circulation (r ~ 300 km), which should contribute to the movement of the inner vortex (r = 0 - 300 km).

It is obvious that the motion of the center is strongly linked to nonlinear processes. To isolate on the tendencies not associated with motion effects, the motion tendency is removed (Fig. 4-18). At t = 6 h, a wavenumber one pattern exists with positive tendencies northwest of the center and negative tendencies to the southeast in a wavenumber one pattern. This distribution would tend to cancel the beta forcing inward of 200 km (see Fig. 4-16) and to rotate the asymmetric gyres beyond r = 200 km. In other words, the balancing noted in the total relative tendencies is formed by a compensation between the linear (beta) and nonlinear effects. By t = 48 h and 72 h (Fig. 4-18b and c), the beta and the relative advective tendencies are out of phase over a much larger area. However, a balance is not achieved far away from the center (r > 700 km), which is indicated by the larger tendencies in this region.

The following general dynamical description of beta drift emerges from the model tendency analysis and supports the hypothesis in Section IV-D. The initially symmetric vortex forces a large-scale, wavenumber one circulation asymmetry through Rossby dispersion (beta). This asymmetry generates nonlinear advective forcing that translates the center. The pattern of the advective terms tends to cancel beta forcing in order to stabilize the asymmetric gyres. The region in which the advective term and the beta term tend to offset then expands outward in time until steady-state motion is achieved over a region on the order of r = 500 - 700 km. The issue now becomes one of isolating the relative role of the symmetric and asymmetric circulations

a

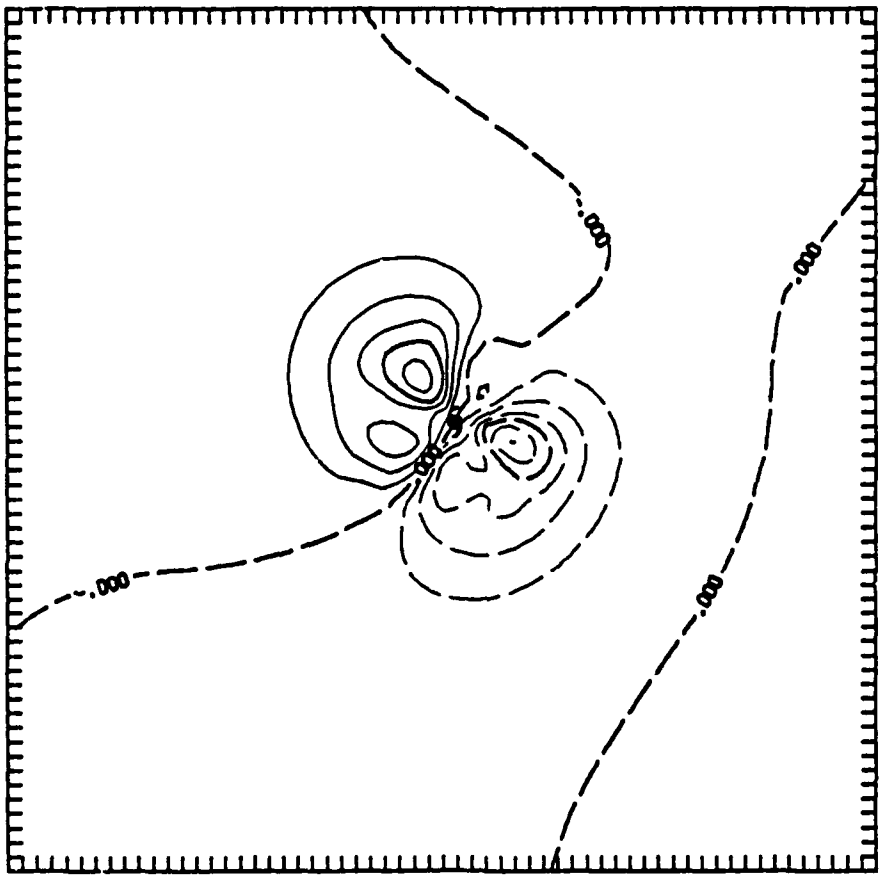

(a) t = 6 h, $|\partial\psi/\partial t|_{max}$ ~ 0.24, contour interval = 0.04

Fig. 4-18. The relative total nonlinear advection tendency at (a) 6 h, (b) 48 h and (c) 72 h.

b

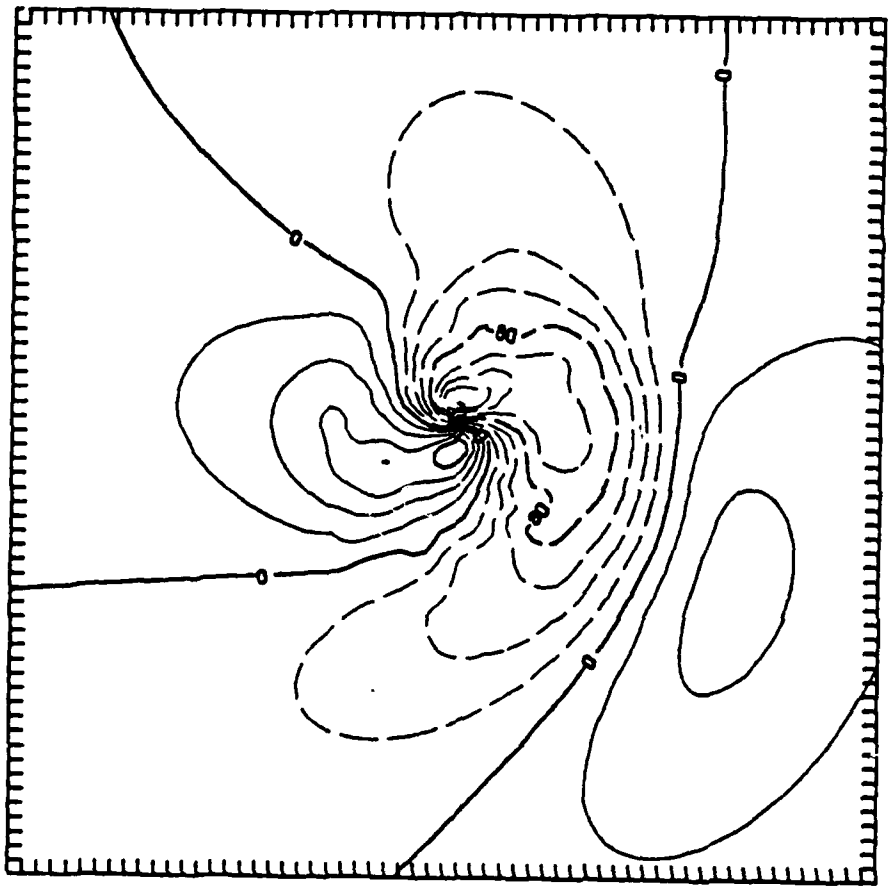

(b) t = 48 h, $|\partial\psi/\partial t|_{max}$ ~ 0.16, contour interval = 20(x10^{-3})

Fig. 4-18. (Continued)

C

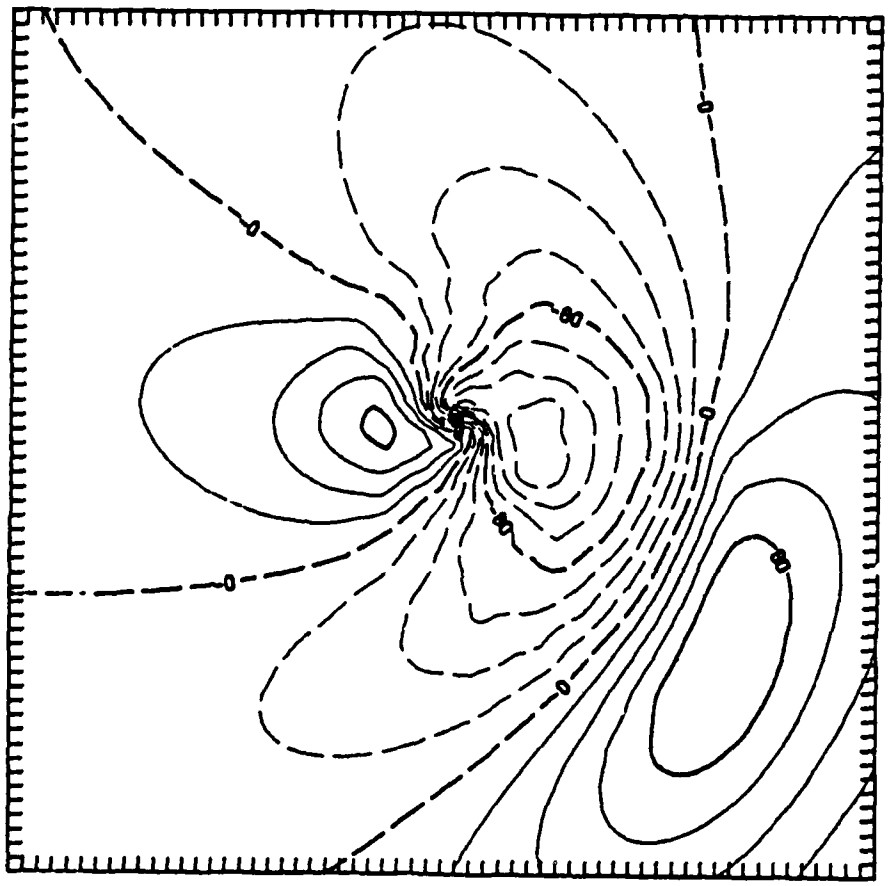

(c) t = 72 h, $|\partial\psi/\partial t|_{max}$ ~ 0.14, contour interval = 20($\times 10^{-3}$)

Fig. 4-18. (Continued)

in the motion, and in the orientation and development of the asymmetric gyres.

2. Symmetric and Aymmetric Tendencies

Although it is possible to separate the total tendency terms into symmetric and asymmetric components, this decomposition does not indicate the separate forcing of the symmetric and asymmetric circulations. That is, it is not possible to calculate the terms that exclusively modify the component flow fields. Rather, both the scale of the forcing and the total ψ field, from which the tendencies are drawn, must be considered. For example, the motion tendency in Fig. 4-14 is wavenumber one in appearance and would generate a wavenumber one asymmetry if the total psi was constant in space. Since the total ψ is predominately symmetric and the total tendency (Fig. 4-13) is applied at the center of the circulation, the system translates with little change in shape. The purpose of decomposing the total tendencies is to understand how each component circulation contributes to the magnitude and structure of the total term.

Interpretations as to how the decomposed terms affect the symmetric/asymmetric flows are possible with consideration of the ψ field and the scale and magnitude of the forcing. The symmetric/asymmetric tendency analysis is applied to understand: (i) the slight weakening of the inner core; (ii) how the asymmetric gyres form; and the motion process of the inner core (r = 0 - 100 km) and of the inner region (r = 100 - 300 km).

a. Weakening of the Maximum Wind

As noted in Sec. IV-B, the symmetric tangential wind field (Fig. 4-2) weakens slightly during the 72-h integration (~ 5%). One explanation is that this reflects a numerically-induced dissipation. However, integrations with a symmetric vortex on an f-plane showed very little (< 0.1%)

change in amplitude due to the numerical solution method. Thus, there must be a dynamical basis for the weakening that is associated with linear processes. Furthermore, a calculation of the absolute vorticity at the moving center revealed that the associated decrease in relative vorticity is much greater than that due to conservation of absolute vorticity (i.e., $\zeta \downarrow$ as $f \uparrow$ for northward motion) alone.

The symmetric component of the β term (Fig. 4-19) at t = 6 h contributes only slight ψ rises within 1000 km of the center with a positive (anticyclonic tendency) over the center. By 72 h, the area of rises (weakening of the symmetric low) has shrunk and an area of falling psi occurs beyond r = 800 km. This tendency may be compared with the "actual" change (Fig. 4-20) in the symmetric streamfunction (ψ_S) , which is found from a finite difference between the ψ_S fields at two times. For instance, the actual change at t = 6 h is calculated from the ψ_S fields at t = 9 and 3 h. The fields used in the calculation are rectified to a common point to eliminate slight shifts of the center as the vortex moves. The comparison between Figs. 4-19 and 4-20 is quite good and supports the idea that the evolution of the symmetric circulation is primarily modified by the beta term, and leads to a slow weakening of the tangential wind in the vortex.

The beta tendency pattern also indicates indirectly the formation of a southerly flow ($\beta v > 0$) over the center. This flow must reach a maximum in the inner region for the beta term to peak at the center. Thus, the northward component (southerly ventilation flow) of the motion is indirectly related to the slight filling of the inner vortex low. Notice also that the β tendency in Fig. 4-19b indicates the development of a <u>cyclone</u> beyond r=700 km whereas the tangential wind profile shows <u>anticyclone</u> flow.

a

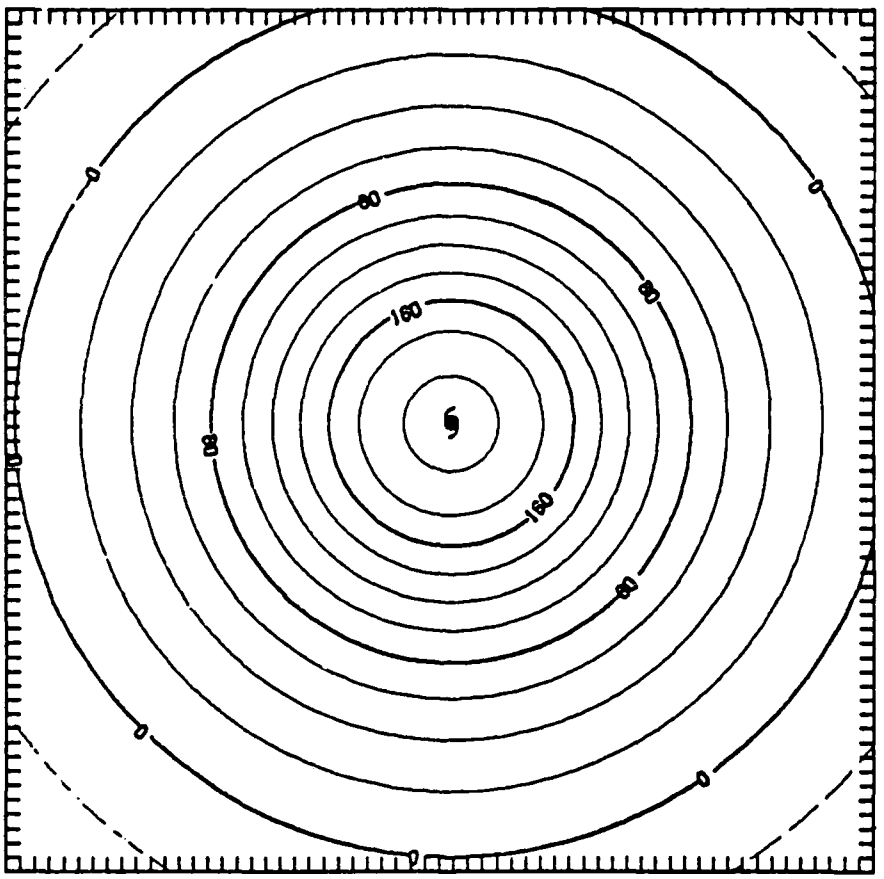

(a) t = 6 h, $|\partial\psi/\partial t|_{max}$ ~ 0.02, contour interval = 20×10^{-4}.

Fig. 4-19. The symmetric component of the β term at (a) 6 h and (b) 48 h.

b

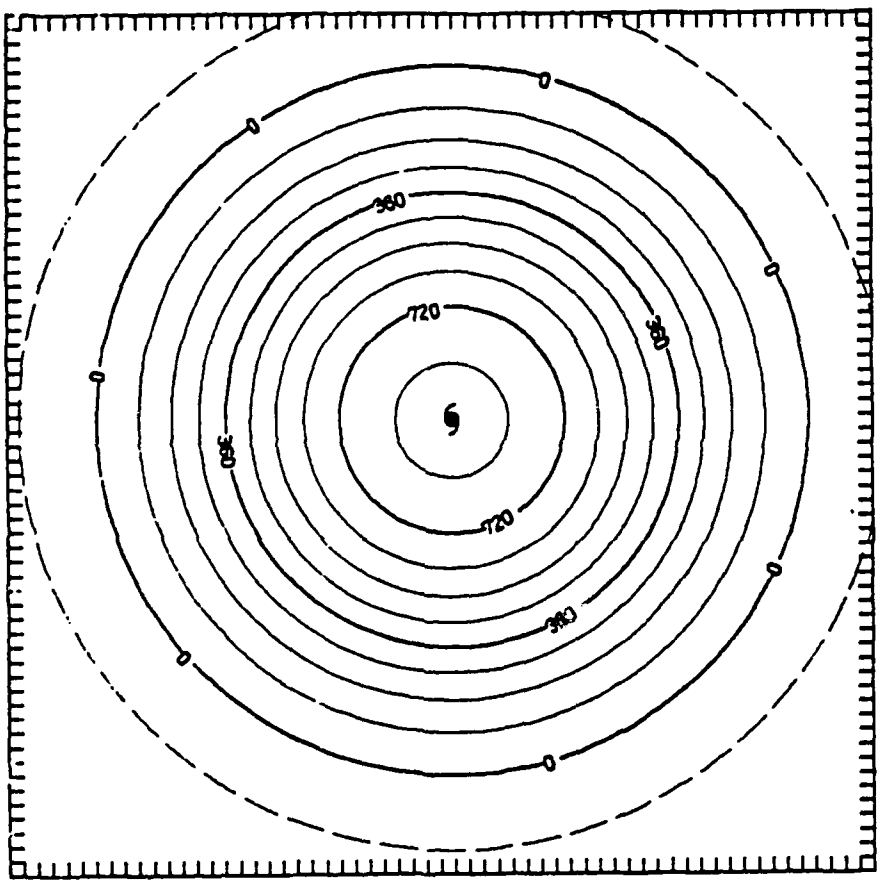

(b) t = 72 h, $|\partial\psi/\partial t|_{max}$ ~ 0.09, contour interval = 90×10^{-4}

Fig. 4-19. (Continued)

a

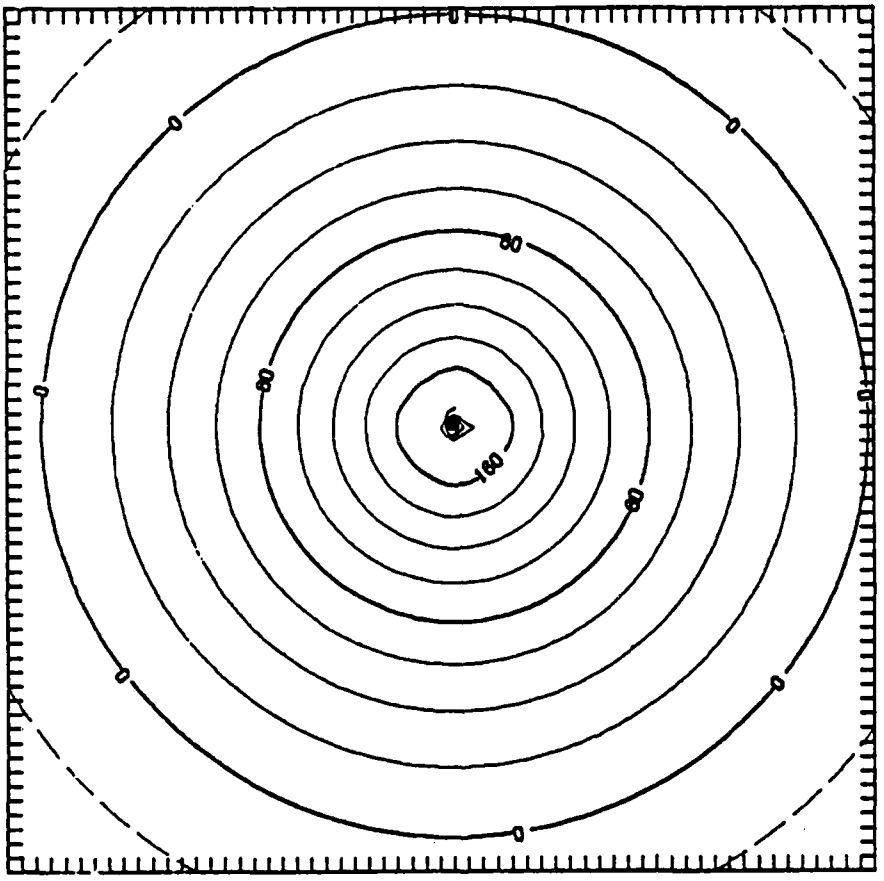

(a) t = 6 h, $|\partial\psi/\partial t|_{max}$ ~ 0.024, contour interval = 20×10^{-4}.

Fig. 4-20. Symmetric tendency calculated with finite differences from the fields at two different times vice the model equation valid at (a) 6 h and (b) 48 h.

b

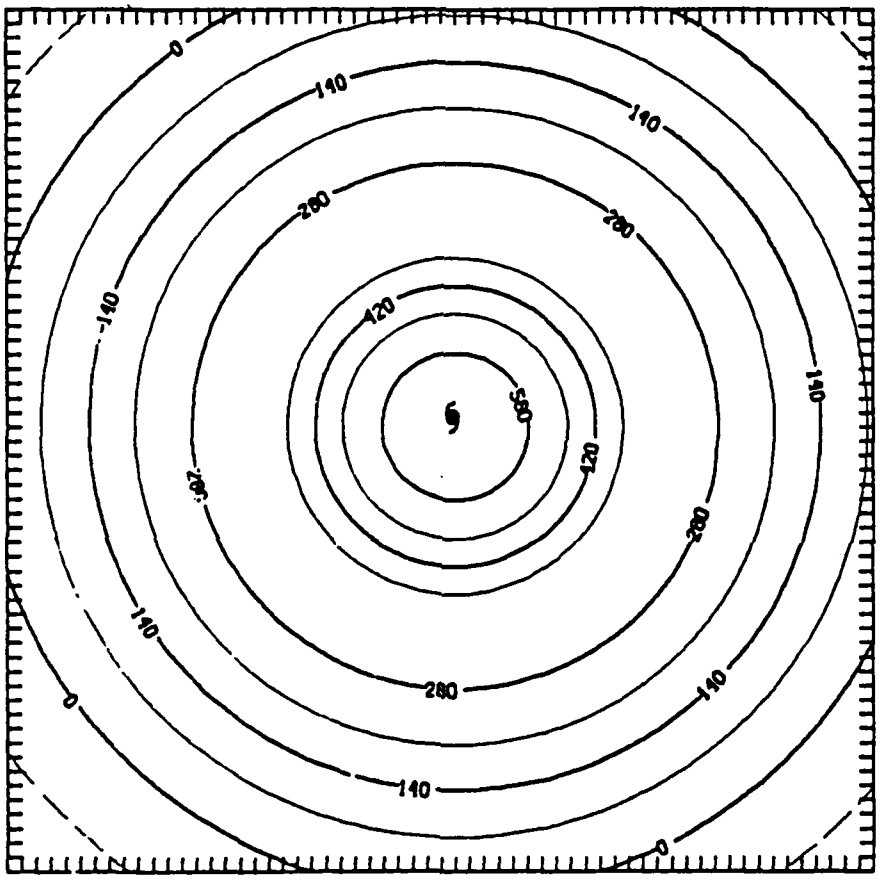

(b) t = 48 h, $|\partial\psi/\delta t|_{max}$ ~ 0.07, contour interval = 70×10^{-4}

Fig. 4-20. (Continued)

Thus, the outer anticyclone must be related to the asymmetric component of the βv tendency.

b. Formation of the Asymmetric Gyres

The asymmetric component of the beta term (Fig. 4-21) accounts for most of the total beta tendency. This asymmetric component is clearly related to the formation of the asymmetric gyres, as evidenced by the large scales and the greater magnitude of the forcing away from the inner regions of the symmetric vortex. The anticyclonic forcing east of the center contracts in time. By t = 72 h (Fig. 4-21c), a second cyclonic forcing center has developed farther to the east, as well as wavenumber two features (two cycles along a circle) around r = 700 km (near the boundaries of the plotting grid).

Another important observation is that the amplitude and distribution of the asymmetric β forcing is also asymmetric. Note the greater areal extent and greater intensity of the cyclonic (< 0) tendencies compared to the anticyclonic tendencies (> 0) in Fig. 4-21c. This asymmetrical distribution will cause a net change in the symmetrical streamfunction $\psi(r)$ during azimuthal averaging and will thus lead to a anticyclonic tendency in the outer region tangential flow as shown in Section IV-C.

The Rossby dispersion process, which is associated with the linear beta term, is strongly linked to the formation of the asymmetric circulation and to the outer wavenumber two features. However, the basis of this forcing is the v component of the vortex flow that is strongly influenced by nonlinear advective effects. Thus, the nonlinear term is examined to understand how the linear forcing is modulated through symmetric/asymmetric interaction and the motion process.

a

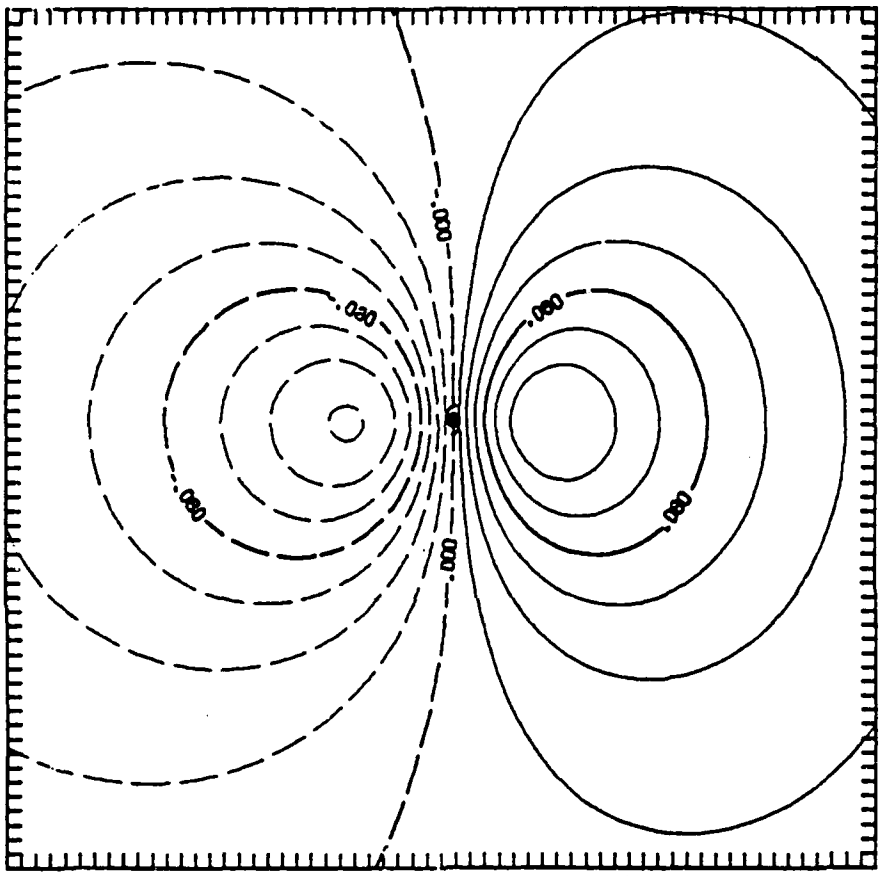

(a) t = 3 h, $|\partial\psi/\partial t|_{max}$ ~ 0.14, contour interval = 0.02.

Fig. 4-21. The asymmetric component of the β term at (a) 3 h, (b) 24 h and (c) 72 h.

b

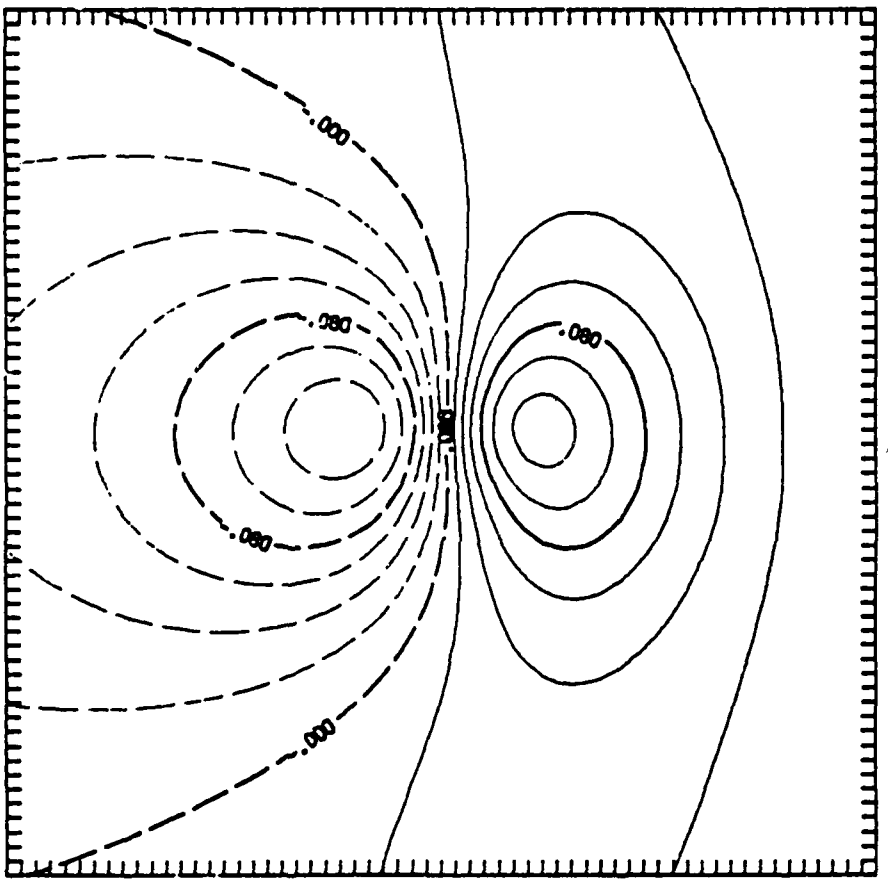

(b) t = 24 h, $|\partial\psi/\partial t|_{max}$ ~ 0.12, contour interval = 0.02.

Fig. 4-21. (Continued)

C

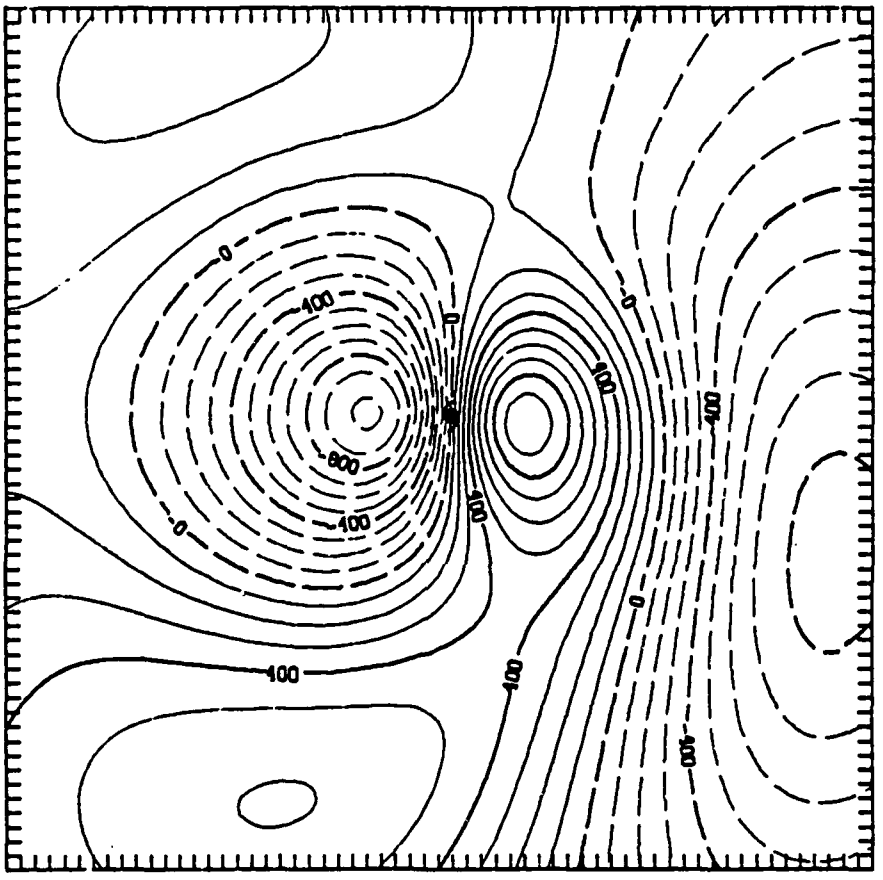

(c) t = 72 h, $|\partial\psi/\partial t|_{max}$ ~ 0.10, contour interval = 100(x10^{-4}).

Fig. 4-21. (Continued)

c. Nonlinear Effects

The advection of the symmetric circulation by the asymmetric flow (ASVA) is portrayed in Fig. 4-22. The motion-type dipole pattern is clearly evident and the scale of the advection is essentially constant throughout the integration. This implies that the vortex on the scale of r = 300-400 km is being moved by this effect. What is more interesting is the cyclonic rotation of the dipole couplet during the first 12 h. The mainly north-south orientation of the dipoles at t= 3 h and 6 h is not aligned with the vortex motion vector, which is toward the northwest. Thus, the advection of asymmetric vorticity by the symmetric flow (discussed below) must be responsible for the movement of the inertially stiff core in the early stages. The symmetrical component of the total nonlinear tendencies (not shown) also suggests that the movement of the vortex occurs on two scales, with ASVA accounting for a majority of the movement on scales larger than the inertially stiff core.

The advection of the asymmetric circulation by the symmetric vortex (AAVS) is displayed in two figures. In the first set (Fig. 4-23), the asymmetric flow is not smoothed in the inner regions (r < 300 km) to reveal smaller-scale effects in the vicinity of the stiff core. In the second group (Fig. 4-24), the asymmetric flow has been heavily smoothed in the inner regions prior to the calculation of the tendency to emphasize this advective effect in the outer portions of the vortex.

A small motion-type dipole (r < 100 km) is present throughout the integration in the unsmoothed tendencies (Fig. 4-23). The inner dipole is initially oriented nearly east-west. When this tendency is added to the ASVA tendency, the net effect is to move the center or stiff core toward the northwest. This small dipole rotates anticyclonically beyond the direction of motion at t = 12 h,

a

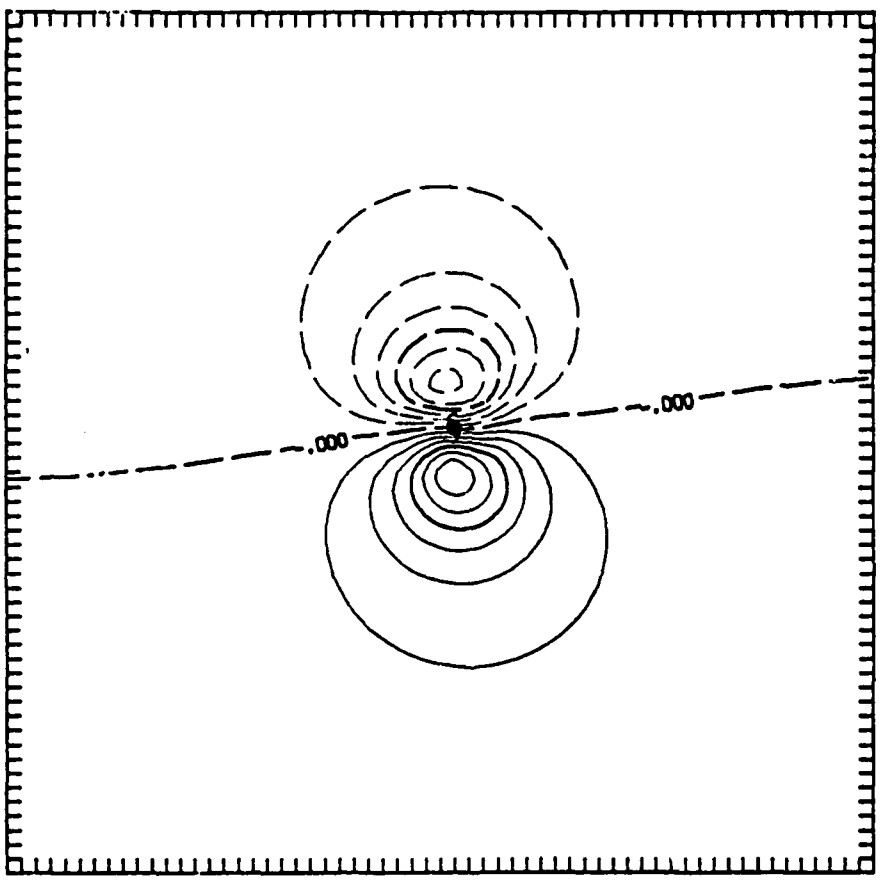

(a) t = 3 h, $|\partial\psi/\partial t|_{max}$ ~ 0.12, contour interval = 0.02.

Fig. 4-22. Advection of symmetric vorticity by the asymmetric flow at (a) 3 h, (b) 6 h, (c) 9 h, (d) 12 h and (e) 72 h.

b

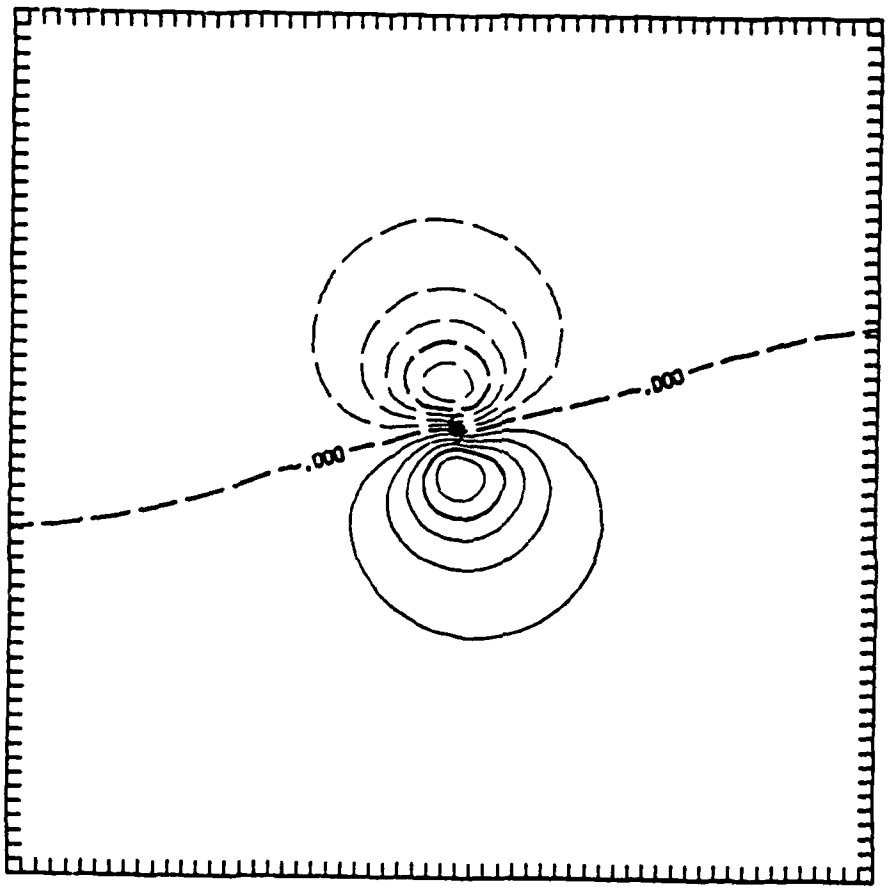

(b) t = 6 h, $|\partial\psi/\partial t|_{max}$ ~ 0.20, contour interval = 0.04.

Fig. 4-22. (Continued)

C

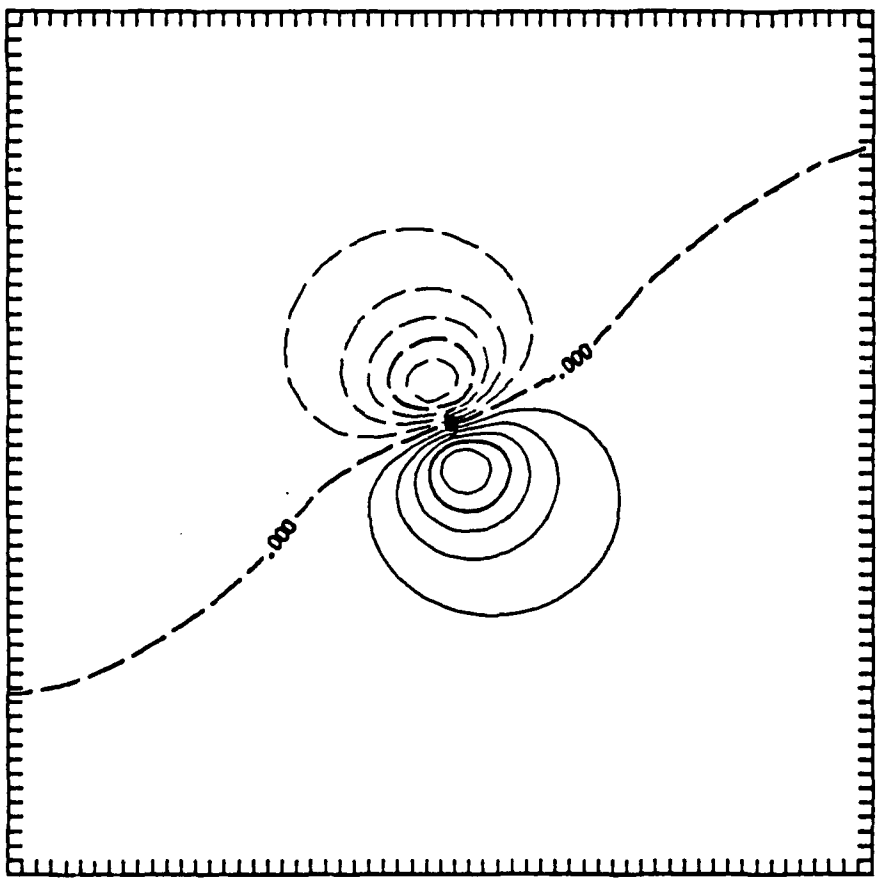

(c) t = 9 h, $|\partial\psi/\partial t|_{max}$ ~ 0.25, contour interval = 0.05.

Fig. 4-22. (Continued)

d

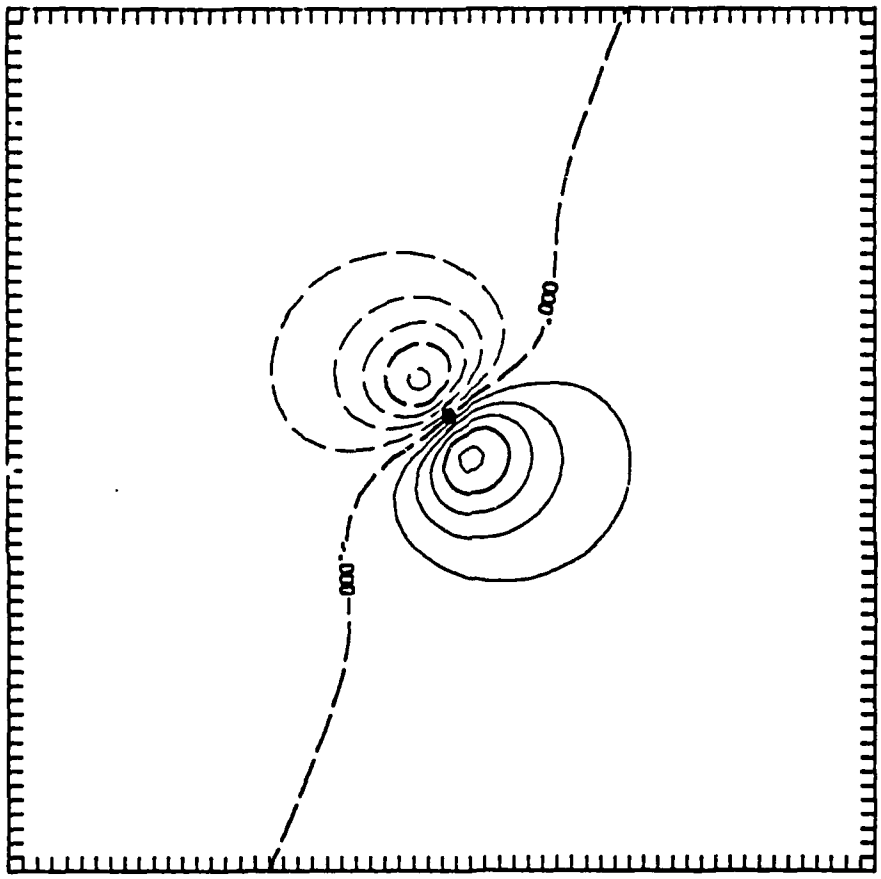

(d) t = 12 h, $|\partial\psi/\partial t|_{max}$ ~ 0.30, contour interval = 0.06.

Fig. 4-22. (Continued)

e

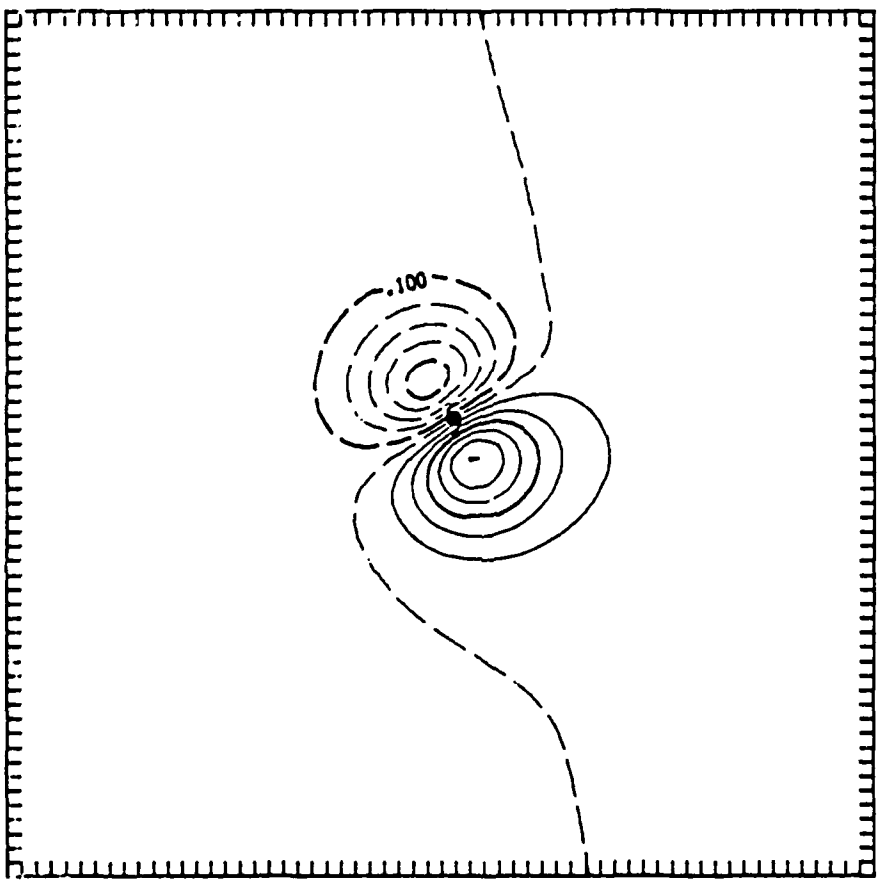

(e) t = 72 h, $|\partial\psi/\partial t|_{max}$ ~ 0.60, contour interval = 0.10.

Fig. 4-22. (Continued)

a

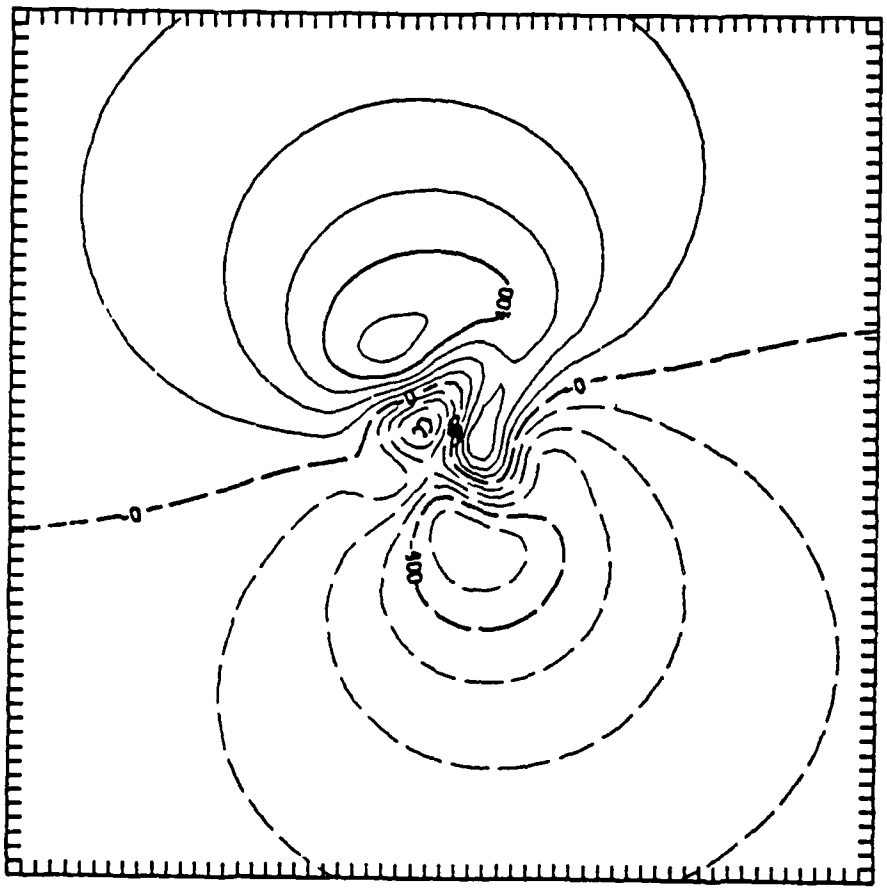

(a) t = 6 h, $|\partial\psi/\partial t|_{max}$ ~ 0.05, contour interval = 100(x10^{-4})

Fig. 4-23. Advection of asymmetric vorticity by the symmetric (AAVS) flow at (a) 6 h, (b) 9 h, (c) 12 h, (d) 24 h and (e) 72 h.

b

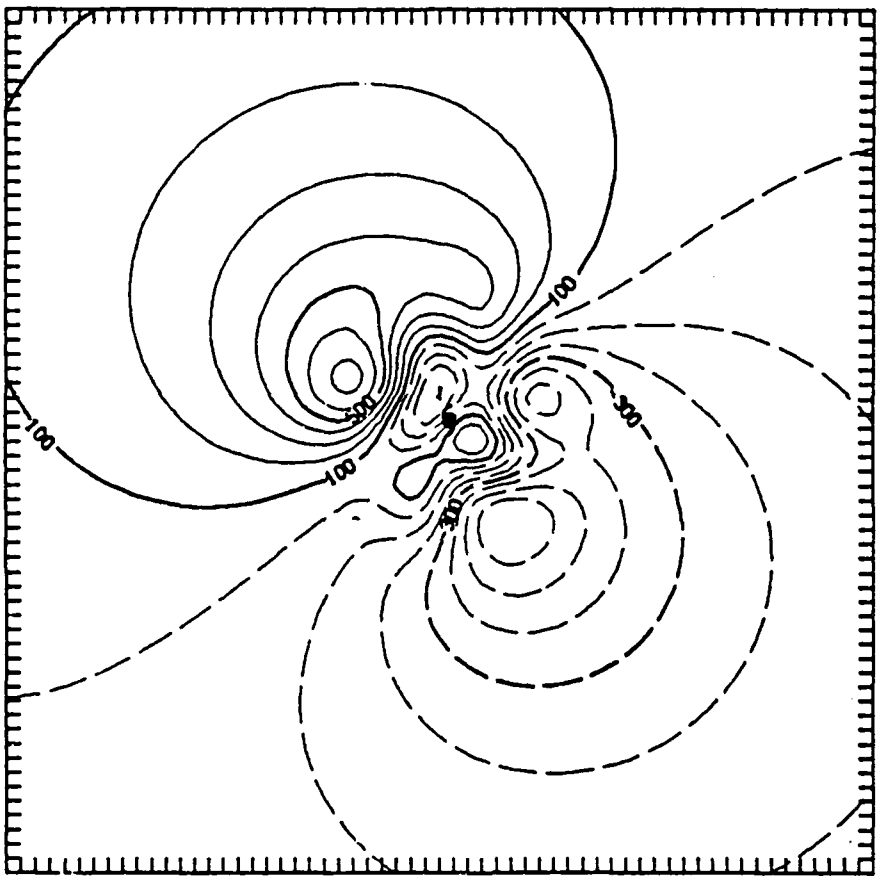

(b) t = 9 h, $|\partial\psi/\partial t|_{max}$ ~ 0.07, contour interval = 100(x10^{-4})

Fig. 4-23. (Continued)

C

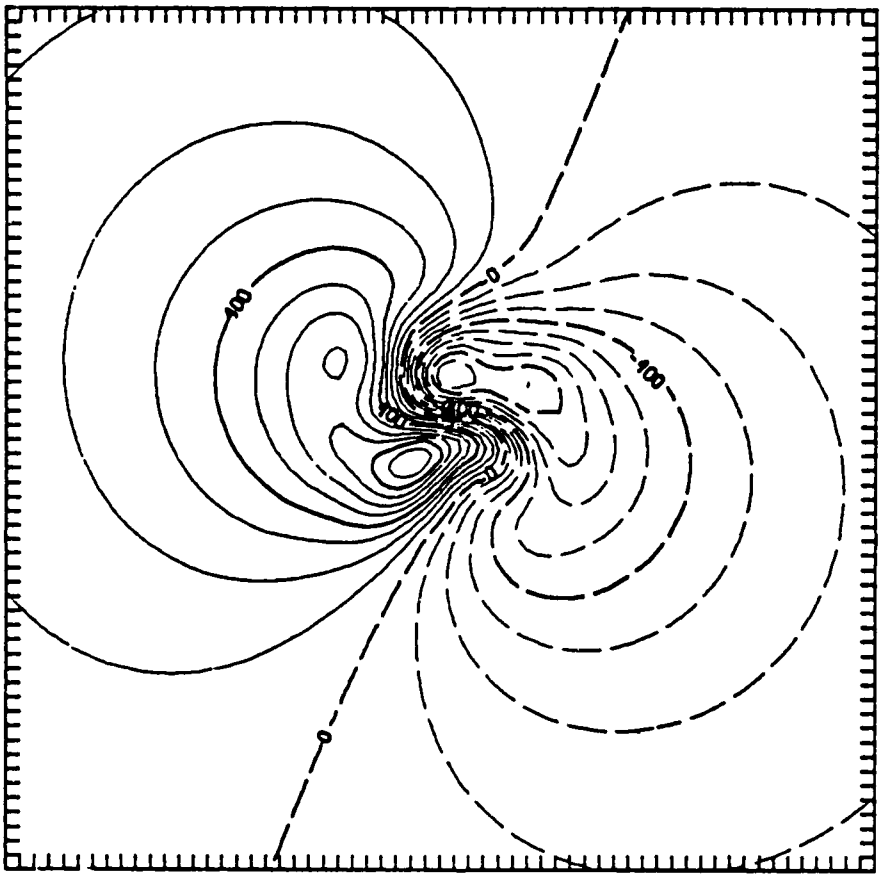

(c) t = 12 h, $|\partial\psi/\partial t|_{max}$ ~ 0.09, contour interval = 100x(10^{-4}).

Fig. 4-23. (Continued)

d

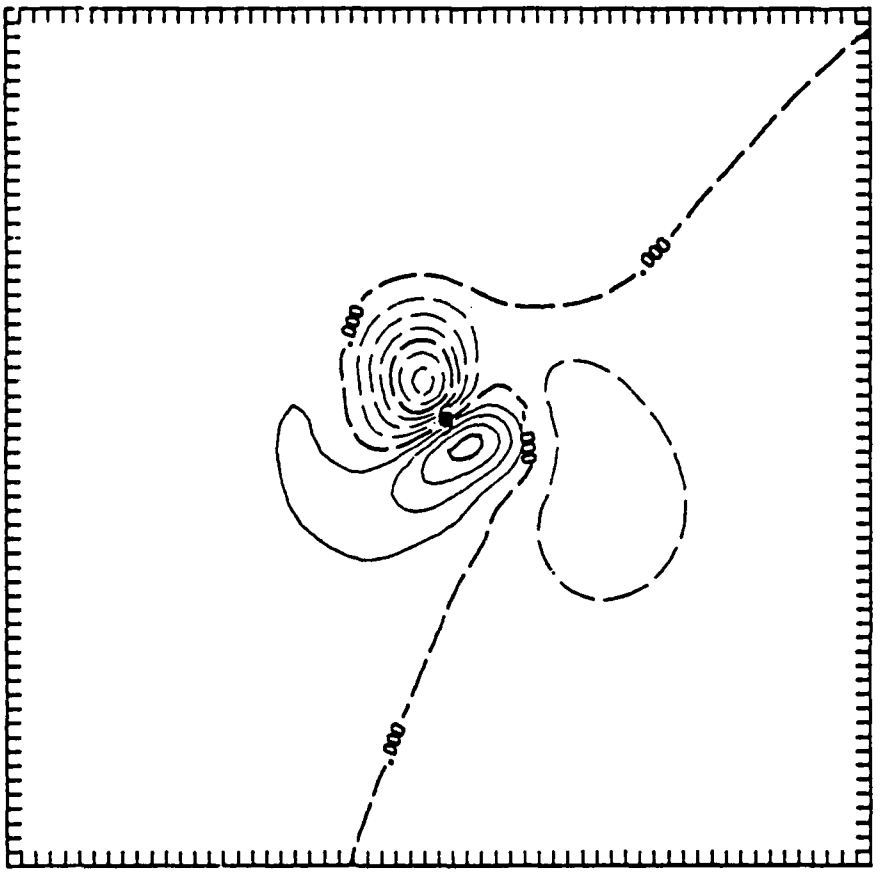

(d) t = 24 h, $|\partial\psi/\partial t|_{max}$ ~ 0.18, contour interval = 0.03.

Fig. 4-23. (Continued)

e

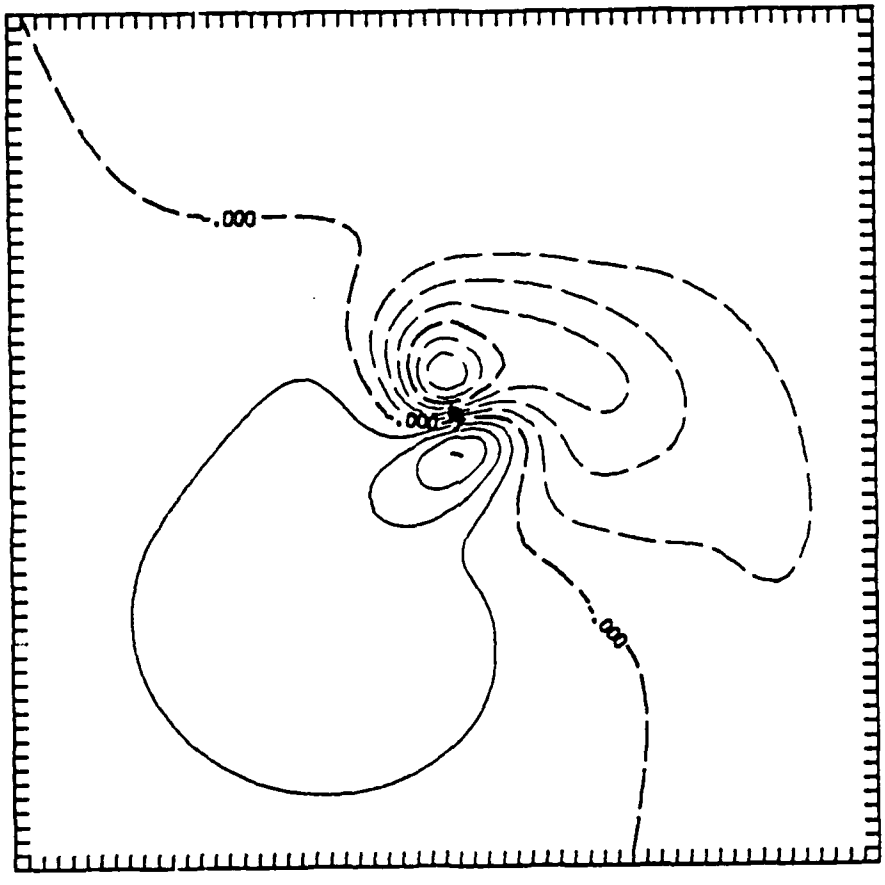

(e) t = 72 h, $|\partial\psi/\partial t|_{max}$ ~ 0.24, contour interval = 0.04.

Fig. 4-23. (Continued)

a

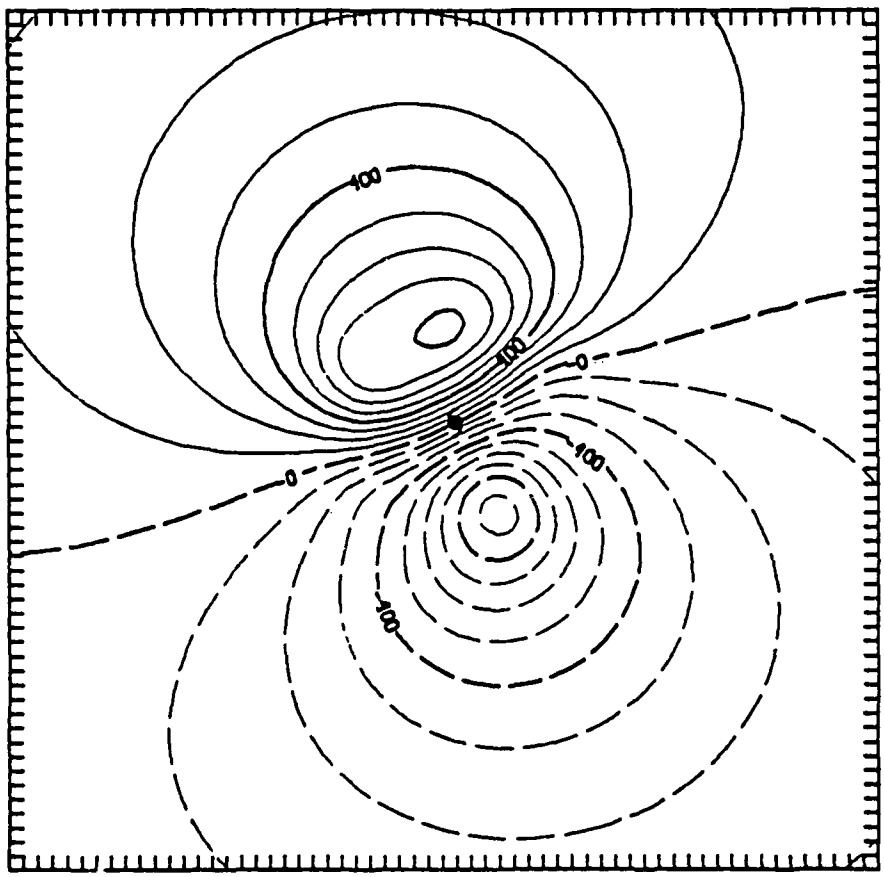

(a) t=6 h, $|\partial\psi/\partial t|_{max}$ ~ 0.08, contour interval = 100(x10^{-4}).

Fig. 4-24. As in Fig. 4-23, except for heavy smoothing in the r < 250 km region.

b

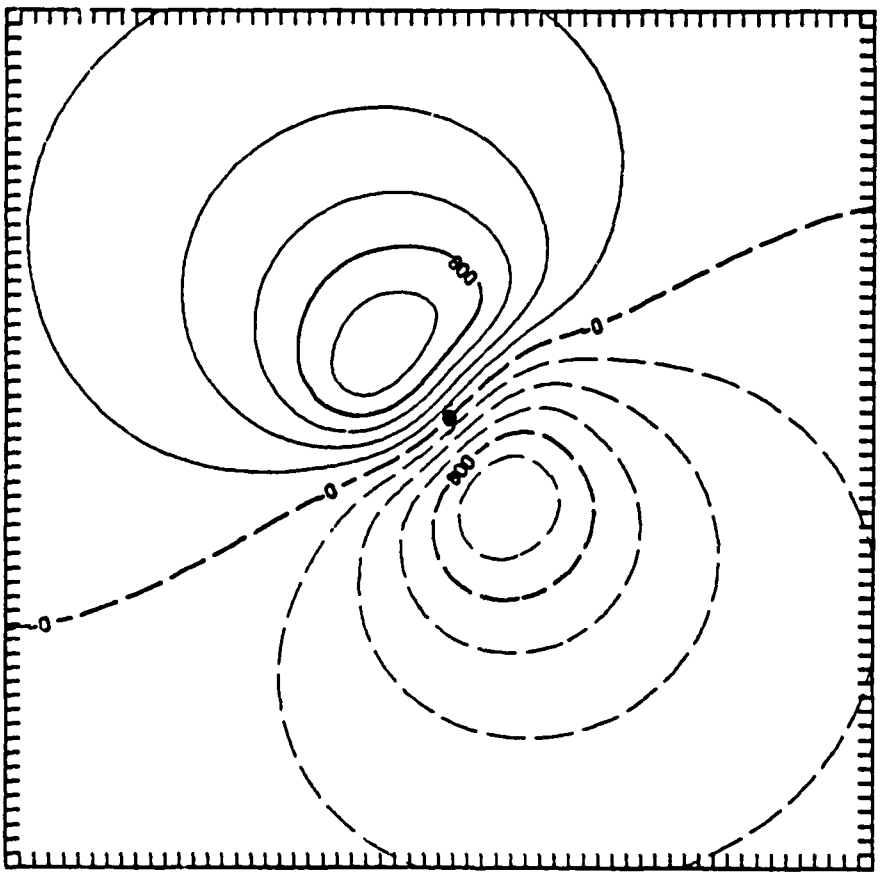

(b) t=9 h, $|\partial\psi/\partial t|_{max}$ ~ 0.10, contour interval = 200(x10^{-4}).

Fig. 4-24. (Continued)

C

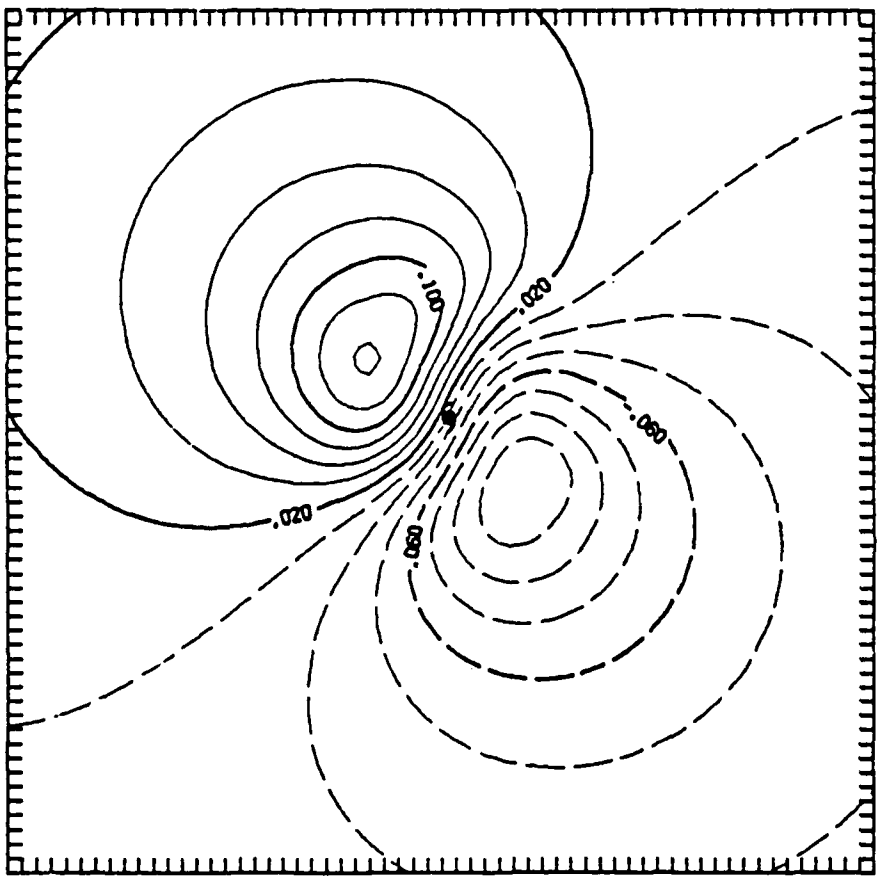

(c) t=12 h, $|\partial\psi/\partial t|_{max}$ ~ 0.14, contour interval = 0.02

Fig. 4-24. (Continued)

d

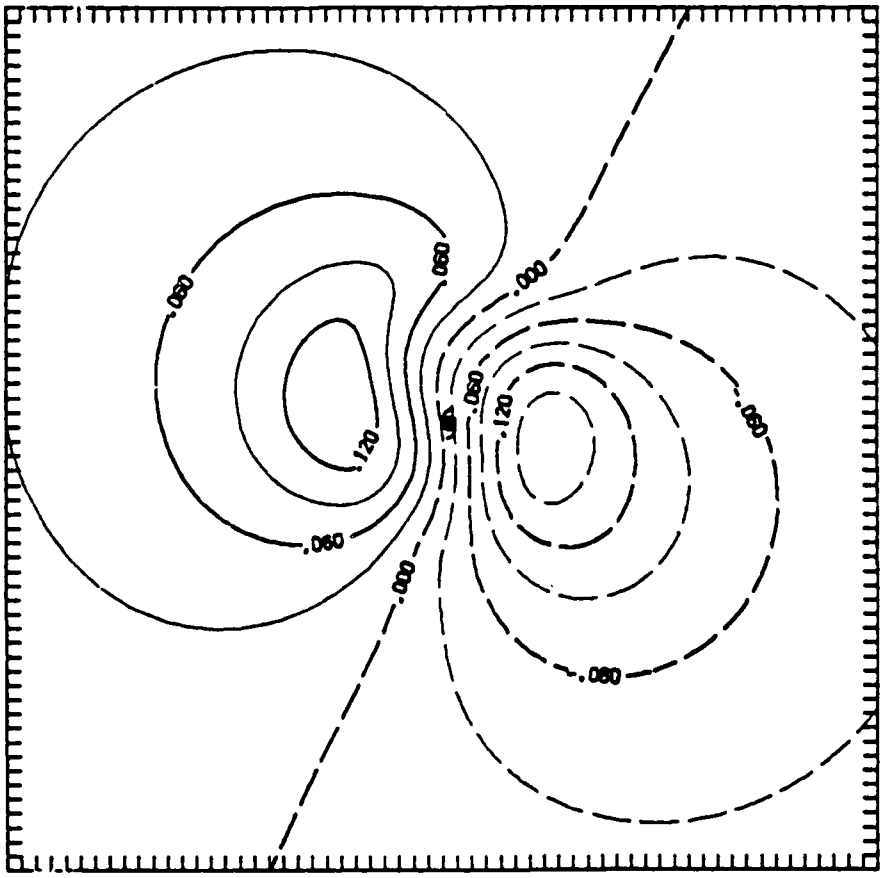

(d) t=24 h, $|\partial\psi/\partial t|_{max}$ ~ 0.15, contour interval = 0.03

Fig. 4-24. (Continued)

e

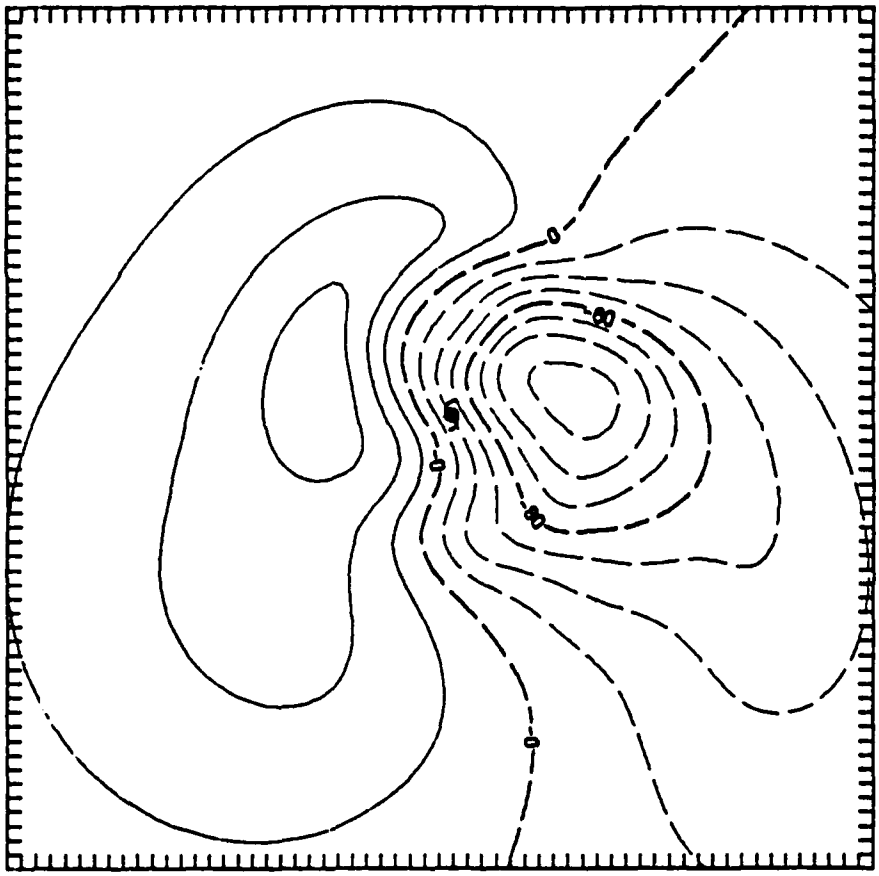

(e) t=72 h, $|\partial\psi/\partial t|_{max}$ ~ 0.14, contour interval = 20(x10^{-3})

Fig. 4-24. (Continued)

but then becomes oriented along the motion vector by t = 24 h and maintains this orientation throughout the remainder of the integration.

The decomposition of the nonlinear tendency terms into advection of symmetric circulation by the asymmetric flow (ASVA) and advection of asymmetric circulation by the symmetric flow (AAVS) reveals two stages in the motion of the vortex. In the early phase (t = 0-12 h) the two terms are 90 ° out of phase, with ASVA indicating a northward movement of the larger-scale vortex and AAVS inducing a westward motion of the stiff core (compare Fig. 4-22 and 4-23). The two advective effects become oriented with the direction of motion in both the linear growth and steady-state stages of the asymmetric flow development. During these growth phases, the two advective processes move both the larger-scale vortex (r = 100 - 300 km by ASVA) and the inner core (r < 100 km by AAVS) in the same direction with the same speed.

d. Rotation of the Large-scale Asymmetric Gyres

The inner-core movement component tends to dominate the AAVS fields for t > 24 h. This tendency is recalculated with a smoothed asymmetric flow in the r < 250 km annulus to better depict forcing beyond the inner region (Fig. 4-24). The dipole pattern now appears on a much larger scale and is associated with forcing of the large-scale asymmetric flow gyres. At t = 6 h, this large-scale component of AAVS is rotating the asymmetric gyres cyclonically as the tendency dipole is approximately 90 ° out of phase. The orientation of the tendency dipole also rotates cyclonically so that by t = 72 h, the forcing is roughly 180 ° out of phase with the asymmetric gyres and balances the large-scale asymmetric gyres against linear (βv) forcing. Also note how the gyre rotation effect (e.g., positive tendencies to the north of the center) is first

halted near the center and then expands outward in time. This implies that the rotation of the asymmetric gyres occurs at all radii initially. As the steady state is approached, the inner rotation is halted.

The symmetric advection of the asymmetric circulation is a very important part of the total nonlinear effects. This term serves three functions: (i) to help move the inertially stiff core; (ii) to induce a cyclonic rotation in the asymmetric gyres to orient the advecting ventilation flow; and (iii) to counteract the beta term to keep the asymmetric flow in a near-steady state.

e. Westward Component of Beta Drift

It is also important to stress the role of nonlinear effects in orienting the ventilation flow. Previous theories (e.g., Adem, 1956; Holland, 1983) associate the westward component of beta drift with Rossby dispersion alone. This was shown to be incorrect by Chan and Williams (1987), who demonstrated that the linear term alone (Rossby dispersion) did not move the center. The results presented here have more precisely illustrated how the nonlinear term induces the motion, and more significantly how advection modifies the direction of motion. The westward component of beta drift arises strictly from advective process and is only indirectly related to linear effects.

F. VENTILATION FLOW VECTOR

The asymmetric flow analysis in the previous sections showed a strong relationship between the nearly uniform flow between the asymmetric gyres (the "ventilation flow") and the motion of the vortex. To precisely illustrate this relationship, the "ventilation flow vector" is calculated as the average asymmetric flow within r = 300 km of the center and compared to the motion vector of the center. The averaging area for the ventilation flow vector is chosen

based on the size of the cyclonic vortex (r ~ 300-500 km) and the best fit to the center motion vector.

A comparison of the ventilation flow speed and the speed of motion for the basic vortex experiment (B1) is given in Fig. 4-25. The speed of motion is calculated over 12-h increments centered on 12, 24, 36, ... 132 h based on hourly positions of the streamfunction minimum. These hourly positions are smoothed prior to the translation speed calculation to remove numerically generated positions oscillations.

As noted earlier, the motion rapidly builds, and then grows linearly in time until a maximum is reached around t = 60 h. After the maximum translation speed has been achieved, the speed of motion slowly oscillates about some quasi-steady value. The ventilation flow speed follows the motion in a nearly lock-step manner, but is about 5-10% smaller (slower) than the actual vortex motion in the steady state. The corresponding directions of motion is given in Fig. 4-26. The greatest departures occur in the rapid growth phase of the asymmetric gyres. During the slowly varying stage, the vortex is moving consistently about 5 ° to the left of the ventilation flow. The composite studies of Chan and Gray (1982) and the geostrophic steering-flow analysis of Brand et al. (1981) showed that tropical cyclones tend to move to the left of some averaged "large-scale" environmental flow vector. However, in these studies, the cyclones tended to move faster than the basic flow vector. Although these results do not fit the observed relationship precisely, they indicate that the observed differences may be a consequence of the dynamical processes discussed in this study.

Several alternatives were explored to account for the slight difference between the ventilation flow vector and the motion of the center. Other averaging schemes for

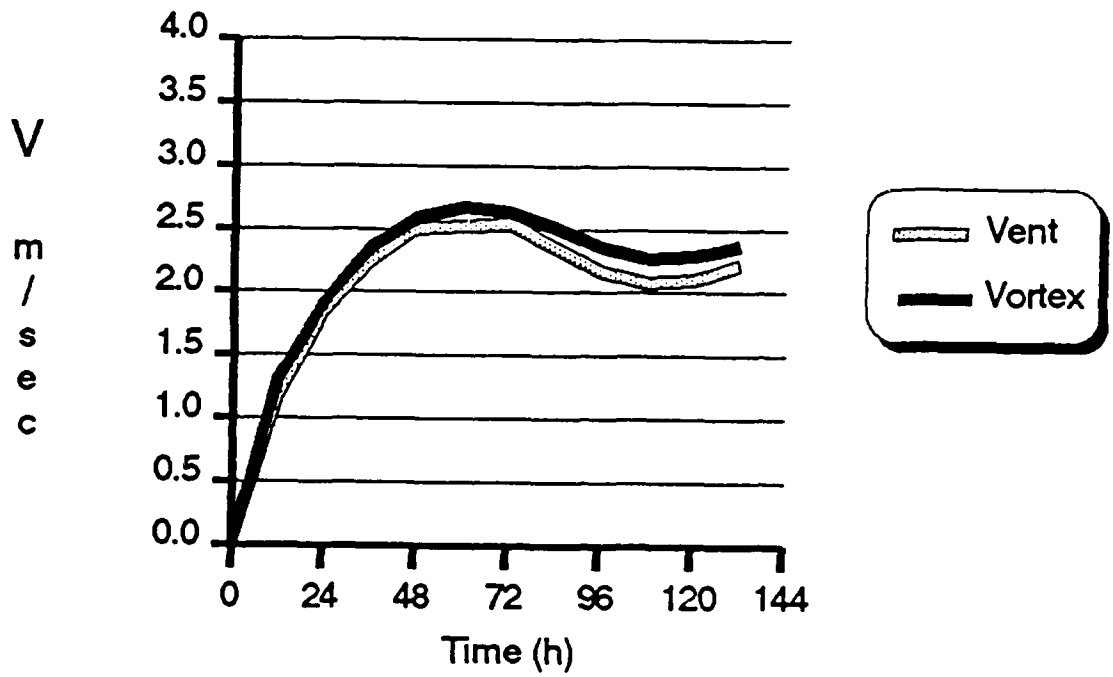

Fig. 4-25. Magnitude of the ventilation flow vector compared to the speed of vortex motion for the B1 vortex.

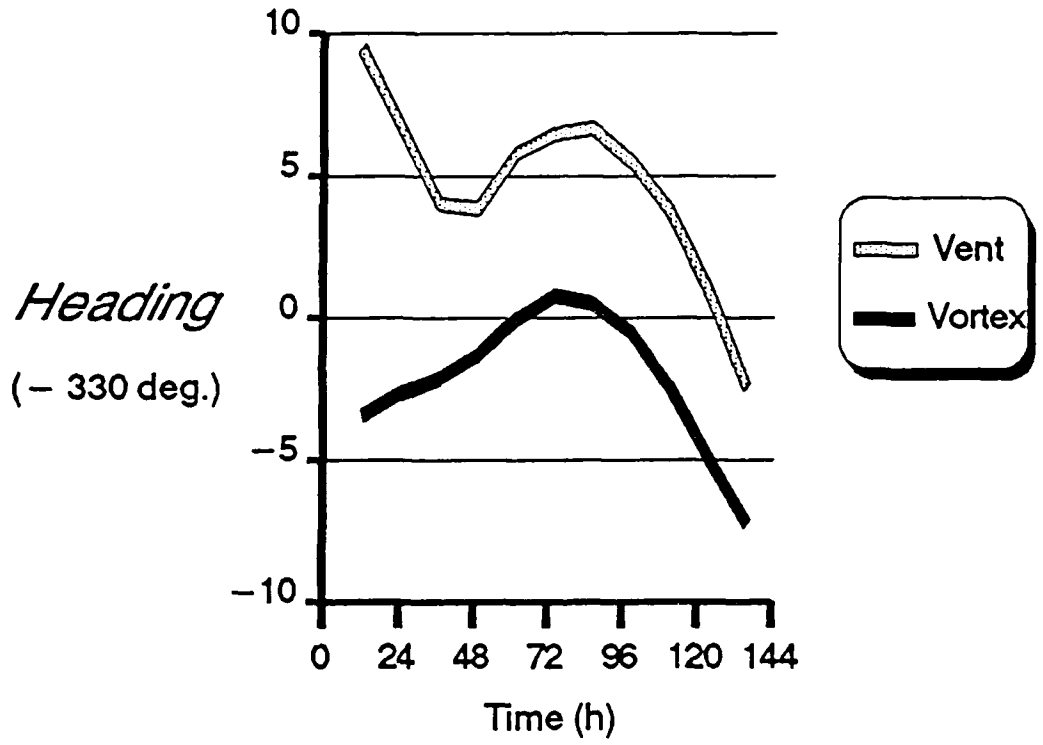

Fig. 4-26. Direction of the ventilation flow vector compared to the direction of model motion in the basic vortex experiment.

calculating the ventilation flow were tried, as well as different time increments in the center motion calculation. All yielded the same pattern of a slower translation that is to the left of the vortex. Comparisons also were made for the other three vortices and the same relationship occurred. Thus, the discrepancy does not appear to be due to inconsistent definitions and is not likely to be a strictly numerical problem.

It is concluded that the difference is due to the two motion processes involved in the translation of the total vortex. The tendency analysis revealed that the advection of symmetric vorticity by the asymmetric circulation (the ventilation flow) accounted for most, but not all, of the motion tendency. The additional tendency comes from the advection of the inner asymmetric gyres by the symmetric flow within the radius of maximum wind as shown in the streamfunction tendency analysis and as suggested by Marks and Houze (1987). The comparison of the ventilation flow and the motion of the center is a further corroboration of this inner-core process.

G. SUMMARY OF THE DYNAMICS OF BETA DRIFT

The development and evolution of the symmetric and asymmetric circulations in a tropical cyclone vortex moving on a β plane has been studied. A procedure has been developed to uniquely and accurately decompose any field on a Cartesian grid into azimuthally symmetric and asymmetric components on the input grid (given a center position). This decomposition has been applied only to the model solution. All other quantities (e.g., vorticity and wind) have been diagnosed to more accurately interpret the model solution. The basic vortex experiment has been analyzed in detail using this procedure to develop a working hypothesis on the dynamics of beta drift and to determine how vortex structure influences the motion. Other vortices

representing the full range of track have also been evaluated in the context of the working hypothesis.

The symmetric flow, as represented by the tangential wind profile, experiences a slight weakening of the maximum wind speed and the formation of an anticyclone beyond r= 600 km. The integrated relative angular momentum in the r = 0 - 2000 km annulus undergoes oscillations during a 144 h integration, although it tends toward a slightly negative value for all vortices. It is also noted that the basic and symmetric perturbation vortices seem to approach a common profile. Further experimentation will be given in Chapter VII.

The asymmetric circulation has a azimuthal wavenumber one appearance with an anticyclone east of the center, a cyclone to the west and a nearly uniform, broad-scale (r ~ 300km) ventilation flow between the gyres. The ventilation flow is almost exactly equal to the storm motion vector over the entire area of significant symmetric vortex. The only exception occurs in the inertially stiff core within the radius of maximum winds. In this inner-core, the winds go to zero, which results in a small dipole in the relative asymmetric flow with an orientation opposite to that of the larger-scale asymmetric gyres.

The dynamical issues are to explain the formation of the gyres, why they rotate to orient the ventilation flow towards the northwest, and why the gyres reach a steady state. The model tendency equation has been analyzed in great detail to demonstrate that the linear β term is responsible for the formation of the gyres. Nonlinear advection fulfills two roles. The first is the advection or movement of the inner 400 km of the system. This component of the nonlinear term has the greatest magnitude. The second role is to balance the β forcing and to orient the ventilation flow toward the northwest. That is, the

nonlinear processes act to maintain the asymmetric flow in a steady state against constant linear forcing and are responsible for the westward component of beta drift through a rotation of the ventilation flow. The hypothesized balance (Fig. 4-12) between the nonlinear and linear effects is thus confirmed, particularly with the tendencies in which motion effects are removed.

The total nonlinear and linear terms are then decomposed into symmetric and asymmetric components to understand how the symmetric and asymmetric circulation systems interact. The slight filling of the cyclone in the inner regions and the formation of the outer anticyclone are due to the symmetric component of β term. This component implies net southerlies in the inner region ($\beta v > 0$ or positive $\partial\psi/\partial t$). The symmetric vortex forces the asymmetric flow through β as the v component is azimuthally wavenumber one. When the motion is in a steady-state, the asymmetric β term has wavenumber two features that are not connected to the motion of the significant vortex low.

The nonlinear advection is separated into two terms representing advection of asymmetric circulation by the symmetric flow (AAVS) and advection of symmetric circulation by the asymmetric flow (ASVA). These terms contribute to the motion of the vortex on two scales. The advection of symmetric vorticity by the asymmetric flow accounted for most of the motion tendency, particularly for the vortex on the r = 100-300 km scale. On the scale of the stiff inner core, the remainder of the motion tendency comes from the advection of asymmetric vorticity by the symmetric flow. This advection has also been shown to rotate the large-scale asymmetric gyres and is responsible for counteracting the β forcing to maintain a steady-state ventilations flow.

The asymmetric flow for the very long integrations (4-6 days in Fig. 4-6) suggests that the motion processes are

localized in a zone of the significant symmetric vortex (r < 500 km), because large changes outside this zone did not affect the motion. In conclusion, the moving vortex can be viewed as set of symmetric/asymmetric circulation subsystems that move and sustain each other in a balanced manner.

V. DYNAMICAL SENSITIVITY

The streamfunction tendency analysis in Sec. IV-E demonstrates how the symmetric and asymmetric circulations interact nonlinearly to move the vortex and to balance ventilation flow forcing due to linear processes. That analysis is "static" in the sense that the tendencies are derived from the model solution at a single time and the physical processes are inferred by the scale and intensity of the tendency patterns. In this chapter, the dominant dynamical processes of vortex motion, as suggested by the "static" tendencies, are studied by directly modifying the model equation during the integration. Such an approach is referred to as "dynamical" sensitivity analysis and is analogous to the "physical" sensitivity tests used in more complete models to study, for example, the role of diabatic processes in midlatitude cyclogenesis (e.g., Keyser and Uccellini, 1987).

Three types of experiments are performed. The first type involves changing the relative magnitude of nonlinear to linear effects to determine how the ventilation flow varies with the speed of motion. The functional dependence of ventilation flow on the vortex motion will then be used to infer how the motion response to a disruption in the ventilation flow/motion balance might vary with vortex structure. In the second set of experiments, the model is initialized with a linear solution and is then integrated with only nonlinear term. The long-term, nonlinear-only solutions demonstrate that once the ventilation flow is established, the symmetric/asymmetric circulations in the vortex are bound together to sustain the motion and the nature of the nonlinear-linear balancing process when steady-state motion is achieved. Finally, the nonlinear

term is decomposed into symmetric and asymmetric components during the integration and the nonlinear interactions are examined by directly modifying the symmetric/asymmetric interaction terms. These experiments confirm the critical role of nonlinear interaction between the vortex (symmetric flow) and asymmetric circulation arising from vortex-environment (the earth's vorticity field gradient or β in this research) interaction.

A. VENTILATION FLOW DYNAMICS

It was hypothesized in Sec. IV-C that the steady-state speed of motion of the vortex resulted from a balance between ventilation-flow generation by Rossby dispersion (i.e., by the β term) and ventilation flow reduction relative to the moving center by the nonlinear processes that cause the vortex to move. Schematically, this balance may be represented (Fig. 4-10) by a curve relating ventilation flow to the speed of motion. Steady-state motion occurs when the ventilation flow equals the speed of motion.

The objective of this section is to calculate the magnitude of ventilation circulation as a function of the vortex structure, and how this is related to the speed of beta drift. As indicated in Sec. IV-C the direction of motion and turning can not be determined as they are strongly related to the nonlinear modification (e.g., rotation) of the large asymmetric gyres and to the orientation of the associated ventilation flow. In the next section, the ventilation flow function is calculated for the four basic vortices. It will be suggested that the shape of the curve as it passes through the "balance point" may be related to the "sensitivity" of certain vortex structures to externally forced disruptions in the ventilation-flow/motion balance.

1. The Hypothesized Ventilation Speed Function

As shown Fig. 4-25, a quasi-steady state does occur in which the magnitude of the ventilation flow approximately equals the vortex speed of motion. The basic idea behind the hypothesized ventilation speed function is: If the vortex motion is much less than the steady-state value (in the extreme case it would be stationary), then the ventilation flow relative to the center would necessarily become very large. Conversely, if the vortex moved very rapidly (e.g., > 20 m/s), then the ventilation flow generation would be smaller because the β forcing could not be applied for a sufficient time to generate the large-scale asymmetric gyres. Thus, it is possible to a priori infer three points on the curve: (i) when the vortex speed is zero, the ventilation flow is a maximum; (ii) at the balance point, the ventilation flow and motion are equal; and (iii) when the speed of motion is very large, the ventilation approaches zero. To find other points on the curve, it is necessary to force the vortex to move faster or slower than the linearly-induced ventilation flow.

Consider the model tendency equation with two scale factors a and b on the advection term and the β term respectively

$$\frac{\partial \zeta}{\partial t} = a(-\vec{V} \cdot \nabla\zeta) + b(-\beta v) \quad . \qquad (5.1)$$

As shown by Chan and Williams (1987), the motion is strictly a nonlinear process, even though the asymmetric circulation generation is basically a linear process. Thus, the relationship between the motion and the ventilation flow will change as the (a,b) scale factors are varied. For example, if a = 0.5 and b = 1.0, then for every unit of ventilation flow the storm would be expected to move only half as fast. Conversely, if a = 2.0 and b = 1.0, the

motion relative to the linearly-induced ventilation would tend to be doubled. Of course, this reasoning is only approximately true and is based on the one-for-one relationship between ventilation flow and motion for (a,b) = (1.0,1.0). This one-for-one correspondence implies that, as a whole, the vortex motion is a steering-type process with the steering flow equal to the ventilation flow. Nevertheless, it is proposed to determine other points of the ventilation flow function by changing a and b and integrating the model to a steady state.

2. Experiment Design

Four vortices are considered (see Figs. 3-4 and 3-8): (i) the basic vortex (B1); (ii) the "large-and-weak" vortex (B3); (iii) the cyclonic symmetric perturbation vortex (S8); and (iv) the anticyclonic symmetric perturbation vortex (S9). The initial vortex structure parameters are given in Table 3-2 of Chapter III. These vortices include a considerable range in the tangential flow in the critical annulus of r = 300 - 800 km and result in a wide range of track orientations and speeds.

Nine model runs are made for each of the four vortices with the characteristics given in Table 5-1. It would have been desirable to hold the β-term scale factor fixed in (5.1) and only vary the factor governing the advection term. However, increasing the advective coefficient (a) would require a decrease in the time step to satisfy the linear computational stability criterion. Instead, the ratio of a/b is increased by decreasing the β forcing and holding a fixed. This allows the time step to be held constant throughout all the integrations.

TABLE 5-1. Characteristics of the model experiments to determine the ventilation flow function.

Exp. No.	a	b	a/b	Integration Length (h)	Comments
1	0.00	1.00	0.00	144	Linear solution
2	0.05	1.00	0.05	144	
3	0.10	1.00	0.10	144	
4	0.25	1.00	0.25	144	
5	0.50	1.00	0.50	144	
6	1.00	1.00	1.00	144	Normal model
7	1.00	0.50	2.00	144	
8	1.00	0.25	4.00	288	Longer integration
9	1.00	0.10	10.00	432	required to reach steady state

The integration times are greater than the standard 72 h to more clearly establish the track behavior after the initial maximum translation speed is achieved. In the cases in which the β term is reduced, a much longer time is needed to linearly build the asymmetric circulation. In Exp. 9, the integration must be extended to 18 days. The model remains stable and energy is nearly conserved in all cases, which further substantiates the numerical quality of the model.

3. Linear Solutions

The asymmetric flow from the basic vortex with the linear solution (Exp. 1 in Table 5-1) at t = 24 h and 72 h is shown in Fig. 5-1. As in the full model solutions, the ventilation flow is fairly uniform, except in the inner core where the asymmetric flow goes to zero. When the nonlinear term is set to zero, the ventilation flow does not pass uniformly through the center as in the full model. Thus, this inner-core asymmetry is strictly a result of the distribution of the meridional v component ($\beta v \sim 0$) near the center. However, the rotational stiffness of the inner-core inhibits the asymmetric flow from penetrating directly into the center.

At 72 h, the ventilation flow has become less uniform with greater flow to the east and lesser flow to the west. This shear across the center tends to be averaged out

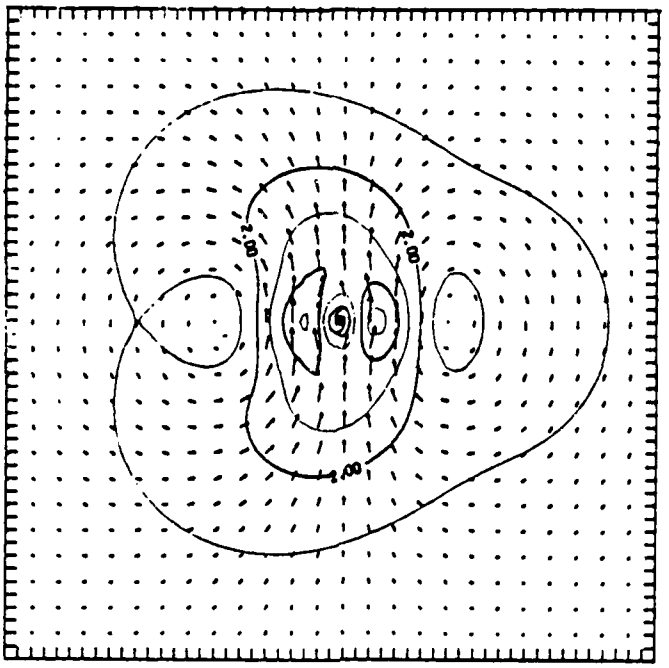

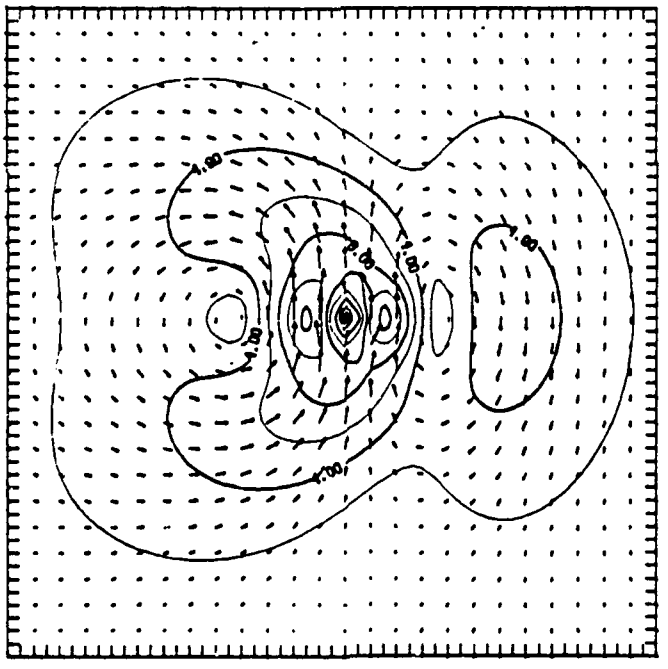

Fig. 5-1. Asymmetric flow from the linear solution for the basic (B1) vortex at (a) t = 24 h and (b) 72 h. The domain is 2000 km on a side and the grid points are indicated by the tick marks. The maximum velocities in (a) and (b) are 5.3 m/s and 11.2 m/s

when a single ventilation flow vector is calculated over the averaging area (r = 0 - 300 km).

The evolution of the ventilation flow vector speed for the linear solution (a/b = 0.0) is shown in Fig. 5-2. The development is fairly rapid, with steady-state values (~ 6 m/s) that are much greater than the vortex motion in the standard integration (a=1.0,b=1.0). The maximum ventilation flow vector speed in Fig. 5-2, and the time to reach the maximum, are proportional to the outer strength in the vortex. For example, the maximum speed increases from 6 m/s for vortex S9 to about 8.5 m/s for vortex B3 as outer strength increases from 4.4 m/s to 8.3 m/s. Also, notice the large oscillation after the maximum for the large-weak vortex (B3). This oscillation corresponds well to the overall greater motion and translation speed increases and decreases observed in the unsmoothed track for the full model integrations. This suggests that the translation of the B3 vortex may be more susceptible to structural changes, particularly because of the smaller values of the nonlinear terms in the inner regions.

It is noteworthy that the magnitude of the ventilation flow vector (referred to as ventilation speed until otherwise stated) does achieve a quasi-steady state. Linear dispersion operating alone would eventually cause the vortex to breakup as noted by oceanographers studying Gulf Stream eddies (e.g., McWilliams and Flierl, 1979). Although the ventilation speed does reach a nearly steady state, the asymmetry in the asymmetric flow continues to increase (not shown). This increased asymmetry is smoothed out during the averaging process used to calculate the ventilation speed. Although a vortex breakup may occur much later, the ventilation speed is not affected on the time scale of 5-10 days. However, the main point is that the "beta drift

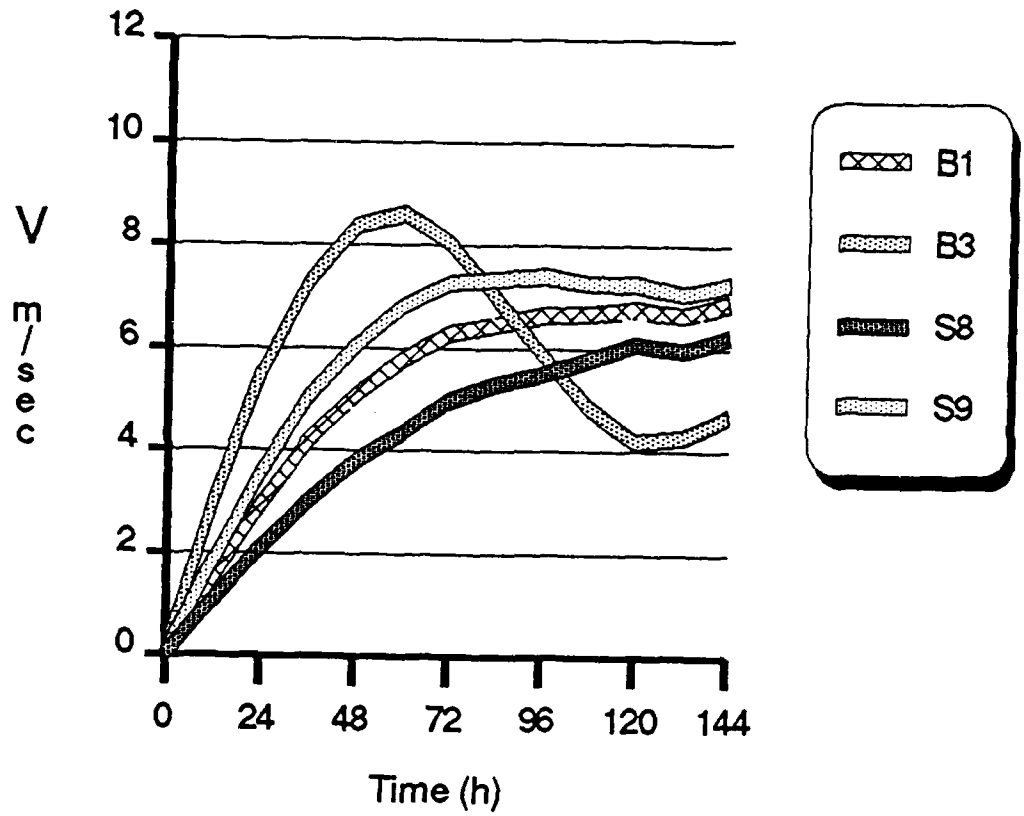

Fig. 5-2. Magnitude of the ventilation flow vector speed for the linear solutions of the four vortices. The vortex number (e.g., B1 for basic, see Table 3-2) is indicated in the figure.

potential," as measured by the maximum ventilation speed, of a tropical cyclone scale vortex can be quite large.

4. Results with Varying a/b Ratios

The general behavior of the ventilation speed in the full model integrations with varying a/b ratios is illustrated in Fig. 5-3 using the basic (B1) vortex. When $a/b \leq 1.0$ (relatively weak nonlinear advection), the ventilation flow increases with decreasing advection (Fig. 5-3a). By effectively slowing the vortex down (decrease in a/b ratio), the ventilation flow has increased as the β-term generates a more intense large-scale asymmetric circulation. Conversely, when $a/b \geq 1.0$ (relatively weak linear term) the ventilation flow decreases with increasing advection (Fig. 5-3b). In this situation, the vortex is moving faster than the ventilation flow. Ventilation flow generation is inhibited as the storm translation is too large to allow the asymmetric flow to build around the center. Also observe that the time needed to reach a maximum is around 60-72 h for $b = 1.0$ and $a \leq 1.0$ (Fig. 5-3a), whereas greater time is required when the nonlinear term is relatively weak ($a=1.0$ and $b \leq 1.0$ in Fig 5-3b).

The dependence of the adjustment to a steady speed on the magnitude of βv (linear effects) suggests that the process by which a steady state is achieved in tropical cyclone vortices is mainly controlled by the linear processes. This dependence on the magnitude of the linear term is more apparent as the β term is weakened (Fig. 5-3b). For example, when the $b= 0.5$ relative to the nonlinear term ($a = 1.0$), the adjustment time is roughly double that with $b = 1.0$. Comparable behavior is observed for the other vortices, except greater oscillations occur after the first maximum in the ventilation flow. These oscillations are likely due to a greater degree of variation in the linear ventilation flow forcing for the large weak vortex (e.g.,

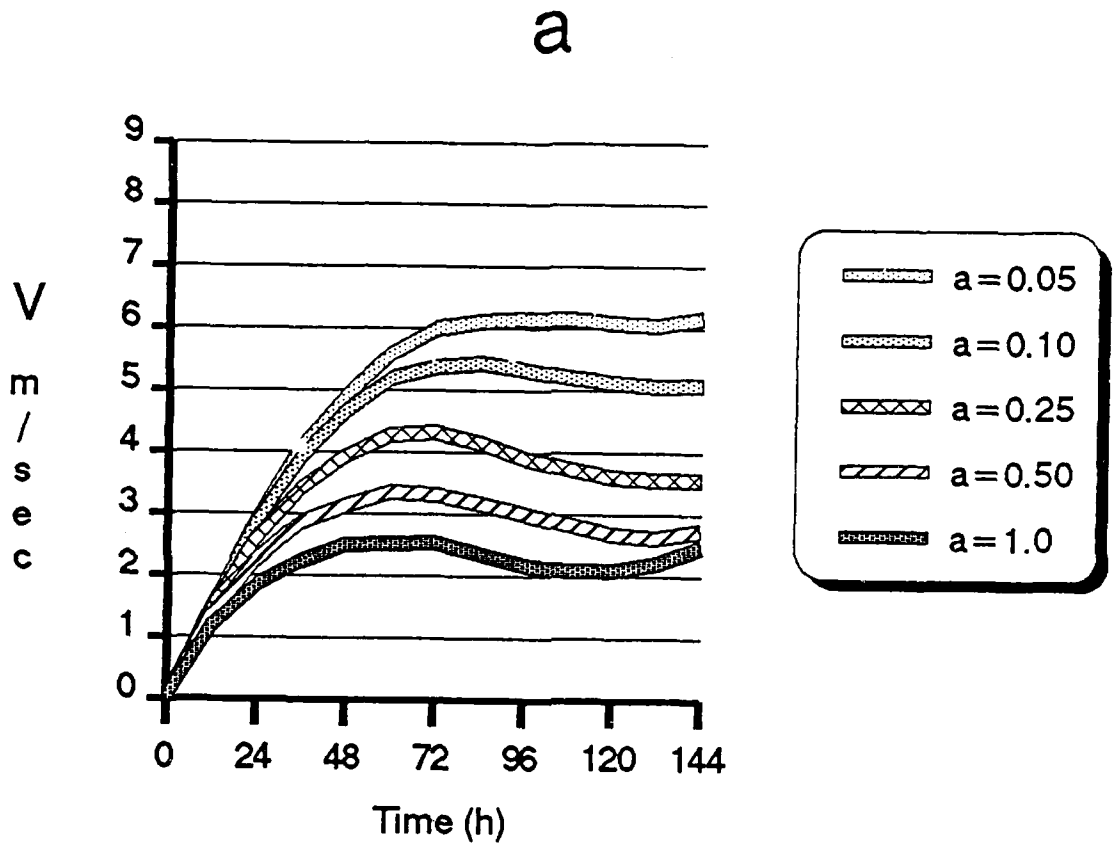

Fig. 5-3. Ventilation speed versus integrat[illegible]
a/b ratio, which controls the relative magn[illegible]
nonlinear-to-linear effects, is varied f[illegible]
vortex for (a), b = 1.0 and a ≤ 1.0 (rel[illegible]
linear effects), and (b), a = 1.0 and [illegible]
the time axis runs from t = 0 - 28[illegible]
- 144 h in (a).

AD-A190 961 THE ROLE OF VORTEX STRUCTURE IN TROPICAL CYCLONE MOTION 3/4
(U) NAVAL POSTGRADUATE SCHOOL MONTEREY CA M FIORINO
DEC 87

UNCLASSIFIED FFG 4/2 NL

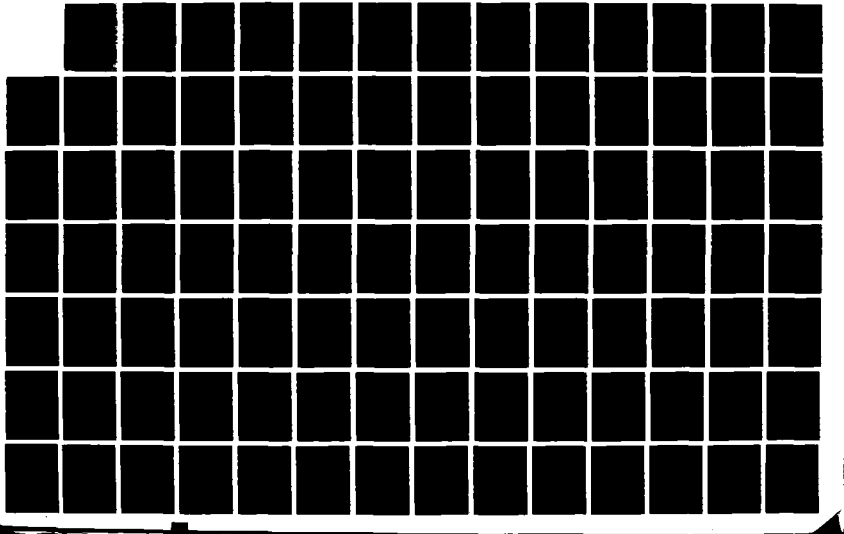

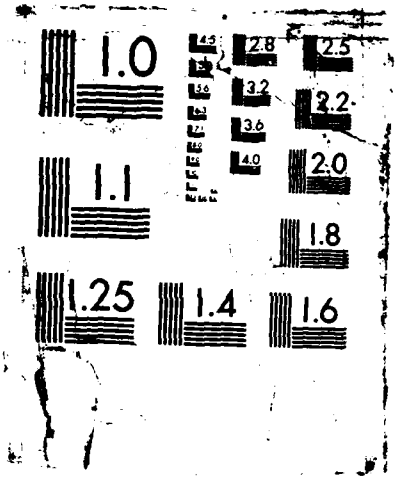
1.0
1.1
1.25
1.4
1.6
1.8
2.0
2.2
2.5
2.8
3.2
3.6
4.0

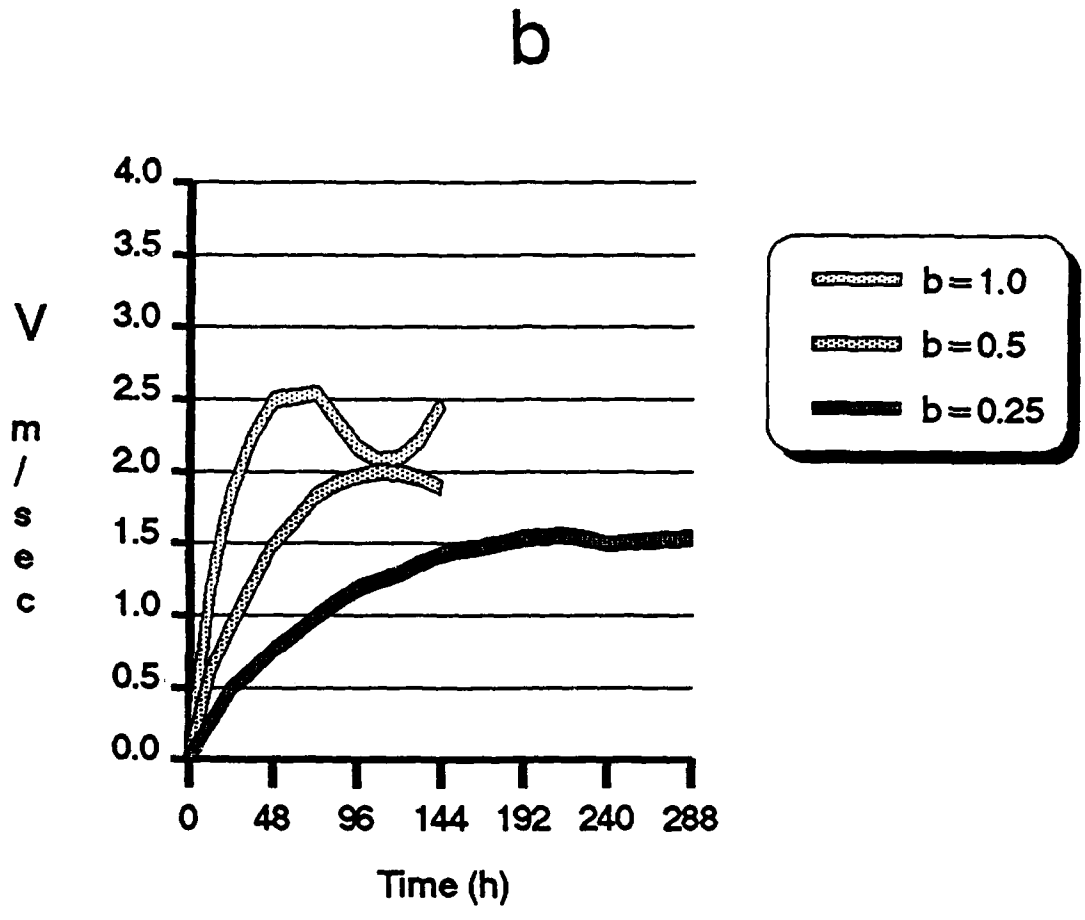

Fig. 5-3. (Continued)

the 24-h linear solution in Fig. 5-7) and the magnitude of the advective effects in the symmetric perturbations in vortex S8 and vortex S9.

To better understand the ventilation speed derived from these model experiments, it is useful to examine the tracks (Fig. 5-4). The anticyclonic perturbation vortex (S9) is representative of the four initial vortices and the nine integrations. The motion in the weak nonlinear (a = 0.05, b = 1.0) experiments (Fig. 5-4a) for all initial vortices has a nearly equal direction and speed of motion toward the NW. As the weighting of the advection term increases relative to the β-term (a tends toward 1.0), the tracks approach the track from the physically correct experiment (a = 1.0, b = 1.0). This demonstrates in a different way the conclusion of Chan and Williams (1987) regarding the great importance of advection in determining both the speed and path characteristics of vortex motion. However, when the advection term is relatively greater than the β-term, the track variations as a function of a/b are less smooth and have greater deviations from the physically correct integration.

The interactions between the advective and dispersive (β) processes that yield consistent track behavior as the a/b ratio varies appear to be sensitive to the vortex structure. In the cyclonic perturbation experiment (Fig. 5-5), a more marked departure from the smooth transition in Fig. 5-4 occurs as the advection term becomes relatively greater (Fig. 5-5b). The large track deflection toward the north in Fig. 5-5b suggests that external-to-the-vortex events that might disrupt the balance between the advection and the β-term may lead to greater track deviations for certain vortex structures.

A possible physical analog might occur when the base-state absolute vorticity gradient (β in this research)

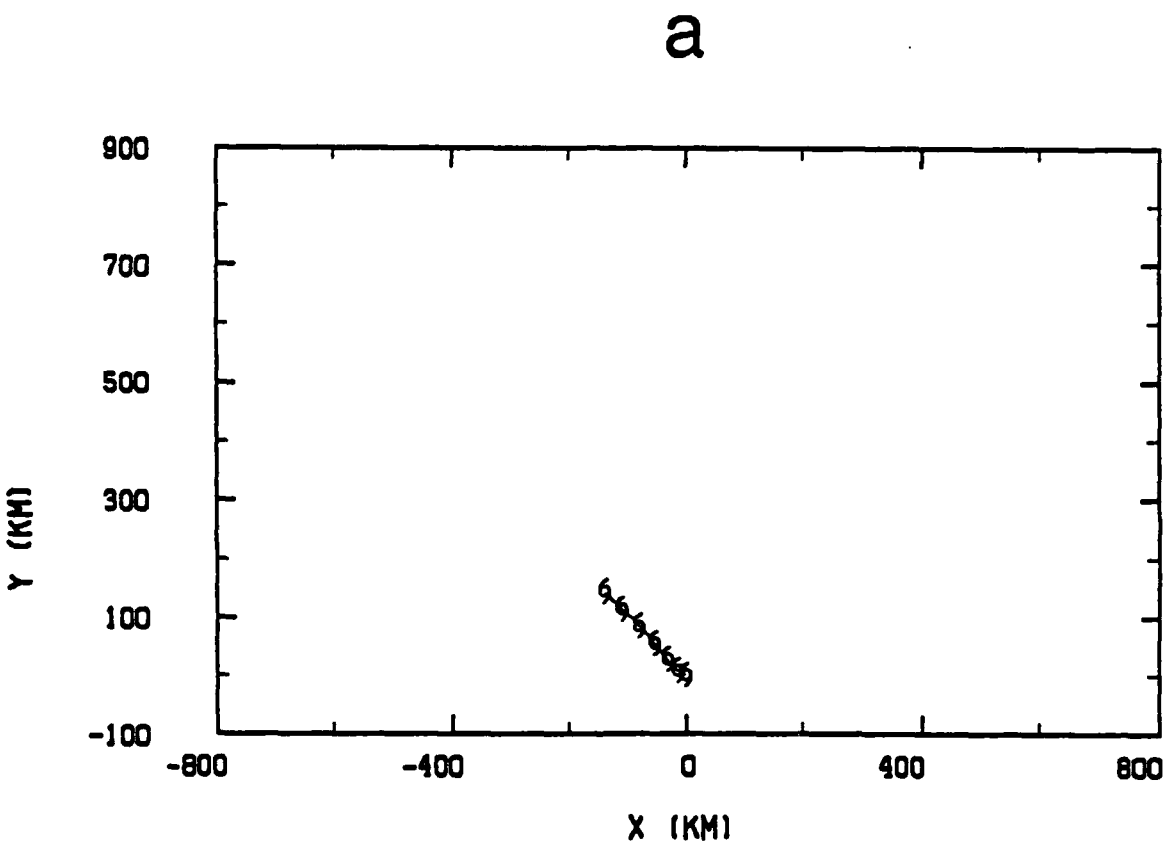

Fig. 5-4. Tracks from the anticyclonic perturbation vortex (S9) integrations with a varying a/b ratio. The hurricane symbol is plotted every 24 h. In (a), (a,b) = (0.05,1.0), in (b), (a,b) = (0.25,1.0) (solid), (0.50,1.0) (short-dashed), and the physically correct model (1.0,1.0), in (c) the nonlinear effects are relatively greater (a,b) = (1.0,0.10) (solid).

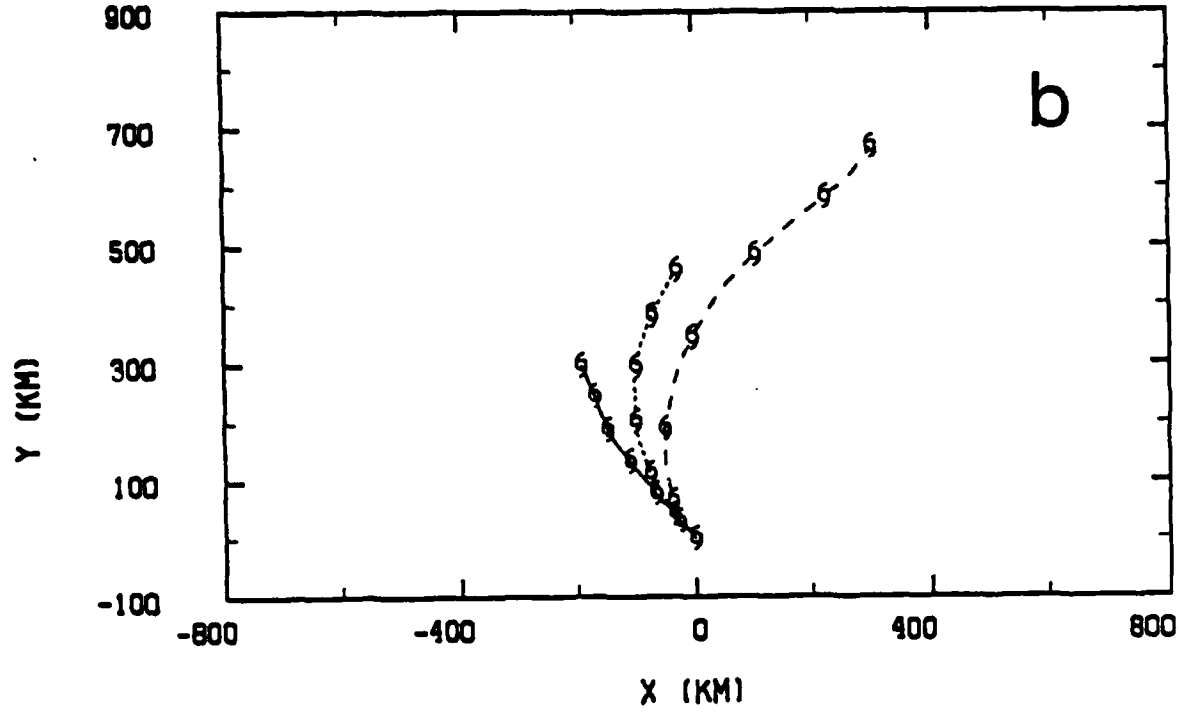

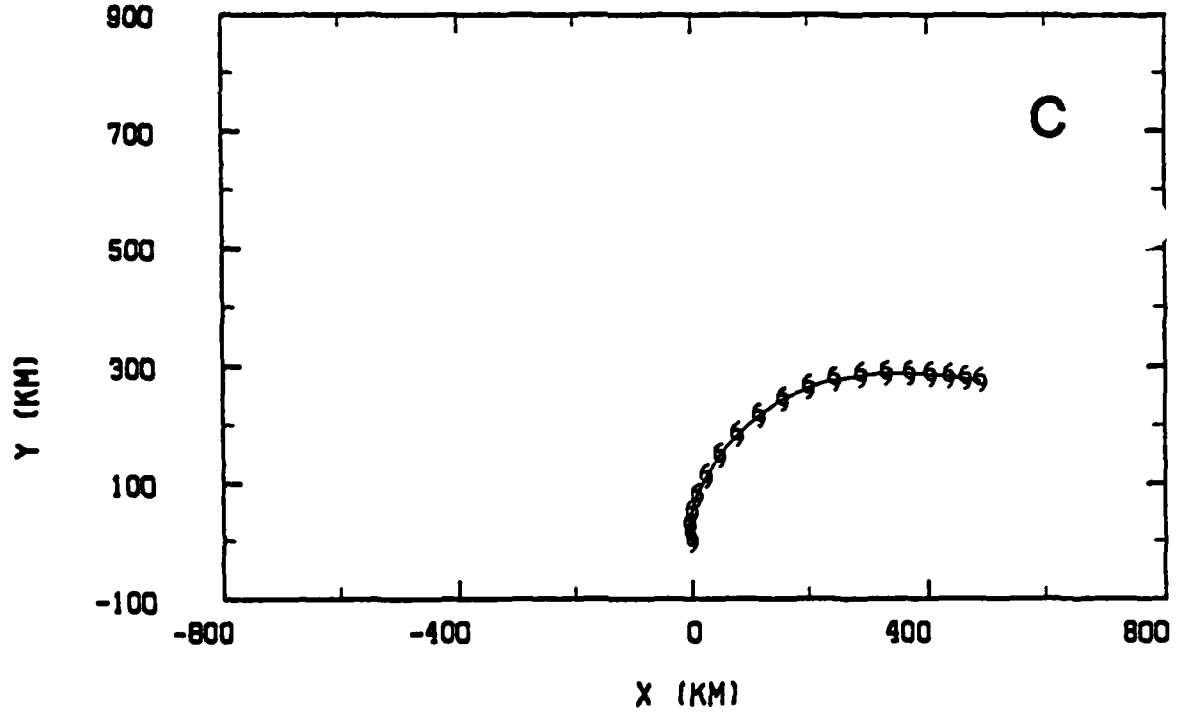

Fig. 5-4. (Continued)

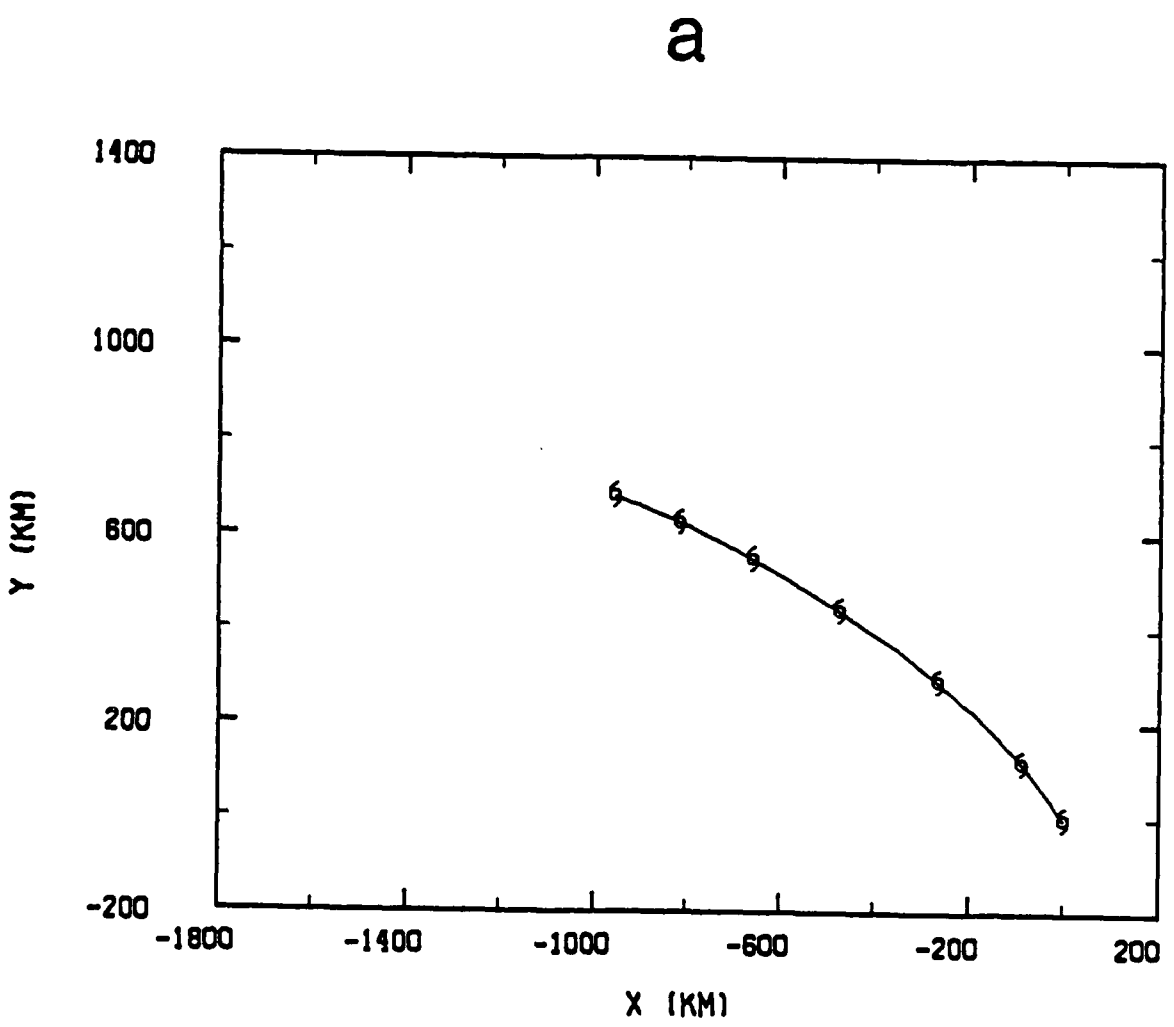

Fig. 5-5. Tracks from the cyclonic perturbation vortex (S8) for (a) the physically correct (a,b) = (1.0,1.0) and for (b) (a,b) = (1.0,0.10) solutions.

b

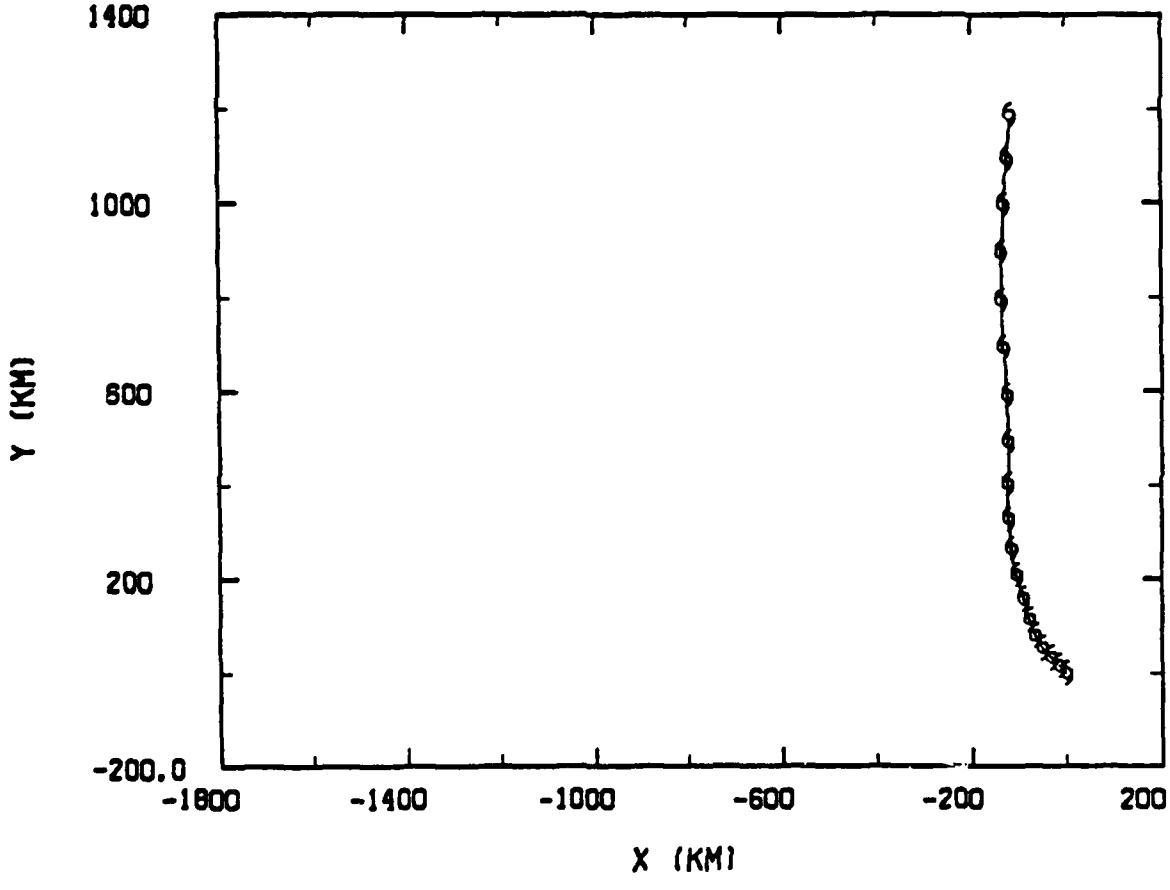

Fig. 5-5. (Continued)

changes in the vicinity of the vortex as it moves. DeMaria (1985) has demonstrated such a sensitivity using a comparable model and suggested that vortex specification would be more critical in certain environments (absolute vorticity gradients) than in others. These experiments suggest a similar sensitivity may exist due to changes in the structure of the vortex that is interacting with an environment flow in which only β is allowed to vary.

5. The Calculated Ventilation Speed Function

The hypothesized ventilation speed functions may be represented by plotting the steady-state ventilation speeds on a straight line with slope equal to the inverse of the a/b ratio used in the experiment. Physically, these lines assume a perfect match between the linear-induced ventilation flow and nonlinear advection. That is, if the advection term is weighted twice the β-term (a/b=2.0), then the storm will move twice as fast as the ventilation flow, or that for every unit of ventilation flow the vortex would move with two units of translation. The position of each ventilation speed on these lines corresponds to the value on the y axis.

The ventilation speed function for the basic B1 vortex is given in Fig. 5-6. As hypothesized, the ventilation speed function decreases rapidly from the linear solution (a = 0.0, b = 1.0) and slowly tails off as the nonlinear motion effects become relatively larger (a = 1.0, b = 0.10). The "balance point," which is the intersection of the straight line with slope equal to 1.0 (a = 1.0, b = 1.0, or the physically realistic model) occurs at approximately 2.2 m/s.

The corresponding steady-state vortex speed are also indicated in Fig. 5-6 (see Table 5-2 for the values). The vortex motions for the case with $b \leq 1.0$ are obtained by multiplying the model motion by the a/b ratio. In other

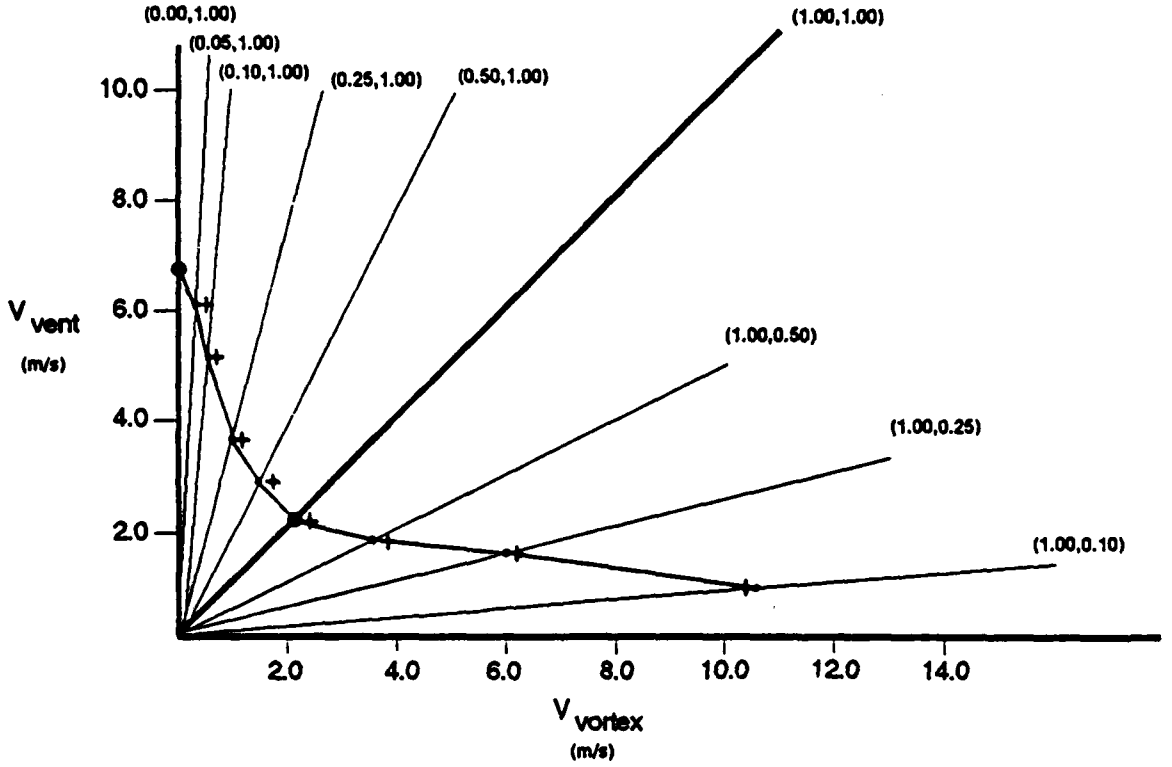

Fig. 5-6. The ventilation speed function for the basic (B1) vortex. The (a,b) pairs for each of the nine experiments is indicated at the end of the lines radiating from the origin. These lines have a slope equal to the inverse of the a/b ratio and represent how the ventilation speed would vary with vortex motion if there was a perfect relationship between ventilation flow and vortex translation. The heavy line is for the physically correct mode. The dots on each line indicate the steady-state ventilation speed for each (a,b) experiment and the + corresponds to the steady-state speed of vortex motion.

words, the model motion is scaled to the physically realistic case (b=1.0). This approximation is validated by running the model with (a,b) = (2.0,1.0) and comparing this motion to that in the (a,b) = (1.0, 0.5) case. The model motion for the (1.0,0.5) case is about half that of the (2.0,1.0) case. A similar result is found when comparing the (a,b) = (4.0,1.0) run to the (1.0,0.25) run and for other vortices. As stated earlier, the main reason for reducing b rather than increasing a was to keep the time step constant in all experiments.

As found in Chapter IV, the vortex motion is slightly faster than the ventilation speed. This behavior is consistent in all the experiments and for all the vortices. The nearly one-to-one relationship between the ventilation flow and the motion of the center even as the relative scaling of the nonlinear and linear processes is changed indicates how the forcing (linearly-induced ventilation) and the motion (nonlinear advection) control the speed of motion.

Ventilation speed curves for the other vortices are shown in Fig. 5-7 for the weak-large vortex (B3) and in Fig. 5-8 for the symmetric perturbations (S8 and S9). Unlike the basic vortex, these curves are not smooth and do not pass through the balance point at the same angle. In the case of the weak-large (B3) cyclone, the ventilation flow actually <u>increases</u> toward the physically correct a/b ratio of 1.0 (the heavy line in the Fig. 5-7) as the speed of motion increases from a/b < 1.0. This is contrary to the B1 vortex in which the ventilation speed decreases uniformly with increasing vortex translation. Also, notice how the slopes of the curves change around the balance point in the symmetric perturbation integrations (Fig. 5-8). This may be indicative of the motion "stability" of the vortex. This "stability" determines how the motion would change in

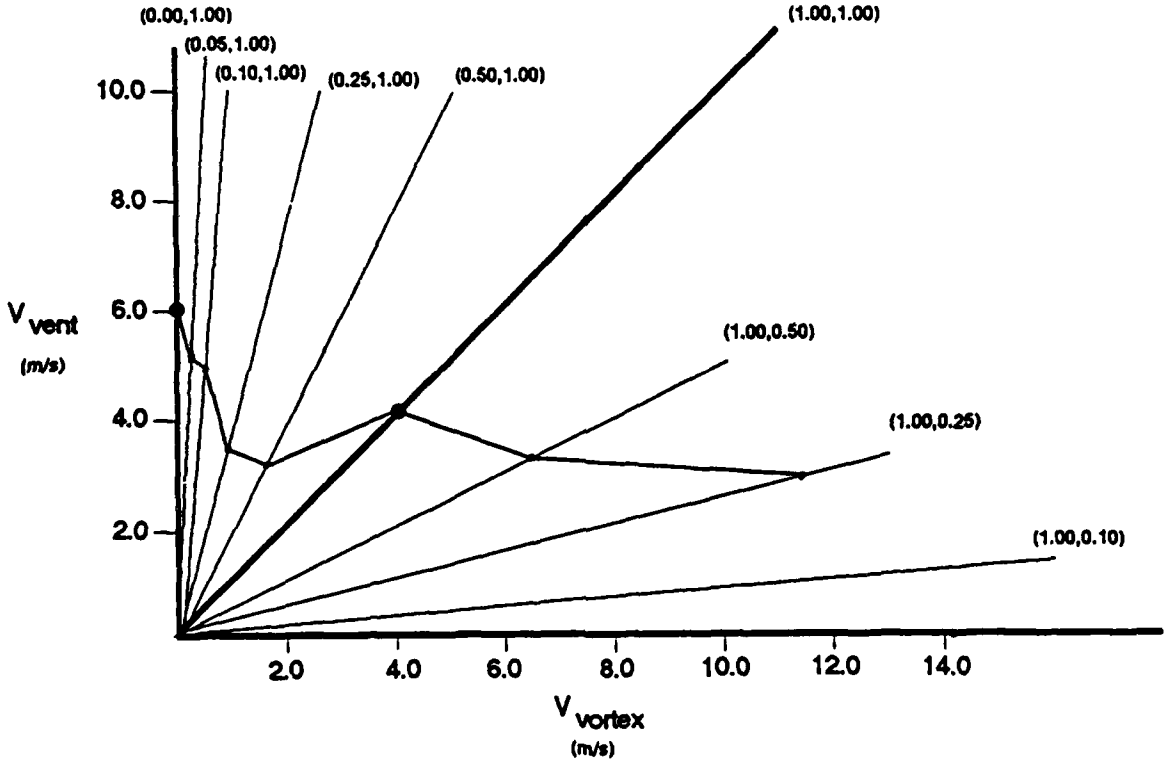

Fig. 5-7. As in Fig. 5-6, except for the weak, large (B3) vortex.

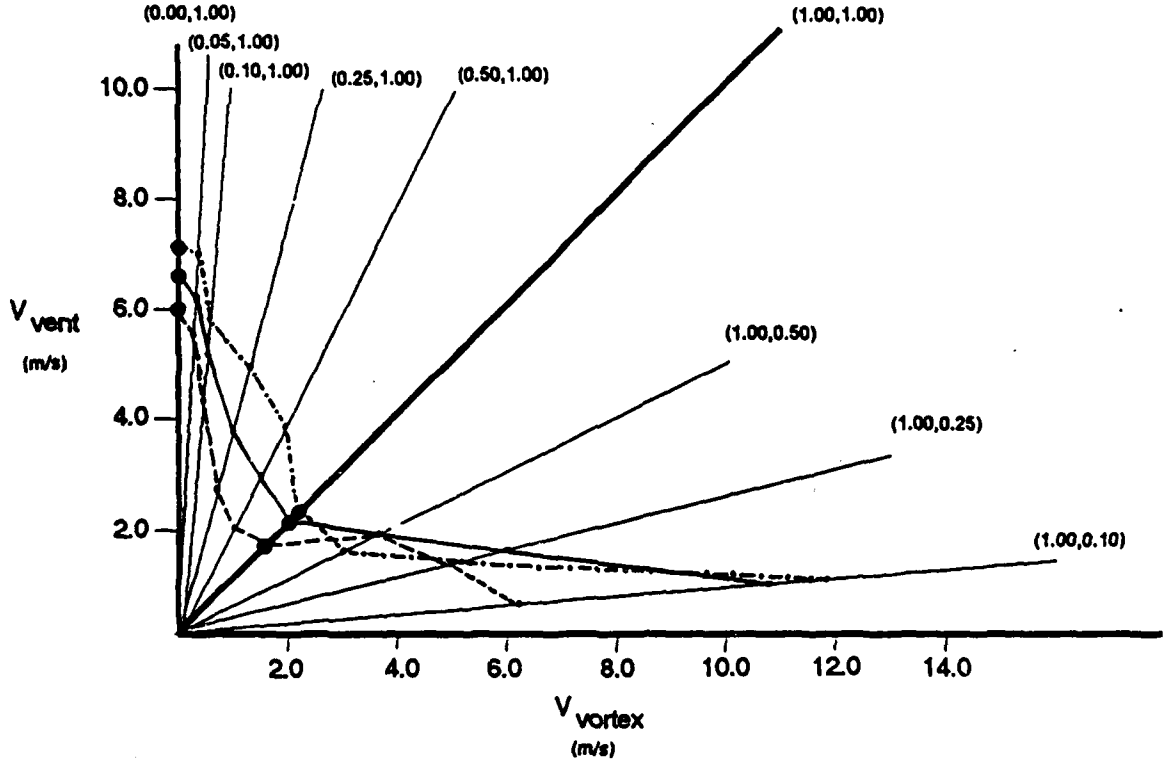

Fig. 5-8. As in Fig. 5-6, except for the basic (B1) vortex (solid) and the cyclonic (dash-dot) and the anticyclonic (dashed) symmetric perturbation vortices.

response to external (synoptic factors) or internal (cyclone factors) changes in the balance involved in beta drift.

Small changes in the vortex motion around the a/b=1.0 curve could lead to large changes in the ventilation flow and subsequent adjustments to the β-induced flow and an external environmental forcing. For example, if the vortex were forced to intensify (e.g., convergence in the lower troposphere) in the critical annulus (greater outer strength), then the asymmetric flow and the ventilation flow would change due to different linear effects (i.e., increased βv). The ventilation speed function suggests that the response of the vortex motion to this change in the ventilation would be different depending on the existing structure in the outer regions.

TABLE 5-2. Comparison of ventilation flow vector and the motion vector for the basic vortex experiment.

SF ADVEC	SF BETA	VRTX SPD MAX	VRTX SPD SS	VRTX DIR SS	VENT SPD MAX	VENT SPD SS	VENT DIR SS	VRTX ADJ TIME	VENT ADJ TIME
0.05	1.00	0.53	0.50	316	6.17	6.10	333	96	96
0.10	1.00	0.77	0.70	316	5.45	5.10	340	72	84
0.25	1.00	1.25	1.10	320	4.33	3.70	334	72	84
0.50	1.00	1.82	1.50	323	3.36	2.70	333	72	84
1.00	1.00	2.69	2.40	327	2.54	2.20	330	72	72
1.00	0.50	4.14	4.00	332	2.00	1.80	335	108	110
1.00	0.25	6.44	6.40	337	1.56	1.50	339	200	220
1.00	0.10	9.50	8.50	333	1.06	1.06	338	300	400

SF ADVEC - Scale factor on the nonlinear advection term
SF BETA - Scale factor on the linear β term
VENT SPD MAX - Maximum speed of the ventilation flow (m/s)
VENT SPD SS - Steady state ventilation flow speed (m/s)
VENT DIR SS - Direction of the steady state vent. flow (°)
VRTX SPD MAX - Max speed of movement of the vortex center (m/s)
VRTX SPD SS - Steady state vortex speed (m/s)
VRTX DIR SS - Direction of vortex motion (°)
VENT ADJ TIME - Time (h) to the maximum vent. flow
VRTX ADJ TIME - Time (h) to the maximum vortex speed

6. Summary

It was hypothesized in Sec. IV-C that the dynamics of beta drift involves a balance between ventilation flow generation by Rossby dispersion (βv) and ventilation flow "reduction" or compensation by the motion of the vortex. In this set of dynamical sensitivity experiments, the ratio (a/b) of nonlinear to linear (βv) effects is varied to understand the relationship between the ventilation flow vector and the speed of motion, and also the nature of the balance.

The ventilation flow vector, which is defined as the mean asymmetric flow within 300 km of the center, is found to be very nearly equal to the motion (scaled by a/b). This correspondence is maintained for various a/b ratios. The "beta-drift potential," which is defined by the maximum ventilation speed from the linear solution, is much greater (~ 6 m/s) than the actual motion. The magnitude of the actual beta drift is constrained by both the nonlinear processes (the motion) and the linear processes (βv that generates the asymmetric advecting flow), and therefore by the vortex structure. However, the nonlinear processes that actually move the vortex effectively limit the maximum speed possible by reducing the time available for development of the asymmetric gyres by linear processes.

The ventilation speed curves in Fig. 5-6 through 5-8 provide another illustration of the balancing between nonlinear and linear effects and how this balance varies with vortex structure. It is also suggested that the relationship between changes in the speed of the vortex due to non beta-drift factors, and the beta forcing (the ventilation flow) at the balance point may be important for understanding how tropical cyclone motion changes can occur.

B. NONLINEAR-ONLY SOLUTIONS AFTER LINEAR FORCING

The tendency analysis in Sec. IV-D shows that large-scale asymmetric gyres are generated by Rossby dispersion (the β term in the model equation). These gyres produce the ventilation flow that advects the vortex. A more important result of the tendency analysis is that the nonlinear processes act to modify the continuously forced gyres through a counteracting tendency.

In this section, the nature of the nonlinear adjustment processes in the large-scale gyres is studied using a dynamical sensitivity approach in which the model is initialized with a linear solution, but is then integrated with only the nonlinear terms. That is, the adjustment of the linear solution (β term only and containing the asymmetric gyres) to the nonlinear effects. This procedure allows the nonlinear advective processes to be studied independently of linear dispersion. Although these experiments are theoretically motivated, they do parallel a physical situation in which the base-state absolute vorticity gradient suddenly (instantaneously in this test) is reduced to zero (e.g., anticyclonic shear in the storm environment exactly offsets the β term).

The key questions are:

(i) How does the motion of the vortex depend on the length of the linear forcing?

(ii) How, and on what time scale, are the asymmetric gyres modified by the nonlinear processes?

(iii) How does the vortex flow in the critical annulus induce turning motions due to nonlinear advection and to what extent do these turning motions depend on the linear forcing?

1. Experiment Design

The same four vortices used in the previous section are again selected to represent a range of vortex structures. In the first set of experiments, two 144-h nonlinear-only integrations are made for each vortex with

initial conditions derived from a previous linear integration (e.g., see Fig. 5-1). During these linear integrations, the amplitude of the asymmetric gyres at 24 h is twice that of the 12-h solution and contains a significant (1-3 m/sec) ventilation flow (Fig. 5-3). Two initial conditions from the 12- and 24-h linear solutions are specified to determine how the motion depends on the amplitude of the forcing. In the second set of experiments, the nonlinear-only integrations (from the 24-h linear solution initial conditions) are extended to 288 h (12 days). These runs are used to establish the very long-term motion characteristics.

2. Track Results

The 144-h tracks for all four vortices are shown in Fig. 5-9 for the complete model forecast and the nonlinear-only forecasts. The reference forecast using the full model equation is initialized with the symmetric vortex rather than the linear solution as in the two nonlinear-only simulations. Full model integrations with initial conditions from the linear solutions (i.e., equivalent to the nonlinear-only runs) yielded essentially the same track (differences on the order of 5%). Whereas the full model has both the linear and nonlinear effects that produce the asymmetric forcing and motion, the model with only nonlinear effects does not include the linear forcing that generates the asymmetric gyres. Thus, the pre-defined asymmetric circulation in the initial condition is not changed by linear processes during the integrations.

The most striking feature of the tracks in Fig. 5-9 is that the length of the nonlinear-only tracks can be scaled by the length of time that the initial linear solution is integrated. As the length of the linear forcing is doubled (12 h versus 24 h), the length of the track is also doubled. Also, observe that the vortex moves rapidly

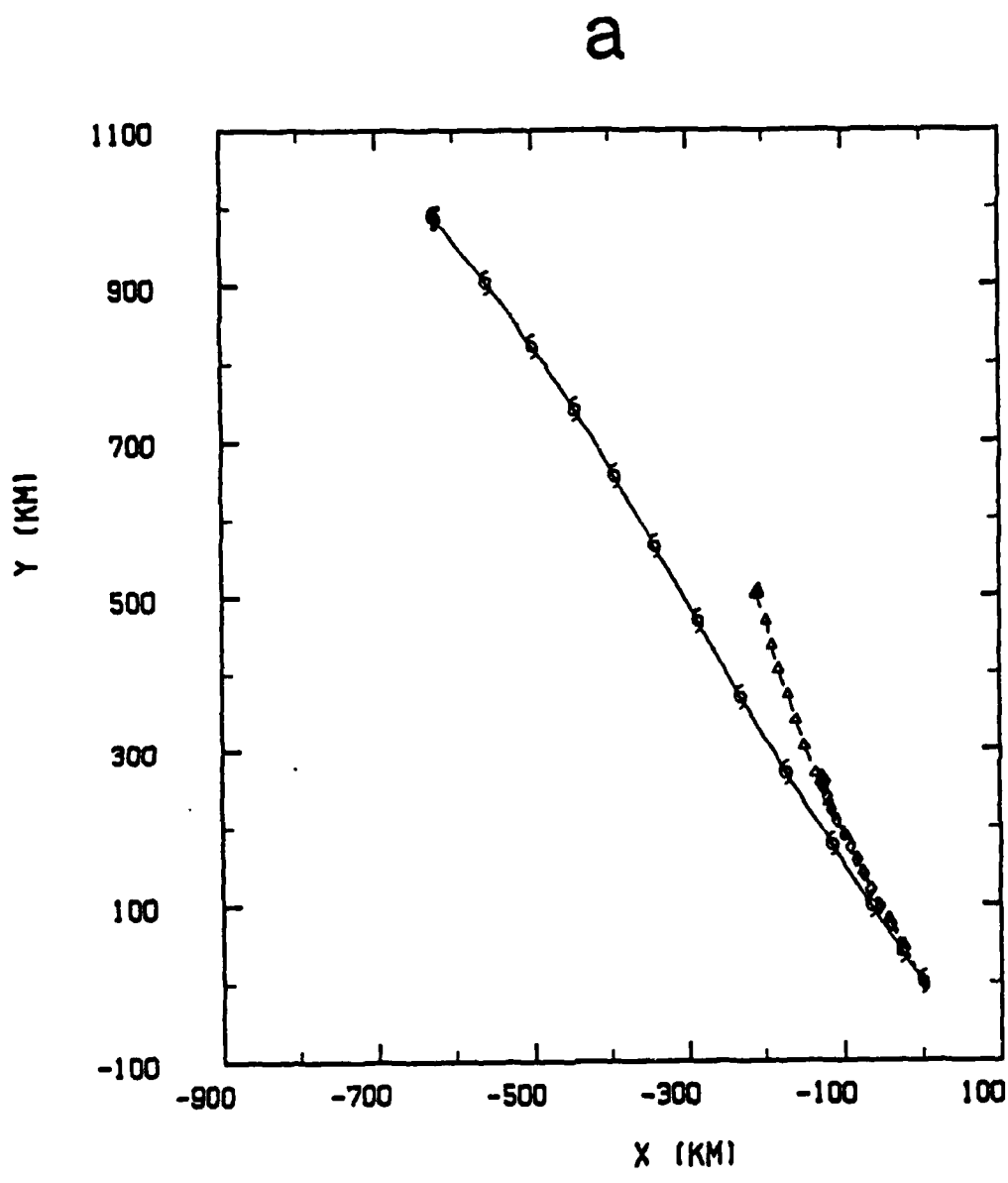

(a) The basic vortex (B1)

Fig. 5-9. Tracks to 144-h for the full model initialized with the analytical symmetric vortex (solid; with a hurricane symbol every 12 h), the nonlinear-only integration initialized with the 12-h (short-dashed, diamonds) and 24-h (long-dashed, triangles) linear solutions. The end points are highlighted to emphasize the differences in the total length of the tracks.

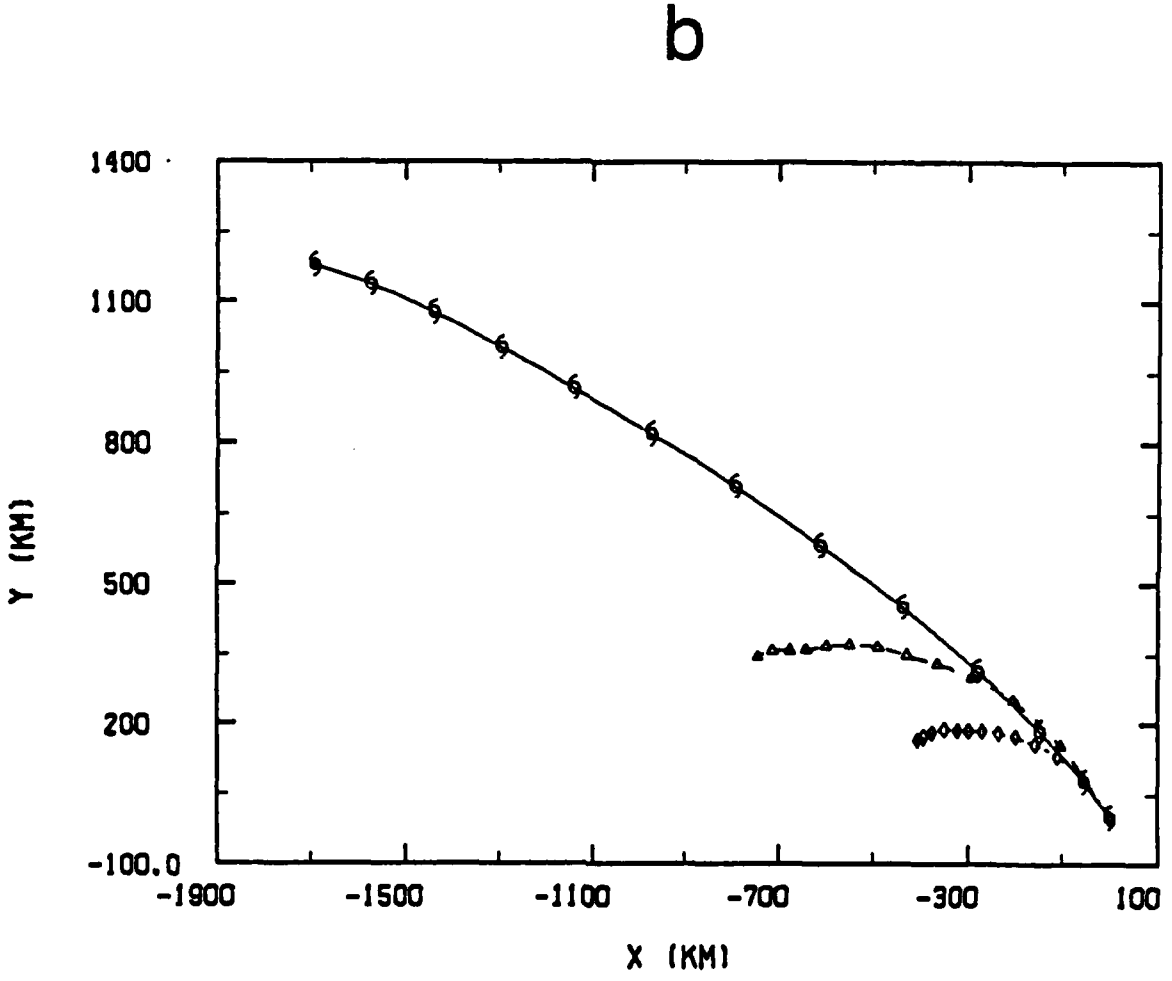

(b) The weak-large vortex (B3)

Fig. 5-9. (Continued)

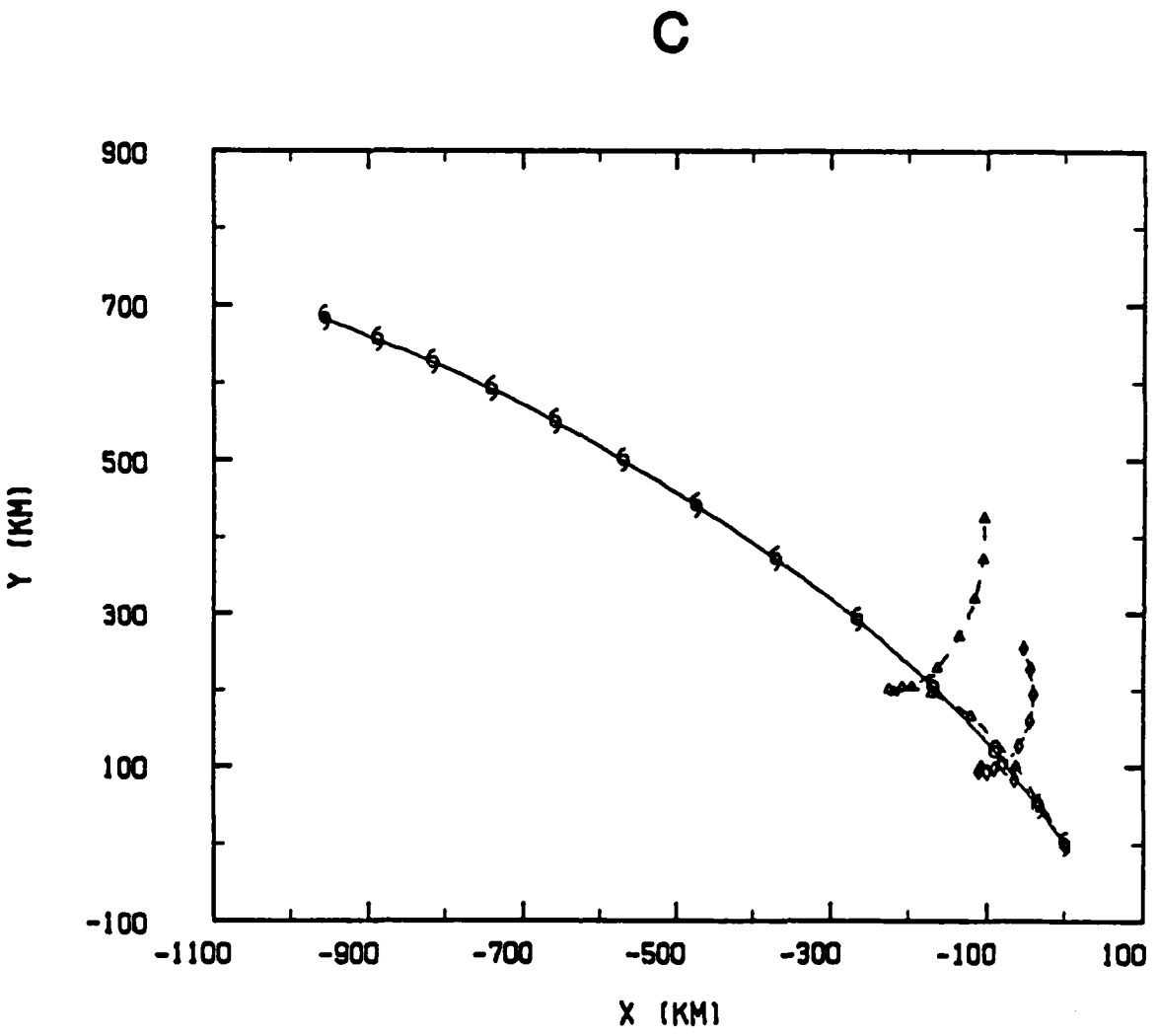

(c) The cyclonic perturbation vortex (S8)

Fig. 5-9. (Continued)

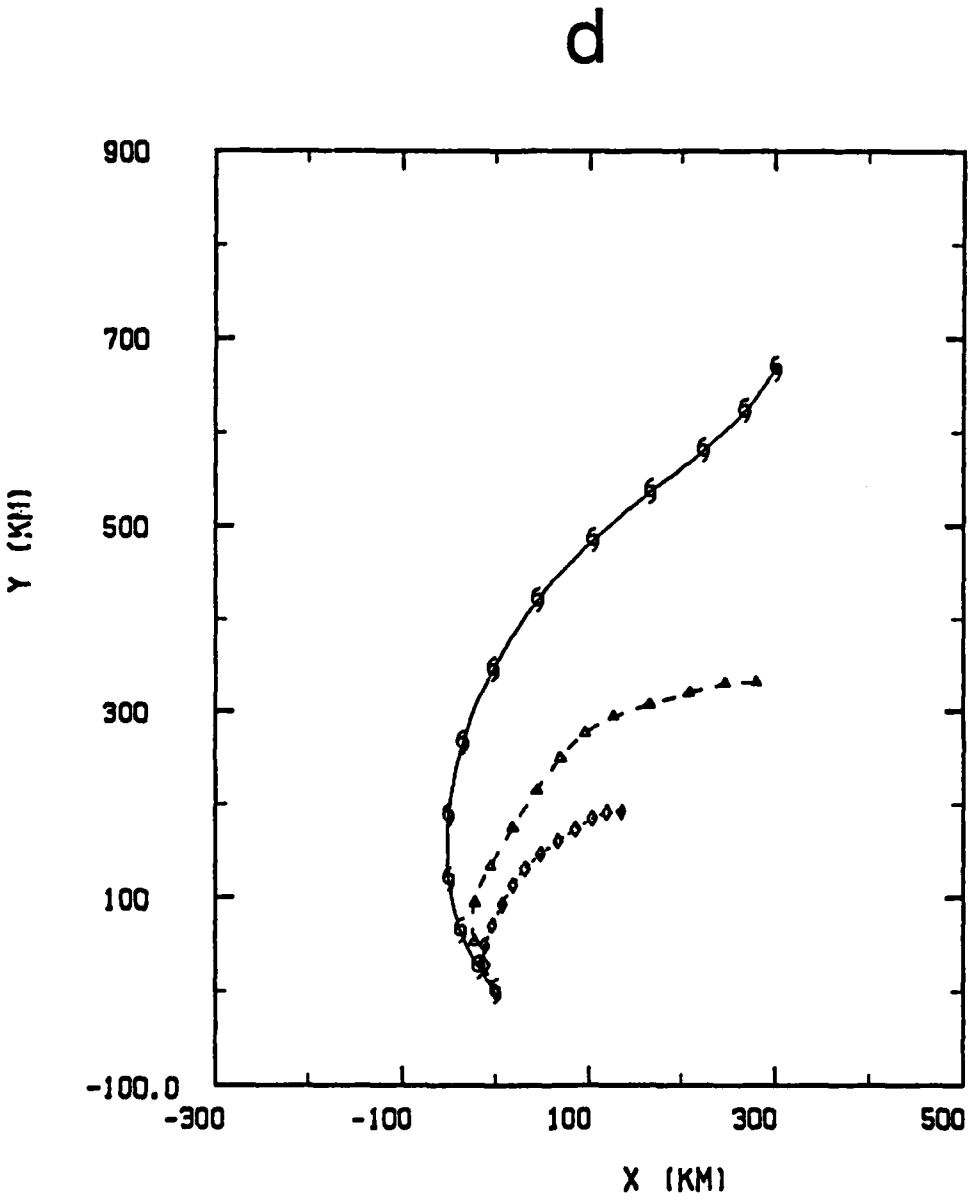

(d) The anticyclonic perturbation vortex (S9)

Fig. 5-9. (Continued)

during the first 12 h, then slows down, and reaches an apparent steady state around t = 72 h.

Another important characteristic of the tracks in the nonlinear-only experiments is the curving away from the reference track. The dynamical interpretation is that the gyre rotation due to the advection of asymmetric vorticity by the symmetric flow (Sec. IV-D) is not being compensated by gyre development. That is, the generation of the asymmetric gyres by Rossby dispersion is not part of the rotation process.

Linear effects alone will produce gyres with a ventilation flow oriented north-south as in the linear solutions (e.g., Fig. 5-1). In the full model, the gyre rotation due to nonlinear advection tends to be "adjusted" toward the linear solution when $\beta \neq 0$. When the β term is set to zero, nonlinear advection continues to rotate the gyres, which causes the vortex to continue on a curved path. For example, in the anticyclonic perturbation vortex case (Fig. 5-9d), the nonlinear-only tracks show greater anticyclonic turning compared to the full model track. When both the nonlinear and linear terms operate, the asymmetric gyre formation tends to counteract the nonlinearly induced rotation by forcing the gyres toward the north-south orientation of the linear solution. The tracks also indicate that the full-model track and nonlinear rotation are functions of both the initial asymmetric flow and the symmetric structure (e.g., the B1 vortex in Fig. 5-9a versus the B3 vortex in Fig. 5-9b).

An unusual track forecast occurred with the S8 vortex (Fig. 5-9c). During the first 72 h of the nonlinear-only integrations, the vortex moves as in the full model. However, the cyclone then loops and finally heads toward the north. To understand this behavior and to more fully

understand the persistent motion in the nonlinear-only integrations, the asymmetric flow is examined.

3. The Asymmetric Streamfunction

The initial asymmetric streamfunctions from the 24-h linear solution for the four vortices are shown in Fig. 5-10. The amplitudes of the gyres (refer to minimum contour) range from 0.7 to 2.5 x 10^5 m^2/sec and are proportional to: (i) the ventilation flow; (ii) the outer strength; and (iii) the length of the tracks in the nonlinear-only integrations starting from the 24-h linear solutions. The patterns for the B1-class (i.e., B1, S8 and S9) vortices are very similar, as each has a separation of approximately 400-500 km between the cyclone center and centers of the gyres at 24 h. The weak-large vortex (B3) produces a more intense and larger scale set of gyres and a greater ventilation flow. A common feature of all the asymmetric flow patterns at 24 h is a weak gradient around the center that is associated with the inner-core gyres (refer to the relative asymmetric flow discussed in Sec. IV-C).

The time evolution of the B1 vortex asymmetric streamfunction field illustrates how the nonlinear processes act to limit gyre development (Fig. 5-11). In the gradient wind relationship, the nonlinear term is approximated as a centrifugal force proportional to v^2/r. The centrifugal force resists deflections from a symmetrical state when the symmetric circulation is much stronger than the asymmetric circulation, which is typical of the tropical cyclone. Applying this approximation to this model, it is expected that the rate of nonlinear restoration toward a symmetrical state would be largest near the center where the centrifugal force is greatest and would become progressively smaller at large radii. The questions are how fast does this process operate and at what radii will the process be effective in

a

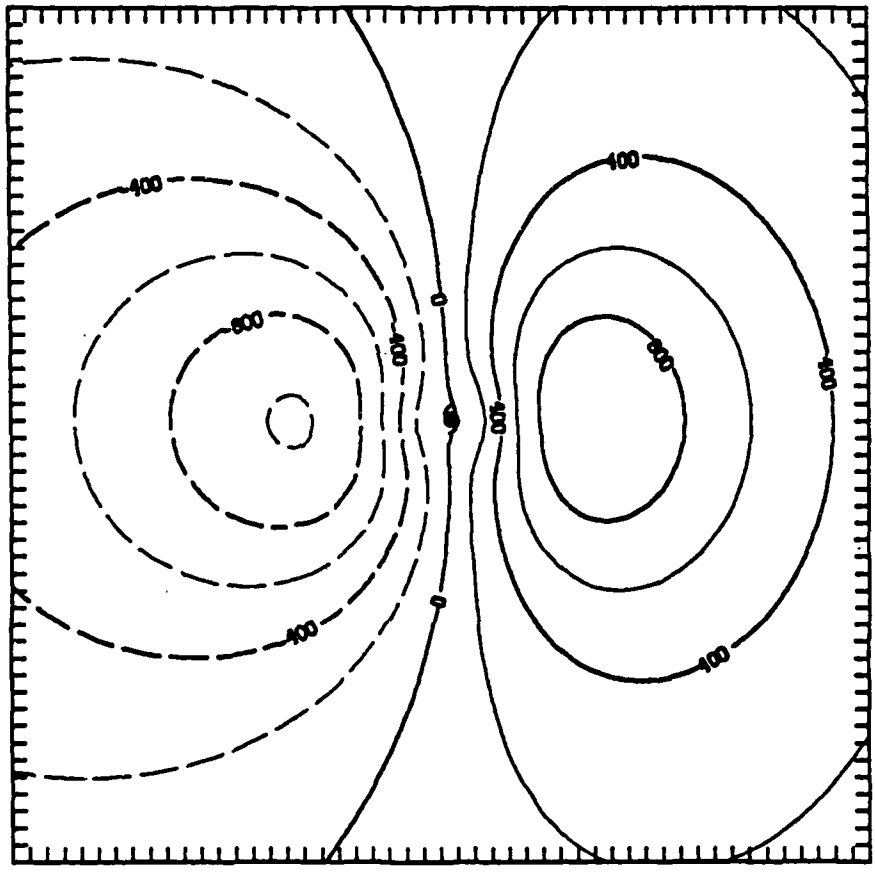

(a) B1 vortex
contour interval = 200 ($x10^3$) m^2/s
maximum contour = 1000 ($x10^3$) m^2/s

Fig. 5-10. Asymmetric streamfunction fields from the 24-h linear solutions that are used as initial conditions for the nonlinear-only integrations. The plotting domain is 2000x2000 km (Δx = 40 km, 51x51 grid points) with the grid points indicated by the tick marks on the border. This domain is used in all subsequent figures unless otherwise noted.

b

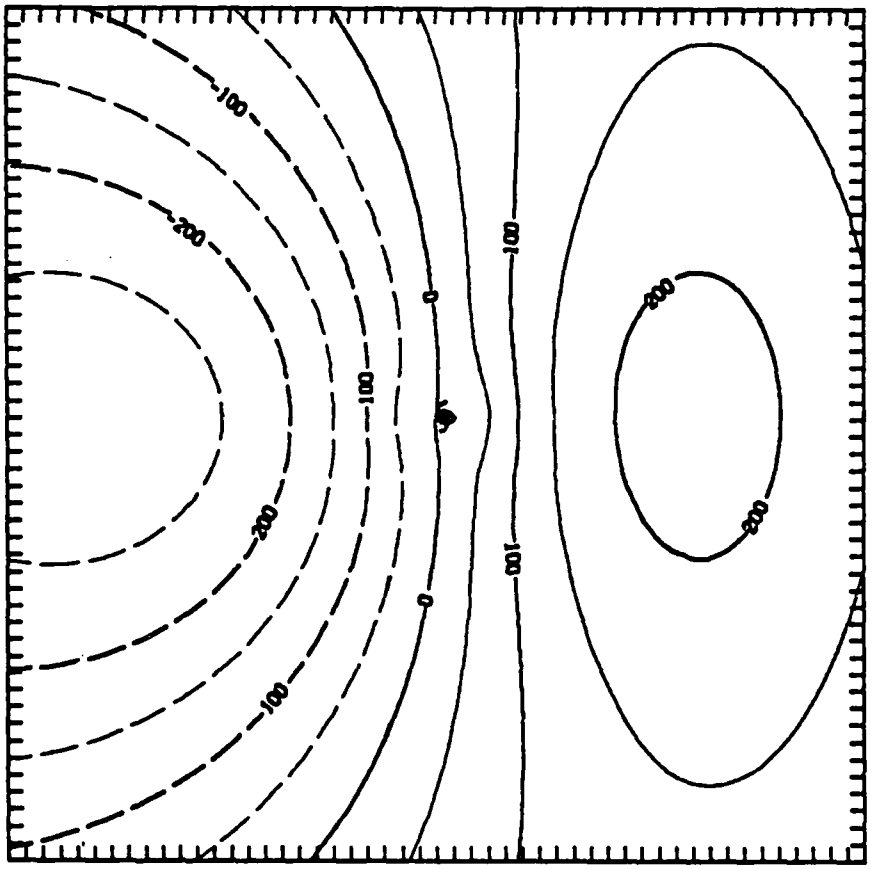

(b) B3 vortex
contour interval = 50 (x10⁴) m²/s
maximum contour = 250 (x10⁴) m²/s

Fig. 5-10. (Continued)

C

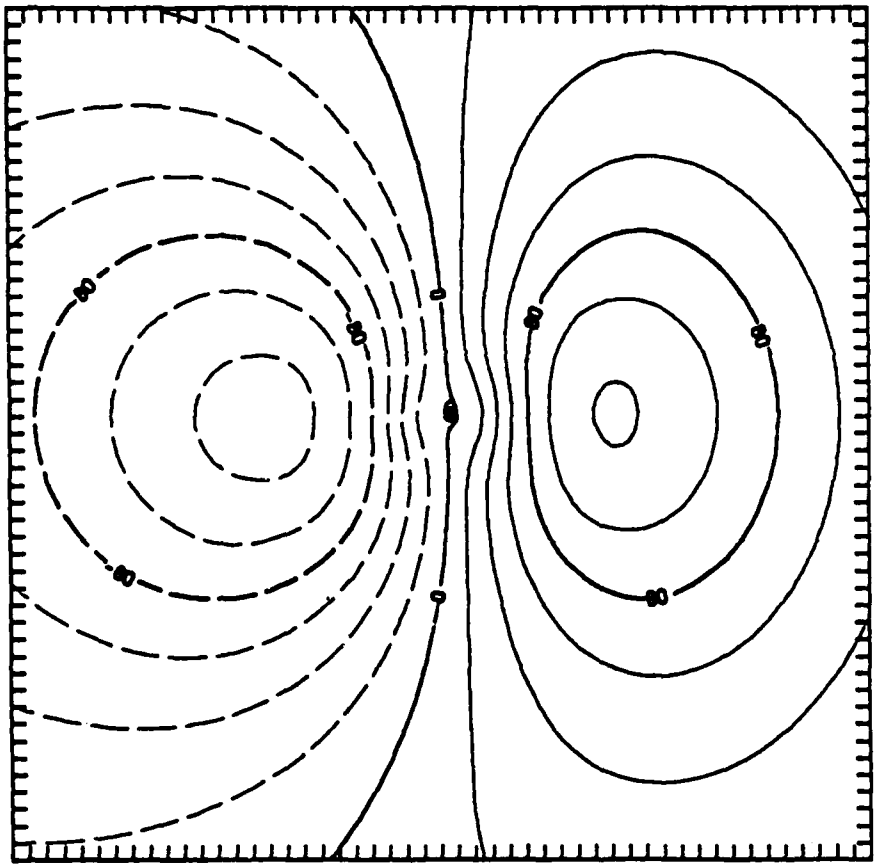

(c) S8 vortex
contour interval = 20 ($x10^4$) m^2/s
maximum contour = 120 ($x10^4$) m^2/s

Fig. 5-10. (Continued)

d

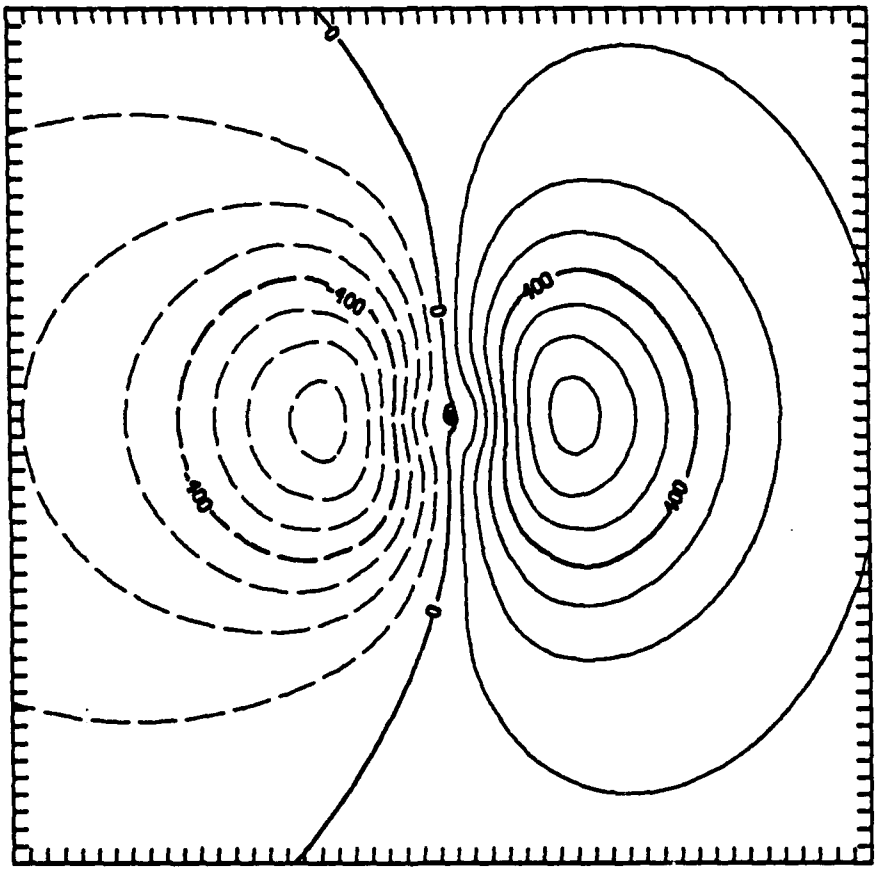

(d) S9 vortex
contour interval = 70 ($x10^3$) m^2/s
maximum contour = 700 ($x10^3$) m^2/s

Fig. 5-10. (Continued)

a

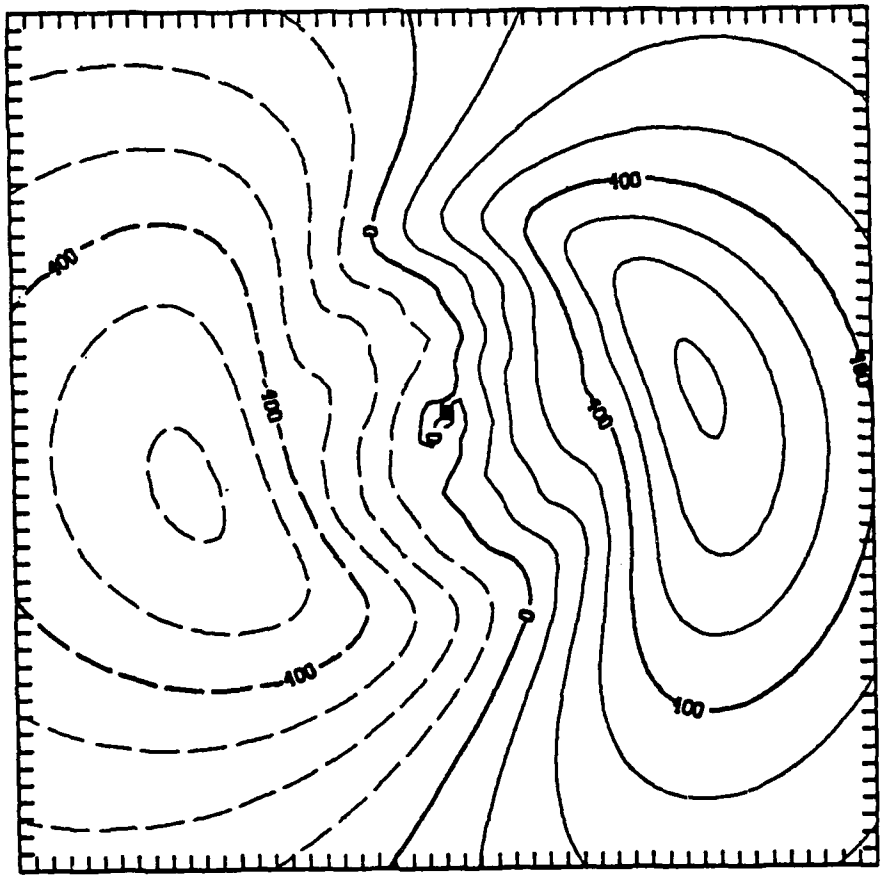

(a) t = 36 h
contour interval = 100 ($x10^3$) m^2/s
minimum contour = -600 ($x10^3$) m^2/s
maximum contour = 700 ($x10^3$) m^2/s

Fig. 5-11. Asymmetric streamfunction fields for the nonlinear-only integration initialized with the 24-h linear solution for the B1 vortex in Fig. 5-10a.

b

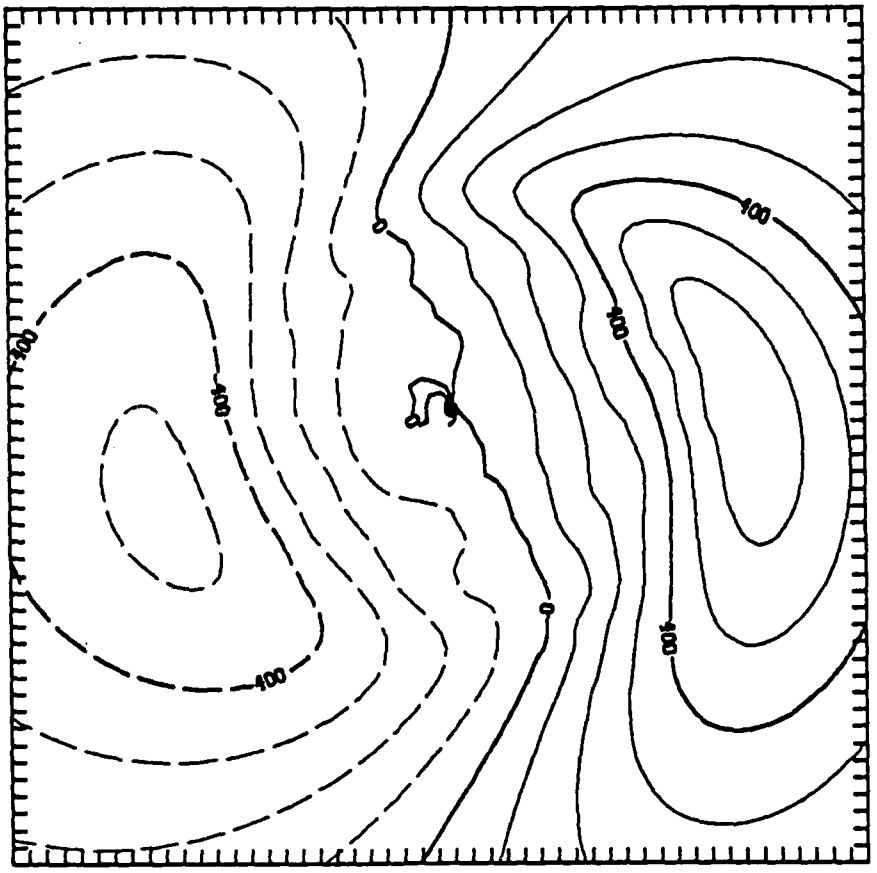

(b) t = 72 h
contour interval = 100 ($\times 10^3$) m^2/s
minimum contour = -500 ($\times 10^3$) m^2/s
maximum contour = 600 ($\times 10^3$) m^2/s

Fig. 5-11. (Continued)

C

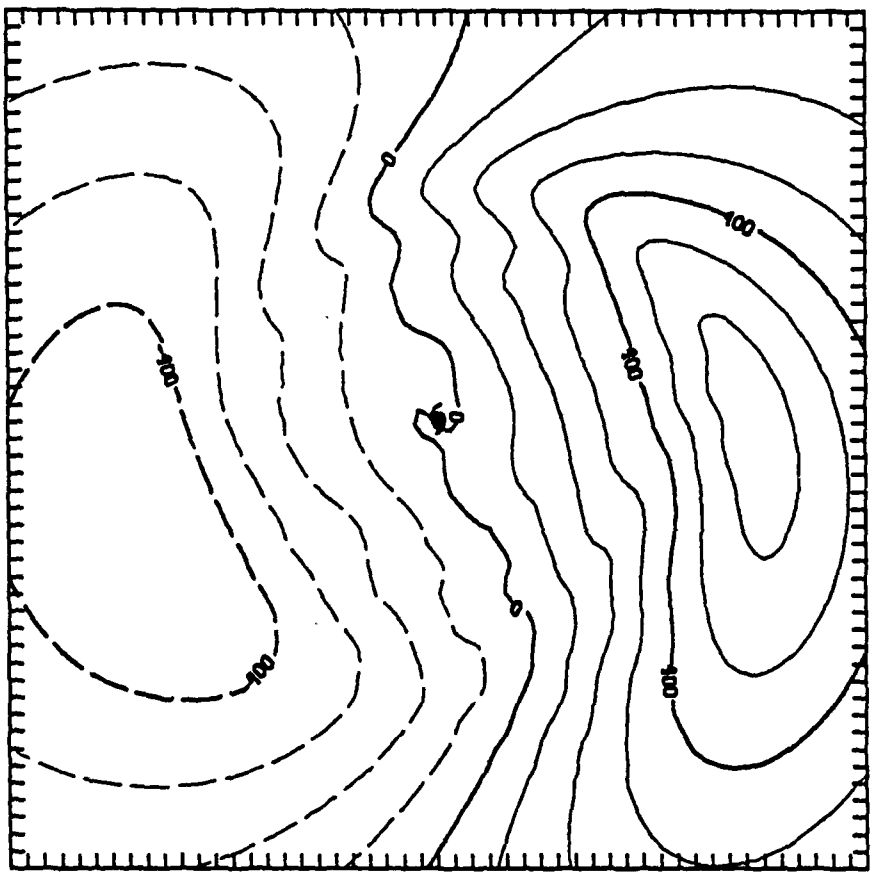

(c) t = 108 h
contour interval = 100 ($x10^3$) m^2/s
minimum contour = -400 ($x10^3$) m^2s
maximum contour = 600 ($x10^3$) m^2/s

Fig. 5-11. (Continued)

d

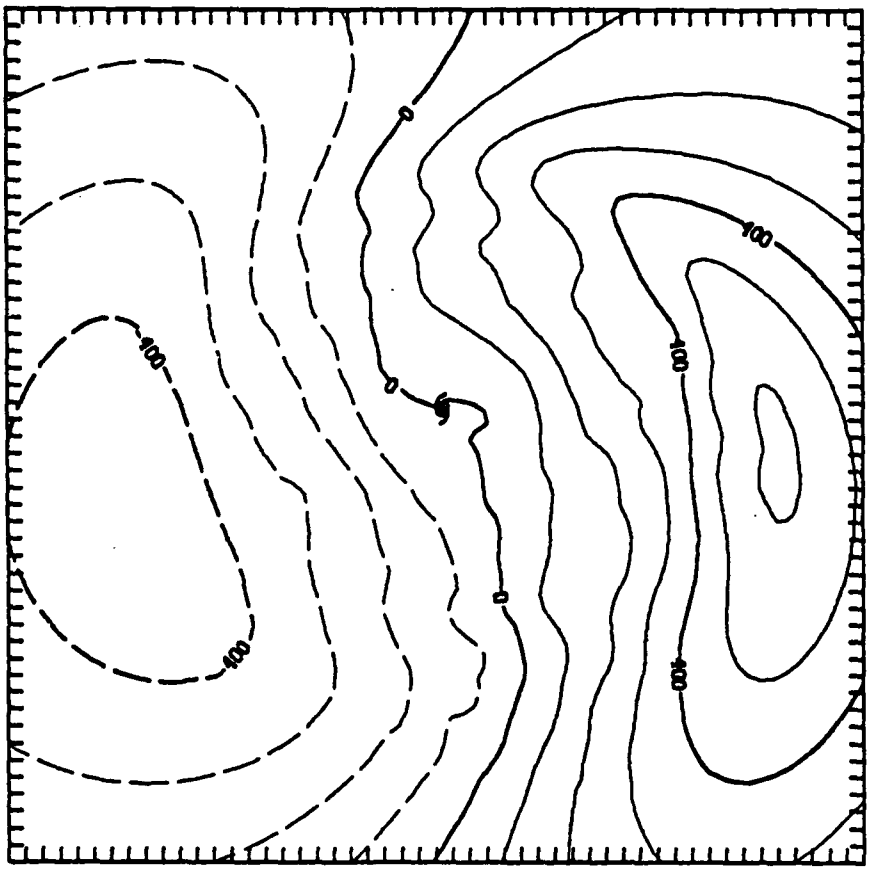

(d) t = 144 h
contour interval = 100 ($\times 10^3$) m^2/s
minimum contour = -400 ($\times 10^3$) m^2/s
maximum contour = 600 ($\times 10^3$) m^2/s

Fig. 5-11. (Continued)

diminishing/offsetting the asymmetric flow in the initial conditions.

The amplitudes of the asymmetric gyres varies smoothly and slowly throughout the 144-h integrations (Fig. 5-11). Thus, examining the field every 36 h will be sufficient to depict major features. At t = 36 h (Fig. 5-11a), the gyres have rotated to orient the ventilation flow toward the north-northwest rather than toward the north as in the initial conditions (Fig. 5-10a). Notice that the streamfunction between the gyres is distorted. This distortion spreads radially outward during the remainder of the integration as the gyres are also spread apart (Fig. 5-11 b and c). Even though the gradient between the gyres has been considerably weakened, a broader-scale ventilation flow through the center remains at t = 144 h (Fig. 5-11d). Although no linear forcing is included in the model, the nonlinear effects do not completely eliminate the asymmetric flow that was present in the initial conditions, presumably because the nonlinear effects become progressively weaker in the vicinity of the gyre centers.

Another way to depict the weakening of the asymmetric flow between the gyres is to examine the relative asymmetric flow (motion vector is subtracted from the asymmetric flow). The relative asymmetric flow (Fig. 5-12) tends to zero when the motion is equal to asymmetric flow, in which case a balance exists between the vortex motion and the ventilation flow forcing. This large-scale balance does not apply at the center where the flow is zero and the relative asymmetric flow contains a small-scale, inner-core gyre. The fields in Fig. 5-12 have been smoothed using a non-complex Shuman (1957) smoother-desmoother so as to emphasize the larger-scale aspects of the flow. Unfortunately, this smoothing also reduces the inner-core gyres. The spreading of the region in which the asymmetric

a

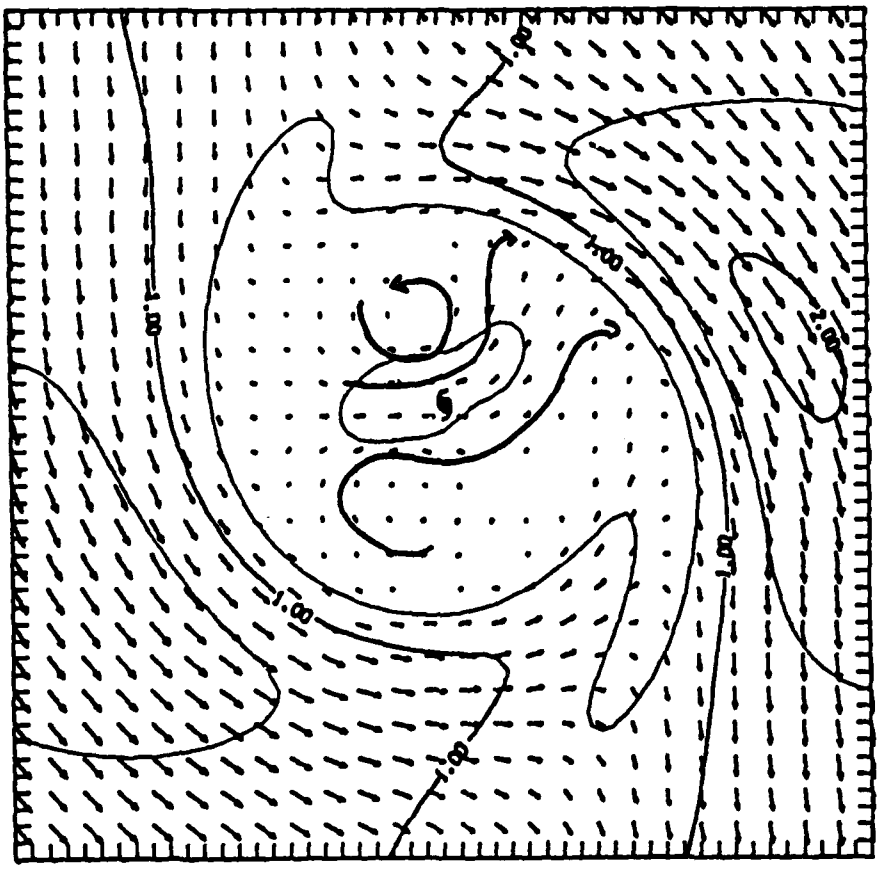

(a) t = 36 h; maximum vector is 2.1 m/s

Fig. 5-12. Relative asymmetric flow for the nonlinear-only integration initialized with the 24-h linear solution for the B1 vortex.

b

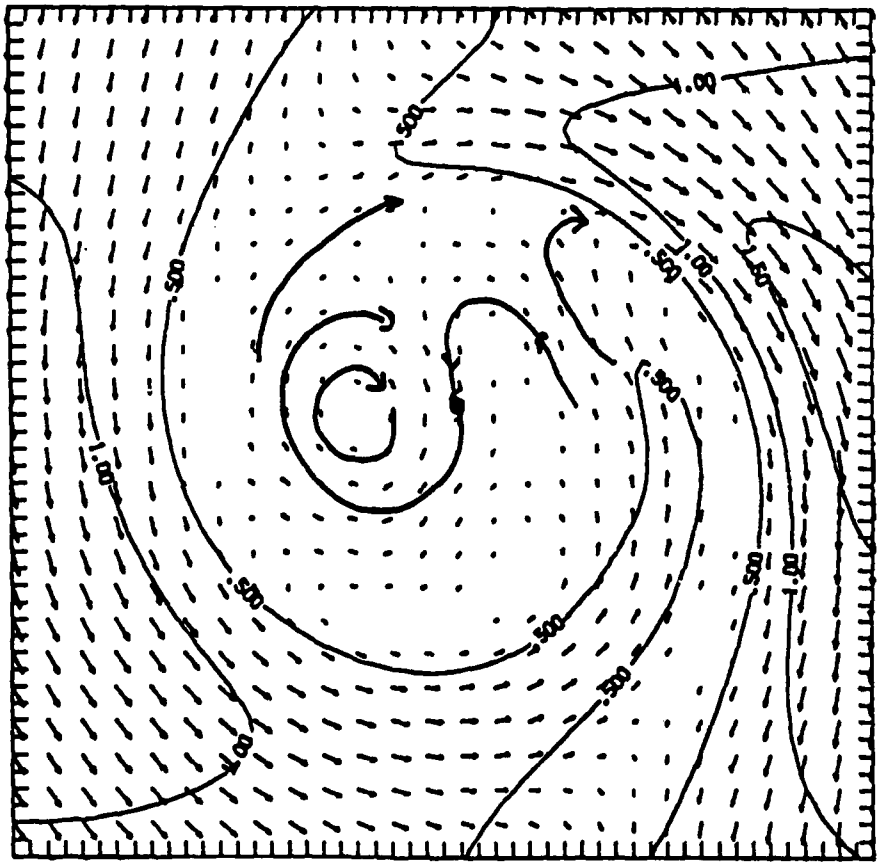

(b) t = 72 h; maximum vector is 1.6 m/s

Fig. 5-12. (Continued)

C

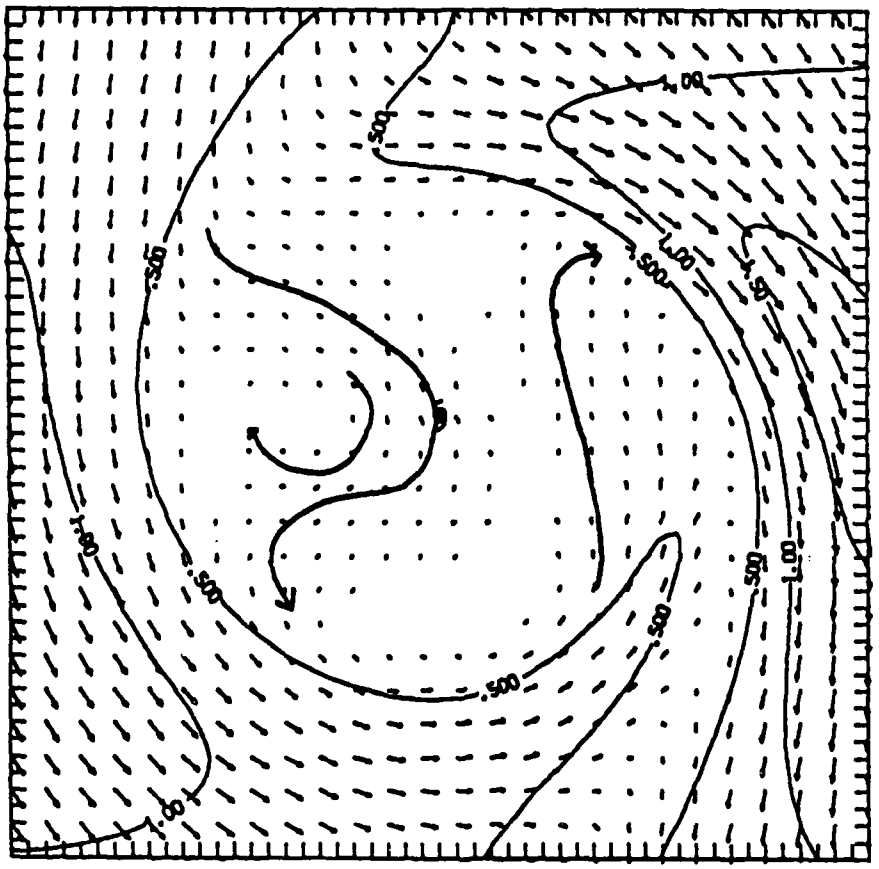

(c) t = 108 h; maximum vector is 1.6 m/s

Fig. 5-12. (Continued)

d

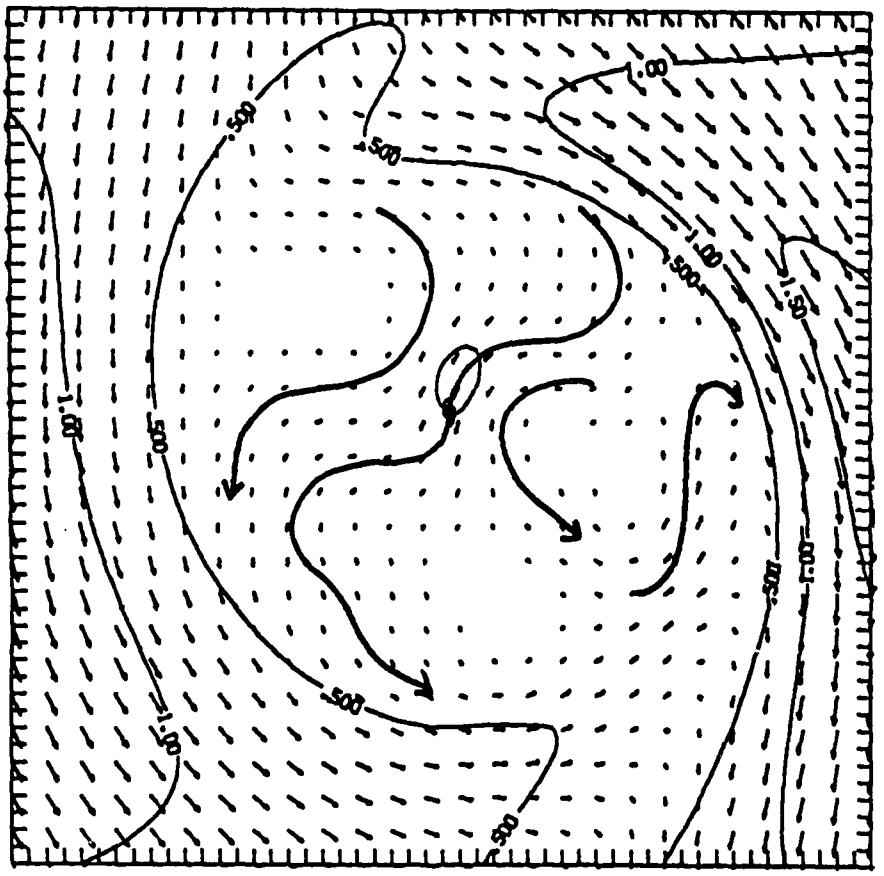

(d) t = 144 h; maximum vector is 1.7 m/s

Fig. 5-12. (Continued)

e

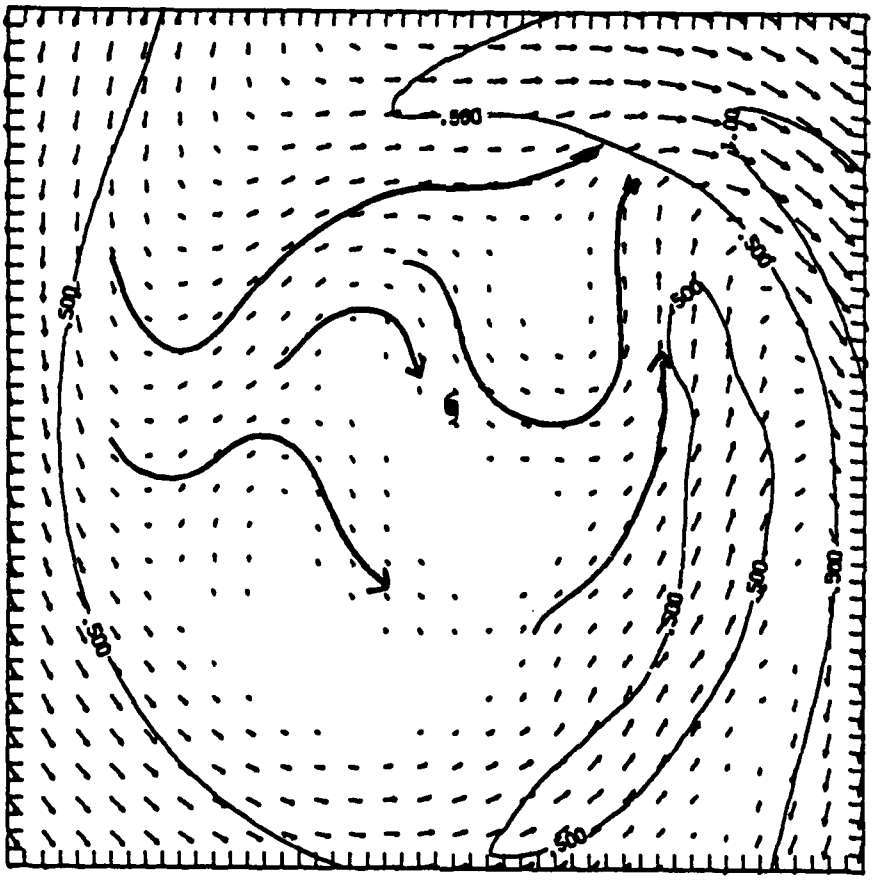

(e) t = 288 h; maximum vector is 1.2 m/s

Fig. 5-12. (Continued)

flow matches the motion is over a progressively larger area until about 72-108 h. Because the processes reduce the asymmetric flow predominately in the inner regions, the much larger scale, "background" asymmetric gyres are not removed and the ventilation flow between the gyres continues to advect the storm. This experiment demonstrates a different type of dynamics occurs within the "balanced region" and cutside this regions.

A final observation on the asymmetric flow is the nearly constant orientation of the gyre centers with respect to the vortex center (t > 72 h). The entire system (both the symmetric and asymmetric components) appears to move in unison and to act as single entity. The nonlinear processes are the obvious key to this cohesiveness.

4. Very Long Integrations

The persistence of the background ventilation as suggested in the relative asymmetric flow is confirmed by continuing the integrations to 288 h from the 24-h linear solutions. These tracks are plotted relative to the corresponding 144-h full model track (Fig. 5-13). First, observe that the turning motions as noted in Fig. 5-9 continue throughout the integration, except for the S8 cyclonic perturbation vortex (Fig. 5-13c). These turning motions relative to the full model track are due to strictly nonlinear effects. As shown earlier, linear forcing would continuously establish a ventilation flow with a north-south orientation and therefore acts to stabilize the turning due to advective processes. Thus, the motion "stability" and the balancing of nonlinear and linear effects will depend on both the vortex structure and the base-state absolute vorticity gradient (linear forcing).

The cyclonic symmetric perturbation vortex (S8) is apparently an example of an "unstable" structure in the sense that the nonlinear processes induce such a large

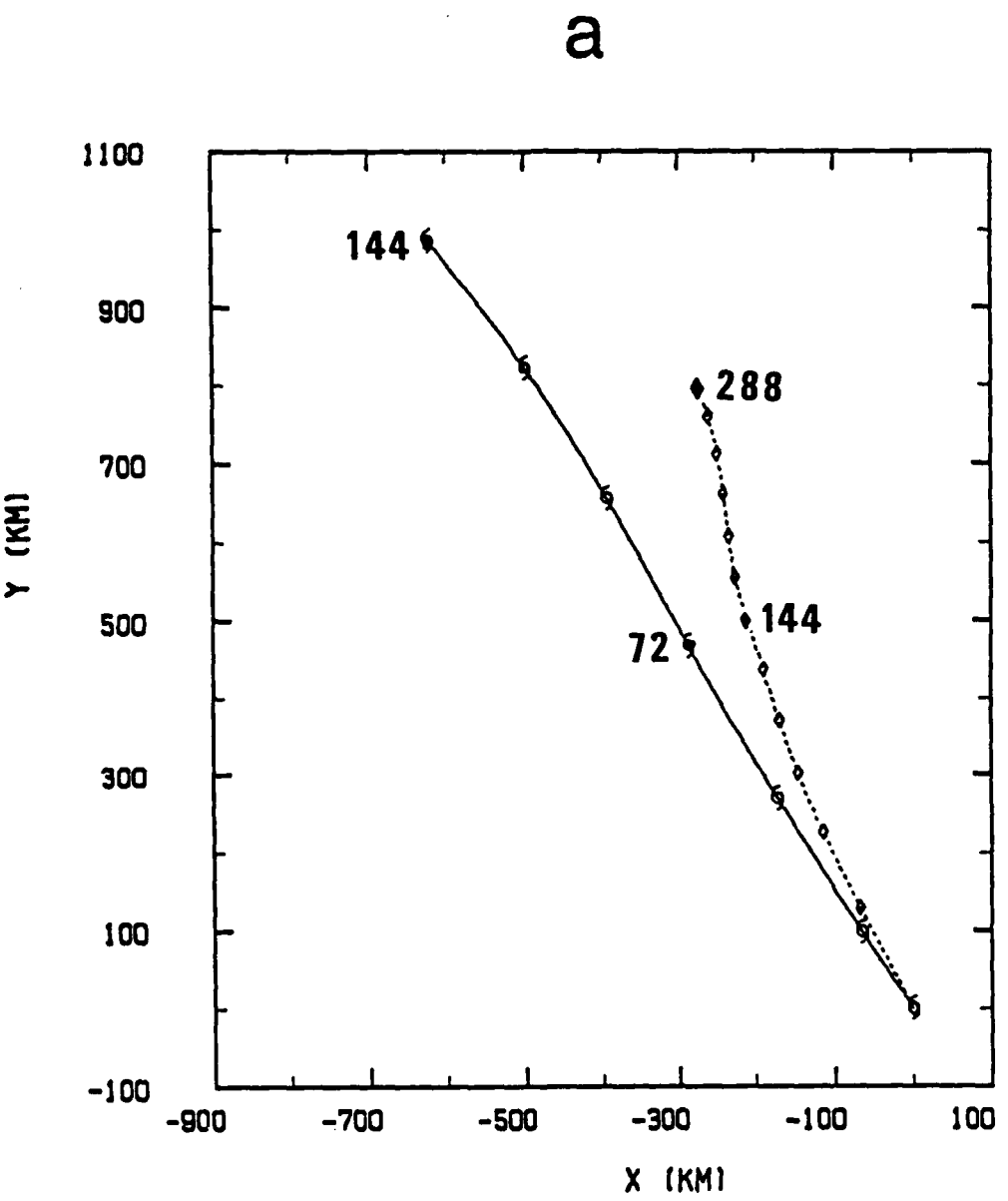

Fig. 5-13. Track from the 288-h nonlinear-only integrations (dashed) compared to the 144-h full model integration (solid) for (a) the basic vortex; (b) weak-large vortex; (c) cyclonic perturbation vortex; and (d) the anticyclonic perturbation vortex. Symbols on the tracks indicate the position every 24 h and the 144 (72) and 288 (144) positions on the nonlinear-only (full model) are highlighted.

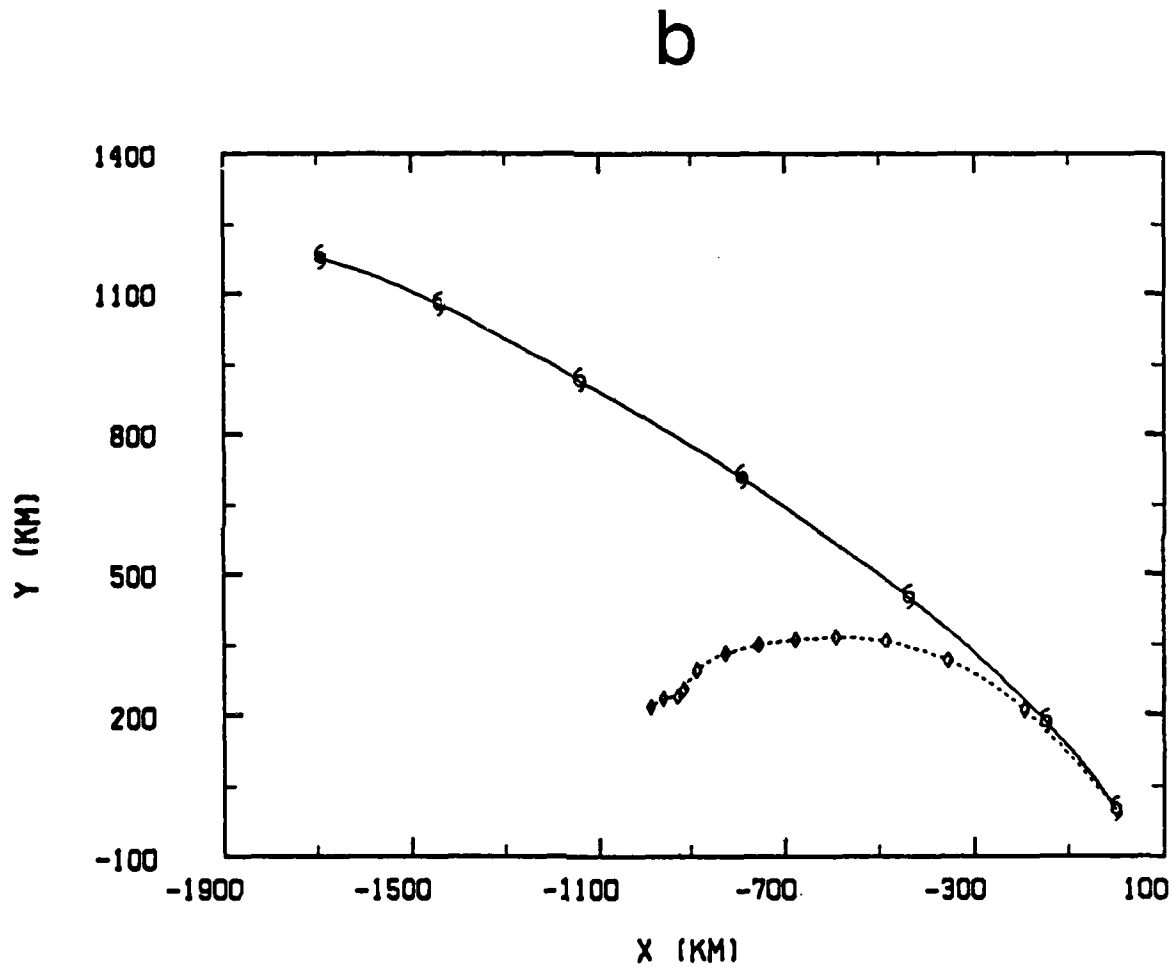

Fig. 5-13. (Continued)

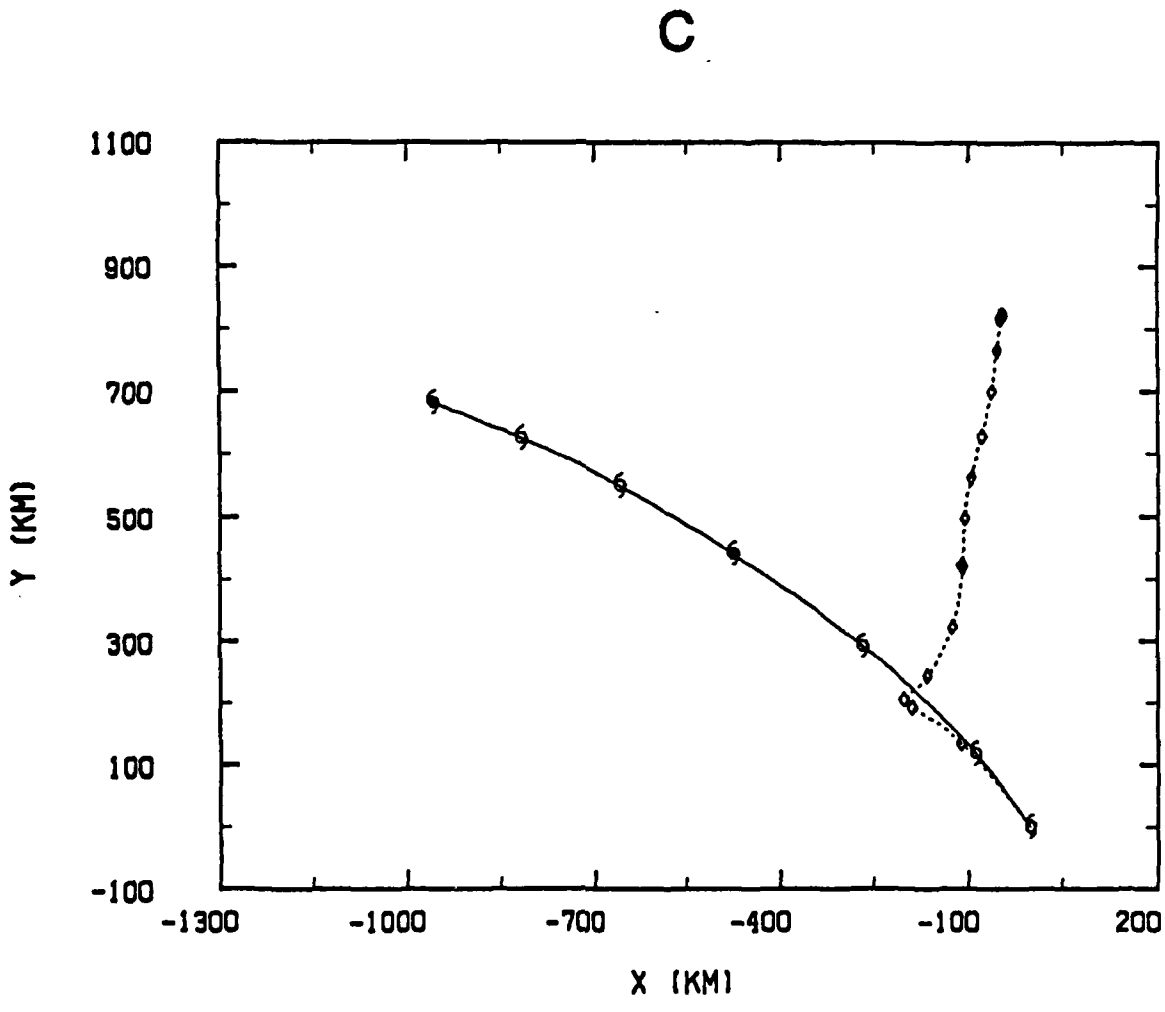

Fig. 5-13. (Continued)

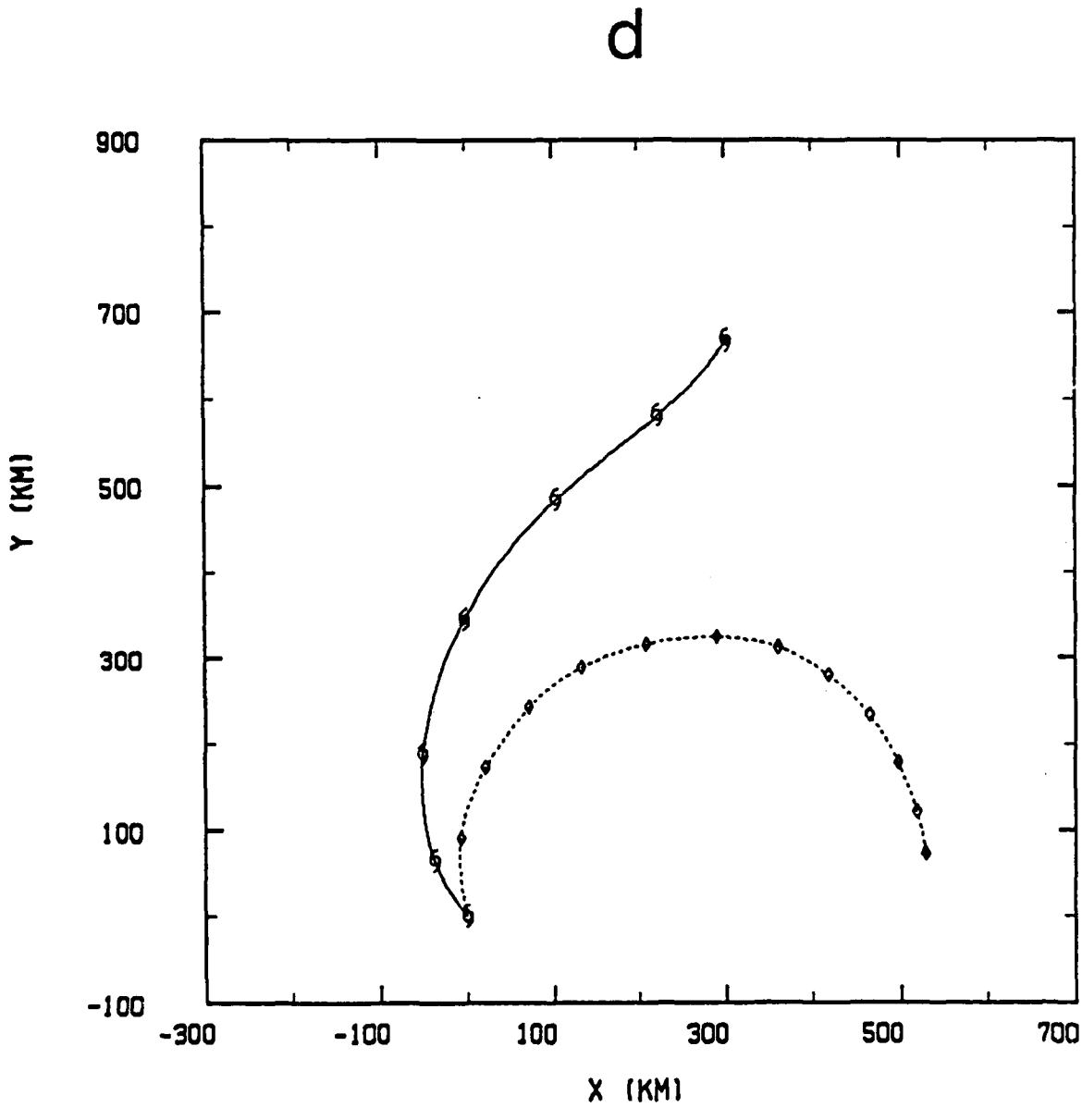

Fig. 5-13. (Continued)

turning motion that the storm actually "loops." After the loop at t = 72 h, the cyclone moves in a straight line. The symmetric perturbation that induces the turning motion causes a complete cyclonic rotation of the asymmetric gyres. At t = 36 h (Fig. 5-14a), a smaller-scale (r < 600 km) set of gyres begins to break away from the larger-scale gyres. In the middle of the loop at t = 72 h (Fig. 5-14b), these smaller-scale gyres have lost amplitude and have rotated 120° from the t = 36 h position, which orients the ventilation flow toward the southeast. The larger scale gyres appear to be disconnected from the ventilation flow. By t = 144 h, the smaller gyres have rotated back to their initial orientation and seem to have "hooked up" with the large-scale gyres to form a more stable arrangement. The ventilation flow orientation is consistent with the northward track beyond t = 144 h.

5. Tangential Wind Profiles

The azimuthal-mean tangential wind profiles (not shown) remained essential invariant during the nonlinear-only integration. This is another indication that the linear processes are responsible for the changes in the symmetric structure, particularly in the outer regions. The slight changes in the tangential wind profiles are also consistent with the consistent turning motions and speed (except for S8) after the initial acceleration when the advection process begins to operate.

6. Summary

A series of dynamical sensitivity tests have been made in which only the nonlinear term is included during the integration. The initial conditions are derived from a previous linear solution at 12 h and at 24 h. The amplitude of the asymmetric gyres in the linear solution grows linearly in time, so that the ventilation flow in a 24-h solution is twice as strong as that in a 12-h solution. The

a

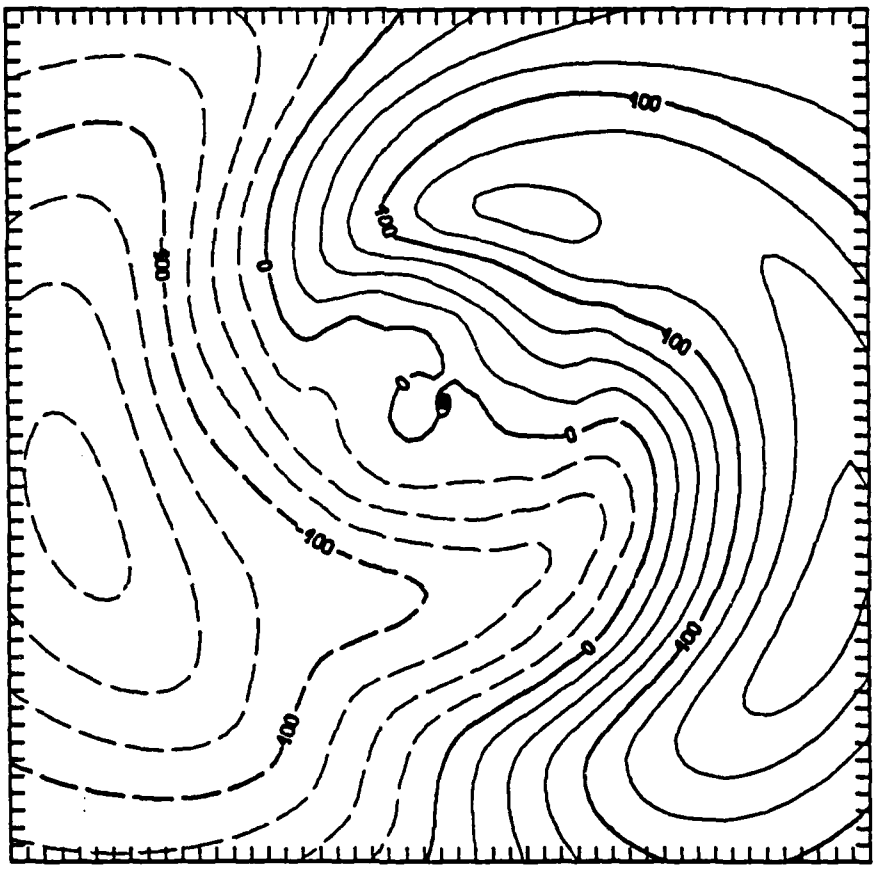

(a) t = 36 h
contour interval = 100 ($x10^3$) m^2/s
minimum contour = -700 ($x10^3$) m^2/s
maximum contour = 700 ($x10^3$) m^2/s

Fig. 5-14. Asymmetric streamfunction for the nonlinear-only integration initialized with the 24-h linear solution for the cyclonic perturbation (S8) vortex (in Fig. 5-10c).

b

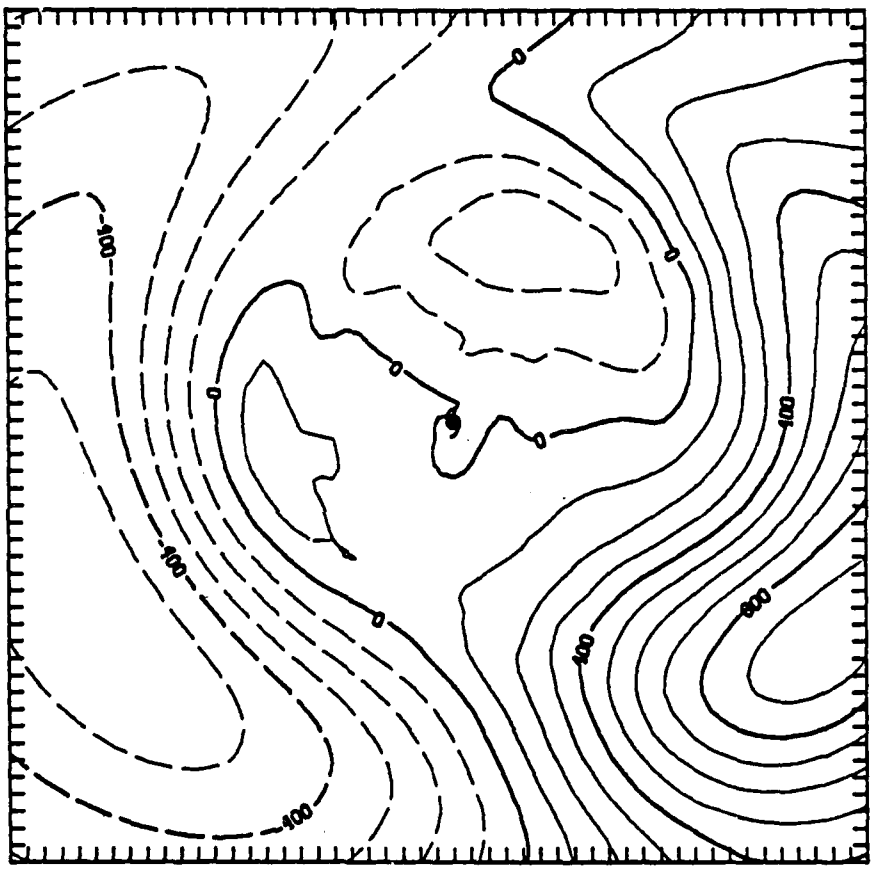

(b) t = 72 h
contour interval = 100 ($\times 10^3$) m^2/s
minimum contour = -500 ($\times 10^3$) m^2/s
maximum contour = 900 ($\times 10^3$) m^2/s

Fig. 5-14. (Continued)

C

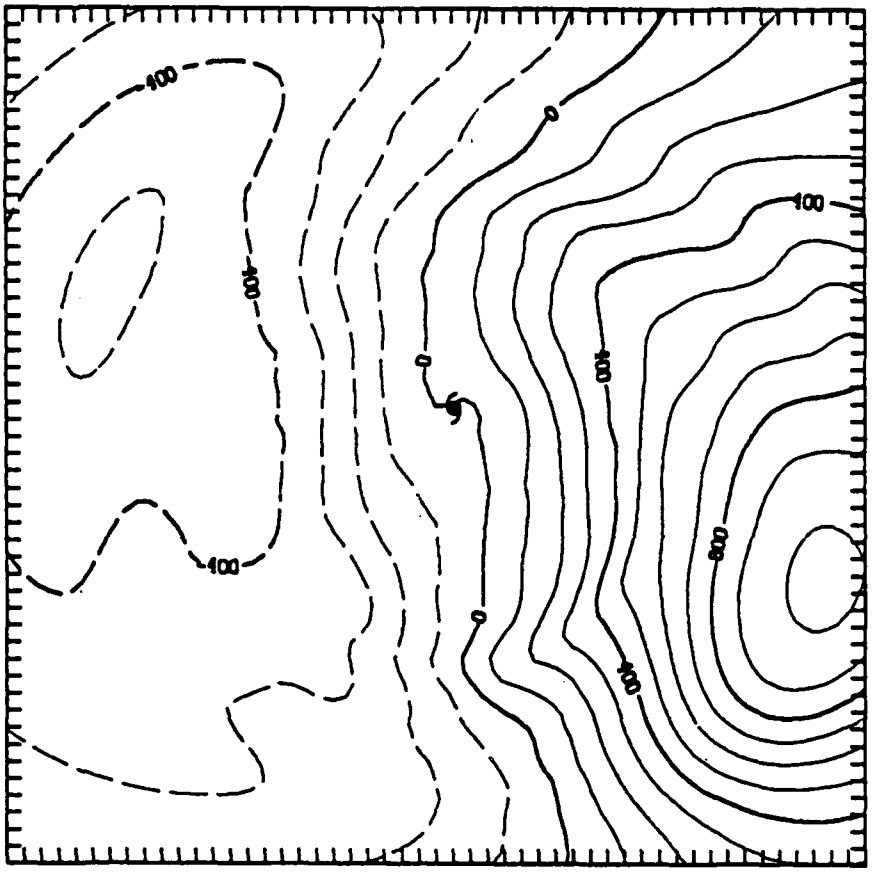

(c) t = 144 h
contour interval = 100 ($\times 10^3$) m^2/s
minimum contour = -500 ($\times 10^3$) m^2/s
maximum contour = 1000 ($\times 10^3$) m^2/s

Fig. 5-14. (Continued)

purpose of these experiments is to understand how the nonlinear processes separately modify the linearly-induced asymmetric gyres.

The length of the track in the nonlinear-only integrations is proportional to the "spinup" time of linear solution used in the initial conditions. That is, the forecast track using the 24-h linear solution is twice as long as from the 12-h solution.

The vortex motion is very persistent even during a 12-day integration that includes only the nonlinear terms. The asymmetric streamfunction shows that the large-scale asymmetric gyres are diminished by the nonlinear term within a region of about 600 km during the first 72 h, but then the gyre flow seems to come into balance within this region. This weakening of the gyres proceeds outward from the inner regions where the largest nonlinear terms exist. Although the nonlinear processes act to weaken the motion-forcing asymmetric flow, a "residual" very large-scale advecting flow still remains without any linear forcing during the integration. It is reasoned that this residual or background flow moves the entire system while the nonlinear processes bind the symmetric and asymmetric circulations together as a single entity.

For all four vortices, there are significant track deviations from the full model integrations that do include the linear terms omitted in these integrations. In general, the deviations are in the same sense and with larger amplitudes than the long-term turning motions associated with vortex structure changes in the full model solutions. Based on the streamfunction tendency analysis in Sec. IV-E, the linear processes continuously generate the asymmetric flow. It is this forcing that tends to resist or "balance" the nonlinearly-induced rotation of the asymmetric gyres. When these two asymmetrical flow processes are in

equilibrium in the full model, the motion reaches a steady state. These nonlinear-only experiments confirm the basic features of this balancing process. In the cyclonic perturbation vortex, the cyclonic gyre rotation effect is initially so strong that the absence of linear compensation causes the gyres to complete a cyclonic loop before stabilizing into a northward orientation (versus the expected westward track). The asymmetric flow within 500 km of the center (region of larger nonlinear effects) in this looping case appears to disconnect from the large gyres during the rotation period.

In conclusion, the nonlinear-only model integrations underscore the balancing aspect of the advection-linear dispersion relationship. Rossby dispersion forces an asymmetric flow with a fixed (north-south) orientation, whereas the nonlinear effects tend to rotate the gyres depending on the strength of the symmetric vortex flow in the r = 300 - 800 km critical annulus. It is the interplay between the rotation effect and the stable Rossby dispersion effect that controls the orientation and strength of the beta drift. It will be demonstrated by very-long integrations of the full model in Chapter VI that the linear processes eventually force a single beta drift motion vector regardless of the initial vortex structure.

C. MODIFYING THE SYMMETRIC/ASYMMETRIC NONLINEAR INTERACTIONS

The nonlinear-only integrations in the preceding section demonstrate that nonlinear advection is responsible for the motion of the center and acts to "bind" the symmetric and asymmetric circulations together in such a way that they translate together. This implies that the essential dynamics of the vortex motion are contained in the nonlinear processes. In particular, a change in the vortex structure modifies the motion through different advective effects. In this section, the nature of the nonlinear motion dynamics is

addressed by integrating a revised model that allows the terms responsible for the interaction between the symmetric and asymmetric circulations to be modified. This type of experimentation may be considered to be another form of dynamical sensitivity analysis. As with more traditional sensitivity tests involving the thermodynamic processes, the purpose is to determine the relative significance of one process in relation to other effects. It should also be noted that such sensitivity experiments implicitly assume that the interaction of the modified processes with the rest of the model processes will not substantially affect the interpretations .

1. The Symmetric/Asymmetric Form of the Model Equation

In the model streamfunction tendency analysis (Sec. IV-E), the total vortex system is divided into a symmetric and asymmetric components (see development in Appendix C). The final form of the revised model equation is

$$\frac{\partial \psi_t}{\partial t} = a(r) \cdot H^{-1}(-J(\psi_a, \nabla^2 \psi_s)) + b(r) \cdot H^{-1}(-J(\psi_s, \nabla^2 \psi_a)) + H^{-1}(\beta v) \quad , \qquad (5.2)$$

ASVA AAVS

where H^{-1} is the inverse operator of $H(f) = \nabla^2 f$, ASVA is the advection of symmetric vorticity by the asymmetric flow and AAVS is the advection of asymmetric vorticity by the symmetric flow.

As suggested by the tendency analysis in Chapter IV, the motion of the center occurs by two advection processes. Advection of the inner-core asymmetries by the symmetric flow (AAVS) yields a small-scale, motion-type tendency pattern that moves the inner core. In contrast, advection of the symmetric vortex by the asymmetric flow (ASVA) produces a larger-scale motion tendency that moves the larger-scale component of the symmetric circulation ($r < 600$ km).

In the following experiments, the terms representing the interaction of the symmetric and asymmetric circulations have been given multiplied by additional factors that vary with radius

$$a(r) = \begin{cases} f_{a_1} & r < r_1a \\ f_{a_1} + \left[\dfrac{f_{a_2} - f_{a_1}}{r_2a - r_1a} \right] \cdot (r - r_1a) & r_1a \le r \le r_2a \\ f_{a_2} & r > r_2a \end{cases}$$

(5.3)

and

$$b(r) = \begin{cases} f_{b_1} & r < r_1b \\ f_{b_1} + \left[\dfrac{f_{b_2} - f_{b_1}}{r_2b - r_1b} \right] \cdot (r - r_1b) & r_1b \le r \le r_2b \\ f_{b_2} & r > r_2b \end{cases}$$

(5.4)

These "radial weighting" factors permit experiments in which the magnitudes of the nonlinear interaction terms may be arbitrarily adjusted to make different contributions to the total tendency as a function of radius.

2. Experiment Design

Two classes of modifications are considered. In the first, the nonlinear interaction terms (ASVA and AAVS) are separately set to zero to illustrate the relative contribution of each advection process to the motion. In the second set, the interaction terms are set to zero outside successively larger radii to illustrate where (in which annulus) the interaction processes are critical.

As shown by the experiment parameters given in Table 5-3, the linear term is held fixed in all the runs. The first character in the Exp. No. refers to type of experiment and to the initial conditions with "A" and "B" signifying that the original analytical profile was used and "C" and

"D" mean that the model was initialized with a previous 72-h full-model solution. These 72-h solutions contain well-developed, quasi-steady state asymmetric flows and are used to illustrate how the model results depend on the existence of an asymmetric circulation.

TABLE 5-3. Parameters of the nonlinear symmetric/asymmetric interaction dynamical sensitivity experiments. ASVA refers to advection of symmetric vorticity by the asymmetric flow and AAVS is the advection of asymmetric vorticity by the symmetric flow. T_m is the time of the initial conditions where 0 refers to the analytical symmetric vortex and 72 means the initial conditions came from a 72-h solution of the full model. The parameters (f_{a_1}, f_{a_2}, etc.) are defined by (5.3) and (5.4).

Exp. No.	f_{a_1}	f_{a_2}	f_{b_1}	f_{b_2}	r_{a_1}	r_{a_2}	r_{b_1}	r_{b_2}	T_m	Comments
A1	0	0	1	1	300	400	300	400	0	ASVA=0
B1	1	1	0	0	---	---	---	---	0	AAVS=0
A2	1	0	0	0	400	500	---	---	0	Modify ASVA
B2	0	0	1	0	---	---	400	500	0	Modify AAVS
B3	0	0	1	0	---	---	200	300	0	Modify AAVS
C1	0	0	1	1	300	400	300	400	72	ASVA=0
D1	1	1	0	0	---	---	---	---	72	AAVS=0
C2	1	0	0	0	400	500	---	---	72	Modify ASVA
D2	0	0	1	0	---	---	400	500	72	Modify AAVS
D3	0	0	1	0	---	---	200	300	72	Modify AAVS

There is no direct physical analog for setting one of the interaction terms to zero everywhere. However, the experiments in which the tendency modification is made outside the inner regions could be relevant to a situation in which the environmental flow (nonlinear effects) are changing.

3. Setting ASVA to Zero

In the inner-core, the advection of asymmetric vorticity by the symmetric flow (AAVS) produces a small-scale, motion-type tendency. This inner-core process is the only nonlinear motion process if ASVA is eliminated. ASVA corresponds to the motion of the larger scale vortex (symmetric circulation) by the ventilation flow (asymmetric circulation).

When the model is begun with the initial symmetric vortices and ASVA is completely eliminated (Exp. A1), the storm moves in nearly the same direction, but with reduced speed (Fig. 5-15). In general, the motion contribution due to the inner-core asymmetric gyres is roughly 1/3 compared to the track from the full-model integration. This percentage does vary with structure, particularly in the symmetric perturbation experiments (S8 and S9 in Fig. 5-15c and d). The track is approximately 60% of the full-model forecast in the cyclonic-perturbation vortex, but only 15% for the anticyclonic-perturbation vortex.

There is a slight variation in the tracks when the model is initialized with a well-developed asymmetric flow (Exp. C2, not shown). However, the basic result of reduced motion along the full model track is very similar to that in Exp. A1. Thus, the motion due to the inner-core process is not a function of an initial large-scale asymmetric flow.

4. Setting AAVS to Zero

When the advection of asymmetric vorticity by the symmetric flow (AAVS) is eliminated throughout the domain (Exp. B1), the only motion process is the large-scale advection by the linearly-generated ventilation flow. It might be expected (e.g., as in Holland, 1983) that the center would move almost straight north as the large-scale gyre rotation due to the advection of asymmetric vorticity by the symmetric flow beyond the inner core would be eliminated. As shown in Fig. 5-16a the center actually moves toward the southeast with a cyclonic hooking motion for the B1 vortex. The anticipated northward track only occurred for the weak intensity, but large B3 vortex (Fig. 5-16b). Furthermore, the unusual motion did not depend on the initial asymmetric flow (Exp. D1, not shown).

Examination of the asymmetric streamfunction in Fig. 5-17 shows that the asymmetric flow for the B1-class

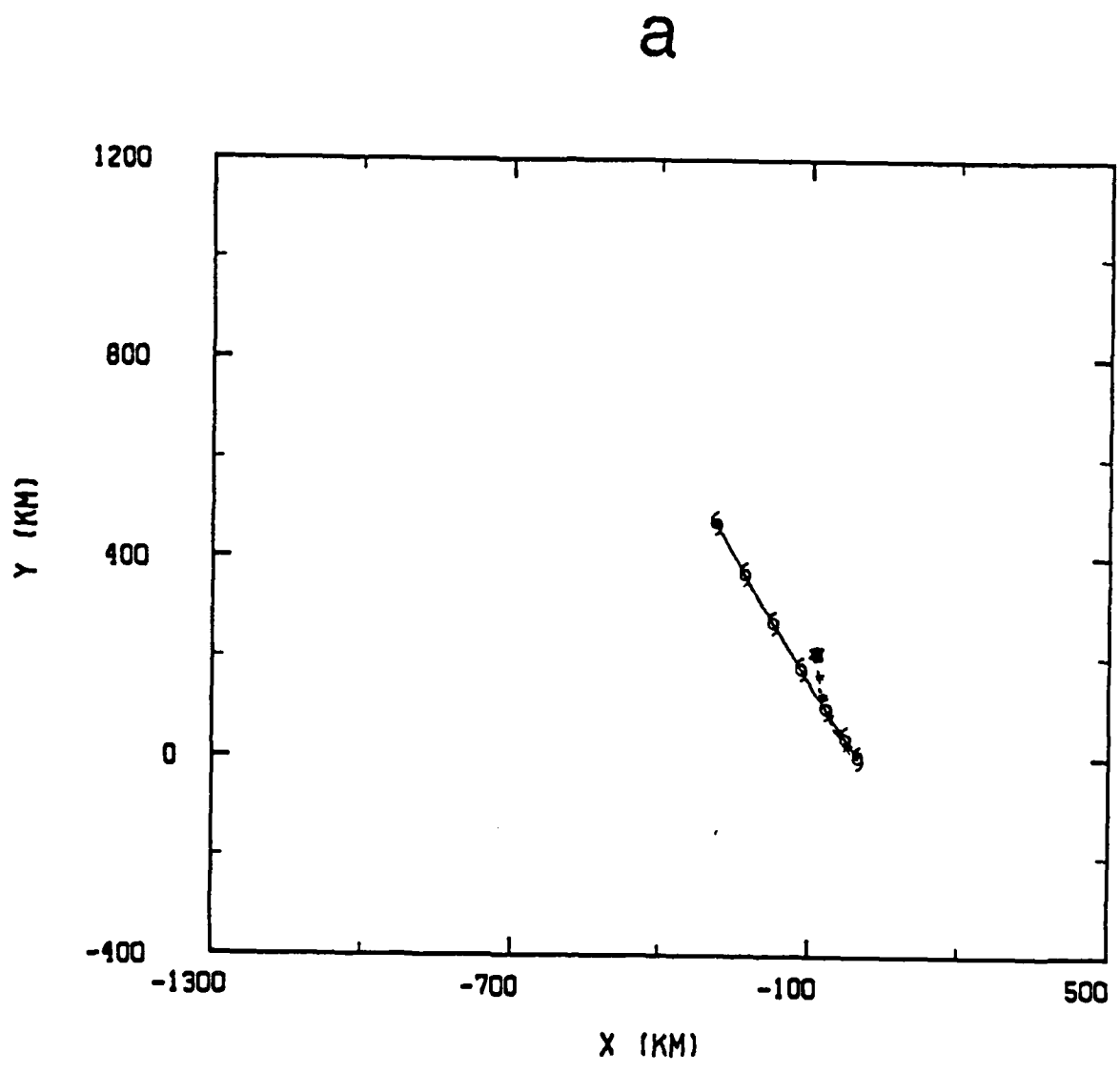

Fig. 5-15. Track to 72 h using the full model equation (solid, hurricane symbol every 12 h) and using the revised model equation in which the advection of symmetric vorticity by the asymmetric flow (ASVA) has been eliminated (short-dashed). Panel (a) is for the basic vortex (B1), (b) is for the weak-large vortex (B3), (c) is for the cyclonic-perturbation vortex (S8) and (d) is for the anticyclonic-perturbation vortex (S9).

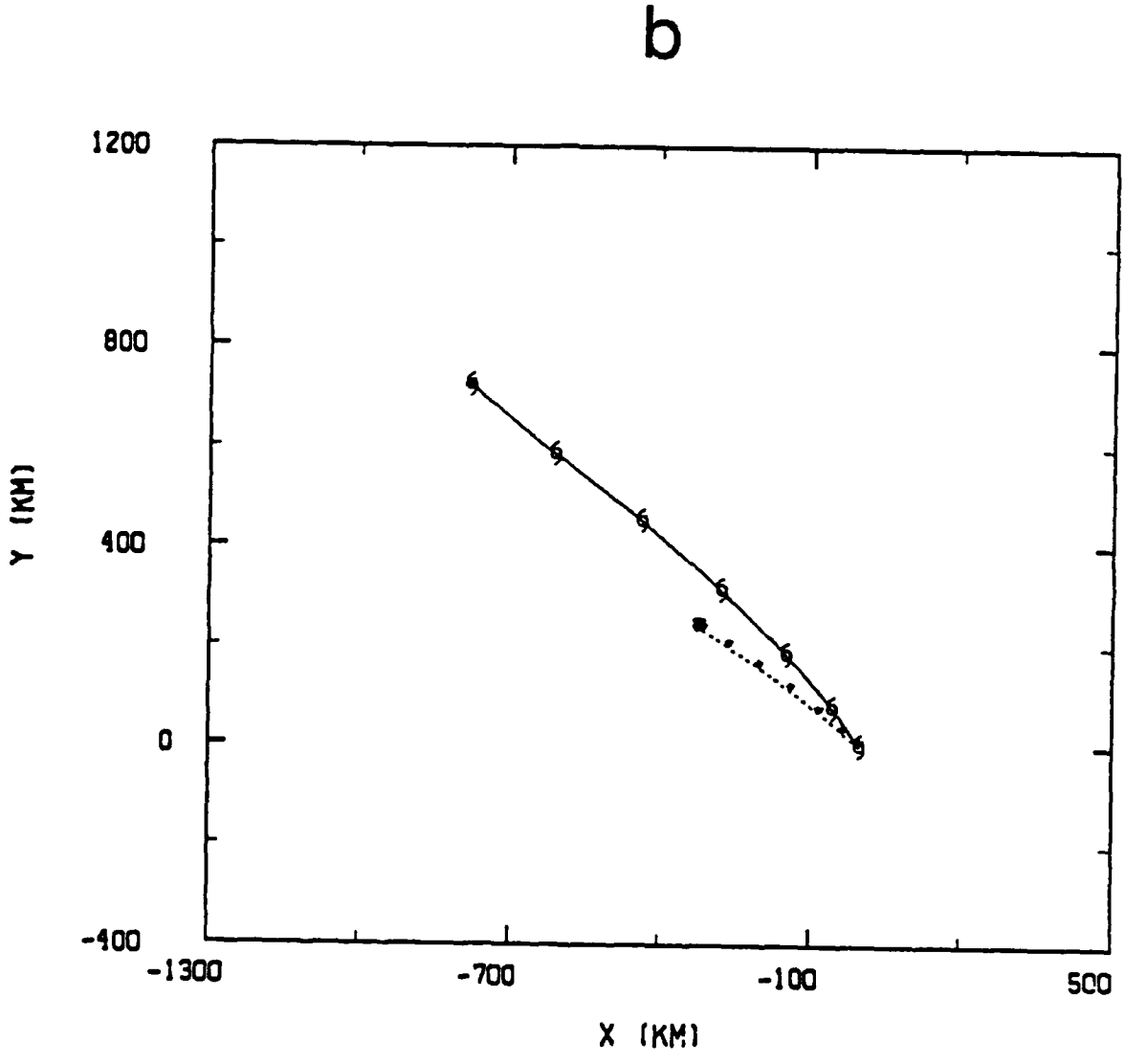

Fig. 5-15. (Continued)

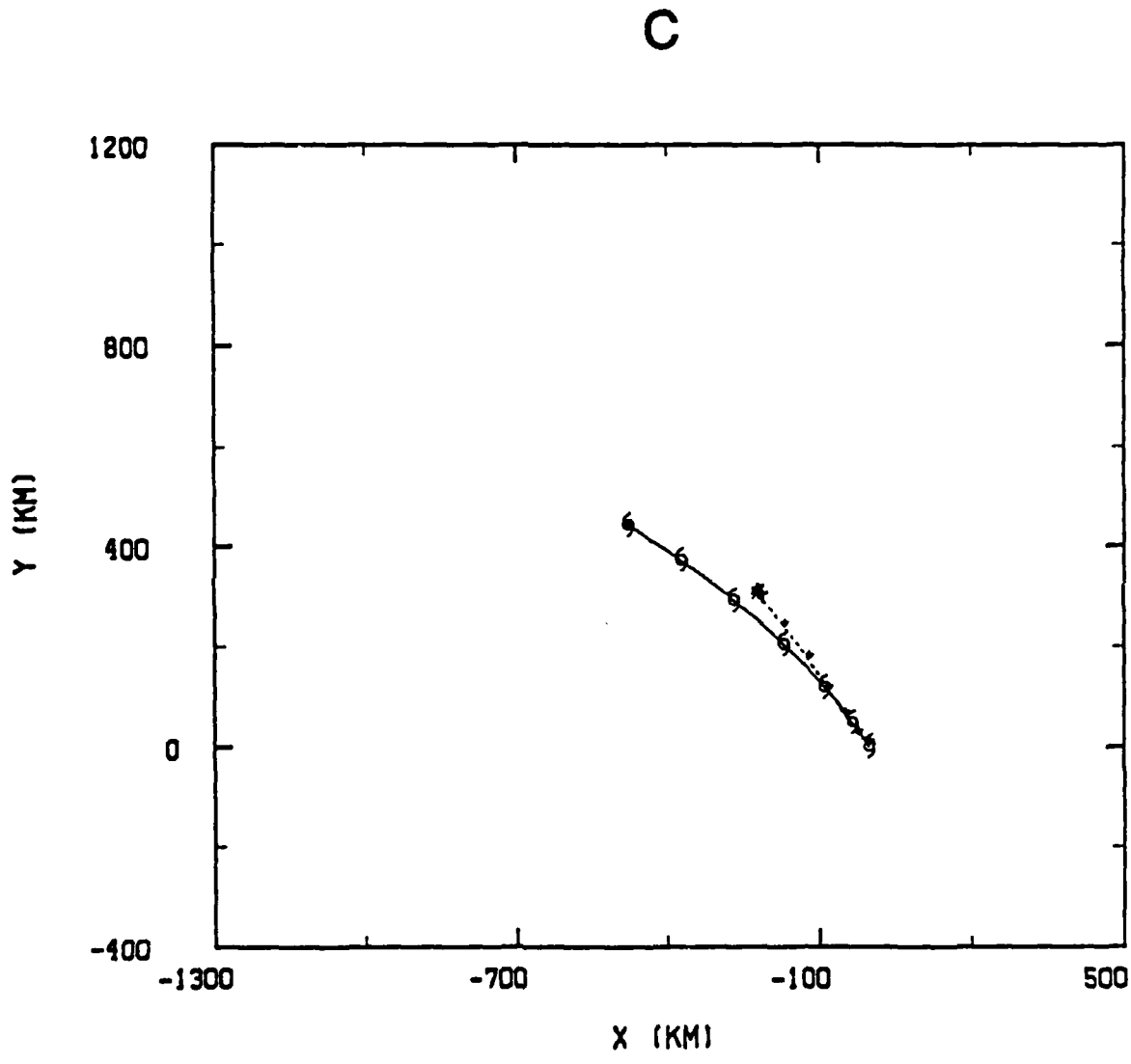

Fig. 5-15. (Continued)

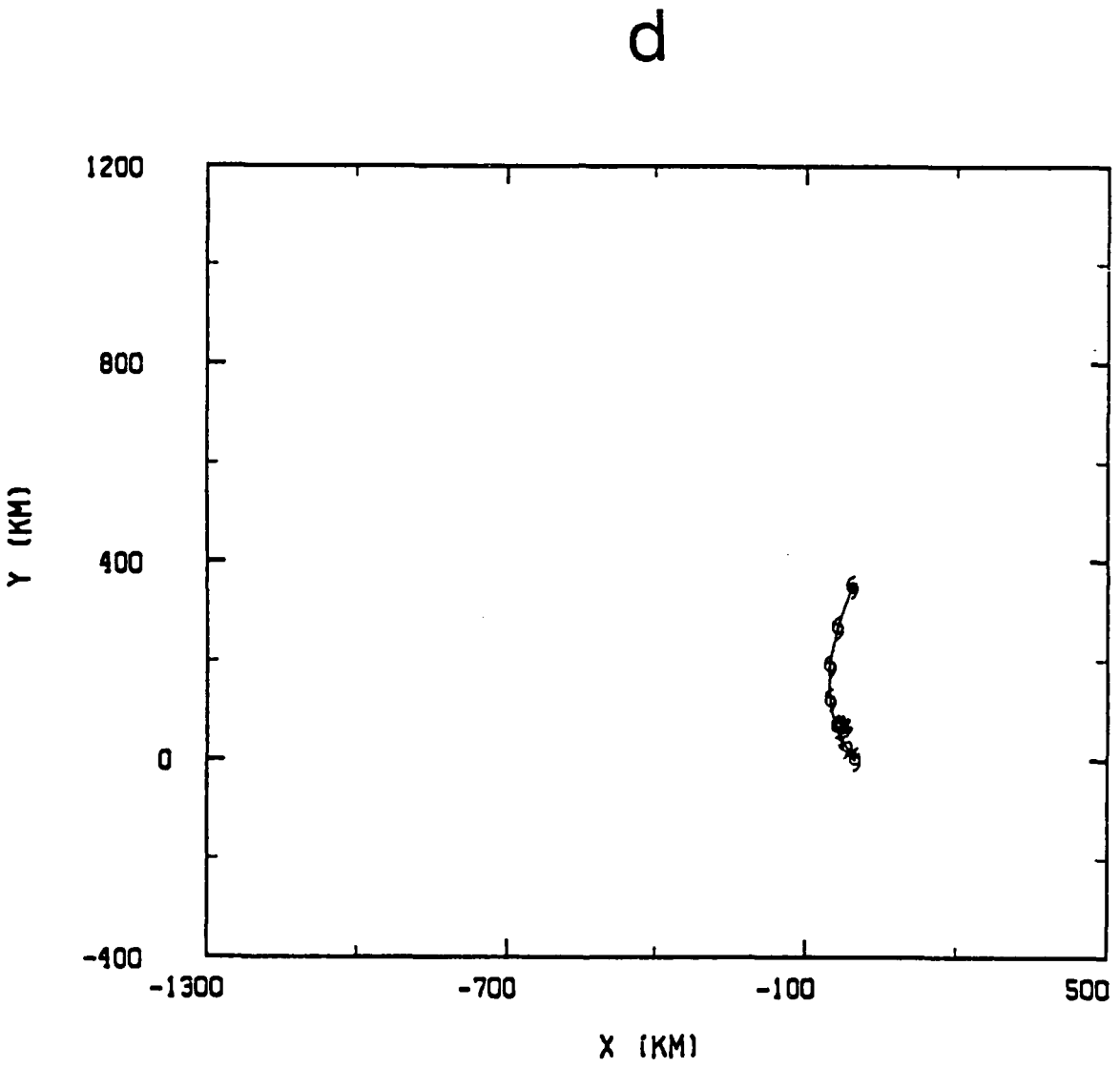

Fig. 5-15. (Continued)

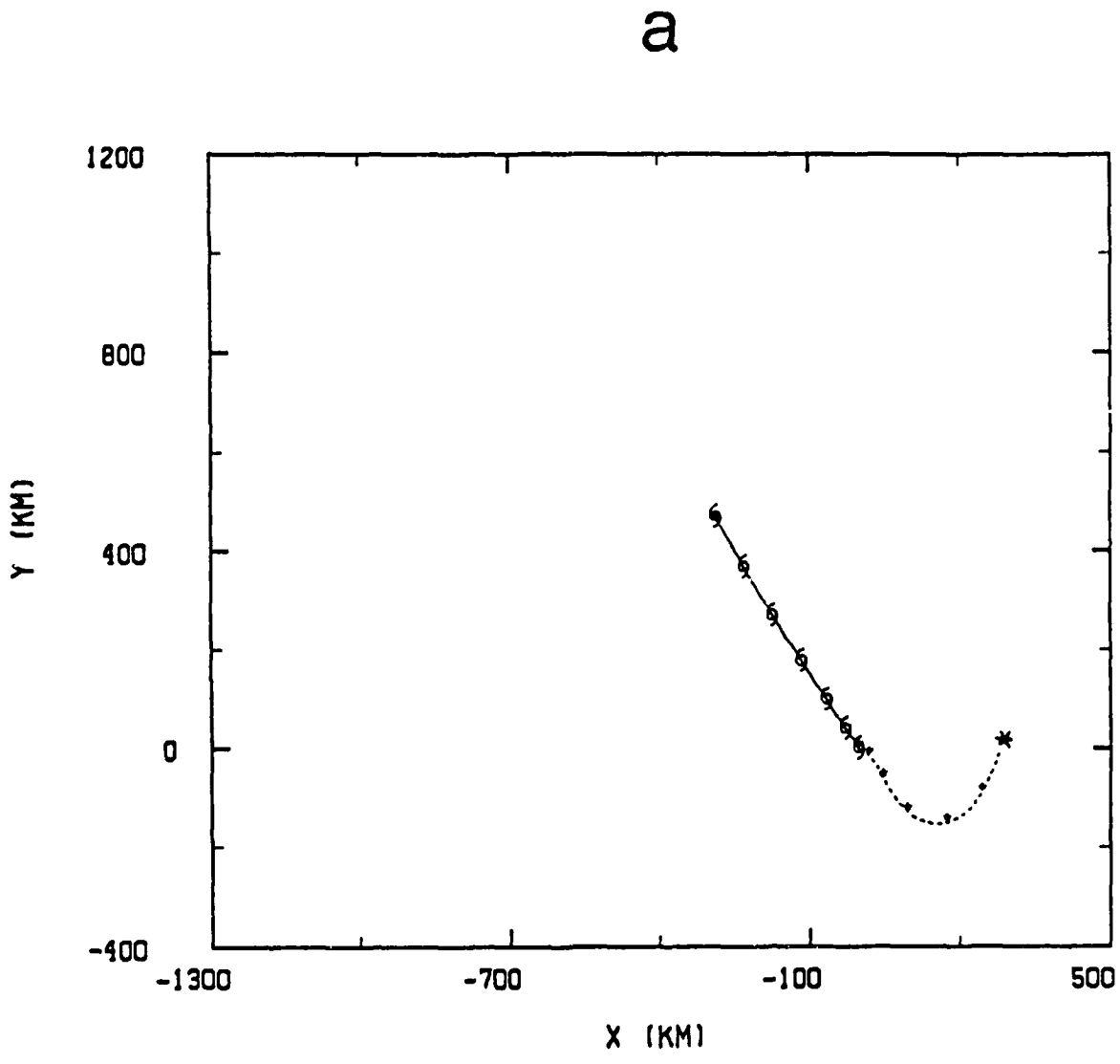

Fig. 5-16. As in Fig. 5-15, except for the revised model with the advection of asymmetric vorticity by the symmetric flow (AAVS) eliminated. Panel (a) is for the B1 vortex and (b) for the B3 vortex. The 72-h positions are highlighted.

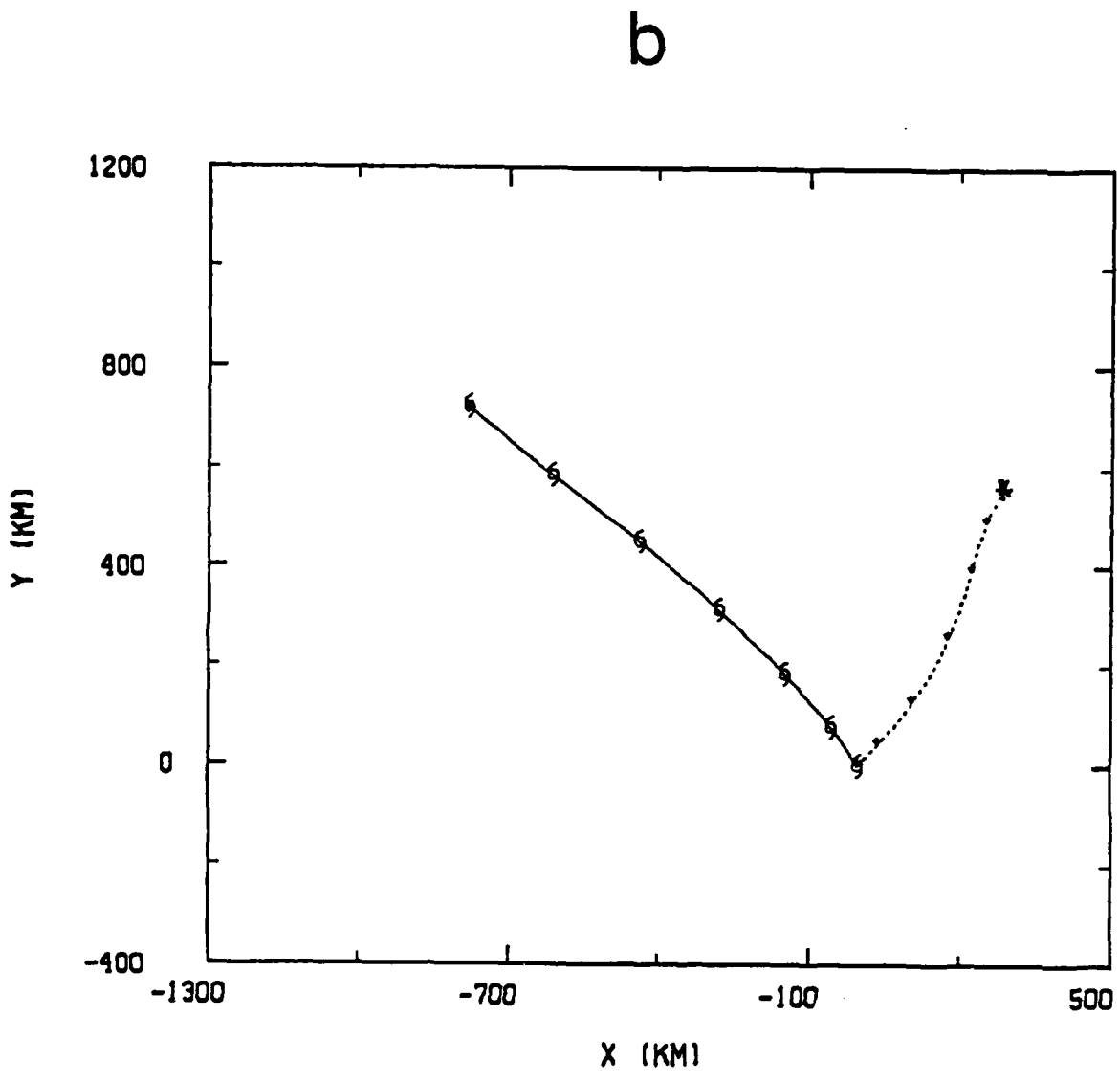

Fig. 5-16. (Continued)

a

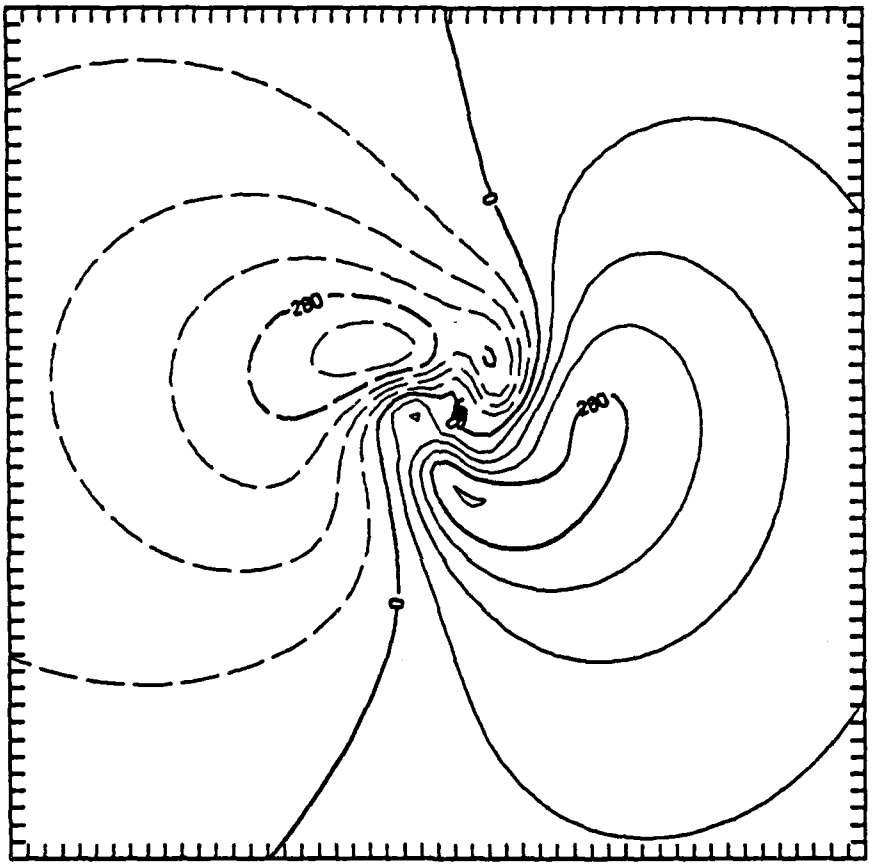

(a) t = 12 h, AAVS = 0
contour interval = 70 ($\times 10^3$) m^2/s
minimum contour = -350 ($\times 10^3$) m^2/s
maximum contour = 350 ($\times 10^3$) m^2/s

Fig. 5-17. Asymmetric streamfunction fields for the B1 vortex in the revised model experiment B1 with the advection of asymmetric vorticity by the symmetric flow eliminated.

b

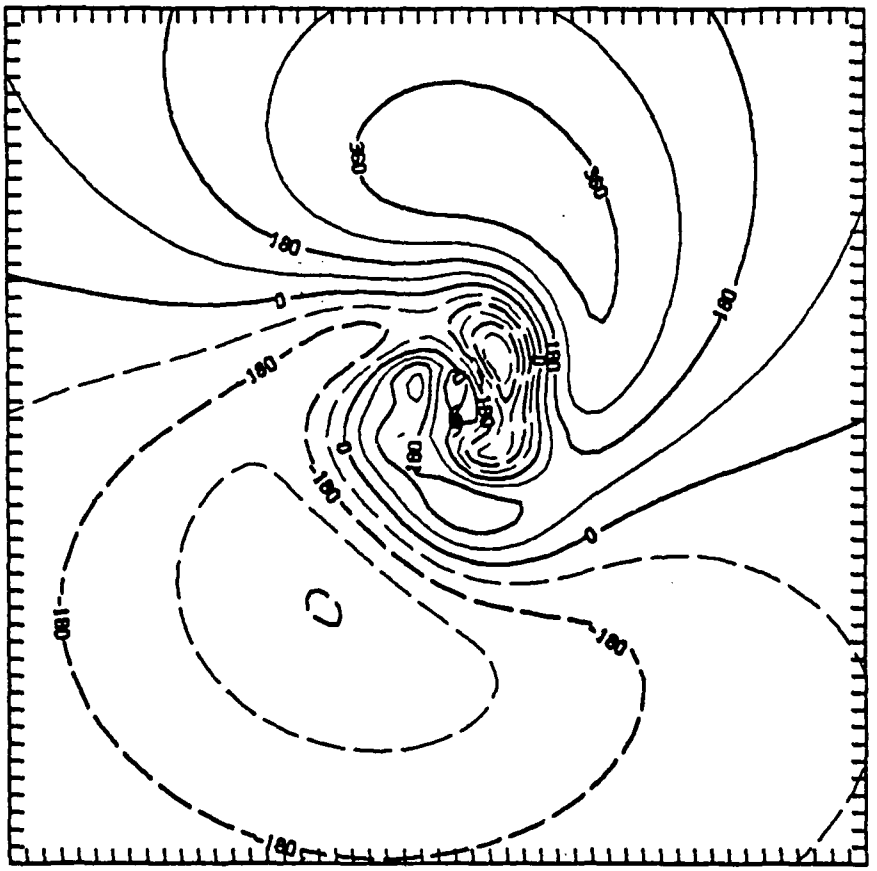

(b) t = 24 h, AAVS = 0
contour interval = 90 ($x10^3$) m^2/s
minimum contour = -450 ($x10^3$) m^2/s
maximum contour = 360 ($x10^3$) m^2/s

Fig. 5-17. (Continued)

C

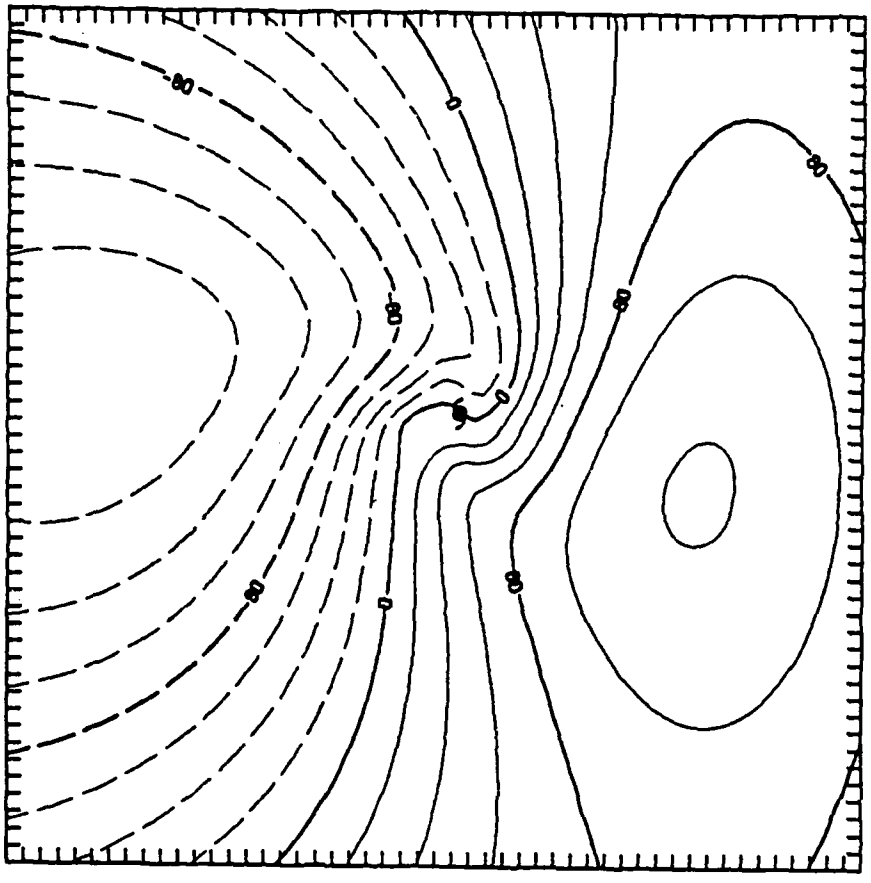

(c) t = 12 h, full model
contour interval = 80 ($\times 10^3$) m^2/s
minimum contour = -400 ($\times 10^3$) m^2/s
maximum contour = 400 ($\times 10^3$) m^2/s

Fig. 5-17. (Continued)

d

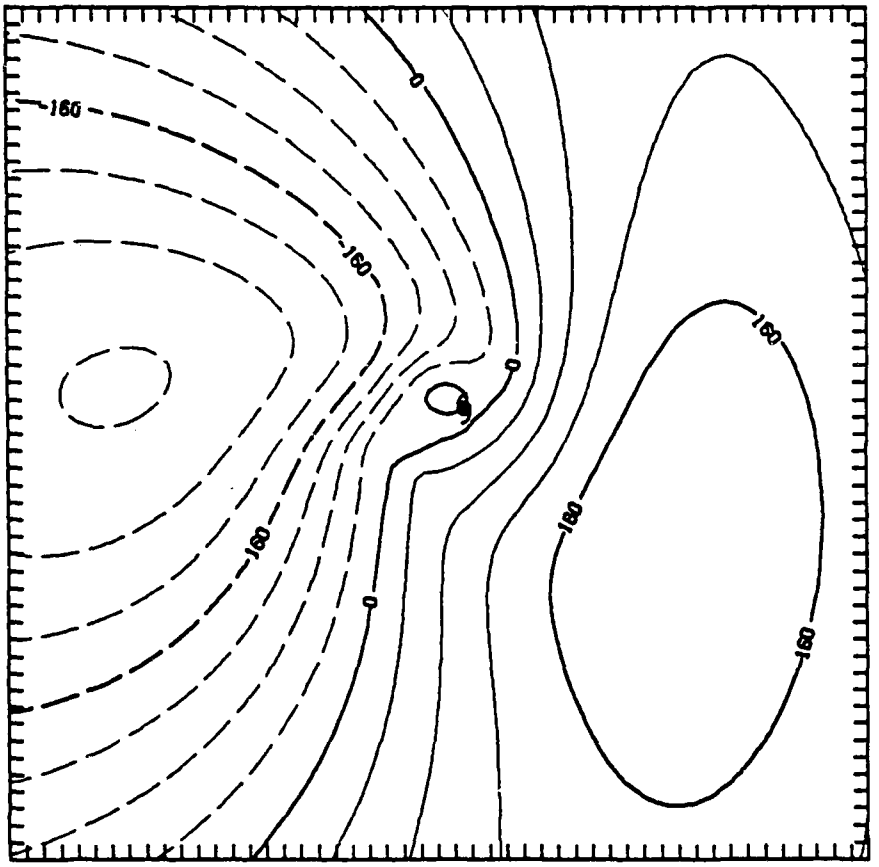

(d) t = 24 h, full model
contour interval = 100 ($x10^3$) m^2/s
minimum contour = -700 ($x10^3$) m^2/s
maximum contour = 700 ($x10^3$) m^2/s

Fig. 5-17. (Continued)

vortices (only B1 is shown) breaks down into two sets of gyres when AAVS is set to zero. The large-scale gyres appear to twist anticyclonically within the inner portion of the storm and then detach to form a separate set of gyres at 24 h. This deflects the ventilation flow at the center toward the east and south. As the small-scale gyres detach, the large-scale gyres rotate cyclonically (as in the full model solution), which leads to a complete separation between the inner and outer gyres.

As shown in Sec. IV-E (see Figs. 4-22 and 4-23), both the large-scale (ASVA) and the inner-core (AAVS) motion-type tendency dipoles have a pattern with ψ falls ahead of the center and ψ rises behind. The centers of the falls and rises are aligned with the motion vector (i.e., are in phase). However, application of such a tendency pattern to a constant streamfunction field or to a stationary nearly symmetric vortex would result in the formation of a cyclone (negative tendencies) to the north and an anticyclone (positive tendencies) to the south (see Fig. 5-17a around the vortex center) in the asymmetric flow.

It was hypothesized in Chapter IV, and suggested by Marks and Houze (1987), that the inner-core region is moved primarily through the advection of asymmetric vorticity by the symmetric flow (AAVS). If this hypothesis is true, then when AAVS is set to zero, the inner-core motion is suppressed and the center will remain stationary. In this situation, the only way for the center to move is if the scale of the ASVA motion forcing becomes small enough to influence the inner-core region. It is further reasoned that the dependence of the inner-core motion on AAVS is a function of the inner strength because AAVS depends on the symmetric circulation (i.e., tangential wind) and will be greater for stronger inner-region flows. The expected northward motion of the weak-large B3 (Fig. 5-16b) vortex

and the unusual results with the basic vortex (Fig. 5-16a) supports this reasoning.

In the case of the B1-type vortices (B1, S8 and S9 with the same inner strength), the inner-core does not move initially and the tendency pattern in the advection of symmetric vorticity by the asymmetric flow (ASVA) generates small-scale gyres in the inner core and an associated ventilation flow (Fig. 5-17a). When these gyres reach sufficient amplitude (~ 12 h), ASVA then moves the inner core. However, the small-scale ventilation has been oriented toward the east (Fig. 5-17a) and southeast (Fig. 5-17b) and thus the center moves with an eastward component. This eastward-directed ventilation is a direct consequence of the small-scale cyclonic (anticyclonic) gyre to the north (south) due to the ASVA tendency dipole. It is also important to notice that the "disconnection" between the small-scale gyre forced by ASVA and the linearly-induced large-scale gyres prevents the center from being influenced by the larger-scale advective forcing. For the weak-large (B3 vortex), a similar set of small-scale gyres starts to form at t = 12 h (Fig. 5-17c). However, the separation of these gyres from the larger-scale gyres does not occur (Fig. 5-17b versus Fig. 5-17d) and the center translates with the linearly-induced ventilation flow.

Because the disconnection (or lack of a disconnection in the weak-large vortex) depends on the vortex structure, the ratio of nonlinear to linear terms may be a critical factor. The <u>inner</u> strength is greater in the basic vortex than in the B3 vortex. This means that the nonlinear terms are stronger in the inner portion of the basic vortex. However, the linear β forcing is greater in the B3 vortex compared to the basic vortex because of greater <u>outer</u> strength. Thus, the magnitude of the nonlinear effects (advection) relative to the linear effects

(strength of the ventilation flow) should be greater throughout the basic vortex than in vortex B3.

When the nonlinear term is relatively stronger than the linear forcing, the motion of the center depends more on inner-core motion process (AAVS). In this situation, AAVS acts to connect the motion of the inner core to the motion of the symmetric vortex on a somewhat larger scale (roughly 300 km for B1).

The conclusion from this reasoning is that the ASVA dipole must have the correct scale (pattern) in order to move the larger-scale symmetric vortex. When the inner asymmetric circulation is distorted through ASVA by setting AAVS to zero as in these dynamical sensitivity experiments, the scale of the ASVA-dipole decreases to such an extent that it prevents the inner core from connecting or "phasing" with the motion of the larger-scale symmetric circulation. The importance of this phasing mechanism depends on the strength of the inner nonlinear terms relative to the linear forcing in the inner region.

5. Modifying AAVS

The second type of nonlinear tendency modification concerns the relative importance of "outer" ($r > 400$ km) versus "inner" advective effects. The largest magnitudes of the nonlinear terms are in the inner regions of the vortex. Even though the nonlinear terms are smaller beyond $r = 400$ km, the linear forcing is also weaker (v is smaller). Thus, it is hypothesized that there may be subtle balances in the outer zone that could affect the motion of the center by influencing the large-scale, asymmetric gyres.

When AAVS is reduced to zero only for $r > 400$ km (Exp. B2), there is a more northward drift and a greater speed of motion for all cases (Fig. 5-18). This is expected as the rotation of the large-scale gyres due to advection of asymmetric vorticity by the symmetric flow has been

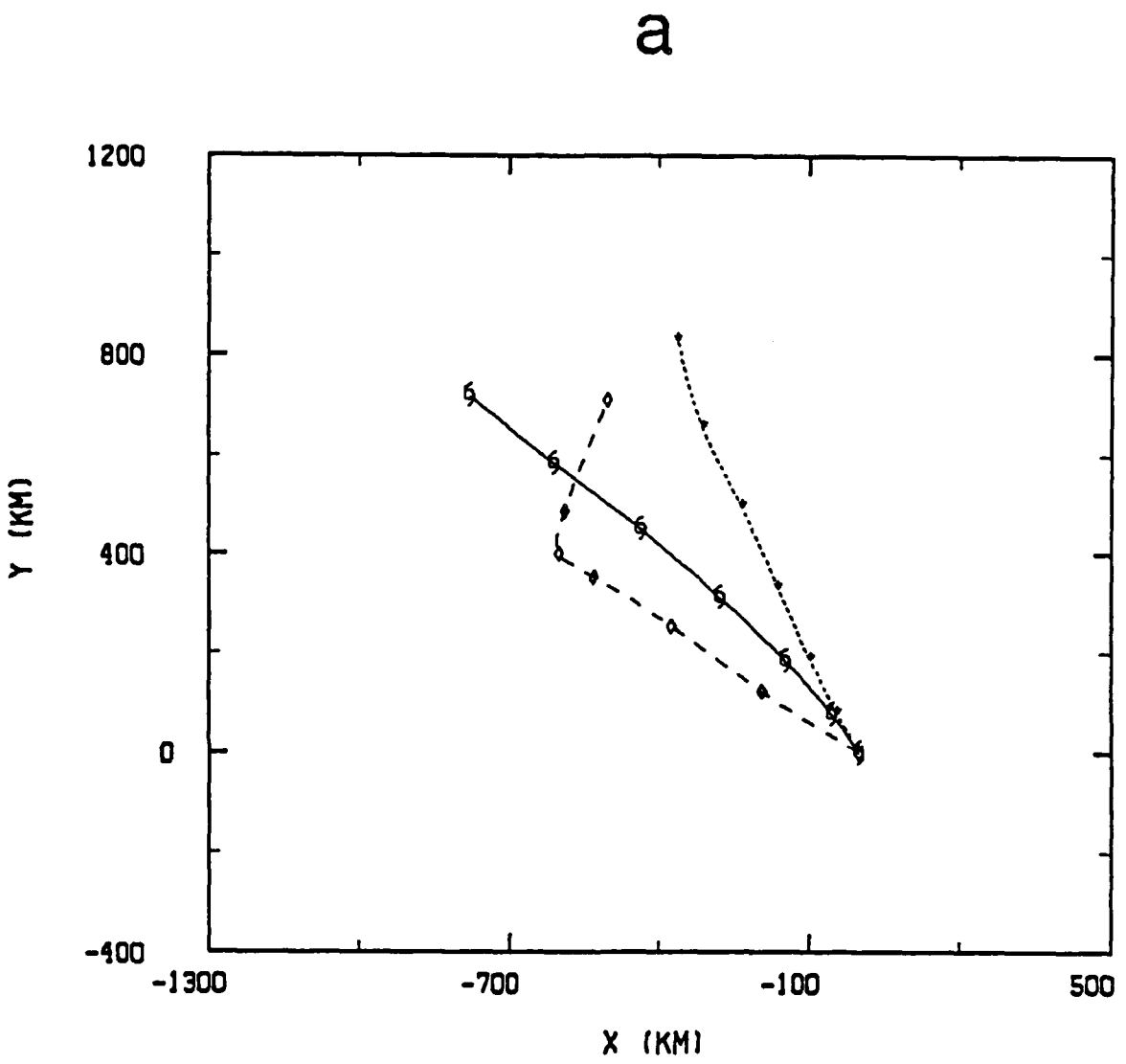

Fig. 5-18. Tracks to 72 h for the full model (solid) and Exp. B2 (short-dashed) and Exp. D2 (long-dashed). In Exps. B2 and D2 the advection of asymmetric vorticity by the symmetric flow (AAVS) is eliminated outward of r = 400 km. The initial vortex for Exp. B2 comes from the analytical symmetric vortex in Exp. B2 and for Exp. D2 comes from a previous integration and therefore contains a model-generated asymmetric circulation. Panel (a) is for the weak-large vortex; (b) for the cyclonic perturbation vortex; and (c) for the anticyclonic vortex.

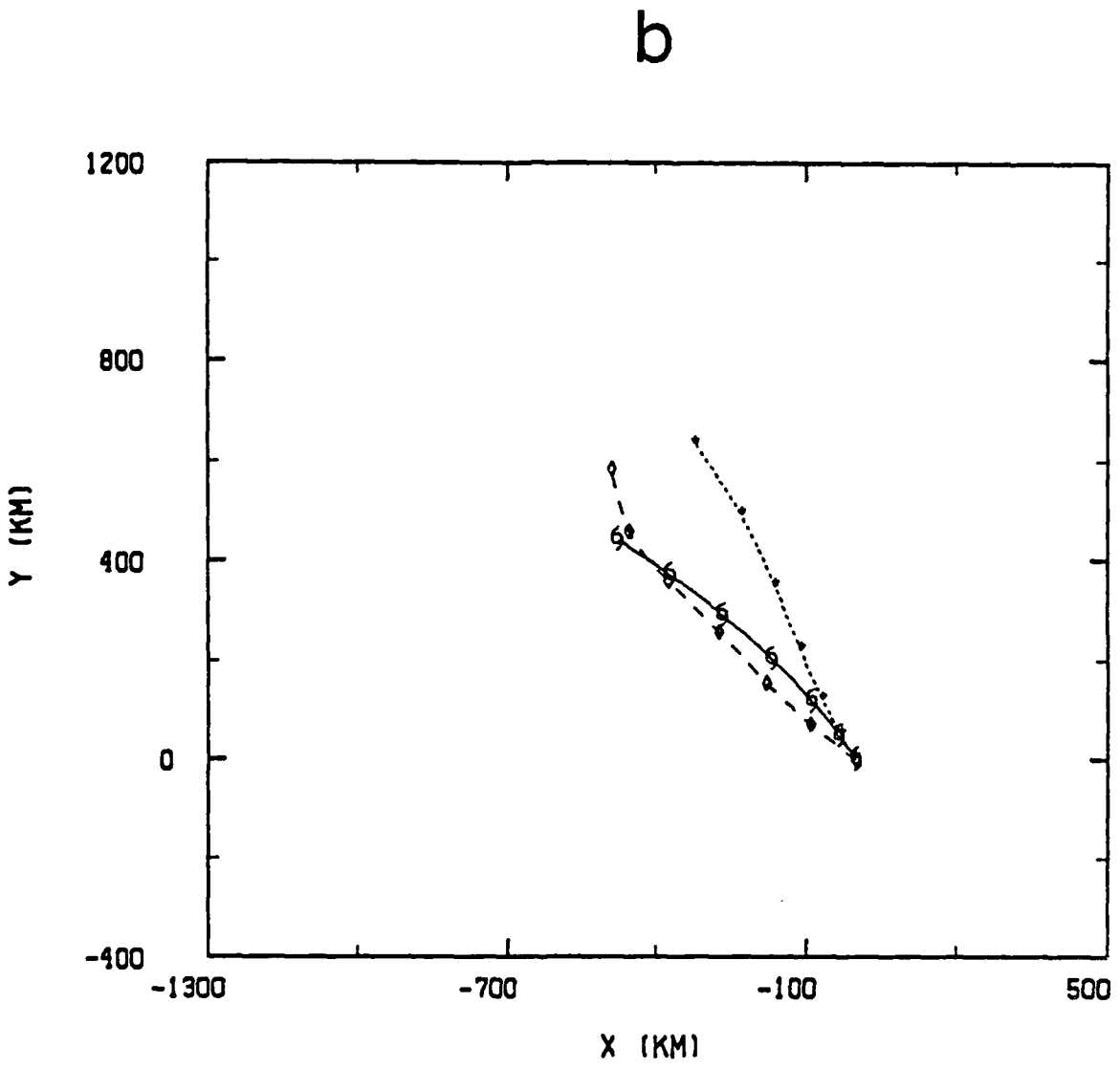

Fig. 5-18. (Continued)

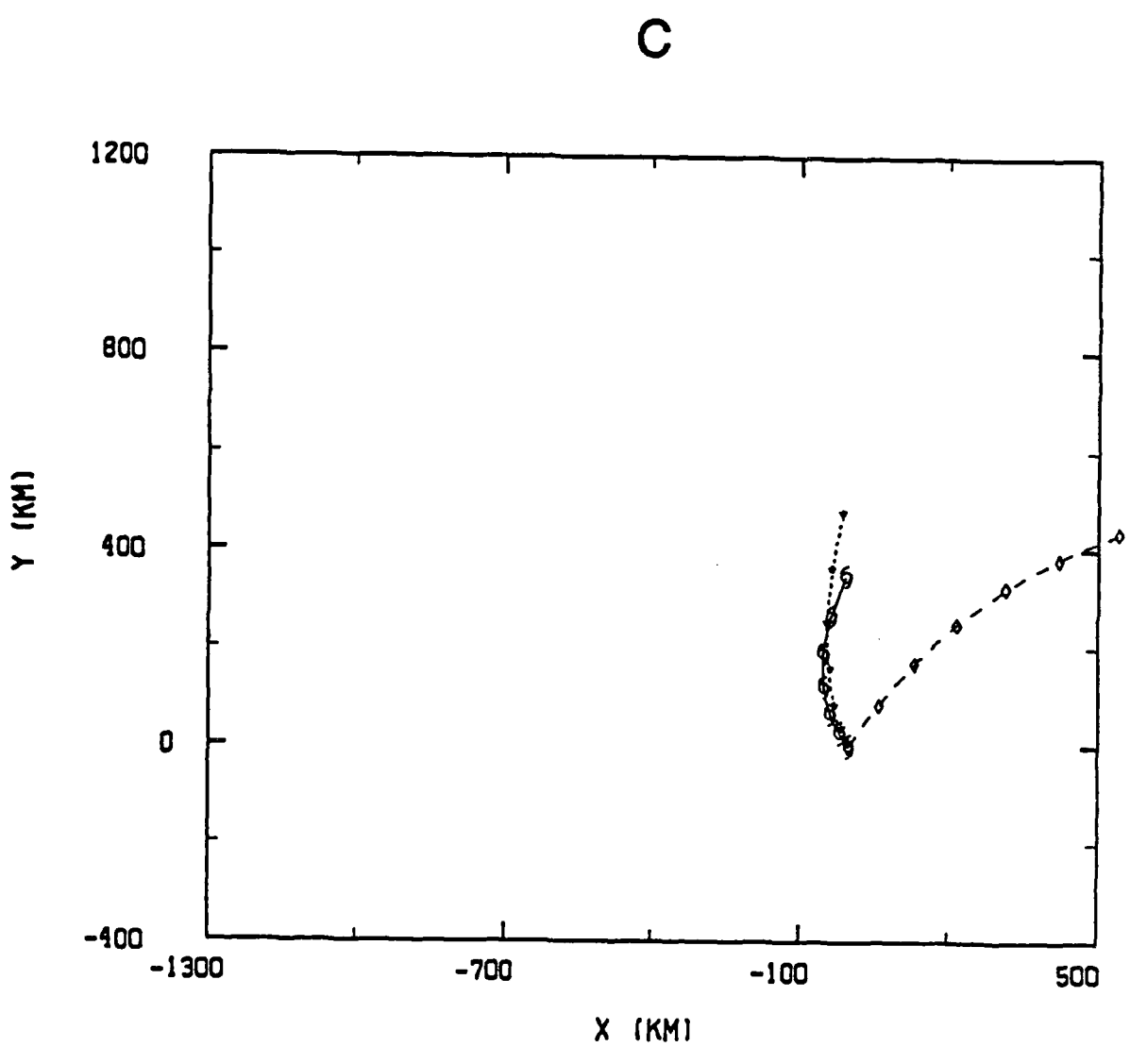

Fig. 5-18. (Continued)

eliminated in the outer region in which the gyres reach peak amplitude. At the same time, the inner-region ($r < 400$ km) continues to move due both to the inner-core motion process (AAVS) and larger-scale ventilation flow (ASVA).

When the model is initialized with a vortex containing a well-developed asymmetric circulation (Exp. D2), the turn to the north does not occur until after 48-60 h for the weak-large B3 and cyclonic perturbation S8 vortex (Fig. 5-18a and b). For the anticyclonic perturbation experiment (S9), the initial asymmetric flow prevented the turn to the north (Fig. 5-18c). For this vortex, the asymmetric gyres are on a smaller scale and the AAVS nonlinear effect is less important beyond $r = 400$ km compared to the other vortices. The different result for S9 is another indication that the nature of the dynamical motion processes is strongly dependent on the vortex structure.

The turn to the north in the cyclones (vortices B3 and S8) with greater cyclonic flow in the critical annulus ($r = 300 - 800$ km) is related to the linear effects. Rossby dispersion tends to create large-scale asymmetric gyres with a ventilation flow oriented north-south (see linear solutions in Figs. 5-1 and 5-10). Thus, if the gyres are initially oriented away from the north-south direction (as in the steady-state full model solution) and are prevented from rotating, then the ventilation flow vector would eventually become northerly as the gyres would be forming with the north-south orientation of the linear solution (i.e., nonlinear effects small). The delayed response to the AAVS tendency modification when the model is initialized with a developed asymmetric flow (Exps. B2 and B3 versus Exps. D2 and D3) suggests that the time scale required for outside flow changes to affect the motion of the center due

to the modified nonlinear forcing is slow compared to the time required to form the asymmetric gyres.

The tendency analysis and the AAVS-only experiments (Exp. A1 when ASVA = 0) show that the AAVS term not only rotates the ventilation flow vector, but also acts to suppress the growth of the large-scale gyres due to linear dispersion. By reducing AAVS, the amplitudes of the large-scale gyres tend to grow beyond the amplitude obtained in the complete model integration. This increased amplitude implies a larger gradient in the asymmetric streamfunction across the center, which increases the ventilation flow and the speed of motion.

In a second set of model experiments, the AAVS term is eliminated outside r = 200 km (Exp. B2) vice 400 km (Exp. B3) to determine the importance of this process closer to the vortex center. The tracks for the Exp. B2 and Exp. B3 integrations (Fig. 5-19) for the basic and weak-large vortices show greater motion disruption when AAVS is eliminated close to the center. Also notice that the disruption is more severe for the basic vortex (compare Fig. 5-19a versus Fig. 5-19b) than for the weak-large cyclone. In the vortices with significant cyclonic flow in the critical annulus, ASVA (when AAVS is set to zero) rapidly modifies the inner asymmetric flow. This apparently prevents the formation of a broader-scale (around 500 km wide) uniform ventilation flow and implies that the nonlinear motion processes for stronger inner strength vortices must "cooperate" in order for the vortex to achieve a steady-state motion. That is, the two nonlinear advective effects do not act separately to move the small and large-scale components of the vortex. Rather, the motion processes produce a combined effect that does not operate independently of one another. This is a further indication of the complicated nature of the nonlinear processes.

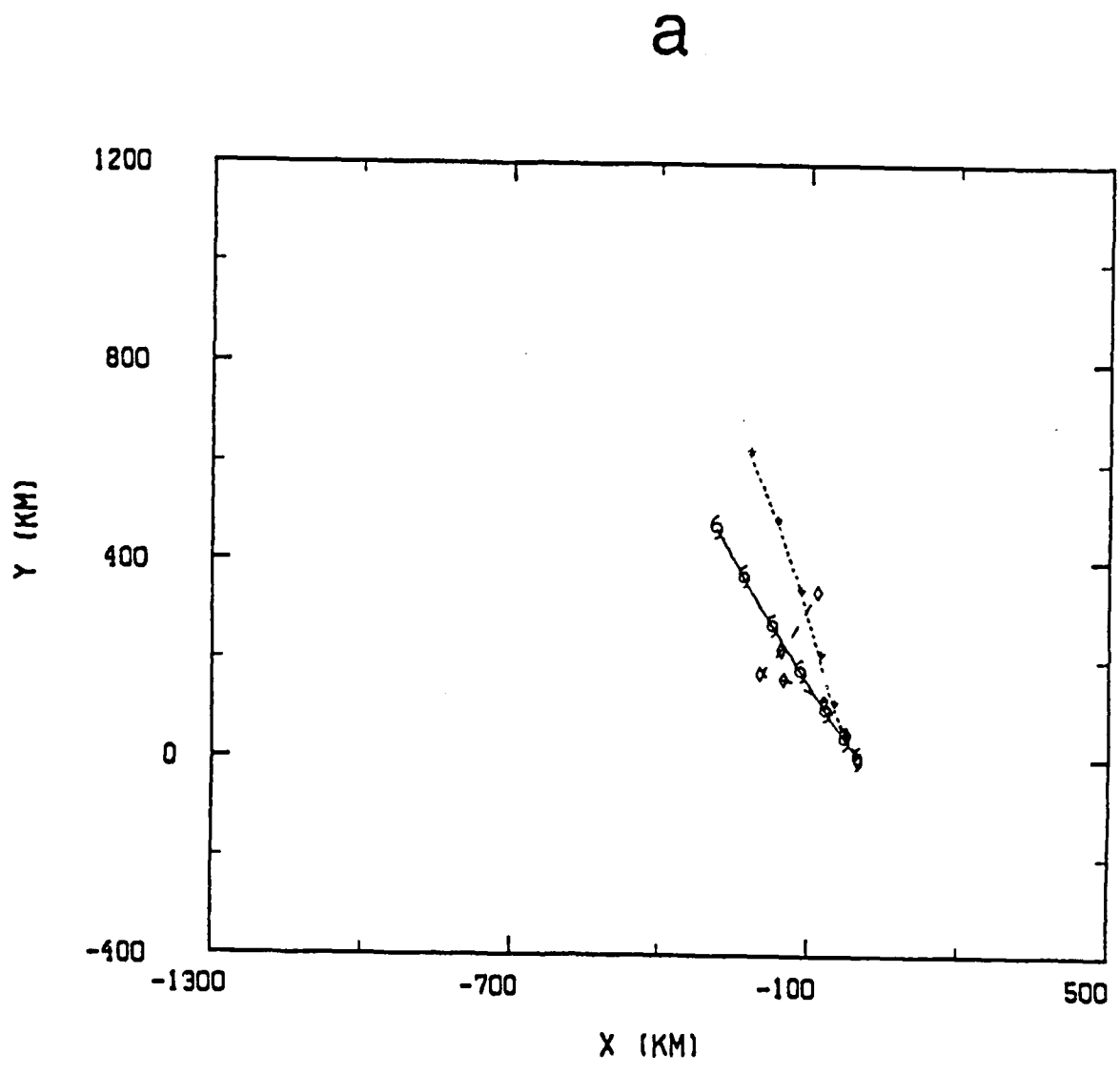

Fig. 5-19. As in Fig. 5-18 except that AAVS is eliminated outward of r = 200 km. Panel (a) is for the basic vortex; and (b) is for the weak-large vortex.

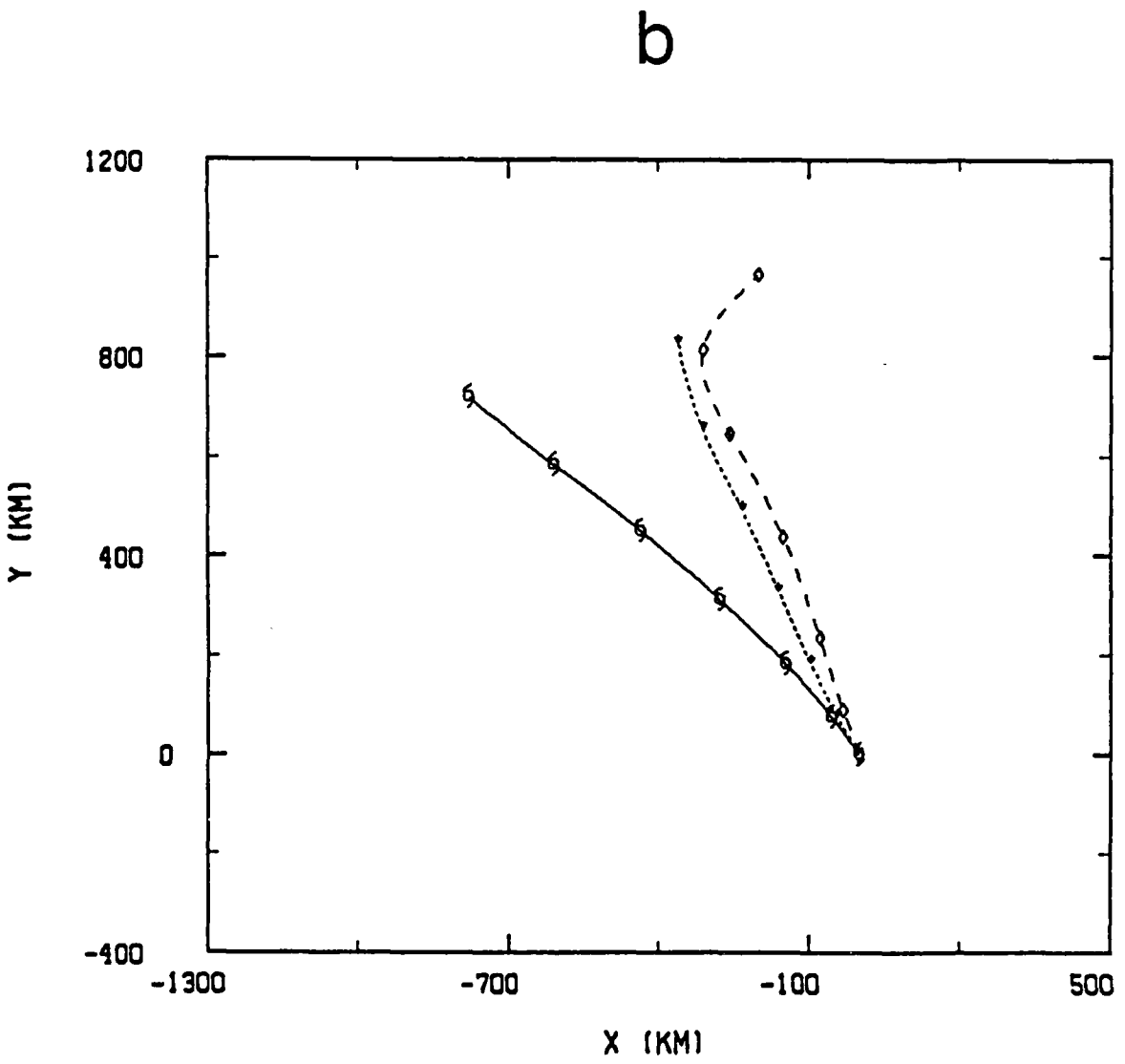

Fig. 5-19. (Continued)

6. Modifying ASVA

As shown in Chapter VI, the advection of symmetric vorticity by the asymmetric flow (ASVA) produces a larger-scale, motion-type tendency dipole pattern with the greatest values inward of r = 400 km. In these experiments, ASVA is set to zero in the outer zone (r > 400 km) to determine how this advection process contributes to the evolution of the large-scale gyres. The tracks (Fig. 5-20) are similar to those experiments in which AAVS is modified, except that the deviation is to the left of the complete model track or a more westerly motion. The asymmetric flow for vortex B1 (Fig. 5-21 compared to Fig. 5-17d) shows that the rotation of the gyres has been exaggerated compared to the full model integration. That is, elimination of ASVA in the outer region has enhanced the gyre rotation by AAVS. Also, observe that the amplitudes of the gyres have been increased to give a greater speed of motion and the sudden streamfunction changes in the zone in which ASVA drops to zero. These results imply that the advection of symmetric vorticity by the asymmetric flow also contributes to the "balancing" between the nonlinear and linear effects that causes the gyres to stabilize in the steady state (refer to Sec. IV-E).

7. Summary

The streamfunction tendency analysis in Chapter VI shows two types of nonlinear processes involved in the motion of the center. Advection of asymmetric vorticity by the symmetric flow (AAVS) yields a motion-type pattern confined to the inner core of the vortex. On the other hand, advection of symmetric vorticity by the asymmetric flow (ASVA) produces a much larger scale motion pattern to move the large-scale component of the vortex.

How the interaction between the symmetric and asymmetric circulations causes vortex motion has been

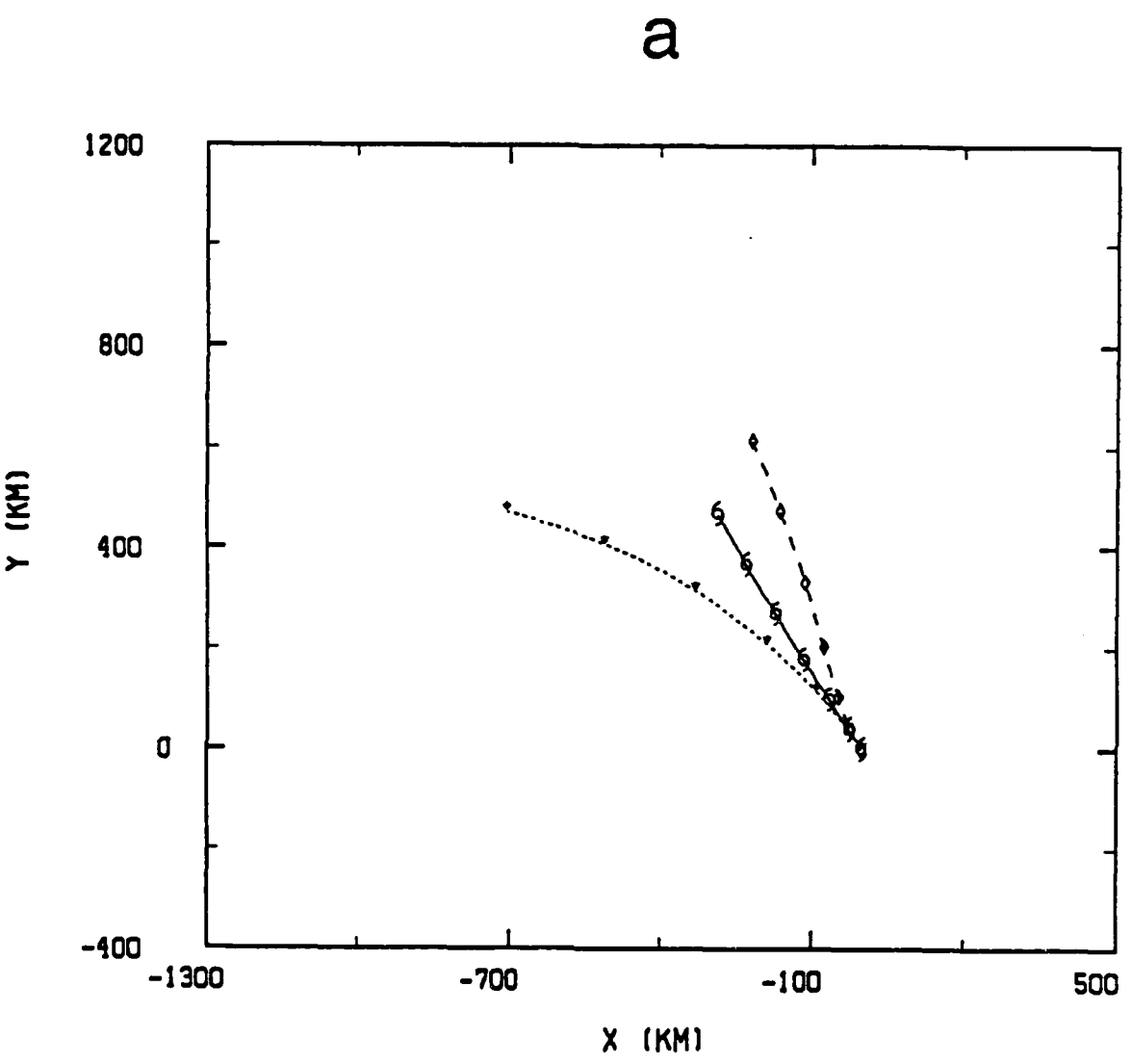

Fig. 5-20. 72-h tracks for the full model (solid) and Exp. A2 (short-dashed) and Exp. B2 (long-dashed). In Exp. A2, the advection of symmetric vorticity by the asymmetric flow (ASVA) is eliminated outward of r = 400 km and in Exp. B2 the advection of asymmetric vorticity by the symmetric flow (AAVS) is eliminated outward of r = 400 km. The initial vortex comes from the analytical symmetric vortex. Panel (a) is for the basic vortex; (b) is for the weak-large vortex; (c) for the cyclonic perturbation vortex; and (d) for the anticyclonic vortex.

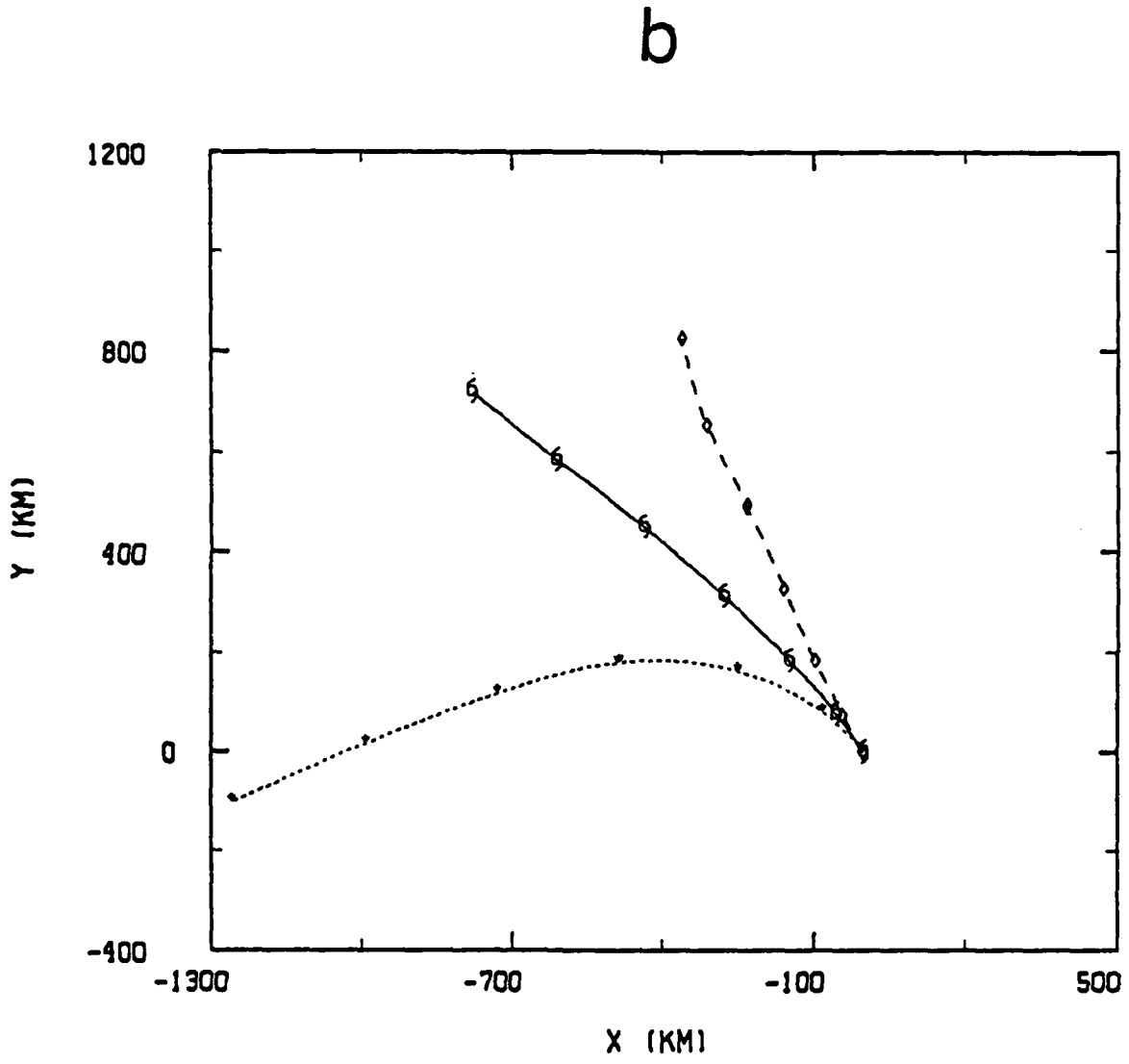

Fig. 5-20. (Continued)

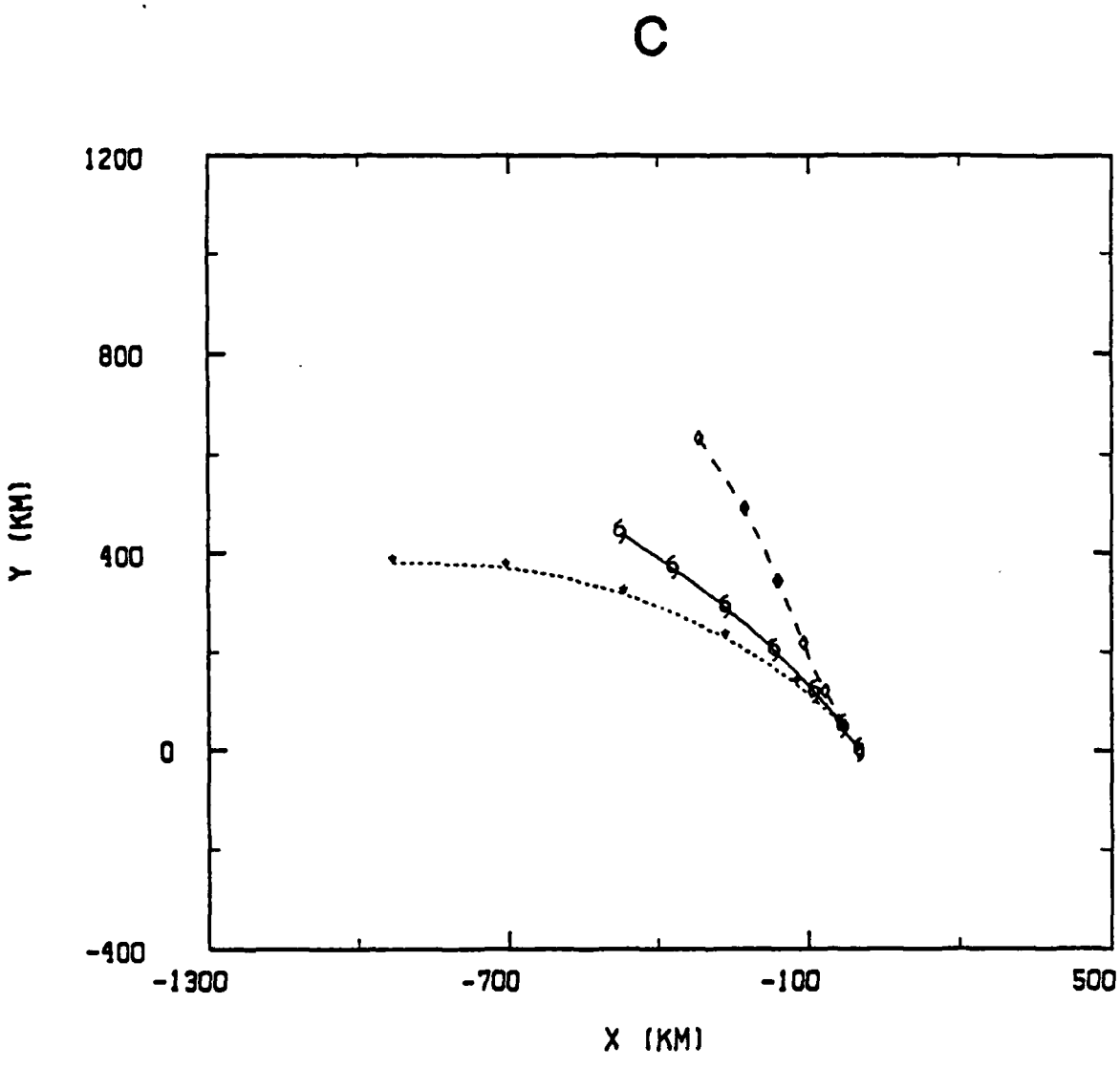

Fig. 5-20. (Continued)

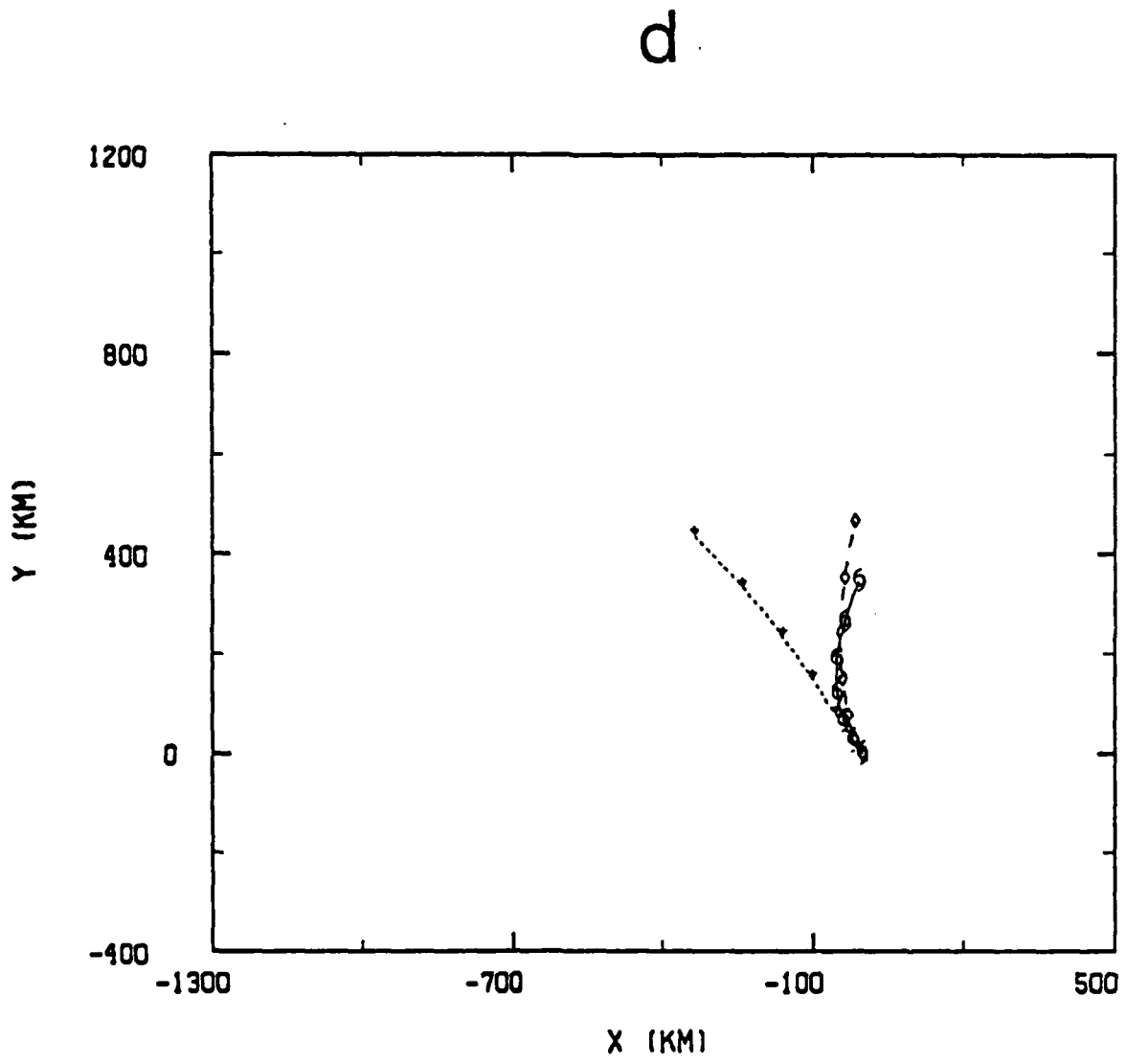

Fig. 5-20. (Continued)

studied using a series of model integrations in which the advection terms responsible for the nonlinear interaction are modified. In these dynamical sensitivity tests, the symmetric and asymmetric components of the model nonlinear term are modified either by setting them to zero throughout the domain or only beyond some radius. In this way, it is possible to determine both the relative importance of an interaction term and the regions of the vortex in which the interaction with the linear term is critical.

When the only nonlinear term is the advection of asymmetric vorticity by the symmetric flow (AAVS), the vortex moves along the same path as in the full (ASVA + AAVS) model, but with reduced speed. The percentage of the total translation accounted for by the inner-core motion process is on the order of 40 % and is a function of vortex structure, with a greater contribution as the outer strength increases. This indicates the magnitude of the inner-core motion process as suggested in the tendency analysis of Chapter VI.

In contrast, when only the advection of symmetric vorticity by the asymmetric flow (ASVA) is included for the vortices with the greatest inner strength (i.e., the B1, S8 and S9 case), the center did not move or moved slowly toward the east. This occurs even when the model is initialized with a well-developed asymmetric flow. It had been anticipated that the ventilation flow would "steer" the center toward the north. However, this result is obtained only in the weak-large (B3) vortex when the nonlinear terms are smaller relative to the linear forcing. The unexpected behavior of the strong inner strength vortices is due to the development of small-scale gyres by ASVA. When AAVS is zero, the inner core does not move initially and the ASVA motion-type tendency dipole causes the formation of the small-scale gyres with a ventilation flow towards the east

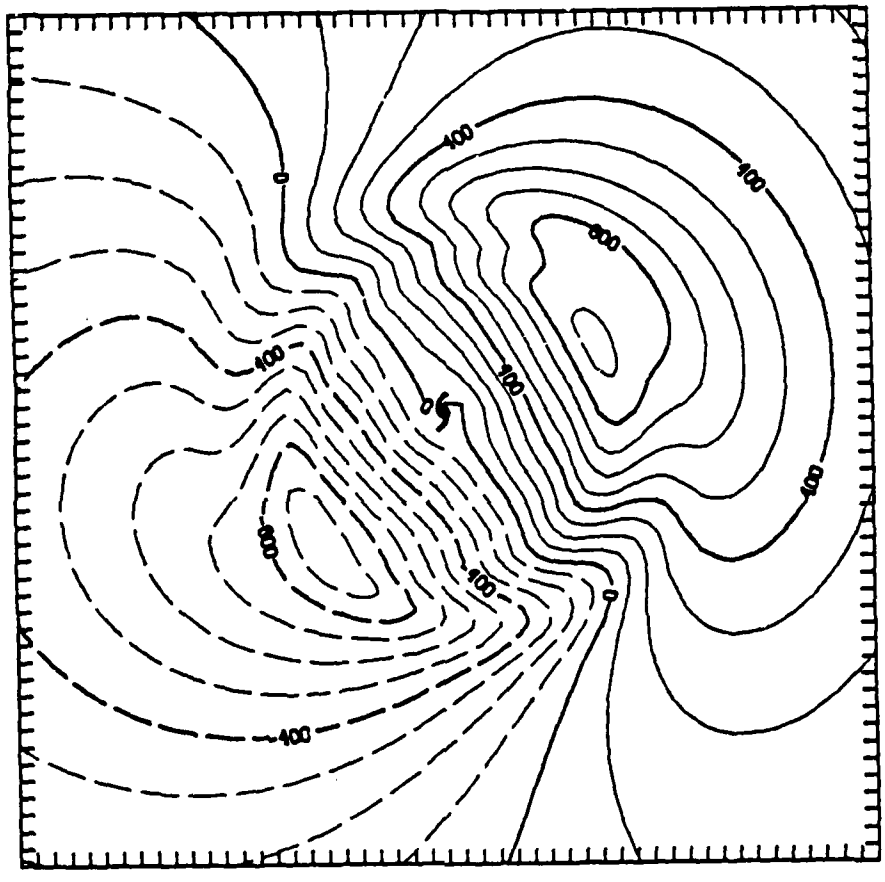

Fig. 5-21. Asymmetric streamfunction for the basic (B1) vortex for Exp. A2 in which the advection of symmetric vorticity by the asymmetric flow is eliminated beyond r= 400 km.

to southeast. As this small-scale ventilation flow grows, ASVA moves the center toward the east and the small-scale gyres become disassociated with the linearly induced large-scale gyres. This result suggests that the advection of the large-scale vortex by the ventilation flow depends on the motion of the inner core as well and that the two motion processes must act in concert to maintain the motion of the entire system.

Although the nonlinear terms are weak outside the inner core of the vortex, they have an important role in orienting the linearly induced, large-scale asymmetric gyres. When the gyre rotation due to AAVS is enhanced by setting ASVA = 0 beyond r = 400 km , the vortex has a more westerly path. In contrast, when AAVS is eliminated beyond r= 400 km, the gyre rotation is reduced (i.e., became more linear) and the vortex has a more northward course. Reducing either nonlinear term in the outer zone allows the asymmetric flow gyres to amplify, which results in greater speed of motion.

D. SUMMARY AND CONCLUSIONS

In this chapter, the dominant dynamical processes of vortex motion, as suggested by the "static" tendencies in Chapter IV, have been studied by directly modifying the model equations during the integration. Such an approach is referred to as a "dynamical" sensitivity analysis and is analogous to the "physical" sensitivity tests (e.g., Keyser and Uccellini, 1987).

Three types of experiments have been performed. In the first set, the relative magnitude of nonlinear to linear effects is modified to determine how the ventilation flow varies with the speed of motion. The "beta-drift potential" (the maximum ventilation flow speed due solely to linear effects) of a tropical cyclone-like vortex is much greater than the actual beta drift and is a function of the outer

weak inner strength vortices. When the inner strength is large (e.g., B1) the two motion effects must operate together to move the center.

The time scale required for outside (r > 400 km) changes, due to the modified advection terms, to affect the vortex motion is much greater (~ 60 h) than the time required to generate the ventilation flow (~ 24 h). These experiments confirm the critical role of nonlinear interaction between the vortex (symmetric flow) and asymmetric circulation arising from vortex-environment (β) interaction.

strength. While linear processes constrain the maximum motion, nonlinear effects determine the point at which the ventilation flow generation matches the apparent ventilation flow reduction due to motion. From the ventilation flow speed-motion relationship, it is suggested that the response to disruptions in the ventilation flow/motion balance would vary with vortex structure.

In the second set of experiments, the model is initialized with a linear solution and is then integrated only with nonlinear term. The nonlinear-only motion is directly proportional to the magnitude of the initial ventilation flow. Nonlinear advection does tend to cancel the large-scale asymmetric gyres. However, a very broad scale (~ 1000 km) ventilation flow is not eliminated by nonlinear effects. The long-term, nonlinear-only solutions demonstrate that once the ventilation flow is established, the symmetric and asymmetric circulations in the vortex are bound together to sustain the motion. Another result from the nonlinear-only integrations is that the turning motion (e.g., cyclonic bending of the track in the cyclonic perturbation vortex) is strictly a nonlinear process and is independent of linear dispersion.

In the third set of dynamical sensitivity tests, the nature of the nonlinear symmetric and asymmetric circulation interaction has been examined. In these experiments, the nonlinear term is decomposed into symmetric and asymmetric components during the integration and the components are then directly modified to control the spatial scale of the interaction. The inner-core motion process related to the advection of asymmetric vorticity by the symmetric flow can move the center without the large-scale motion process of advection of symmetric vorticity by the asymmetric flow. However, the large-scale process cannot separately move the center in the typical way toward the northwest except for

VI. ULTRA-LONG INTEGRATIONS

The nonlinear-only integrations in Chapter V showed how the symmetric perturbations can induce persistent turning motion over very long time scales (288 h). It is hypothesized that in the full model integrations for extended periods (e.g., beyond 144 h) any of the four initial vortices will eventually assume the north-northwest direction of motion due to the generation of the linearly induced, large-scale asymmetric gyres. In this chapter, "ultra-long" integrations of 288 h (12 days) with the full model (both nonlinear and linear terms) are made for the four vortices used in Chapters IV and V. These runs would have been extremely expensive in a high-resolution model without the capability of moving the grid during the integration, as a very large domain would have been required to contain the very long (3000 km) tracks.

A. TRACK RESULTS

The 288-h tracks for the B1-type vortices (basic and the two symmetric perturbations), and for the basic (B1) versus the weak-large (B3) cyclone, are shown in Figs. 6-1 and 6-2 respectively. The basic vortex moves with a remarkably steady direction of motion, although there are some speed oscillations. The long-time scale turning motion due to the symmetric perturbations (Fig. 6-1) lasts for approximately 144 h (six days), and then the perturbed vortices move parallel to the track of the unperturbed vortex. The cyclonic bending in the track for the weak-large vortex (Fig. 6-2) persists longer than in the cyclonic perturbation case due to the stronger cyclonic flow in the critical annulus. However, the weak-large vortex track after nine

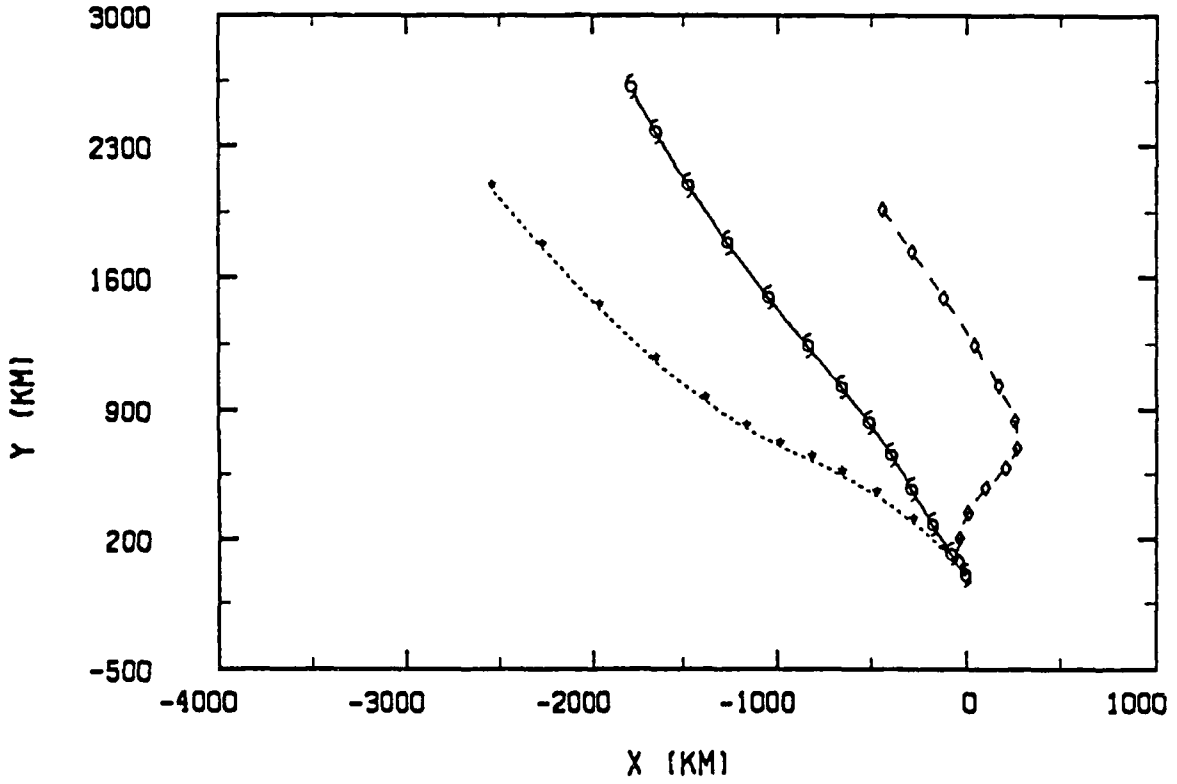

Fig. 6-1. Track forecasts to 288 h for the basic vortex (solid), the cyclonic perturbation vortex (short-dashed) and the anticyclonic perturbation vortex (long-dashed). The symbols plotted along the track indicate the position every 24 h.

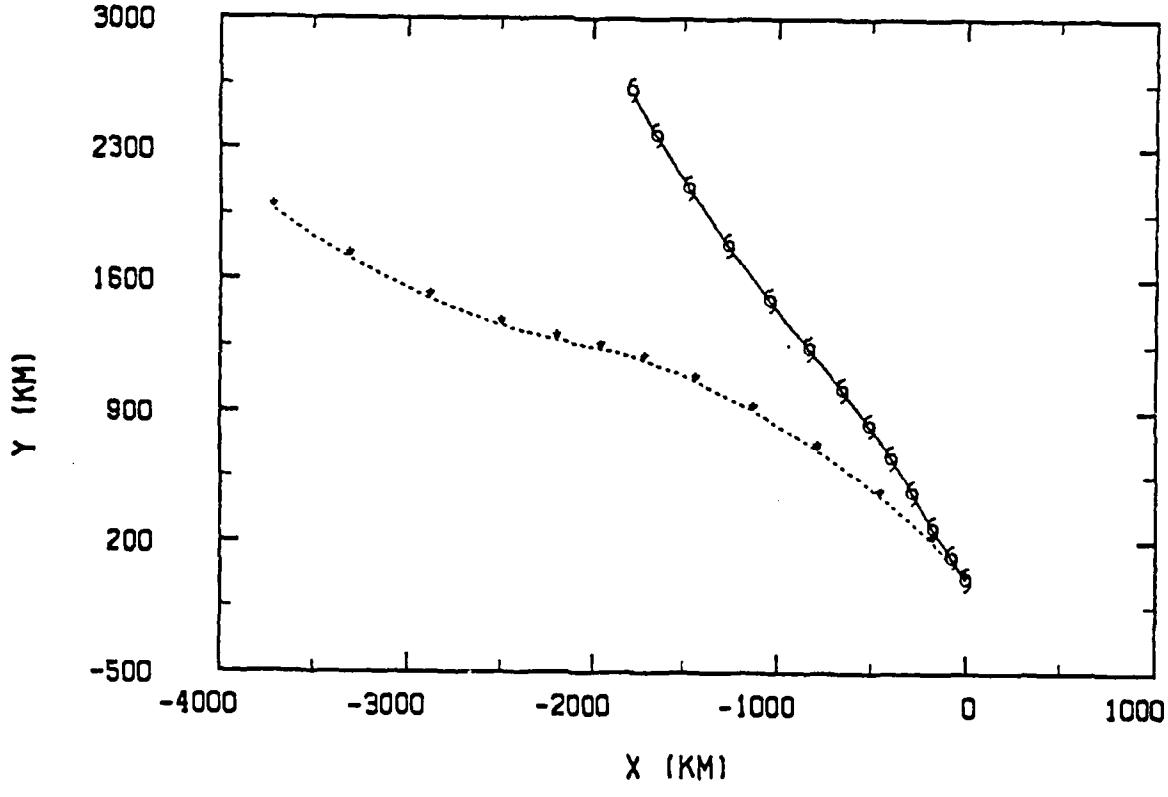

Fig. 6-2. As in Fig. 6-1, except for the B1 (solid) and the weak-large B3 vortices (short-dashed).

days appears to curve and begin to assume a more northwest direction as in the basic vortex.

B. TANGENTIAL WIND PROFILES

The tangential wind profiles in the symmetric perturbation experiments are given in Fig. 6-3. The initial perturbations (Fig. 6-3a) are concentrated in the r = 300 - 800 km annulus. However, the profiles are very similar by 288 h, which is consistent with the similar direction and speed of motion in the later portion of the integration (Fig. 6-1). The time evolution of the weak-large vortex profile is shown in Fig. 6-4. Notice the large reduction in the strong cyclonic flow in the critical annulus by 144 h. By 288 h, the outer portions (beyond r = 500 km) of the profile become quite similar to that in the basic vortex experiment (Fig. 6-5).

C. DISCUSSION AND SUMMARY

The tangential wind profiles in these long integrations appear to approach a common structure, especially for the B1, S8 and S9 vortices. The B3 profile has a sharp reduction in outer strength, which suggests that such a large vortex in nature may require external forcing (e.g., low-level convergence). For this type of vortex, Rossby dispersion acts to reduce the scale of the vortex (smaller outer strength) outside the inner region where the nonlinear effects are strongest.

These integrations also suggest that a single "universal" structure exists that is hypothesized to depend only on β. Vortices near this structure all move toward the northwest with a nearly constant speed of 2-3 m/sec. Departures from this "β-neutral" vortex (e.g., symmetric perturbations) result in track deviations for a period of time before the wind profile is modified toward the "universal" structure.

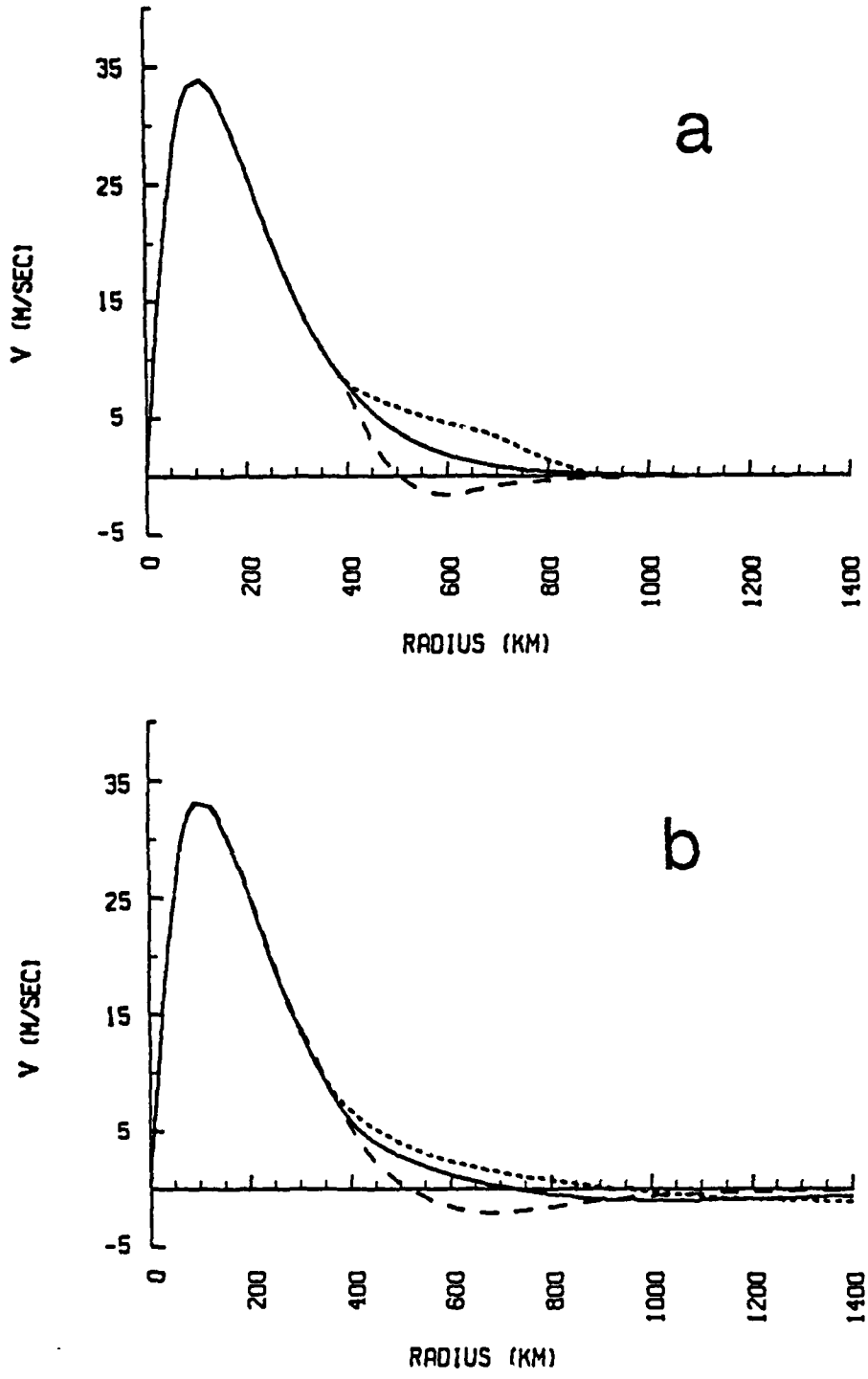

Fig. 6-3. Tangential wind profiles in the ultra-long integrations with the basic vortex (solid), the cyclonic perturbation vortex (short-dashed) and the anticyclonic perturbation vortex (long-dashed) at (a) t = 0 h; (b) t = 72 h; (c) t = 144 h; and (d) t = 288.

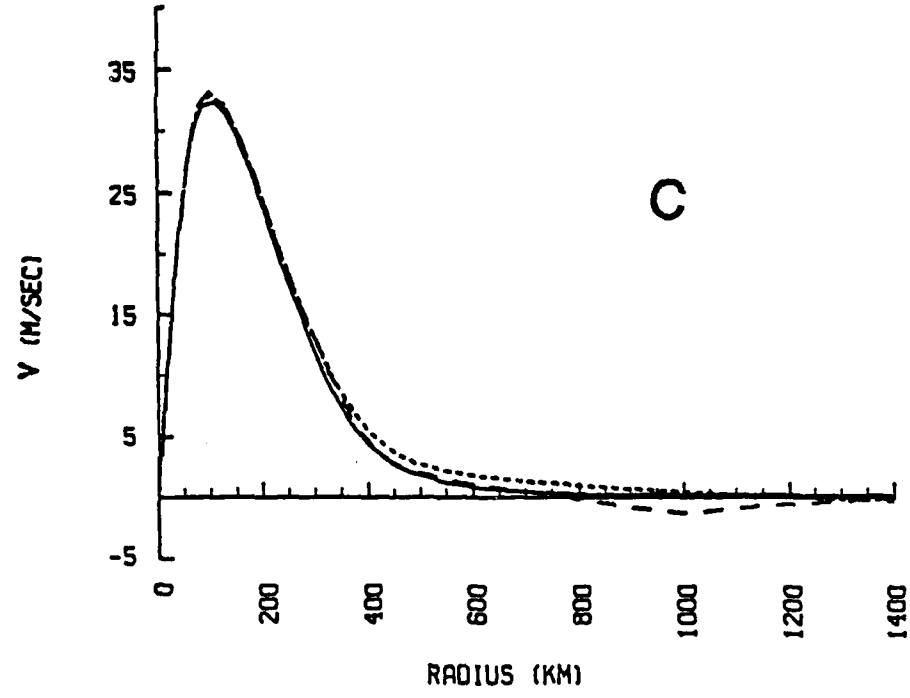

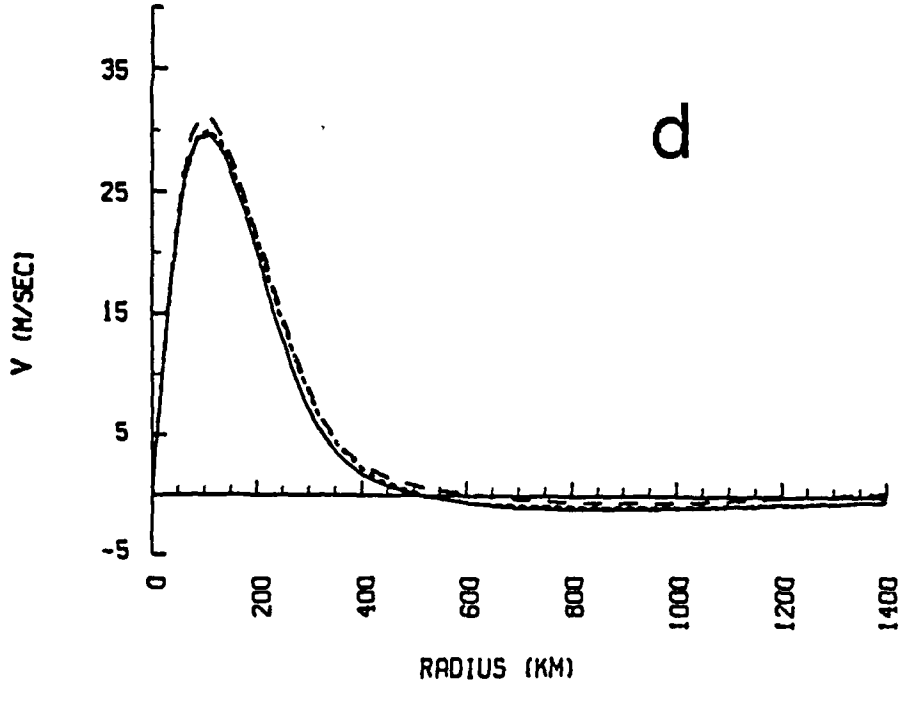

Fig. 6-3. (Continued)

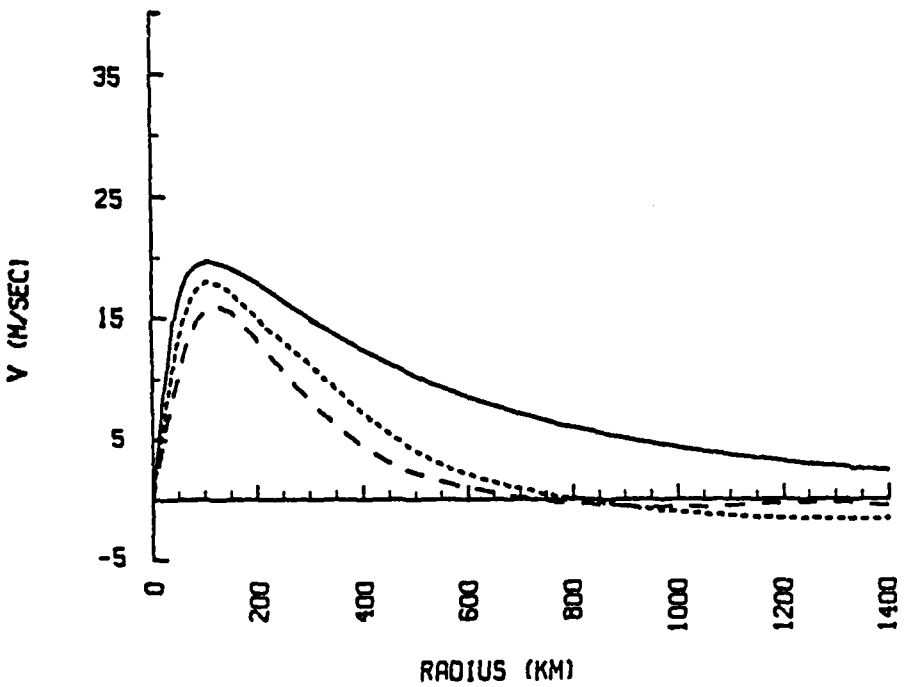

Fig. 6-4. Tangential wind profiles during the ultra-long integration for the weak-large vortex at t = 0 (solid), at t = 144 h (short-dashed) and at t = 288 h (long-dashed).

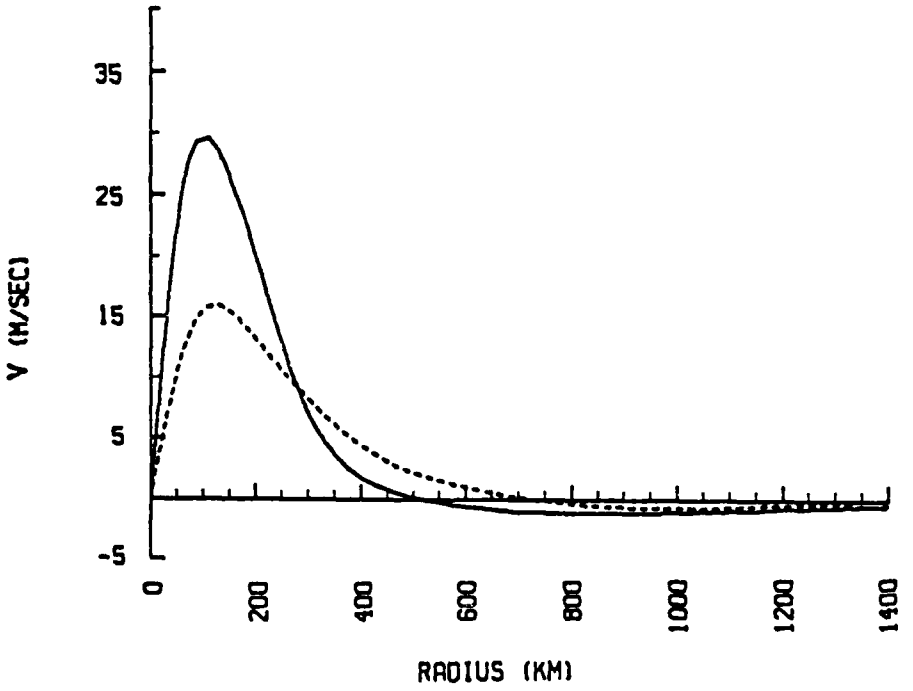

Fig. 6-5. A comparison of the basic vortex and the weak-large vortex tangential wind profiles at t = 288 h.

Kitade (1981) also varied the scale of the tangential wind profile in a similar model and found large differences in the direction of motion. However, his integrations were for only 72-96 h. Longer integrations may have shown that a steady-state motion vector would have developed as they approached the universal β-neutral profile.

In summary, ultra-long integrations of the model have shown that the speed and direction of motion at the end of very long forecasts is very similar for all vortices considered. This common motion vector is consistent with the adjustment toward a common tangential wind profile at the end of the integrations, especially in the outer portions of the vortex. That is, there appears to exist a natural, "β-neutral" profile that is hypothesized to only be a function of latitude, at least for the simple dynamics of this model.

Departures from the neutral profile result in track deviations. Furthermore, linear processes (β) are responsible for forcing the the vortices to the β-neutral profile as the nonlinear-only integrations showed very little change in the tangential wind even after long integrations. Thus, other energy (e.g., baroclinic processes) and vorticity sources (e.g., divergence) and environmental interactions are thought to be required to sustain deviations from the β-neutral structure and to explain the wide variety of structures found in nature.

VII. CONTRIBUTION TO THE MOTION BY DIFFERENT SCALES IN THE INITIAL VORTEX

The initial-condition sensitivity experiments in Chapter III demonstrate that vortex flow beyond r = 300 km controls beta drift. Furthermore, reductions in the flow beyond r = 800 km in the weak-large vortex (B3) caused the speed of motion to be smaller with little change in path. These experiments imply that the large scales of motion (1000-2000 km) are critical to the motion process. In this Chapter, the initial-condition sensitivity experiments are extended by selectively retaining or eliminating (by filtering) the different scales of motion in the specification of the initial vortex. Several implications for tropical cyclone observing systems and track forecast models will be drawn based on these experiments.

The "scale" of motion is defined here by the wavelength of the Fourier basis functions (sines and cosines). Fourier representations of atmospheric variables have been widely used in meteorology to derive linear solutions to the equations of motion and to analyze nonlinear interaction (e.g., Haltiner and Williams, 1980). For this tropical cyclone application, a Fourier transform procedure for general fields on 2-D rectangular grids is used to modify selectively the scales in the initial conditions from the analytical symmetric wind profile.

A. THE FOURIER TRANSFORM PROCEDURE

The general 2-D Fourier transform method used in these experiments was originally developed by Errico (1985) to study the spectra of a limited-area model solutions. In a later study, Errico and Baumhefner (1987) used the same procedure in a mesoscale model predictability study in which

they made two model integrations with and without a perturbation ("twin" experiment method). They used the general 2-D Fourier transform to control the scale of the perturbation.

The Errico (1985) procedure is a two-step process. The field is first "detrended" by removing the domain-wide, linear trend along each row and column. Consider a rectangular grid with N points in the north-south or y direction and M points in the east-west or x direction. A 2-D function with equally spaced discrete points, $f_{i,j}$, where i = 1, 2, ... , M in the x direction and j = 1, 2, ..., N in the y direction is detrended by first removing the domain-wide y linear variation at each i point. The corresponding slope for the domain-wide y linear variation is

$$s_{yi} = \frac{f_{i,N} - f_{i,1}}{N - 1} \tag{7.1}$$

and the detrended field, $f'_{i,j}$, in y is

$$f'_{i,j} = f_{i,j} - 0.5(2j-N-1)s_{yi} \tag{7.2}$$

The slope for the domain-wide x linear variation is

$$s_{xj} = \frac{f'_{i,N} - f'_{i,1}}{M - 1} \tag{7.3}$$

and the final detrended field, $f^{D}_{I,j}$, is

$$f^{D}_{I,j} = f'_{i,j} - 0.5(2i-M-1)s_{xj} \tag{7.4}$$

The trend field, $f^{T}_{I,j}$, is

$$f^{T}_{I,j} = 0.5(2j-N-1)s_{yi} + 0.5(2i-M-1)s_{xj} \tag{7.5}$$

Subtracting the linear variation ($f^{T}_{I,j}$) results in a field ($f^{D}_{I,j}$) that is cyclically continuous in both directions. This detrending step is required to correctly

trends that form due to the extrapolation-type boundary conditions on the north and south boundaries.

In the second step, the detrended field is transformed using a discrete, 2-D Fast Fourier Transform (FFT) from the NCAR Scientific Subroutine Package called "FOURT." The mathematical form of the FOURT FFT was determined by inputting analytical 2-D waves of a specified amplitude and wavelength into the routine and examining the output. The forward (field --> coefficients) transform is

$$F_{m,n} = \sum_{i=1}^{M-1} \sum_{j=1}^{N-1} f^{D}_{i,j} \exp\left[-(-1)^{1/2}\{k_m(i-1) + l_n(j-1)\}\right] , \tag{7.6}$$

where

$$k_m = \begin{cases} \dfrac{2\pi}{M-1}(m-1) & , \quad m = 1, K_{max} \\ \dfrac{2\pi}{M-1}(m-K_{max}) & , \quad m = K_{max}+1, \ldots, M-1 \text{ (M odd)} \\ \dfrac{2\pi}{M-1}(m-K_{max}-1) & , \quad m = K_{max}+1, \ldots, M \text{ (M even)} \end{cases} \tag{7.7}$$

and

$$l_n = \begin{cases} \dfrac{2\pi}{N-1}(n-1) & , \quad n = 1, L_{max} \\ \dfrac{2\pi}{N-1}(n-L_{max}) & , \quad n = L_{max}+1, \ldots, N-1 \text{ (N odd)} \\ \dfrac{2\pi}{N-1}(n-L_{max}-1) & , \quad n = L_{max}+1, \ldots, N \text{ (N even)} \end{cases} \tag{7.8}$$

and $K_{max} = M/2+1$ and $L_{max} = N/2+1$ (integer division).

The 2-D wavelength of the Fourier modes is defined by

$$\lambda_{m,n} = \frac{2\pi}{L_{m,n}} , \tag{7.9}$$

where the 2-D wavenumber is

$$L_{m,n} = (k_m^2 + l_n^2)^{1/2} \quad . \tag{7.10}$$

The amplitude $A2_{m,n}$ of a 2-D mode is found from the Fourier coefficients, $F_{m,n}$, according to

$$A2_{m,n} = \begin{cases} \dfrac{|F_{1,n}|}{(M-1)(N-1)} & , \quad m = 1 \\ \dfrac{|F_{m,n}|}{(M-1)(N-1)} + \dfrac{|F_{m,n-N+1}|}{(M-1)(N-1)} & , \quad m \neq 1, \; n \neq 1 \\ \dfrac{|F_{m,1}|}{(M-1)(N-1)} & , \quad n = 1 \end{cases} \quad , \tag{7.11}$$

where | | indicates the magnitude of the $F_{m,n}$ complex number.

The Fourier filtering is accomplished by setting to zero the amplitude of the wavelengths (modes) to be filtered and then reconstructing the field with the truncated Fourier coefficients via the "backward" Fourier transform

$$f_{I,j} = \frac{1}{(M-1)(N-1)} \sum_{i=1}^{M-1} \sum_{j=1}^{N-1} \times$$

$$F_{m,n} \exp\left[(-1)^{1/2} \{k_m(i-1) + l_n(j-1)\}\right] \quad . \tag{7.12}$$

B. EXPERIMENT DESIGN

The scales in the initial vortex are arbitrarily grouped into three categories according to following definition:

SMALL	-	0 km	$\leq \lambda \leq$	500 km
MEDIUM	-	500 km	$< \lambda \leq$	1500 km
LARGE	-		$\lambda >$	1500 km

These categories represent different vortex flow regimes. The "small" scales represent the inner region of the vortex ($r < 250$ km for zone ~ 500 km wide), the "medium" scales

include the critical annulus (r = 300 - 800 km) and the "large" scales include the vortex flow far from the center (r > 800 km).

Based on the above definitions, six model experiments are performed for a given vortex as described in Table 7-1. The experiments are designed to demonstrate how the small-, medium- and large-scale components of the vortex behave on an individual (i.e., separately) basis (Exps. F4-F6) and how they contribute to the overall motion (Exps. F1-F3).

TABLE 7-1. Description of the model experiments with filtered initial conditions.

Exp.	Scales Removed	Scales in the Initial Conditions	Purpose
F1	Small	Medium/Large	Role of inner region
F2	Medium	Small/Large	Role of critical annulus
F3	Large	Small/Medium	Role of large scales
F4	Small/Medium	Large	How large-scale component of the vortex moves
F5	Medium/Large	Small	Motion of the small scales
F6	Small/Large	Medium	Motion of the medium scales

The filtering is first applied to the total solution (with all scales) to provide the initial conditions and to serve as a basis for comparison. For example, even though the middle scales are filtered out of the initial conditions (Exp. F2), energy will be transferred through nonlinear scale interaction from the small and large scales to the medium scales during the integration. Comparing the spectrum of the unfiltered model solution to the model run without medium scales in the initial conditions indicates how much energy transfer did occur.

Four vortices are tested: (i) the basic vortex (B1), (ii) the weak-large vortex (B3); (iii) the cyclonic perturbation vortex (S8); and (iv) the anticyclonic

perturbation vortex (S9). These vortices represent a variety of structures and motion behaviors and have been used in the previous chapters.

C. PERFORMANCE CHARACTERISTICS OF THE FOURIER FILTER

Before discussing the track solutions, it is important to establish the accuracy of the 2-D Fourier transforms and the filtering procedure. The amplitudes of the 2-D modes of the initial streamfunction for the basic vortex (B1) are shown in Fig. 7-1. A log-log plot is used to emphasize the smaller mode numbers that contain the greatest energy. The mode number is translated (via 7.10) to a physical wavelength in Table 7-2 for the standard model configuration (101x101 points, Δx = 40 km). The normal convention is to use 0 for the mode number corresponding to the mean and 1 for the gravest mode (one cycle over the domain). However, the FORTRAN computer code that performs that FFT uses 1 for the first mode number. Thus, to minimize confusion in relating the analytical equations to the code, the computer convention for the mode number is used.

TABLE 7-2. Wavelength of the 1-D waves as a function of mode number. The wavelength is the same in x and y as the grid is square.

Mode Number	Wavelength (km)	
1	∞	(the mean)
2	3920	(length of the domain)
3	1960	
4	1307	
5	980	
6	784	
7	653	
8	560	
9	490	
10	435	
11	392	
12	356	
13	327	
14	301	
15	280	
.	.	
.	.	
.	.	
51	80	(Nyquist wavelength)

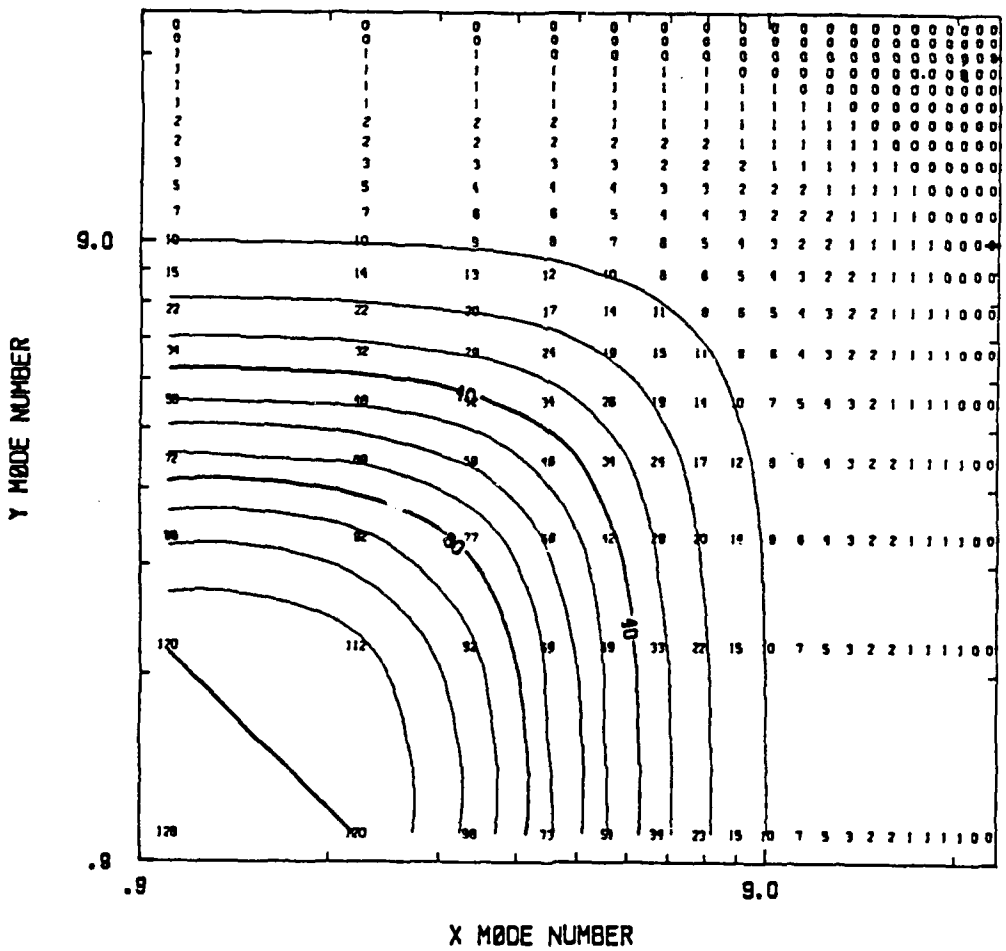

Fig. 7-1. Amplitudes (small numbers) of the 2-D modes of the initial streamfunction for the basic B1 vortex. The units are 10^3 m^2/s with a contour interval of 10 ($x10^3$) m^2/s. The mode numbers are indicated on the axes.

AD-A190 961 THE ROLE OF VORTEX STRUCTURE IN TROPICAL CYCLONE MOTION 4/4
(U) NAVAL POSTGRADUATE SCHOOL MONTEREY CA M FIORINO
DEC 87

UNCLASSIFIED FFG 4/2 NL

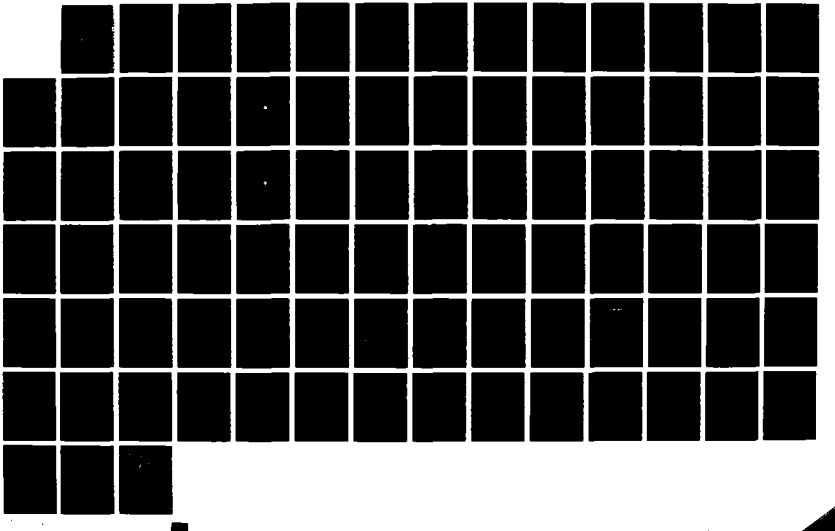

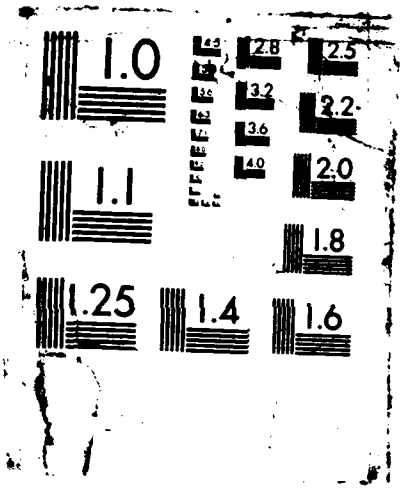
1.0
1.1
1.25
1.4
1.6
1.8
2.0
2.2
2.5
2.8
3.2
3.6
4.0

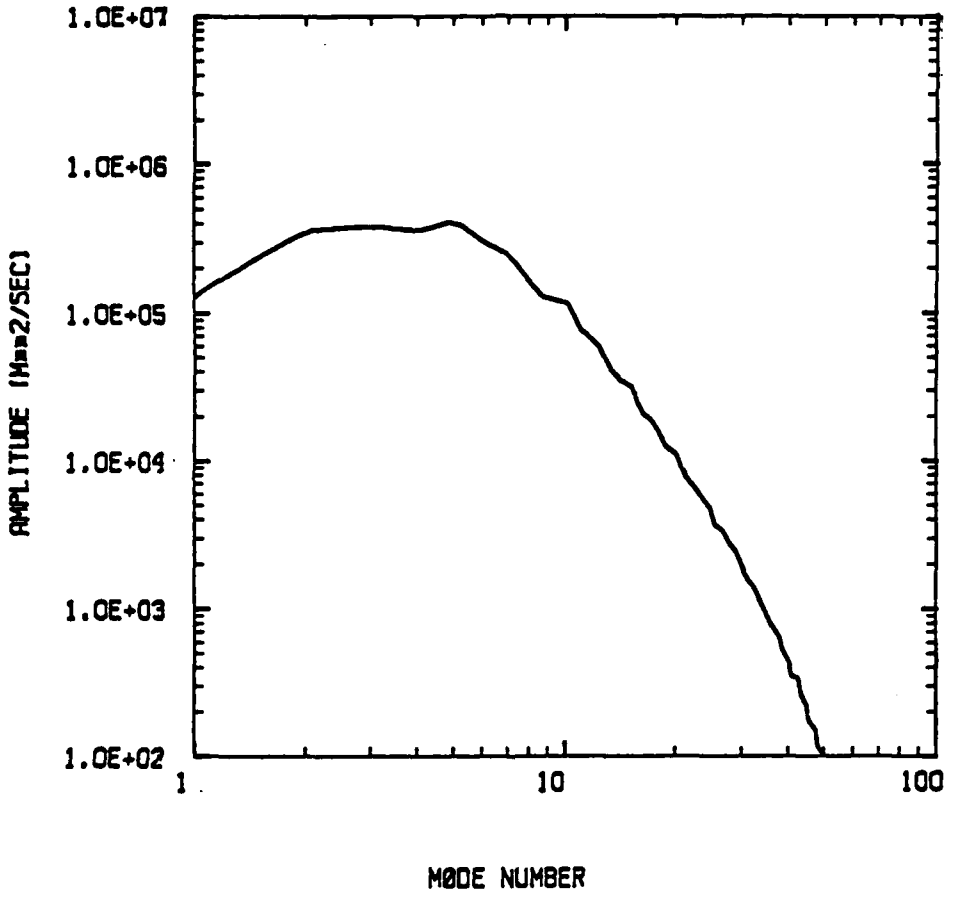

Fig. 7-2. 1-D spectra calculated from the 2-D spectrum of the initial streamfunction for the basic B1 vortex.

The 2-D spectra in Fig. 7-1 shows that most of the amplitude in the initial streamfunction is contained in mode numbers less than 10 or wavelengths greater than 400 km. Thus, most of the structure of a typical tropical cyclone vortex is "projected" large scales. Even though a tropical cyclone appears to be a "small" synoptic-scale feature, much of the structure is contained in much larger scales when viewed using a Fourier series representation. It is this projection onto the large scales that is critical to the beta drift of the vortex as these scales are the most dispersive waves on a beta plane.

This 2-D spectra can be "condensed" into a more compact 1-D spectra by summing the amplitudes of the 2-D modes of similar wavelengths. Following Errico (1985), this is accomplished by summing the amplitude of all modes in an modal annulus that depends on the minimum wavenumber. Mathematically, the 2-D wavenumber annuluses (1-D mode #) are defined by

$$+(1/2)\cdot n\cdot k_{min} \leq L_{m,n} < -(1/2)\cdot n\cdot k_{min} \quad ,$$

where the largest resolvable wave (smallest wavenumber) is

$$k_{min} = \frac{2\pi}{M-1} \quad , \tag{7.11}$$

and the 1-D spectrum is calculated as

$$Al_l = \sum_{-½l\cdot k_{min}}^{+½l\cdot k_{min}} F_{m,n} \quad . \tag{7.12}$$

The 1-D spectrum of the basic vortex streamfunction in Fig. 7-2 is derived from the 2-D spectrum shown in Fig. 7-1. Although the maximum amplitude is contained in the 5th mode (wavelength = 980 km) with a value of about 4.0×10^5 m^2/s, modes 2-4 also contain similar amplitudes. The amplitude is

reduced by more than an order of magnitude for mode 10, with a rapid decrease at still larger modes.

An example of the 1-D spectrum of a filtered vortex (Exp. F1) is illustrated in Fig. 7-3. The filtering of the initial symmetric vortex (Fig. 7-3a) is very effective with an extremely sharp cutoff. By contrast, the vortex after 72 h of integration contains additional asymmetric components that were not present in the original vortex. Thus, the efficacy of the filtering is somewhat degraded (Fig. 7-3b) because the 2-D distribution of amplitude is not symmetrical as implied by the annulus summing convention. Nevertheless, the scale removal procedure reduces the amplitude of the filtered scales by at least two to three orders of magnitude.

The 1-D spectra of initial streamfunctions used in model Exps. F2-F6 for the basic vortex are shown in Fig. 7-4 (see Fig. 7-3a for Exp. F1). The sharp cutoff in the spectrum after the filtering clearly indicates which portion of the spectrum is being truncated.

Table 7-3 is a summary of how the filtering reduces the total streamfunction amplitude (proportional to energy) in the initial conditions and what percentage of the total amplitude is accounted for by each wave group. The total amplitude is roughly proportional to the outer strength, which implies that the outer portion of the vortex determines the overall energy as the inner regions are the same in for all vortices, except for B3 which is a weaker vortex. More important is how the distribution of amplitude among the scales depends on the vortex structure. Much more amplitude is projected onto the largest scales in the weak-large vortex compared to the basic vortex (60 % vs 26 %). Furthermore, the amplitude in the smallest scales is nearly constant in the basic vortex and the symmetric perturbation vortices (B1, S8 and S9). The vortex specification

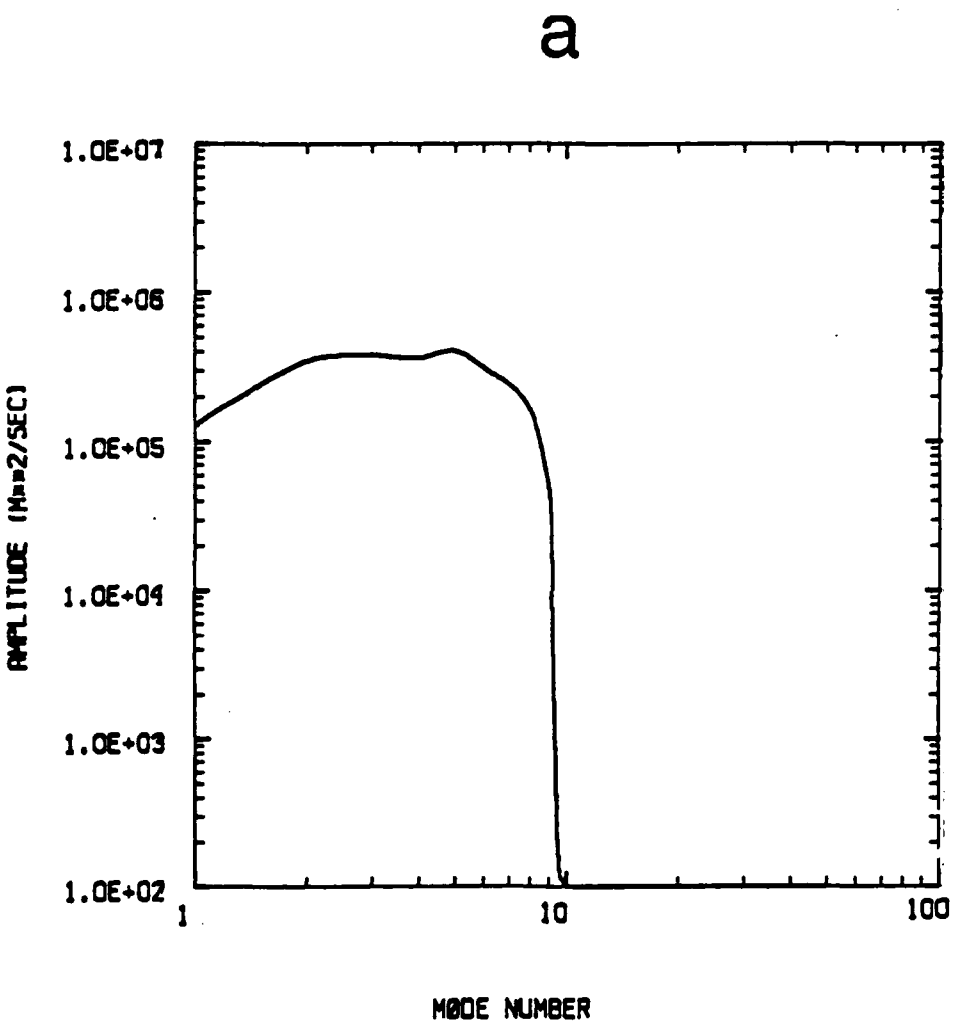

Fig. 7-3. 1-D spectra of the basic vortex in which all scales < 500 km have been removed for (a) the initial conditions and (b) the filtered 72-h solution. This filtering is used in Exp. F1.

b

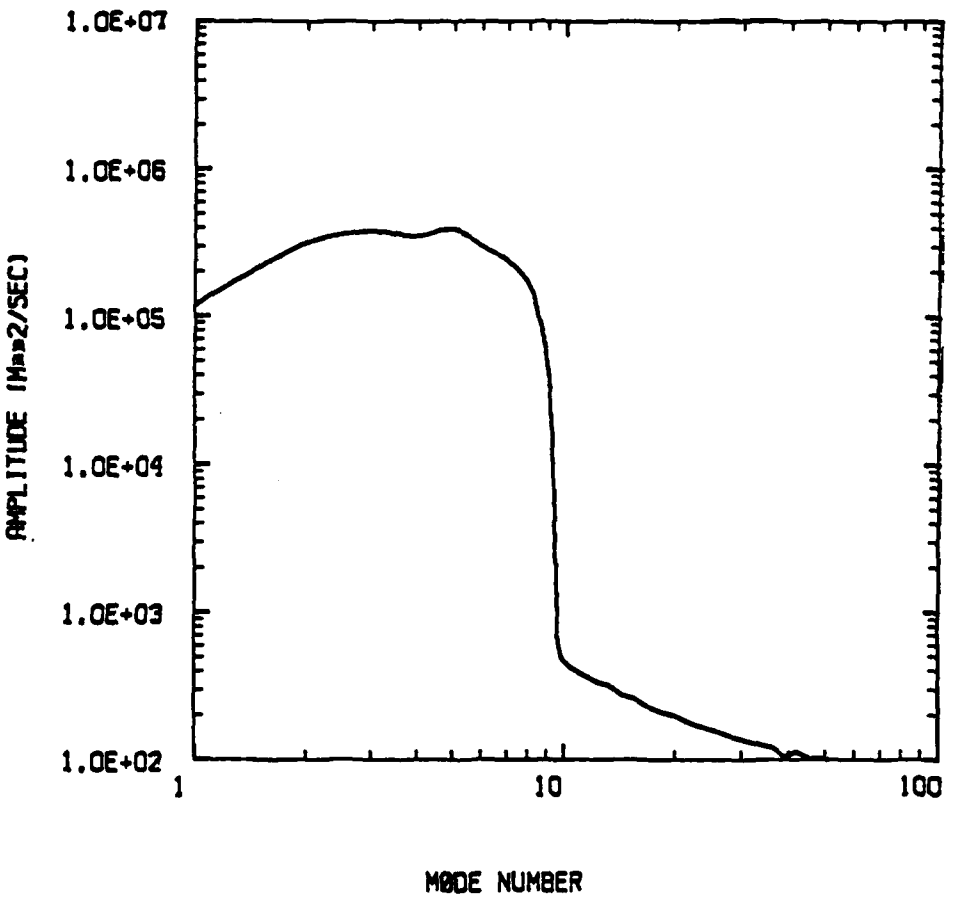

Fig. 7-3. (Continued)

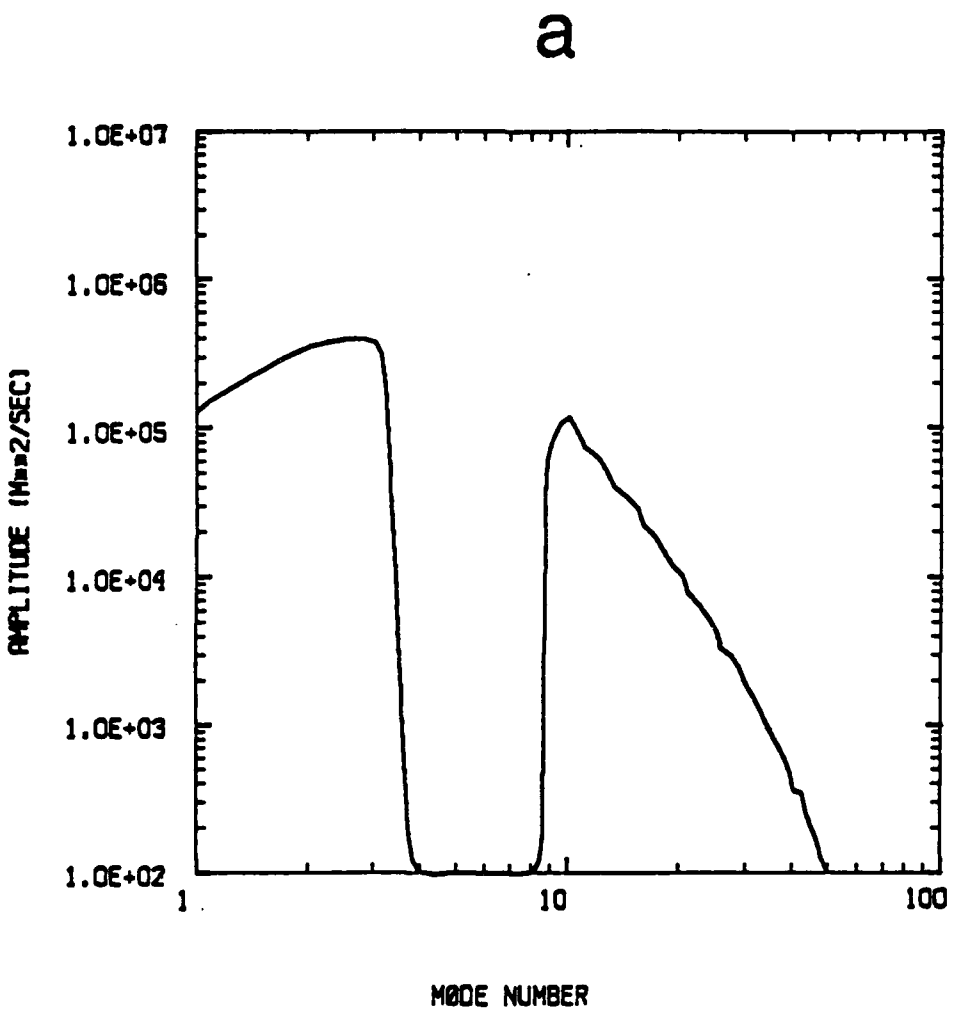

(a) Exp. F2 -- remove the medium scales

Fig. 7-4. As in Fig. 7-3a, except for the other model experiments.

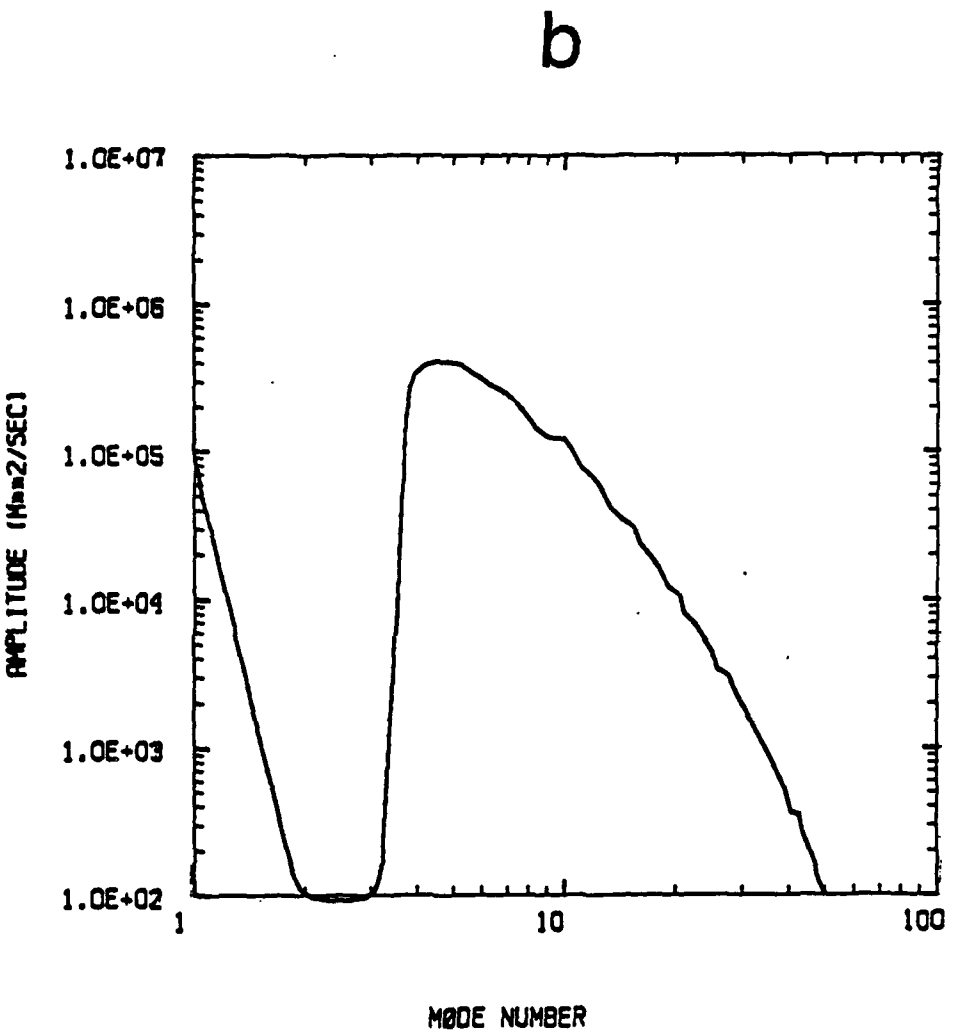

(b) Exp. F3 -- remove the large scales

Fig. 7-4. (Continued)

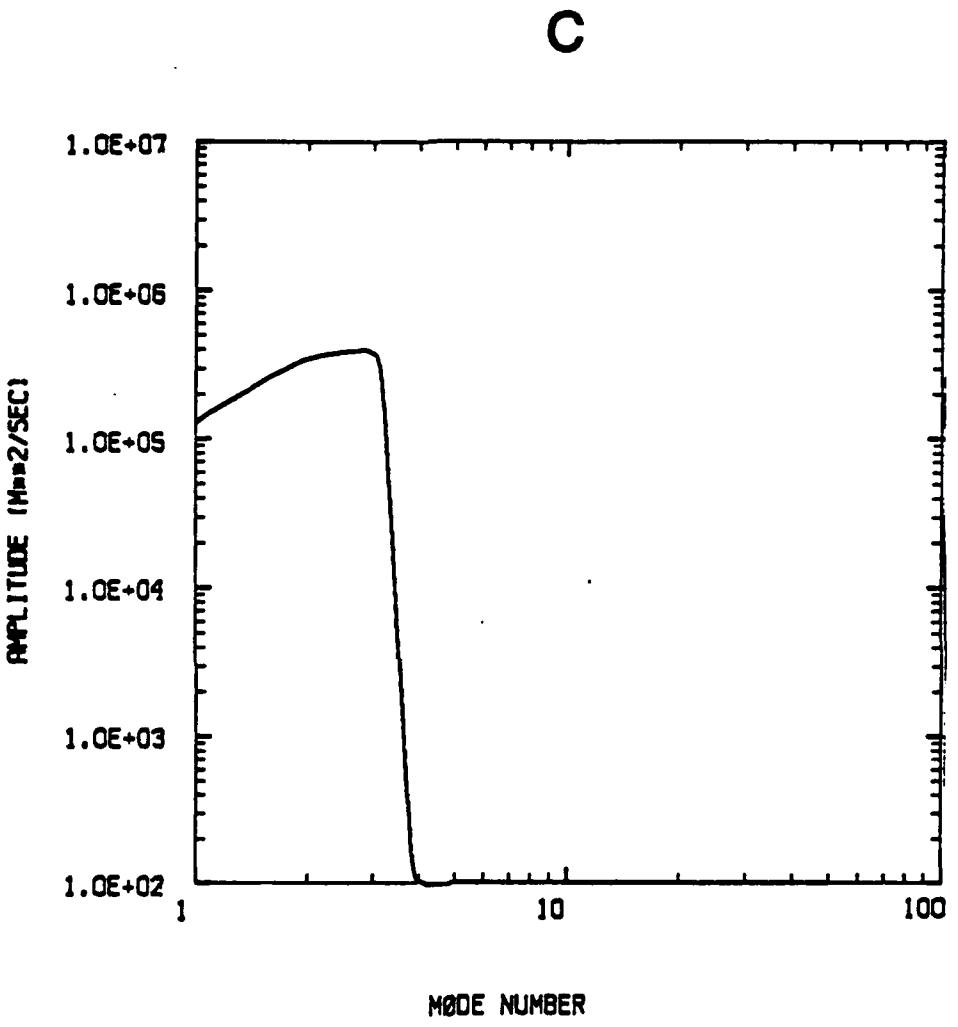

(c) Exp. F4 -- retain only the large scales

Fig. 7-4. (Continued)

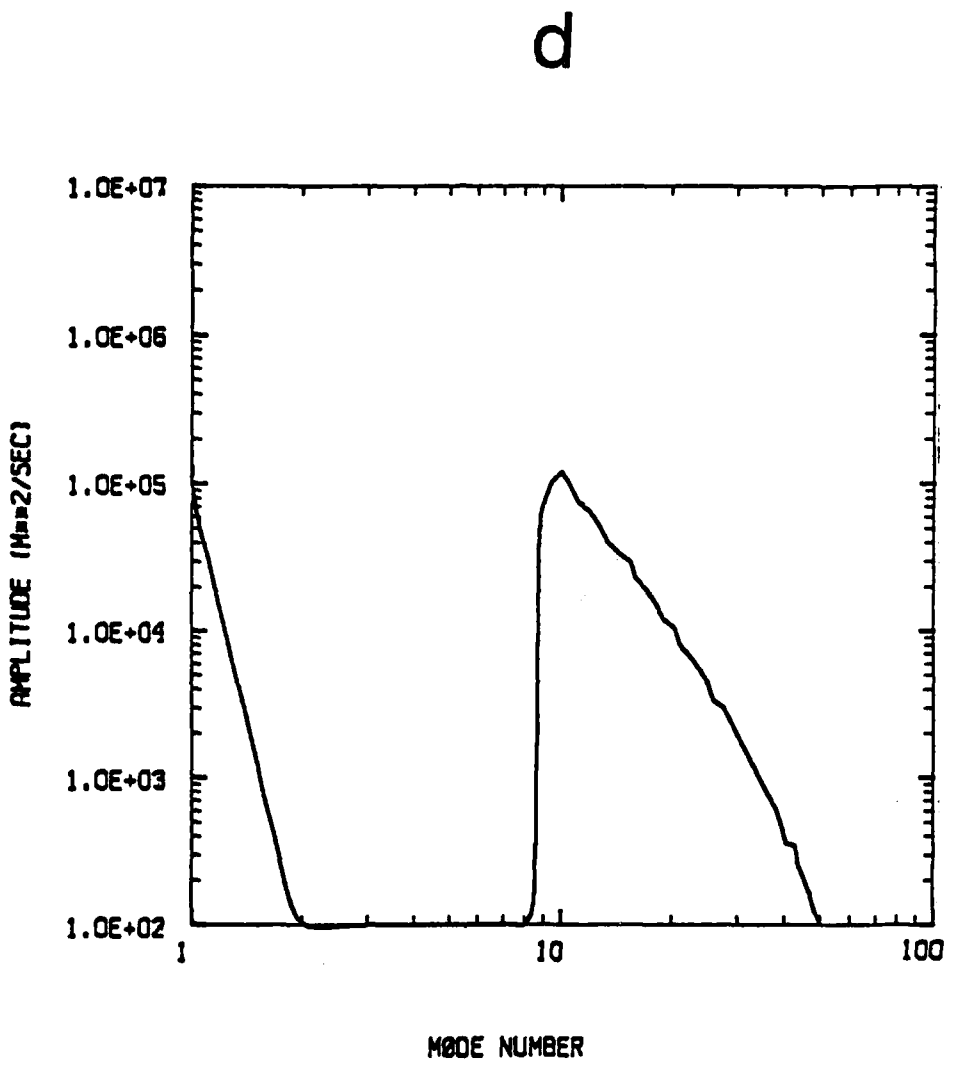

(d) Exp. F5 -- retain only the small scales

Fig. 7-4. (Continued)

e

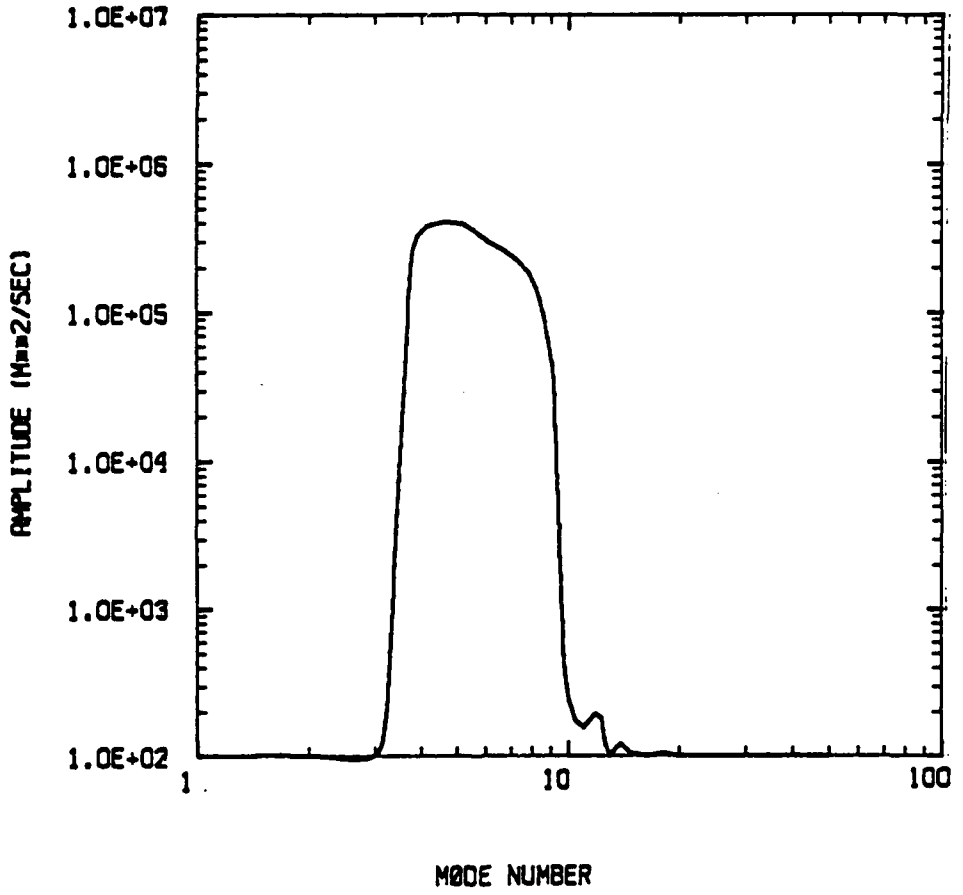

(e) Exp. F6 -- retain only the medium scales

Fig. 7-4. (Continued)

procedure used to perturb the symmetric flow in the "critical annulus" is thus very effective in confining changes to the medium and large scales. In particular, notice how the perturbations had the greatest effect on the medium scales, as intended.

TABLE 7-3. Total streamfunction amplitude for the four vortices in the six experiments. The number in parentheses is the percentage of the unfiltered streamfunction amplitude accounted for by the filtered streamfunction. The outer strength and the steady state speed of motion is also provided.

Total Streamfunction Amplitude

(10^6 m^2/s)

Vortex:	B1 Basic	B3 Weak Large	S? Cyclonic Symmetric Pert.	S9 Anticyclonic Symmetric Pert.
Exp. #				
--	2.82 (100)	4.62 (100)	3.23 (100)	2.47 (100)
F1	2.24 (79)	3.86 (84)	2.52 (78)	1.92 (78)
F2	1.32 (49)	3.10 (67)	1.64 (51)	0.91 (37)
F3	2.10 (75)	1.40 (30)	2.10 (65)	2.09 (85)
F4	0.73 (26)	2.78 (60)	1.03 (31)	0.37 (15)
F5	0.58 (21)	0.32 (7)	0.80 (24)	0.55 (22)
F6	1.51 (53)	1.52 (33)	1.49 (45)	1.57 (63)
	Outer Strength (m/s)			
--	3.70	8.00	4.50	3.30
	Speed of Motion (m/s)			
--	2.65	4.40	3.10	1.80

The initial streamfunction in the model experiments for the basic vortex is shown in Fig. 7-5 to illustrate how the filtering modified the initial conditions. Notice that the case in which the small scales have been removed (Fig. 7-5b

a

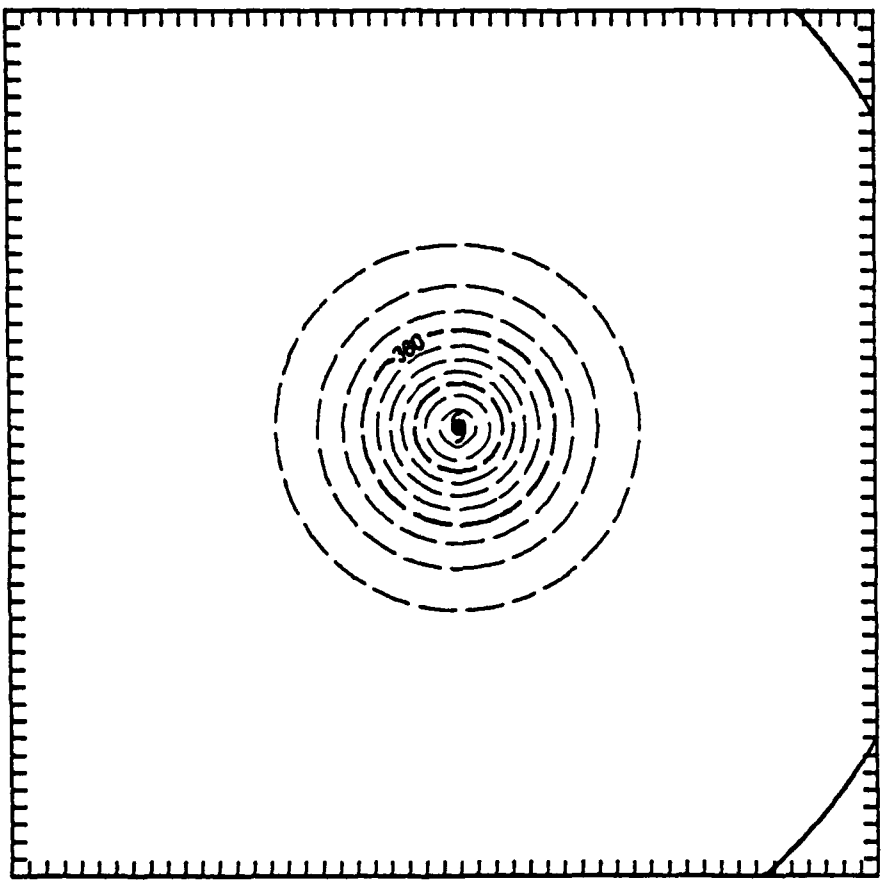

(a) Unfiltered
contour interval = 90 ($\times 10^4$) m^2/s
minimum contour = -900 ($\times 10^4$) m^2/s

Fig. 7-5. Initial streamfunction (m^2/s) for the unfiltered and filtered experiments for the basic vortex. The grid is indicated by the tick marks and the domain is a 2000x2000 km. This domain will be used in all subsequent figures unless otherwise noted. The hurricane symbol denotes the center of the vortex.

b

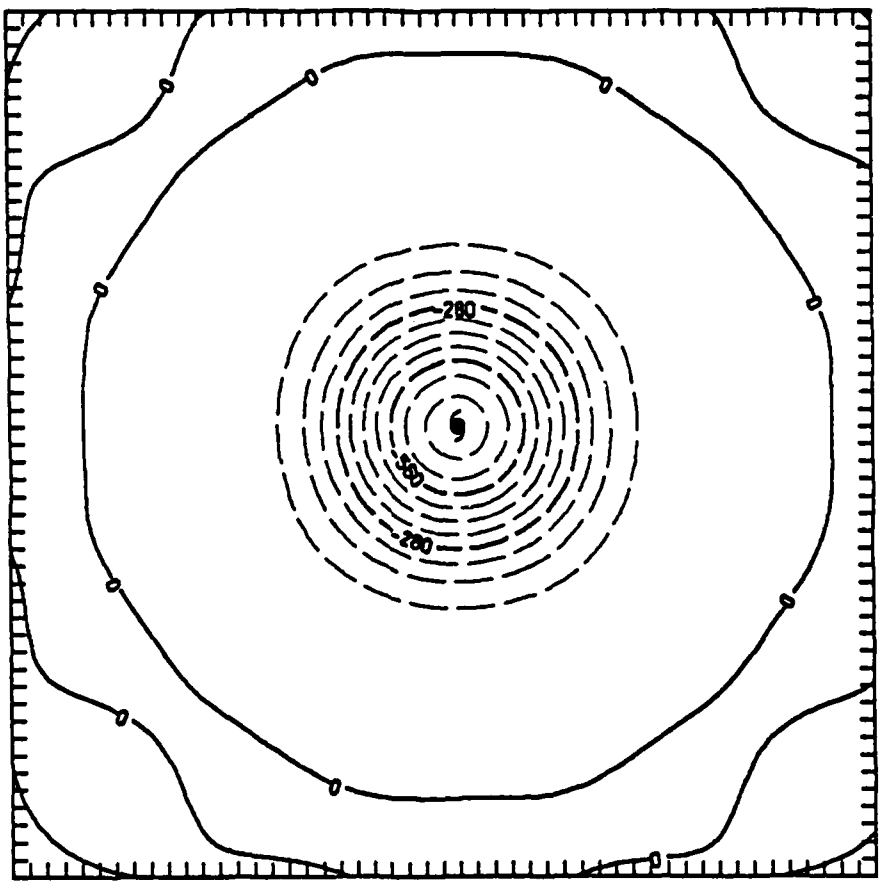

(b) Exp. F1 -- remove small scales
contour interval = 70 ($\times 10^4$) m^2/s
minimum contour = -700 ($\times 10^4$) m^2/s

Fig. 7-5. (Continued)

C

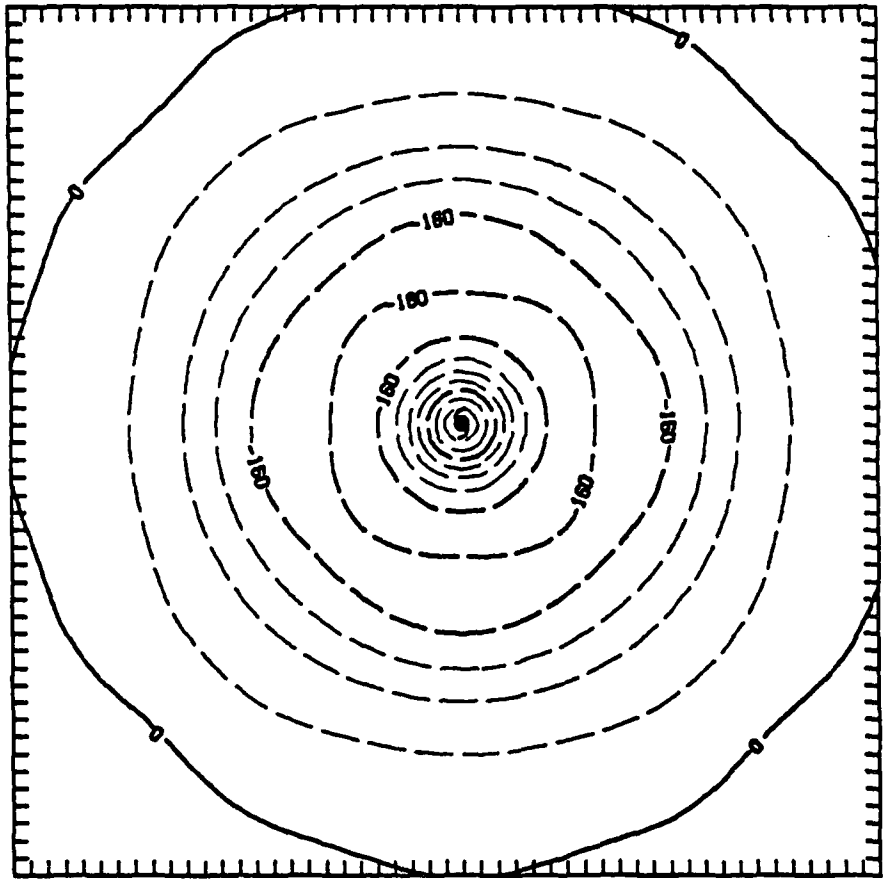

(c) Exp. F2 -- remove medium scales
contour interval = 40 ($\times 10^4$) m^2/s
minimum contour = -400 ($\times 10^4$) m^2/s

Fig. 7-5. (Continued)

d

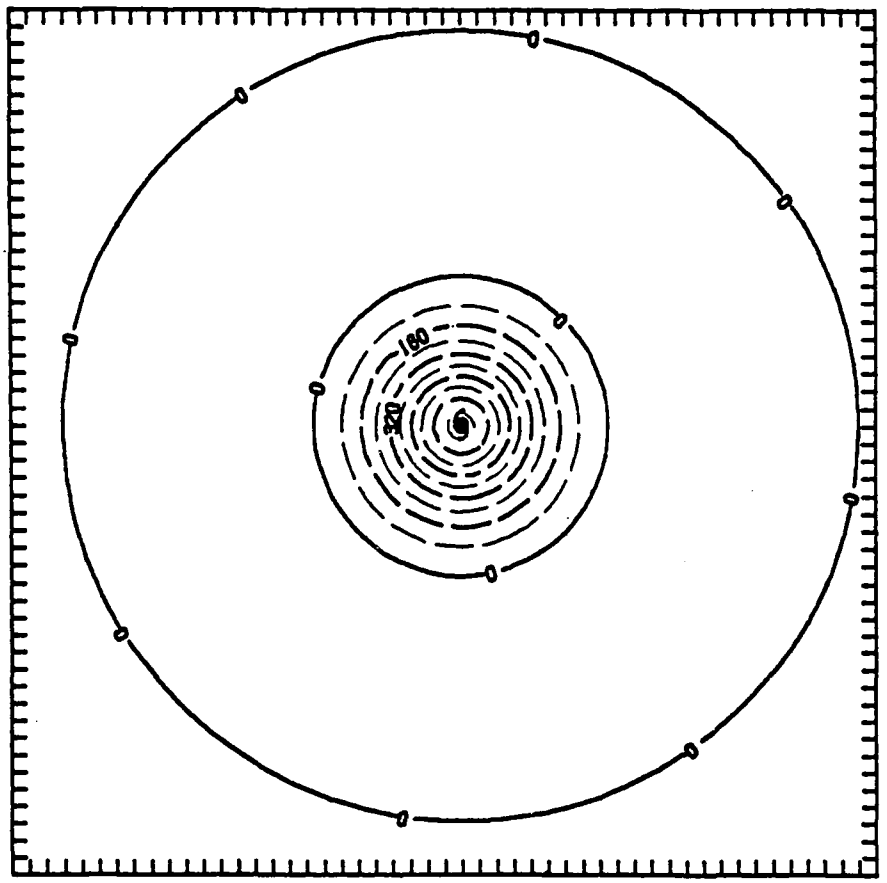

(d) Exp. F3 -- remove small scales
contour interval = 80 ($\times 10^4$) m^2/s
minimum contour = -720 ($\times 10^4$) m^2/s

Fig. 7-5. (Continued)

e

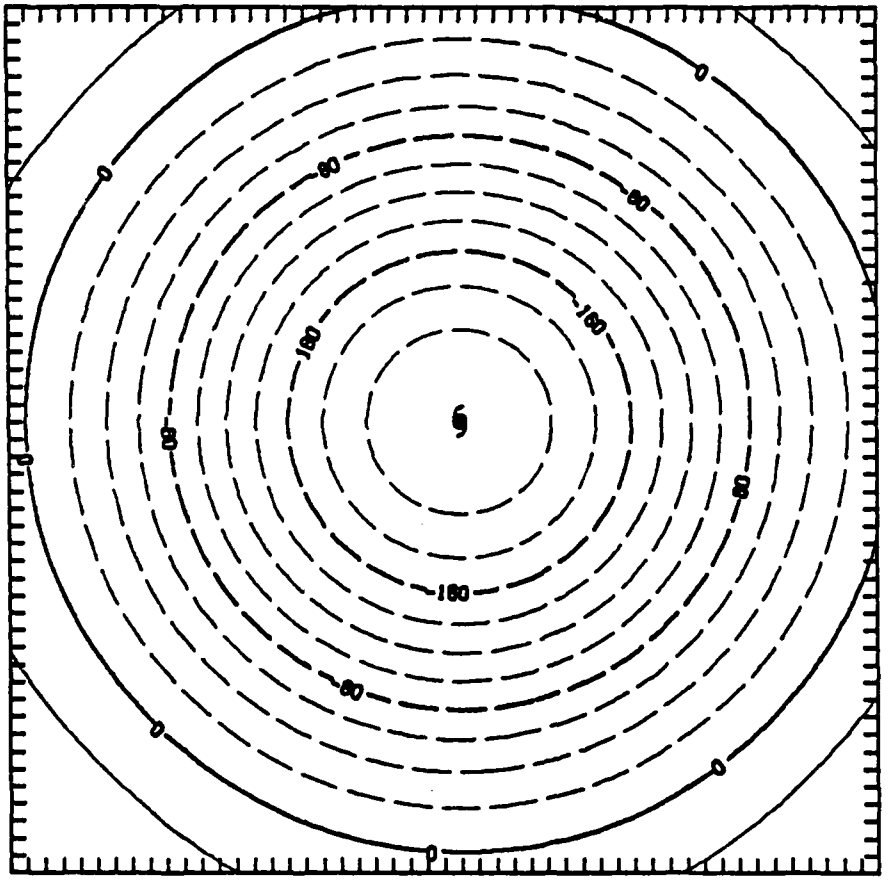

(e) Exp. F4 -- large scales only
contour interval = 20 ($\times 10^4$) m^2/s
minimum contour = -200 ($\times 10^4$) m^2/s

Fig. 7-5. (Continued)

f

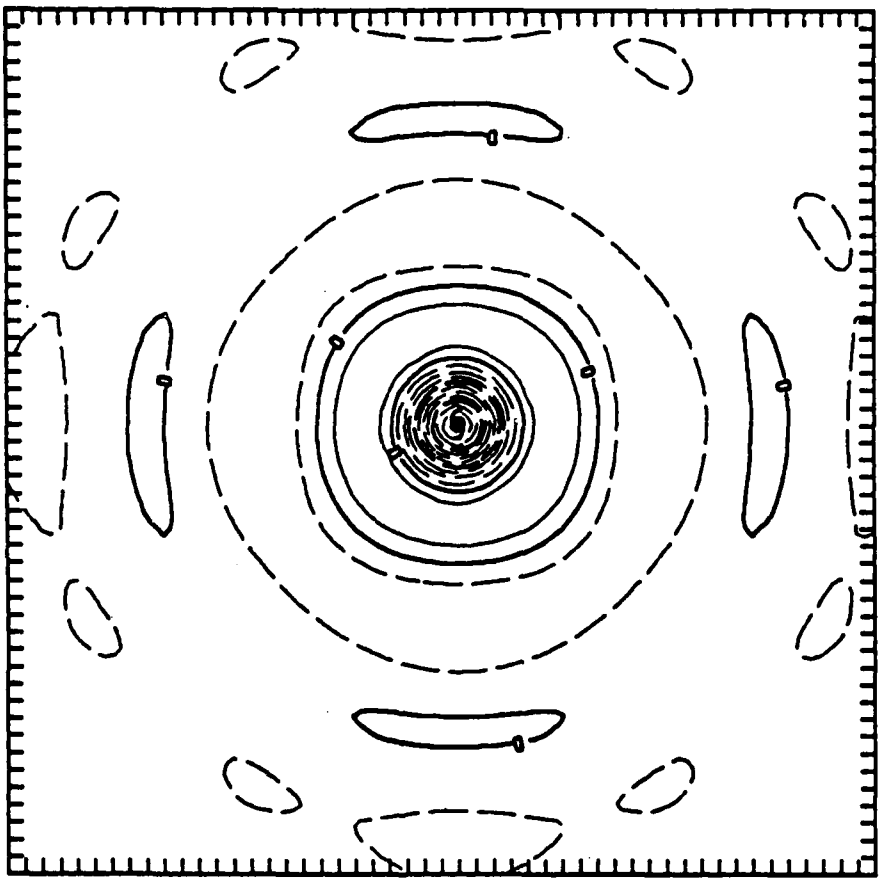

(f) Exp. F5 -- small scales only
contour interval = 70 ($\times 10^4$) m^2/s
minimum contour = -700 ($\times 10^4$) m^2/s

Fig. 7-5. (Continued)

g

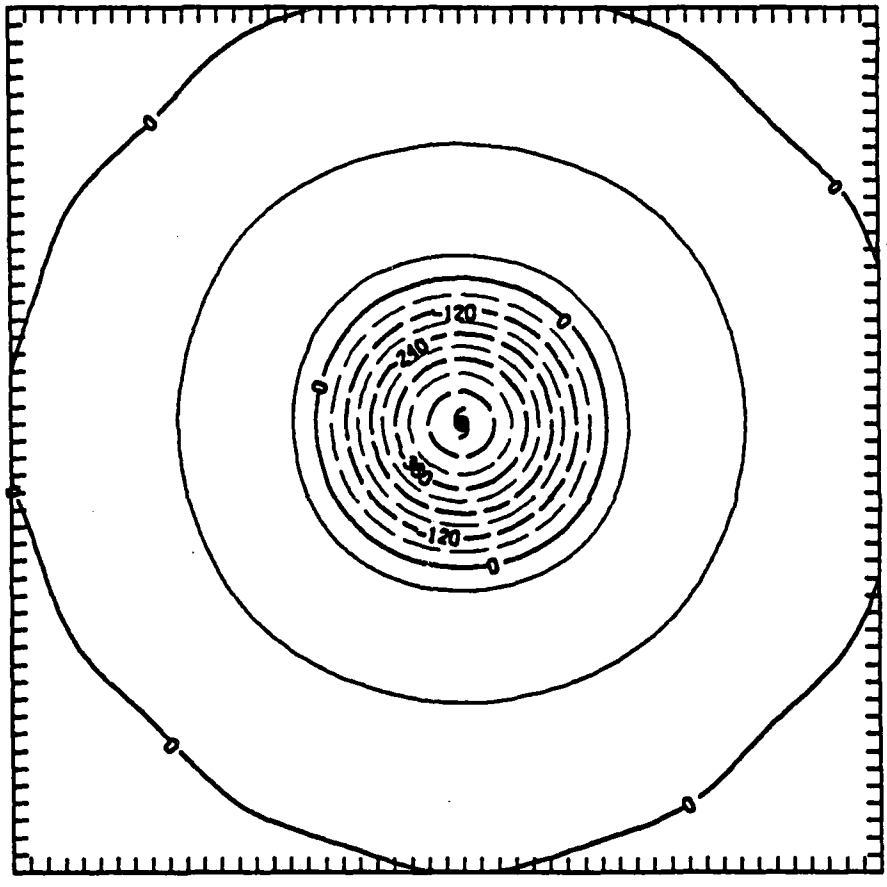

(g) Exp. F6 -- medium scales only
contour interval = 60 ($\times 10^4$) m^2/s
minimum contour = -480 ($\times 10^4$) m^2/s

Fig. 7-5. (Continued)

versus 7-5a) is very similar except in the inner regions where the gradients and the minimum streamfunction have been reduced. Similarly, examining the wave groups on an individual basis (Fig. 7-5 e-g) shows how the filtering changes the structure of the vortex. Adjusting the small (Fig. 7-5b) and/or medium (Fig. 7-5c) scales causes a distortion in the circularly symmetric streamfunction. This reflects the difficulty of representing a radial function on a Cartesian grid with Fourier basis functions (refer also to Fig. 7-5f). A more natural set of basis functions for the radial component of fields on a cylindrical grid would be Bessel functions. Nevertheless, the distortion is not severe and the filtering does modify the vortex structure as desired.

The tangential wind profiles of the filtered and unfiltered vortices (Fig. 7-6) show how the total vortex can be considered as a combination of vortices of various scales. The profiles appear similar to Bessel functions of the first kind, which are the symmetric component of the solution to the linear wave equation in cylindrical coordinates (Haberman, 1983). The solution to the wave equation in Cartesian coordinates involves sines and cosines (Fourier basis functions). Thus, the Fourier filtering appears to be equivalent to modifying the natural basis function for the symmetric component of a field (Bessel functions).

Because the inner structure is determined by the small and medium scales, the streamfunctions containing only small and medium scales have a similar maximum wind speed, but with a different RMW. Beyond r = 400 km, the medium and large scales make the greatest contribution to the outer structure. In the modified streamfunctions from the symmetric perturbation experiments, there are considerable differences in how the medium and large scales determine the

flow in the critical annulus (see Fig. 7-6c versus Fig. 7-6d). It is also noteworthy that the sum of the filtered profiles appears to reproduce the main features of the unfiltered profile, which verifies that the filtering is able to cleanly partition the scales.

Comparison of the 1-D spectrum at t = 72 h in Fig. 7-7 with the spectrum of the initial conditions (after removal of selected waves) shows some (about 5% of the original) energy has been transferred to the filtered scales. That is, nonlinear advection processes have not restored the deleted scales by a significant transfer of streamfunction amplitude between the scales after 72 h. Thus, modification of scales in the initial vortex will have long-term effects on the structure and the beta drift. This result may not be applicable to more complicated models with energy sources (e.g., diabatic physics) and dynamics that can generate smaller scales (e.g., baroclinic instability). To the extent that the tropical atmosphere is barotropic and nondivergent, it is likely that the tropical cyclone vortex structure modifications will tend to be persistent and that motion due to the beta effect will tend to be constant unless the environment or external forcing changes significantly.

D. TRACK RESULTS

The 72-h forecast tracks for the unfiltered vortex and the initial conditions in which the large scales are retained or are removed are shown in Fig. 7-8. For all four vortices (two not shown), eliminating the large scales reduces the speed of motion, although the path is unchanged. The initial tangential wind profiles for these experiments are given in Fig. 7-9 to understand the motion. Removing the large scales results in an anticyclone beyond r = 400 km for both the B1 and S8 vortices, which reduces the relative

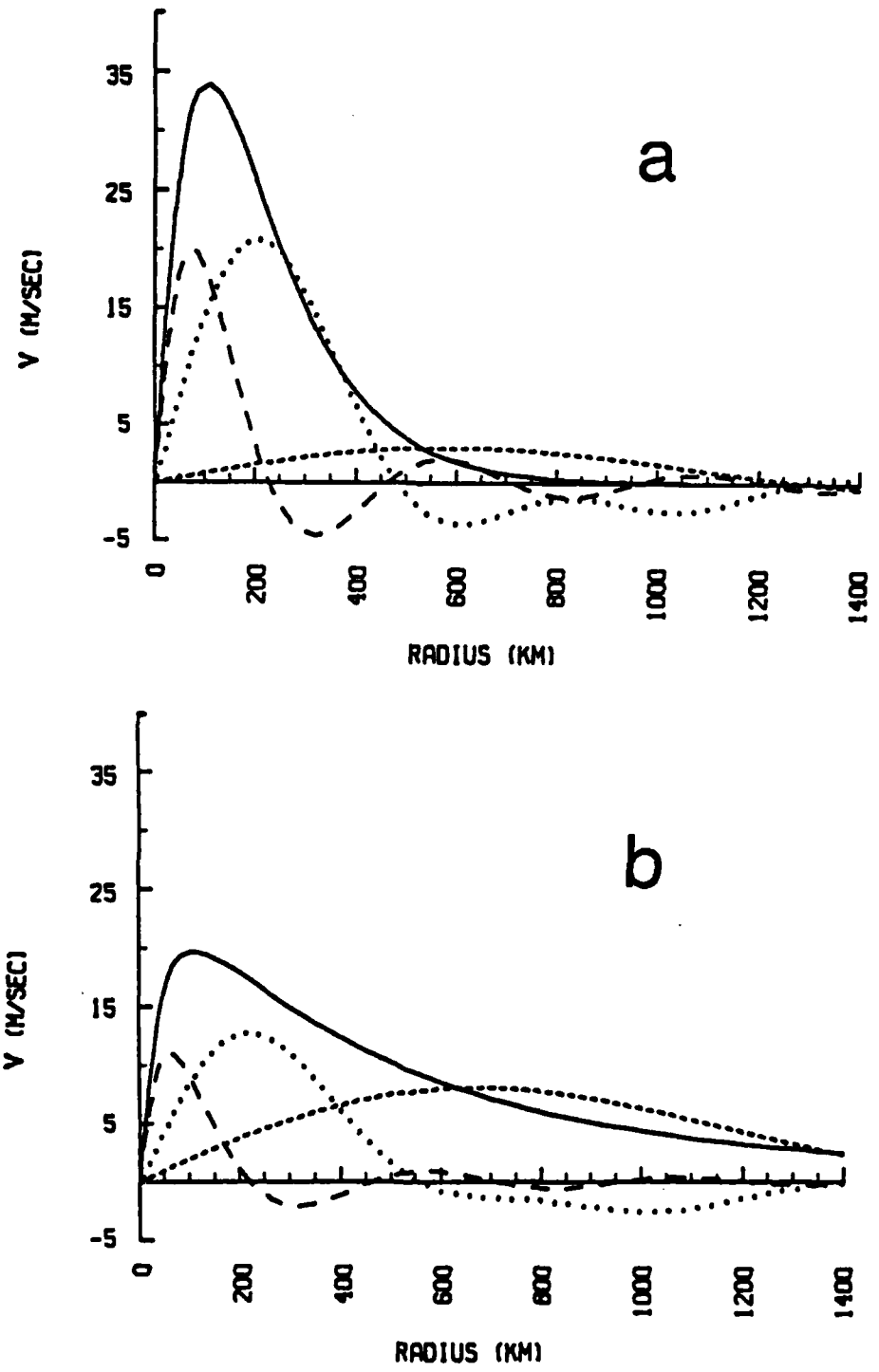

Fig. 7-6. Tangential (m/s) wind profiles for the unfiltered vortex (solid), the small scales (long dashed), the medium scales (dotted) and the large scales (short-dashed). Panel (a) is for the basic vortex (B1); (b) the weak-large vortex (B3); (c) The cyclonic perturbation vortex (S8); and (d) the anticyclonic perturbation vortex (S9).

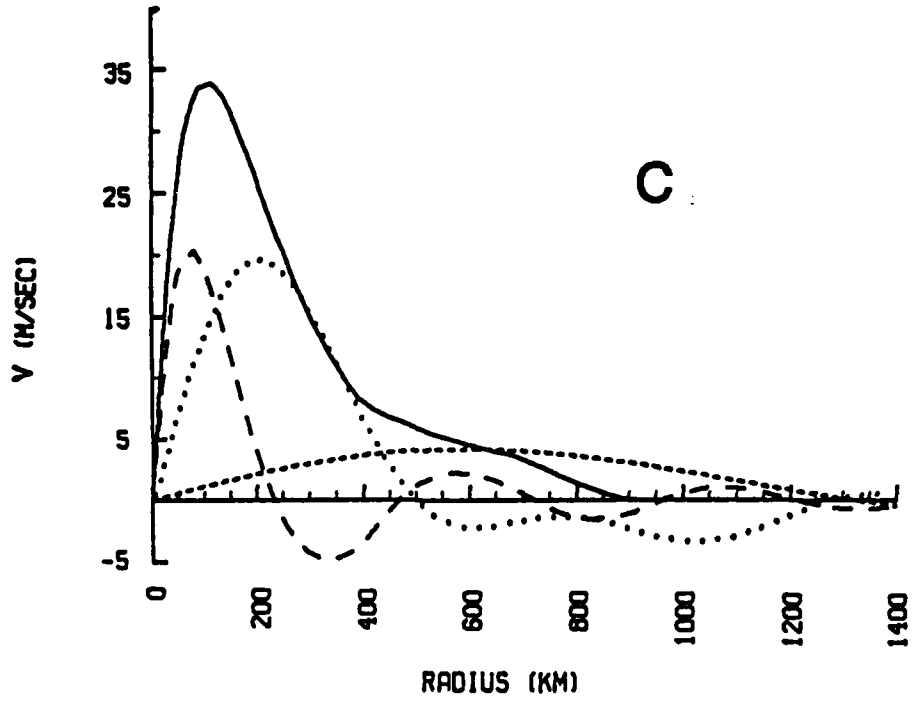

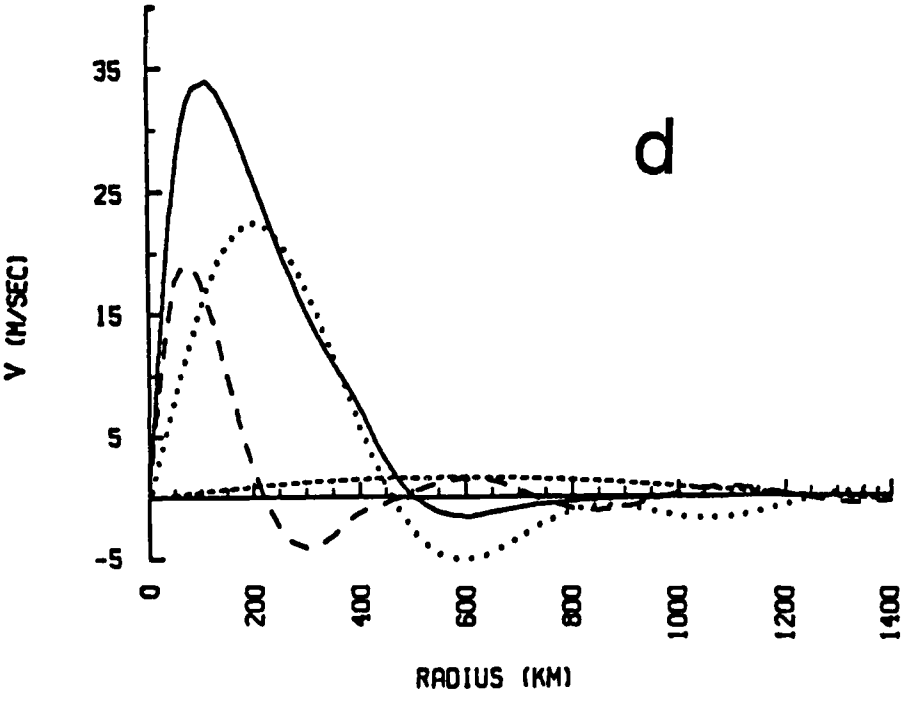

Fig. 7-6. (Continued)

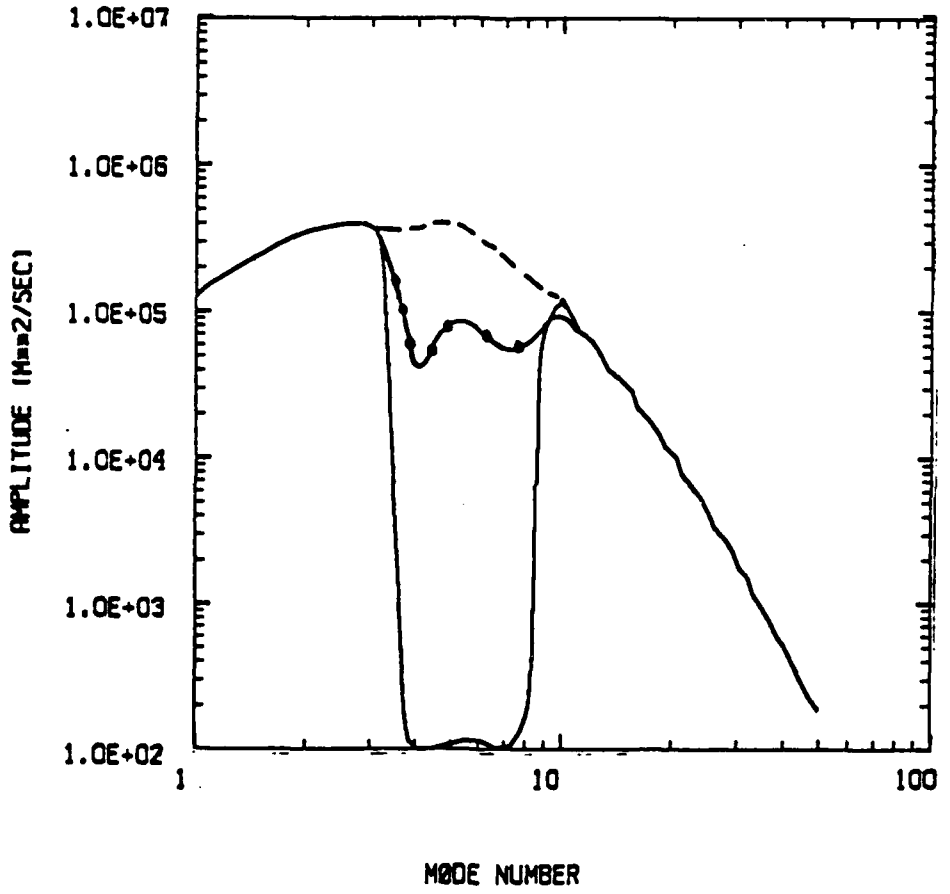

Fig. 7-7. 1-D spectra for the basic vortex at t = 72 h from the unfiltered integration (dashed) and the t = 72 h forecast from initial conditions with medium-scale filtering (dots, solid).

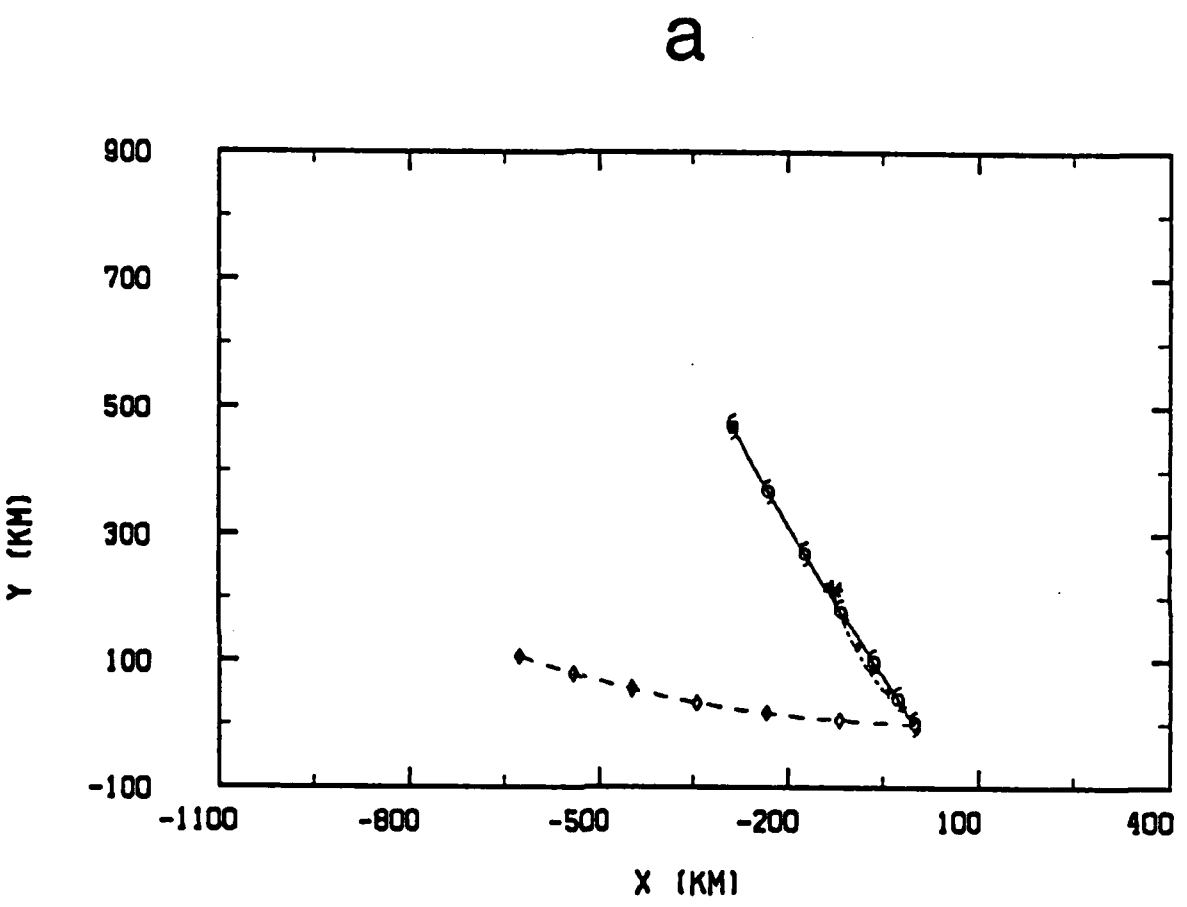

Fig. 7-8. Tracks to 72 h for (a) the basic vortex and for (b) the cyclonic perturbation. The unfiltered case is solid (hurricane symbol every 12 h), large scales filtered case is short-dashed (asterisks every 12 h) and large scales retained case is long-dashed line (diamond every 12 h). The 72-h position is highlighted.

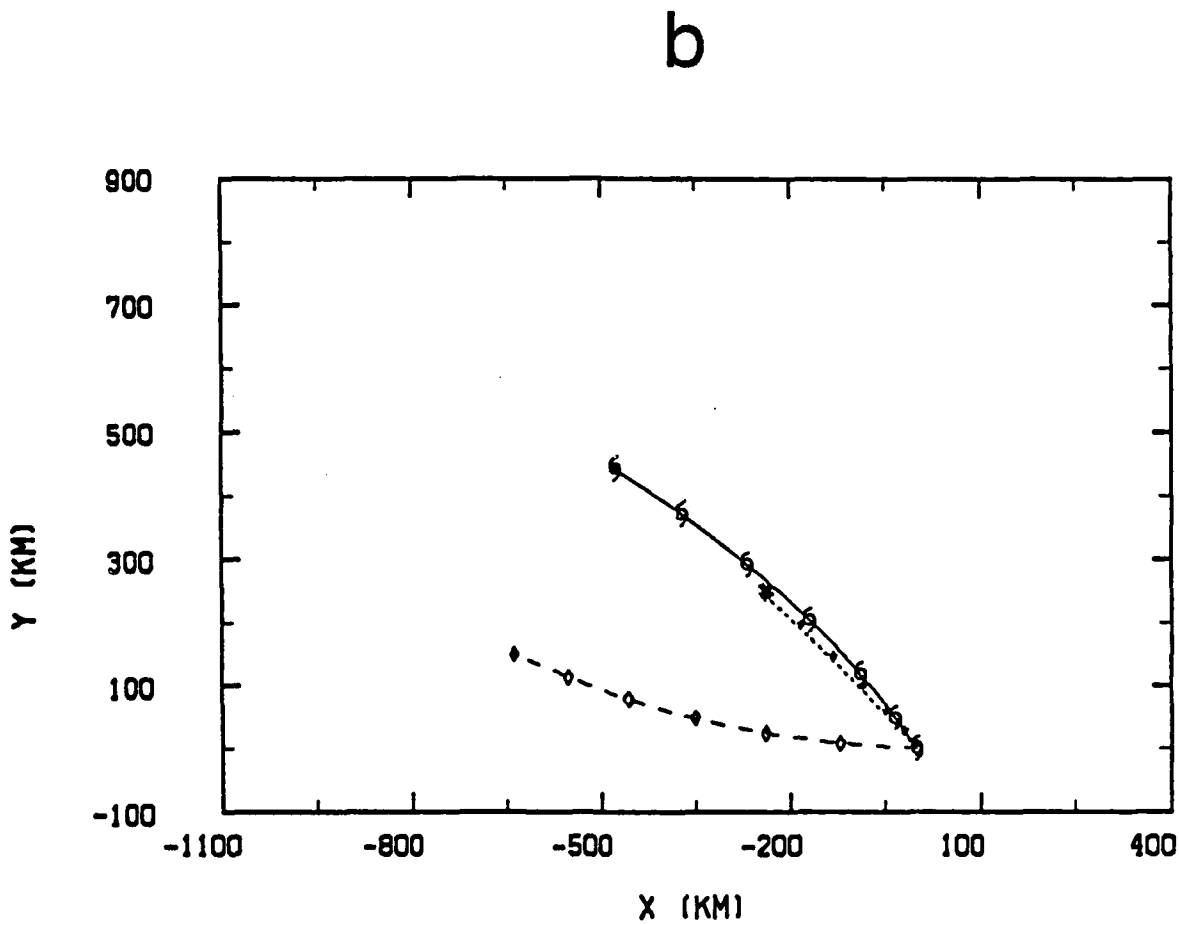

Fig. 7-8. (Continued)

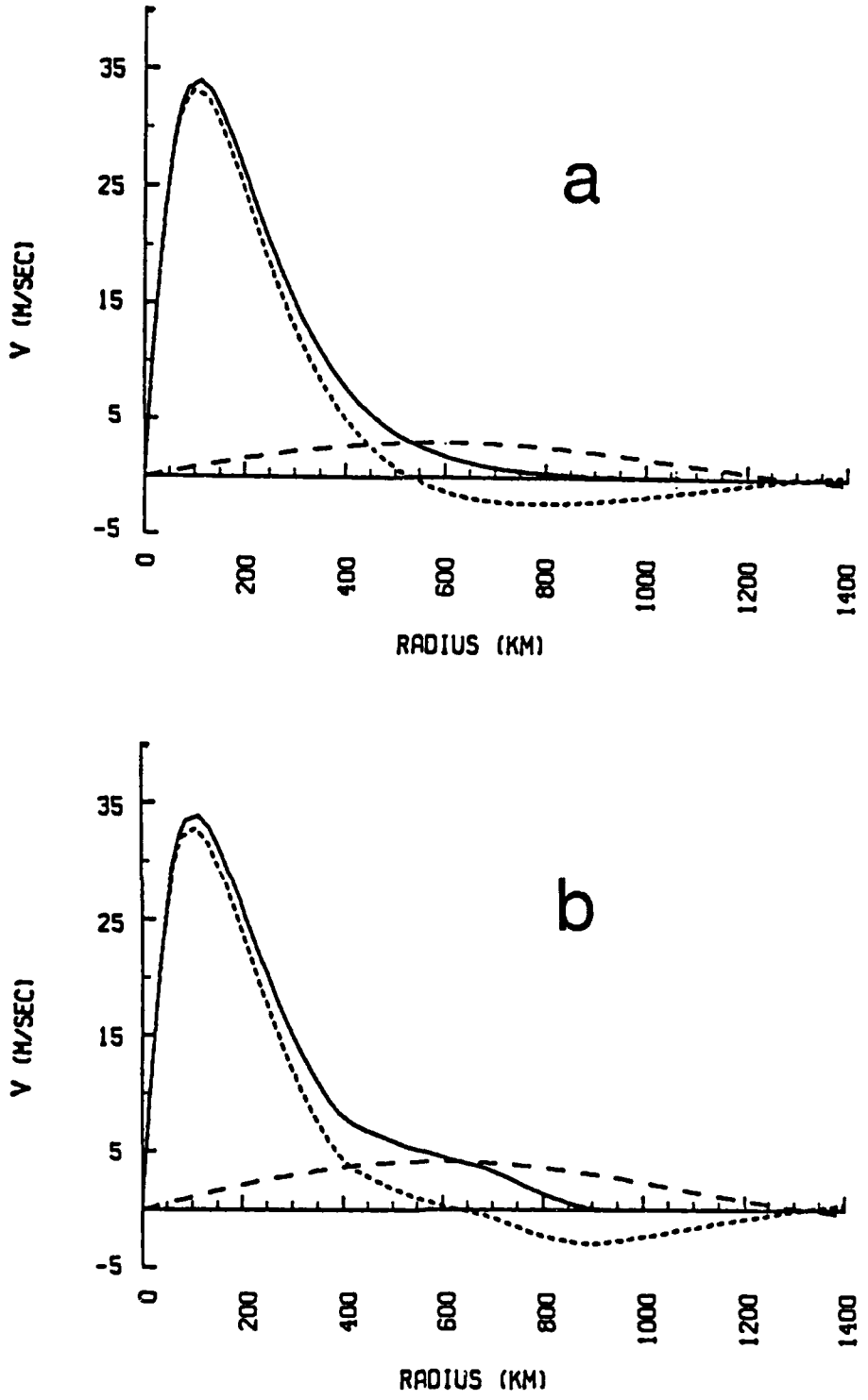

Fig. 7-9. Initial tangential wind profile (m/s) for (a) the basic vortex and for (b) the cyclonic perturbation. The unfiltered case is solid, the case with the large scales removed is short-dashed and the case with only the large scales retained case is long-dashed.

angular momentum (RAM) and increases the anticyclonic rotation of the large-scale asymmetric gyres (not shown). DeMaria and Biak (1987) demonstrated that as the amplitude of the outer anticyclone is increased (smaller RAM), the speed of motion is reduced and the vortex tends to have smaller (or even equatorward) displacements. This suggests that as RAM is decreased, there may be a point at which the motion relative to the basic current (here equal to zero) goes to zero. Removing the large scales results in a stronger outer anticyclone in B1 compared to S9 (not shown) and it is consistent with the DeMaria and Biak (1987) study that the speed of motion is also smaller in the B1 case with the large scales removed.

The track forecast in which the large scales are retained is consistently toward the west with only a slight northward component (Fig. 7-8). To distinguish the role of nonlinear advection from linear dispersion in the motion of this large vortex (see Fig. 7-5e and Fig. 7-9a), the track for linear-only solution is compared to full nonlinear solution in Fig. 7-10 for the basic vortex. The only difference between the forecast tracks is the greater northward motion in the nonlinear run. This is another clear demonstration of how nonlinear advection is responsible for the poleward component of beta drift. The westward translation in the linear solution implies that a vortex of this scale behaves as a Rossby wave, as assumed by Holland (1983) in a pseudo-linear treatment of vortex motion on a beta plane. However, similar comparisons of linear and nonlinear solutions using the medium- and small-scale vortices (Exps. F5 and F6, not shown) showed a very small (< 0.1 m/s) westward translation for the linear case in agreement with the results of Chan and Williams (1987).

Although these results are not unexpected, they do explicitly demonstrate the dynamical ideas that have been

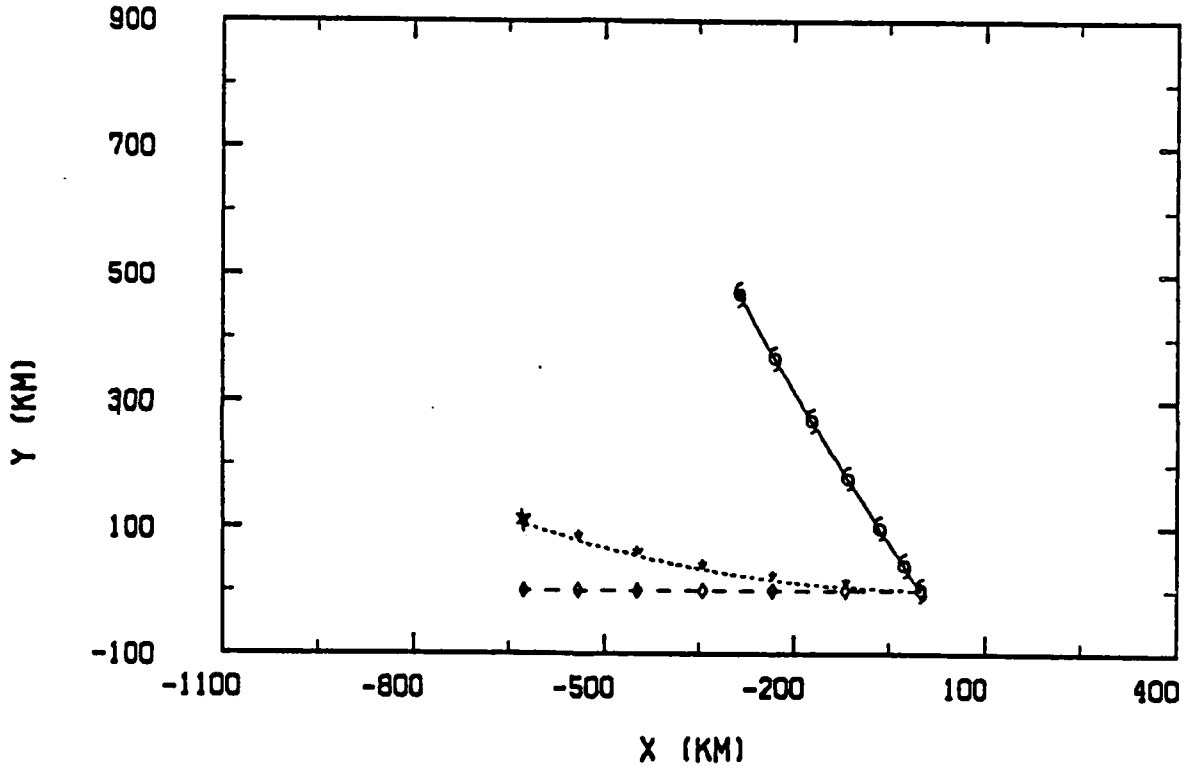

Fig. 7-10. Comparison of the 72-h track from the linear (long-dashed, diamonds every 12 h) and nonlinear (short-dashed, asterisks every 12 h) integrations initialized with the large scales (Exp. F4) only and the nonlinear solution with the unfiltered vortex (the basic vortex). The 72-h position is highlighted.

the basis for simpler analytical-type models (e.g., Chan, 1982 and Holland, 1983). For example, in the analytical treatment of the vortex motion on a beta plane by Holland (1983), it was assumed that the westward component of beta drift is due to linear effects and that the northward component is due to nonlinear advection. However, this assumption is only applicable to the large-scale component of the vortex and is not valid for the smaller scales, and is not directly responsible for the motion of the center.

The motion of the large-scale component of the vortex can be seen in the symmetric component of filtered solutions from the model initialized with the unfiltered vortex (Fig. 7-11). The center of the total vortex is in the middle of the grid. Likewise, the center of the small- (Fig. 7-11b) and medium-scale (Fig. 7-11c) components are in the same position. However, the center of the large-scale component is approximately 500 km to the west of the other centers. This displacement of the centers fits the conceptual model of beta drift discussed by Elsberry (1987), in which the large-scale vortex moves to the west faster than the smaller scales. Because the "center" is then in the southerly flow to the east of the large-scale vortex, the large-scale vortex would advect the smaller scales (the "center") northward. While this model is conceptually reasonable, it does not explain the westward motion or the role of the smaller scales.

The forecast tracks (Fig. 7-12) in which the small-scale (Exp. F1) and medium-scale (Exp. F2) components are removed demonstrate that these scales are important to the motion of the center. When the B1-type vortices (Figs. 7-12a, c and d) are modified by removing the small scales, a greater translation along a more northerly course results. Removing the medium scales gives less total displacement, but a large northward drift. The S9 case (Fig. 7-12d) shows less of an

a

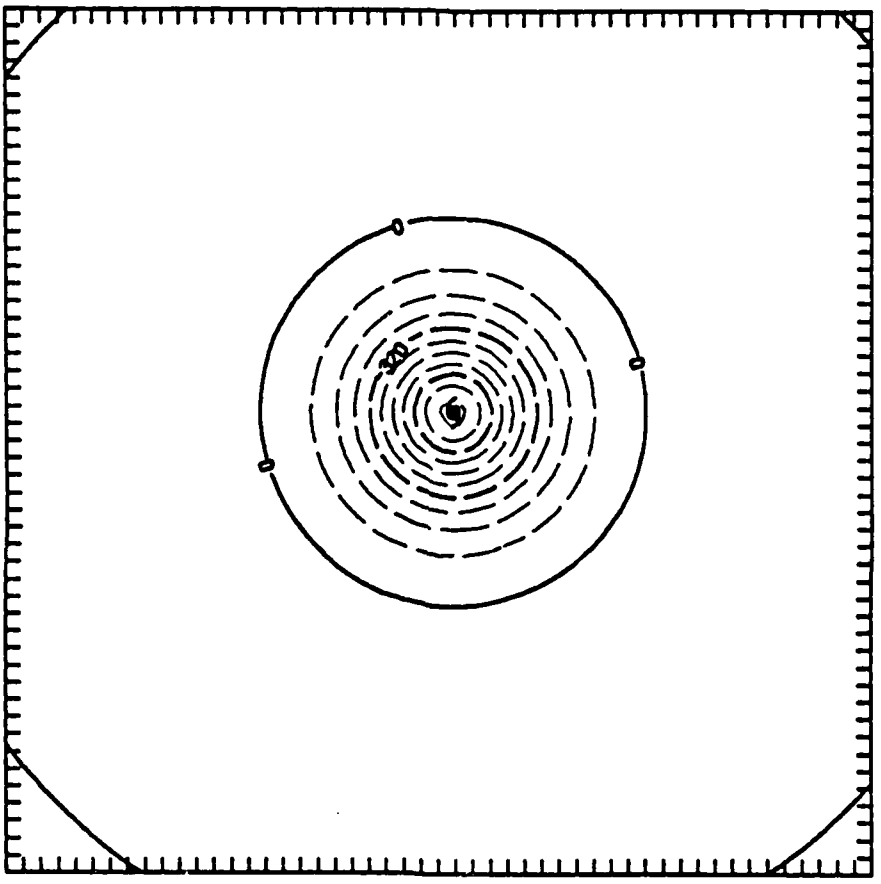

(a) The unfiltered vortex
contour interval = 80 (x10⁴) m²/s
minimum contour = -800 (x10⁴) m²/s

Fig. 7-11. Symmetric streamfunction after 72 h integration for the basic vortex.

b

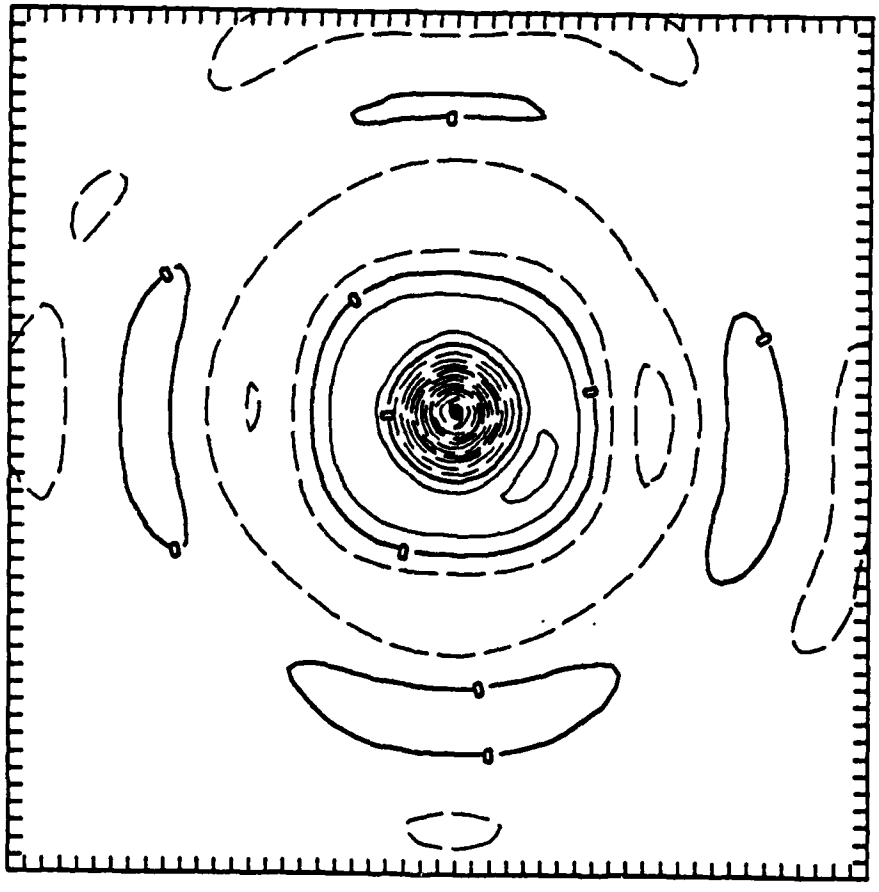

(b) The sma.. .e component
contour .erval = 20 (x10⁴) m²/s
minimum .ontour = -220 (x10⁴) m²/s

Fig. 7-11. (Continued)

C

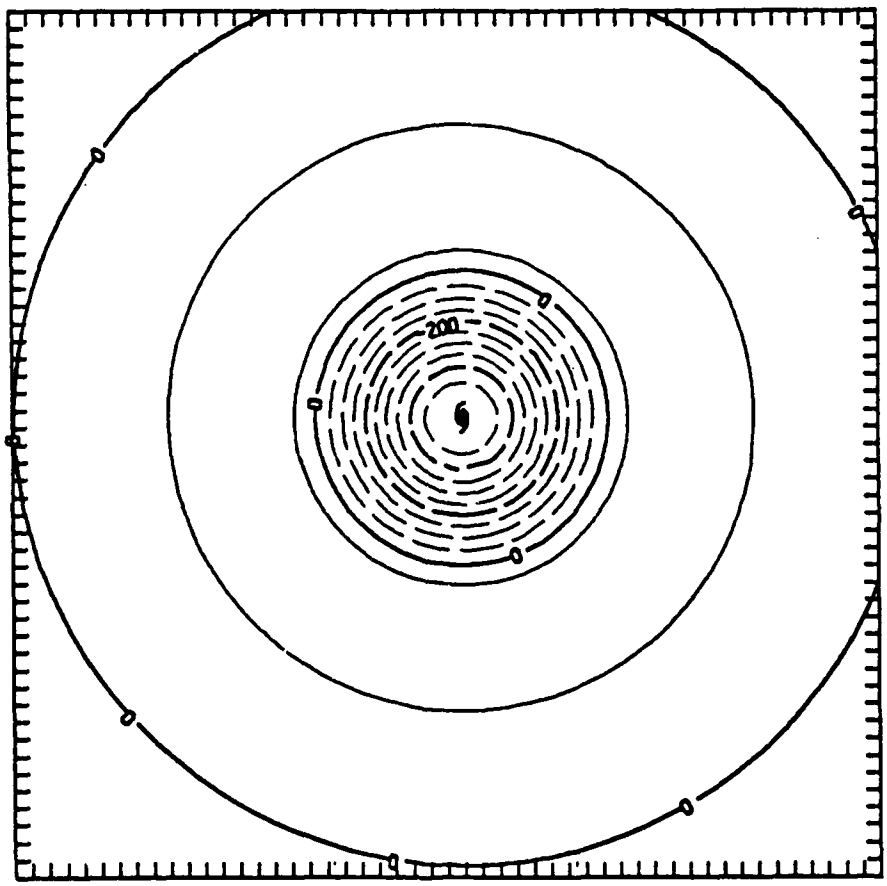

(c) The medium-scale component
contour interval = 50 ($\times 10^4$) m^2/s
minimum contour = -500 ($\times 10^4$) m^2/s

Fig. 7-11. (Continued)

d

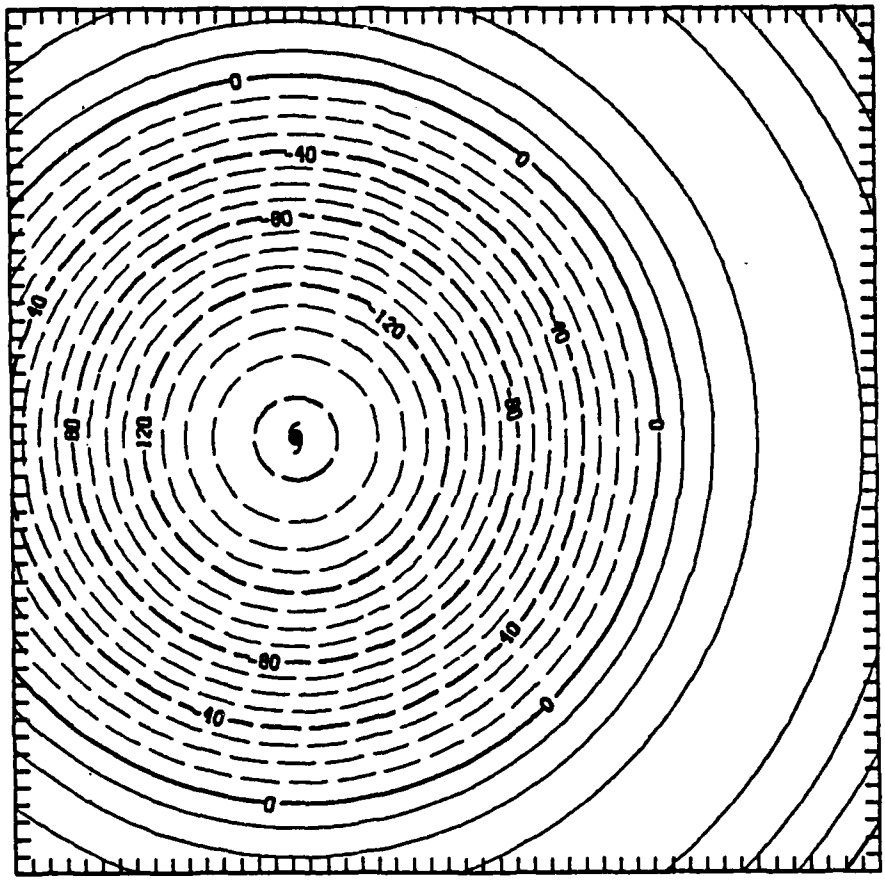

(d) The large-scale component
contour interval = 10 ($\times 10^4$) m^2/s
minimum contour = -160 ($\times 10^4$) m^2/s

Fig. 7-11. (Continued)

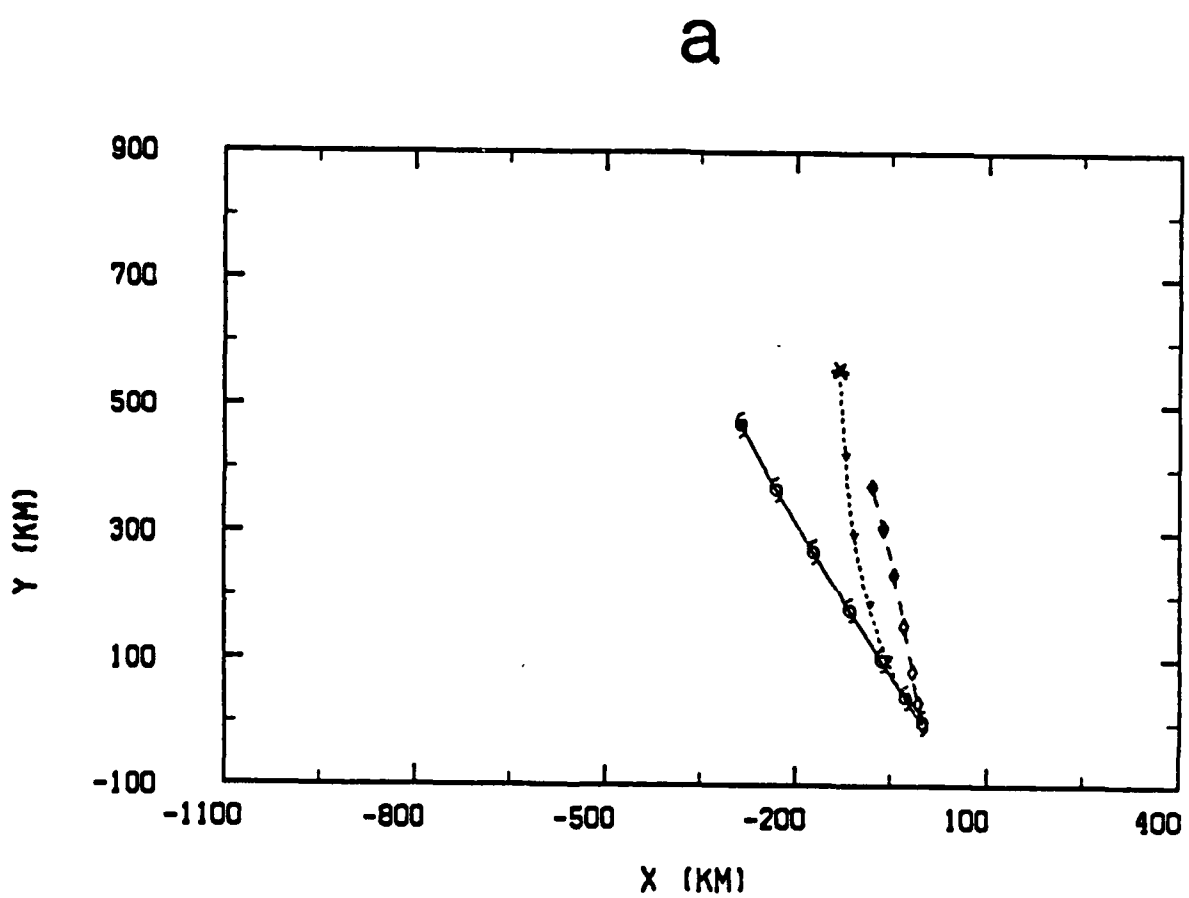

Fig. 7-12. Forecast tracks to 72 h for the unfiltered vortex (solid, with hurricane symbols every 12 h), the no small scales (Exp. F1; short-dashed, with asterisks every 12 h), and for the no medium scales (Exp. F2; long-dashed, with diamonds every 12 h). Panel (a) is for the basic vortex; (b) the weak-large vortex; (c) the cyclonic perturbation vortex; and (d) the anticyclonic perturbation vortex. The 72-h positions are highlighted.

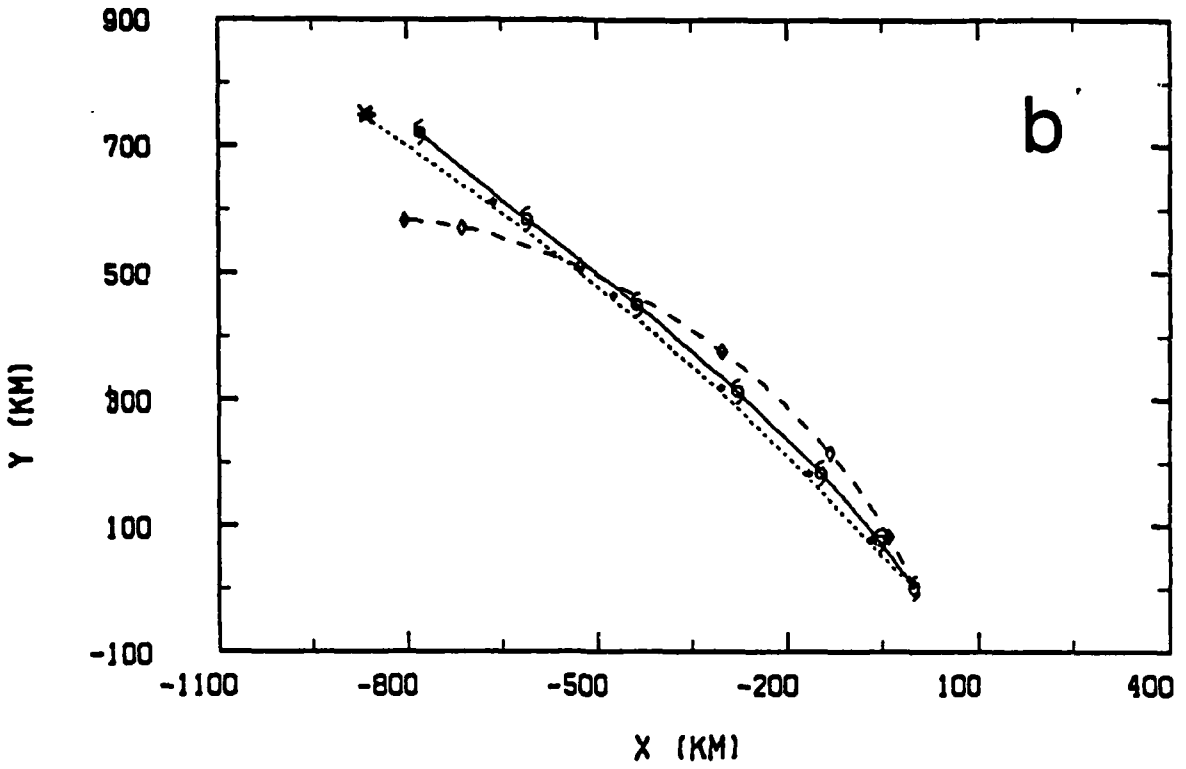

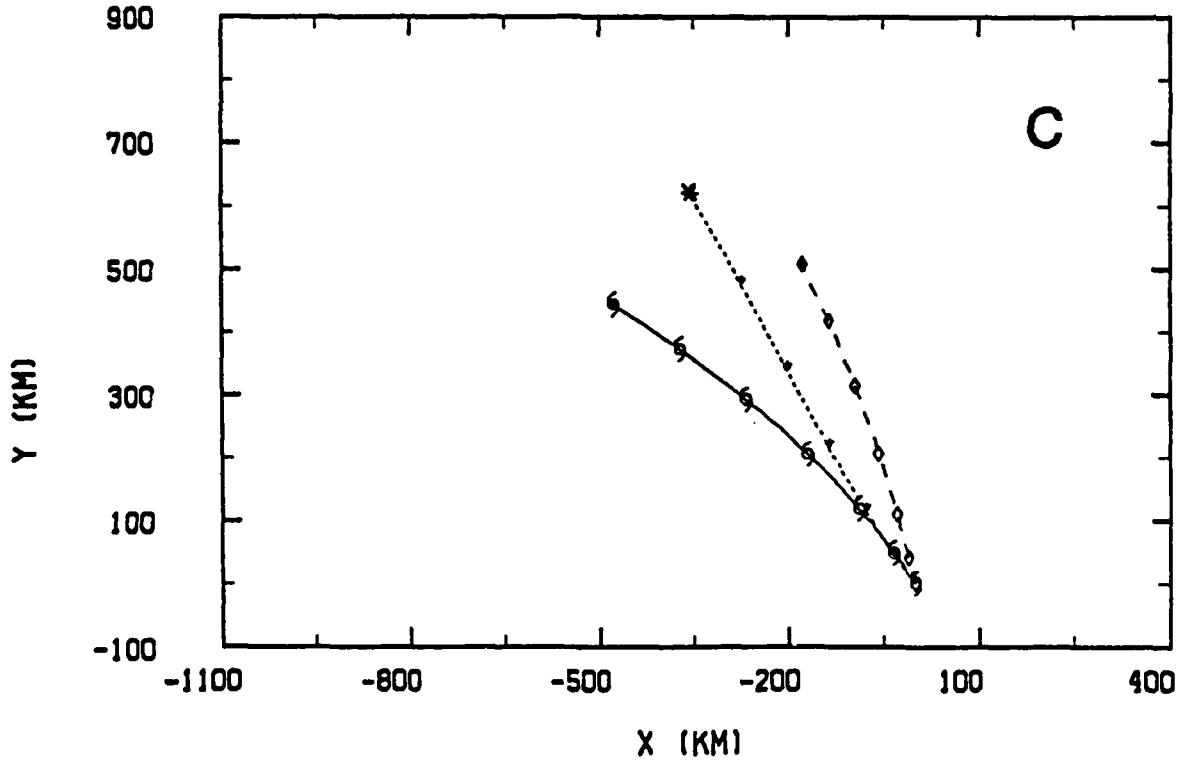

Fig. 7-12. (Continued)

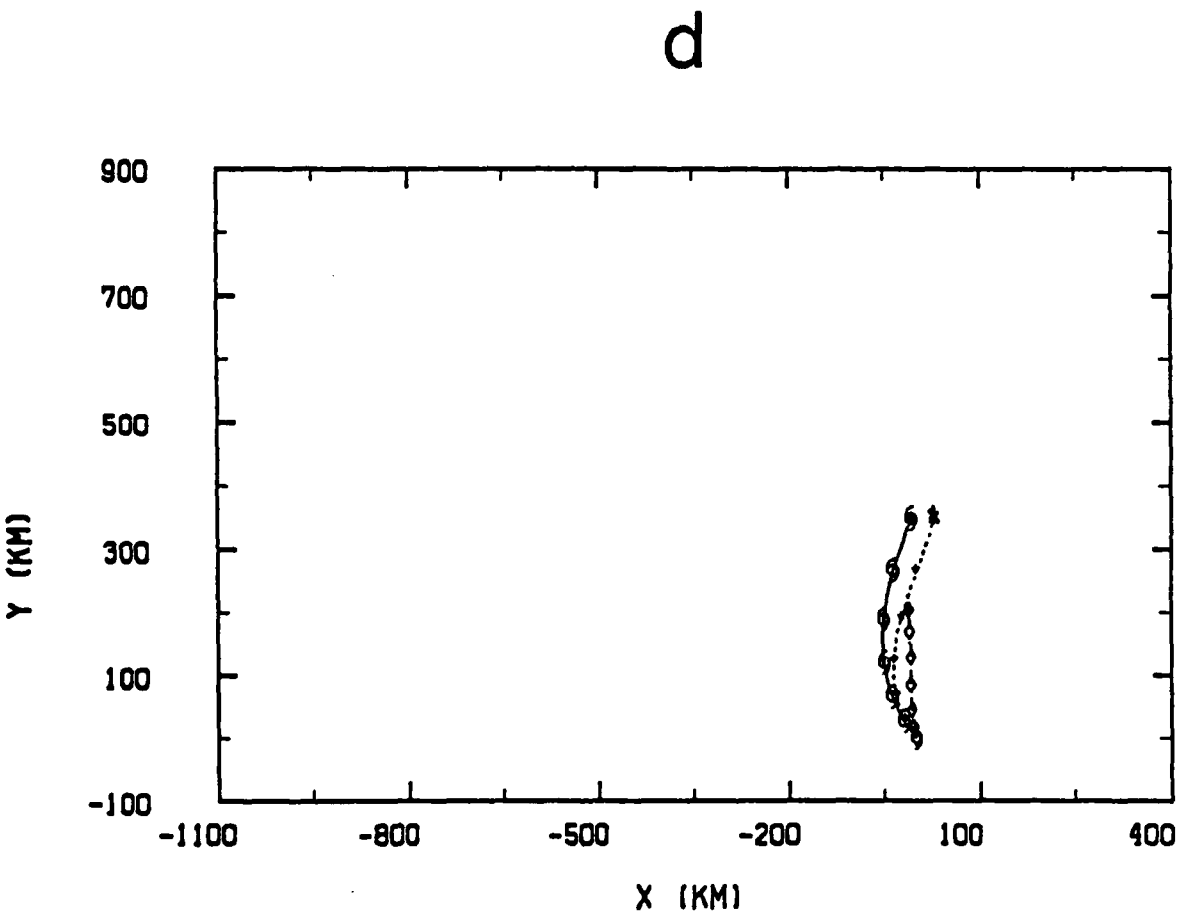

Fig. 7-12. (Continued)

effect, as the unfiltered vortex track is primarily to the north. In contrast, the weak-large vortex (Fig. 7-12 b) exhibits little sensitivity to the small and medium scales as the tracks are very similar in all cases.

There are two basic reasons why the small and medium scales have such a strong influence on the motion. As discussed in Chapters IV and V, the center is translated in this model through the advection of asymmetric vorticity by the symmetric flow in the inner core. The small scales make their greatest contribution to the total vortex in the inner portion of the storm. Thus, removing this component would change the inner-core asymmetries, and would affect the motion process by leaving the advection of symmetric vorticity by the asymmetric flow as the more dominant motion process.

The greater northward motion when the medium scales are removed suggests that these scales affect the large-scale asymmetric gyres. The cyclonic perturbation (S8) case is used to illustrate this influence as the deviation from the unfiltered (all scales) vortex track is greatest for this case (Fig. 7-12c). The asymmetric streamfunction at t = 36 h from the total vortex has a ventilation flow toward the northwest. If the medium scales are removed (Fig. 7-13b) from this total vortex solution (all scales initially), the ventilation flow is shifted toward the north (Fig. 7-13a). A similar rotation is found in the asymmetric streamfunction from an integration started with the filtered initial conditions in which the scales have been removed (Fig. 7-13c).

The interpretation of these cases is that the large-scale asymmetric gyres consist of two components. One is on a larger scale (e.g., r ~ 700 km) and has a more north-south alignment of the ventilation flow (Fig. 7-13b). The other is a "rotated" smaller scale (e.g., r ~ 300 km) component

a

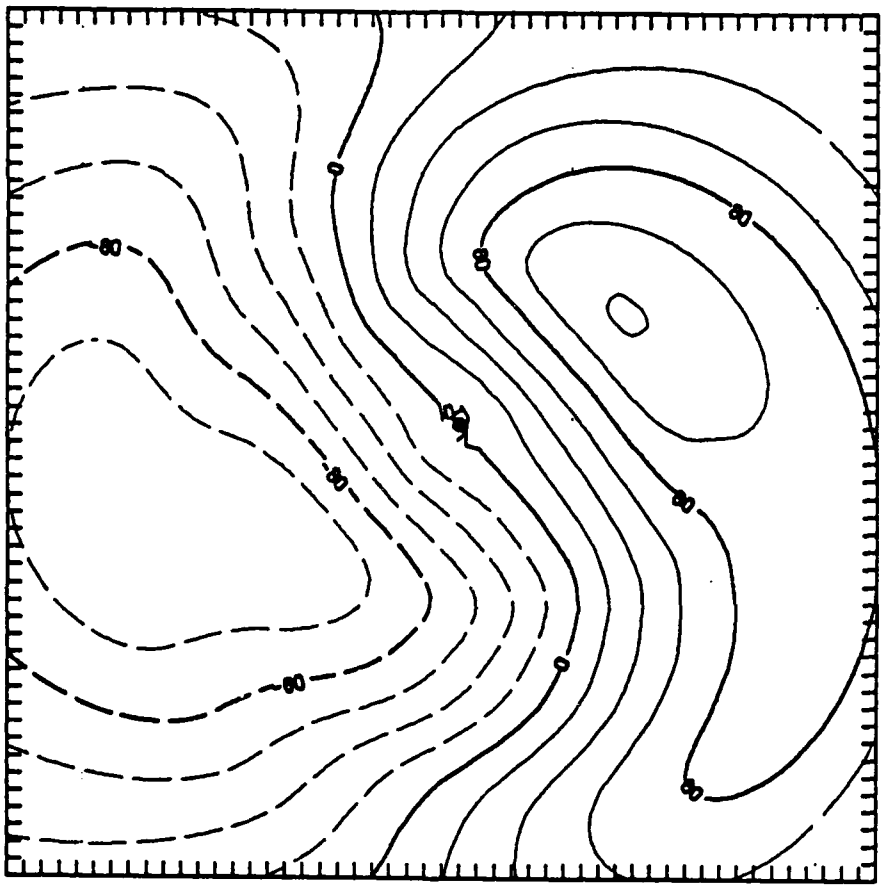

(a) The unfiltered or total vortex
contour interval = 20 (x10⁴ m²/s)
minimum contour = -100 (x10⁴ m²/s)
maximum contour = 120 (x10⁴ m²/s)

Fig. 7-13. The 36-h asymmetric streamfunction for the S8 vortex.

b

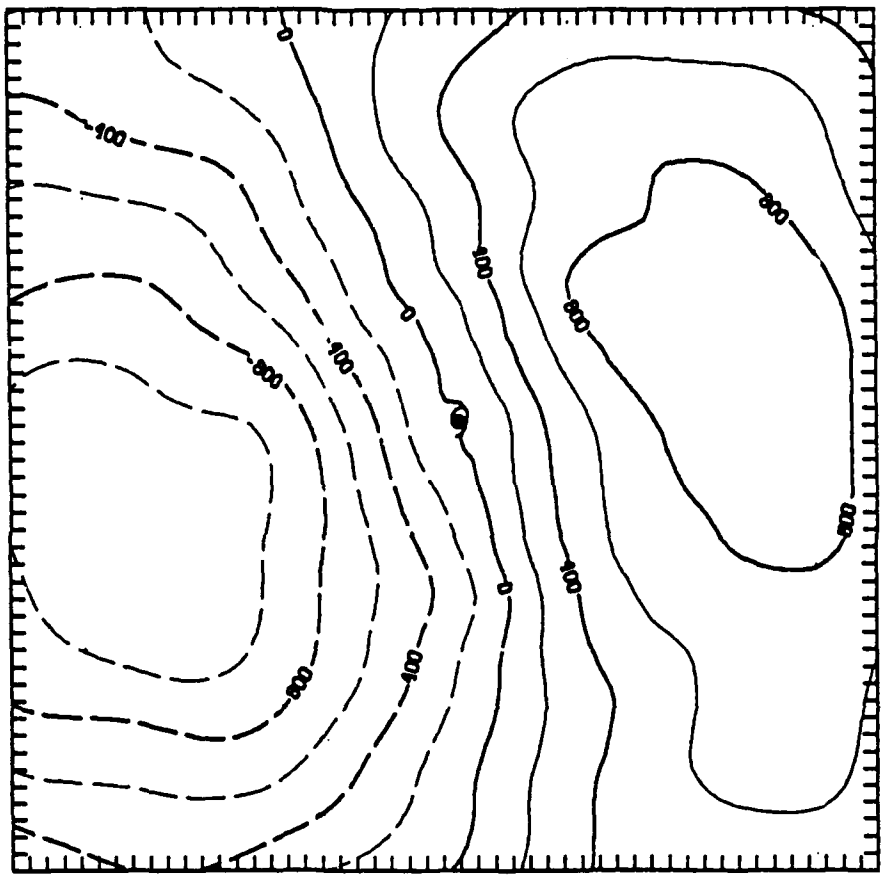

(b) With the medium scales of the vortex in (a) removed by filtering
contour interval = 200 ($x10^3$ m^2/s)
minimum contour = -1000 ($x10^3$ m^2/s)
maximum contour = 1200 ($x10^3$ m^2/s)

Fig. 7-13. (Continued)

C

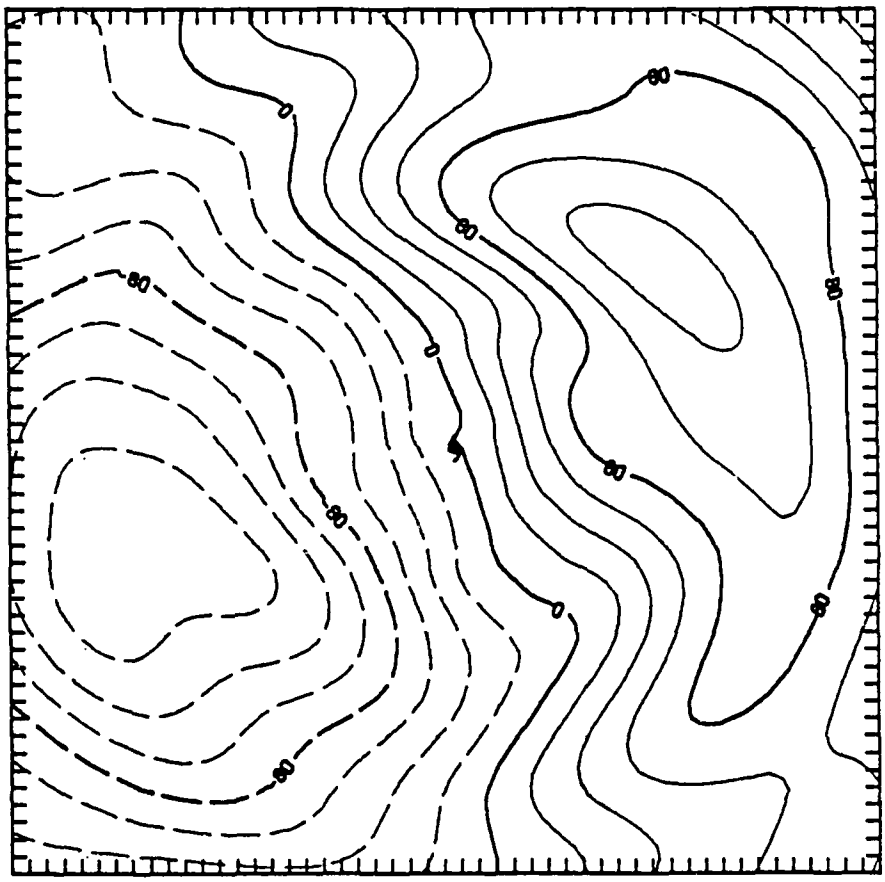

(c) The solution from the filtered initial conditions in which the medium scales have been removed (Exp. F2).
contour interval = 20 ($\times 10^4$ m^2/s)
minimum contour = -140 ($\times 10^4$ m^2/s)
maximum contour = 120 ($\times 10^4$ m^2/s)

Fig. 7-13. (Continued)

d

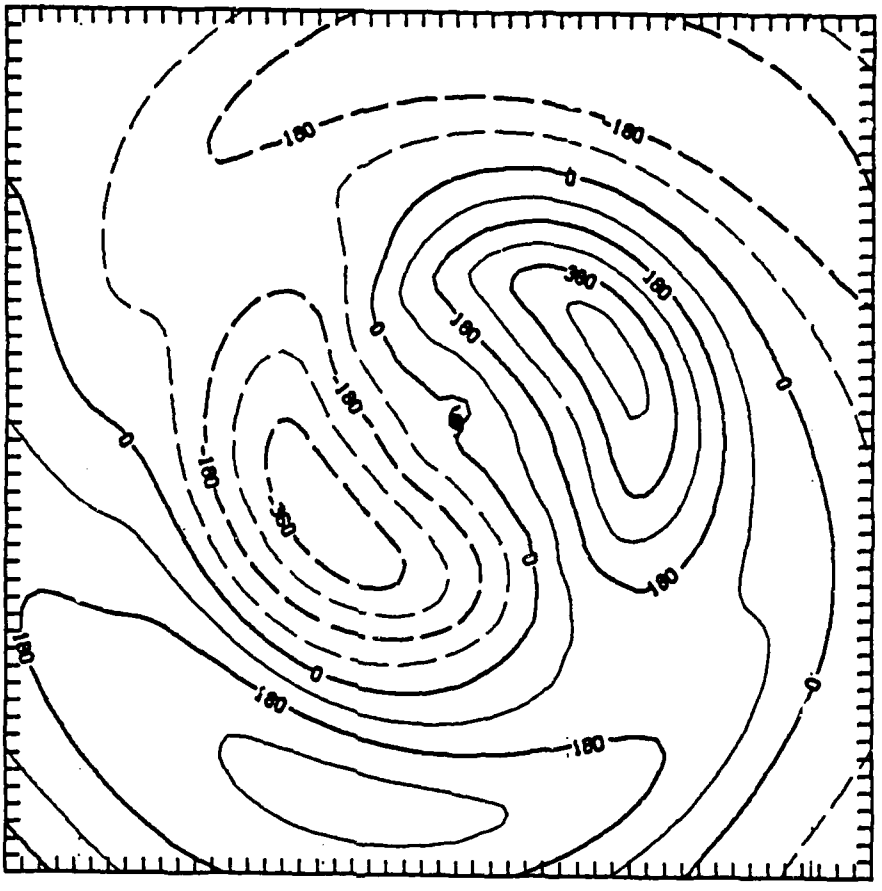

(d) The solution from the filtered initial conditions in which the large scales have been removed (Exp. F3).
contour interval = 90 ($x10^4$ m^2/s)
minimum contour = -360 ($x10^4$ m^2/s)
maximum contour = 360 ($x10^4$ m^2/s)

Fig. 7-13. (Continued)

that is deflected from the north-south orientation. This rotated component is more clearly illustrated by only removing the large scales (Fig. 7-13d) and it is suggested that the rotation process is occurring on scales smaller than the large scales. It is also interesting that the asymmetric streamfunction from the filtering of the total solution (Fig. 7-13b) is quite similar to that obtained from the solution with filtered initial condition (Fig. 7-13c). This suggests that medium scales were not significantly modified by the large and small scales which is demonstrated by the 1-D spectra in Fig. 7-7.

E. IMPLICATIONS FOR VORTEX SPECIFICATION IN TRACK FORECAST MODELS AND TROPICAL CYCLONE ANALYSIS

The current set of operational tropical cyclone track prediction models (see Fiorino, 1985b) can be divided into two categories: (i) coarse resolution (e.g., the One-way influence Tropical Cyclone Model (OTCM) of Fleet Numerical Oceanography Center (FNOC) with a Δx = 205 km); (ii) and fine resolution (e.g., the Movable Fine-mesh Model (MFM) of the National Meteorological Center (NMC) with a $\Delta x \sim 60$ km). The coarse resolution models have a grid spacing of between 100-200 km, whereas the finer resolution models have a spacing of 41-80 km.

An additional set of model runs is made in which the B1-type vortices are Fourier filtered to eliminate scales not well-resolved by these two classes of fine and coarse resolution models (< 150 km and < 300 km respectively). Removing scales less than 150 km has very little effect on the tangential wind profile, whereas filtering scales less than 300 km reduces the maximum wind speed and shifts the RMW outward (Fig. 7-14). Even though the RMW in this study is larger than that of a typical tropical cyclone, the minimal effect of filtering scales with $\lambda < 150$ km implies that a smaller RMW would also have a small effect on the

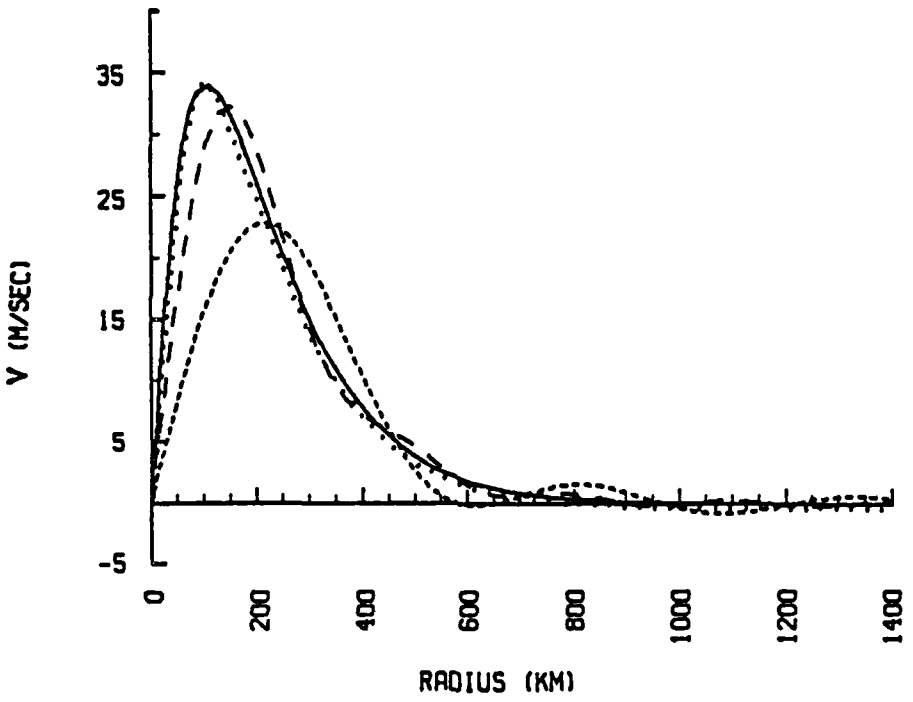

Fig. 7-14. Tangential wind profiles for the unfiltered basic vortex (solid), a vortex with scales < 500 km removed (short-dashed, scales < 300 km removed (long-dashed) and a vortex with scales < 150 km removed (dotted).

flow in the critical annulus. The profile for the F1 filtered vortex (remove scales less than 500 km) is also shown as a further demonstration of the outward shifting of the RMW as the larger scales are removed. Changes in the outer flow for the 150- and 300-km truncations are very small. However, for the 500-km filtering there are noticeable changes in the outer region flow.

The tracks for the two small-scale (150 and 300 km) filtered initial conditions are given in Fig. 7-15. Eliminating scales less than 150 km has virtually no influence on the track, which is not surprising given the minimal effect of filtering on the tangential wind profile. Removal of scales less than 300 km in the initial profile causes the vortex to move to the left and have a slower speed than the track of the unfiltered vortex. However, the track for the 500-km filtering case (Fig. 7-12) shows a deviation to the right and greater speed of motion which indicates that the outer flow has been modified. The slower and to the left result for the 300-km filtering cases is due to the changes in the inner regions that affect the inner-core motion process (advection of asymmetric vorticity by the symmetric flow). Similar magnitudes and direction deviations relative to the unfiltered vortex are found for the symmetric perturbation vortices (Figs. 7-15b and c).

These experiments with removal of the smallest scales suggest that the beta drift effect does not necessarily require high-resolution models to resolve scales in the 100-300 km range. However, modifying the initial large and medium scales does significantly affect the vortex motion. Generally speaking, the large scales control the speed of motion and the small and medium scales have the greatest influence on track direction. The importance of the small and medium scales depends on vortex structure with the

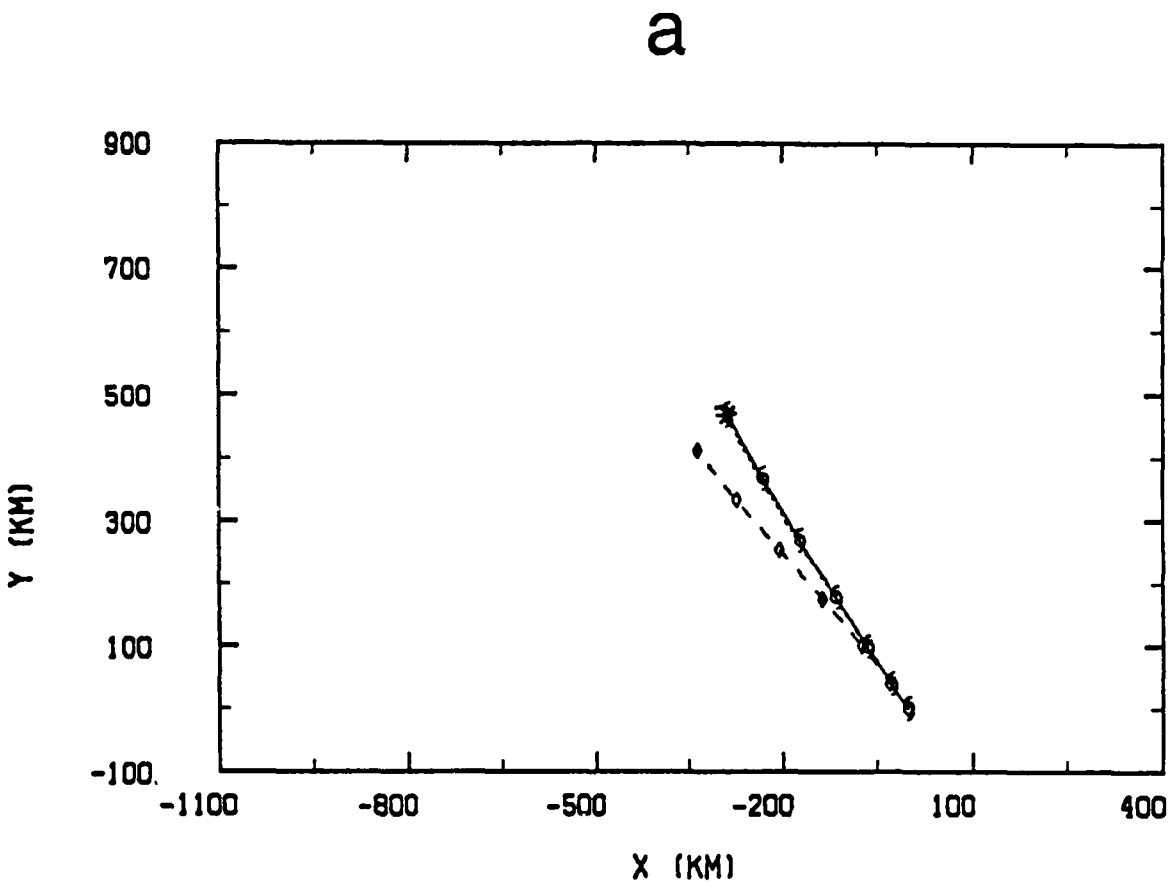

Fig. 7-15. Forecast tracks to 72 h for the unfiltered vortex (solid, with hurricane symbols every 12 h), an initial vortex with scales < 150 km removed (short-dashed, with astericks every 12 h) and an initial vortex with scales < 300 km removed (long-dashed; with diamonds every 12 h). Panel (a) is for the basic vortex; (b) the cyclonic perturbation vortex; and (c) the anticyclonic perturbation vortex.

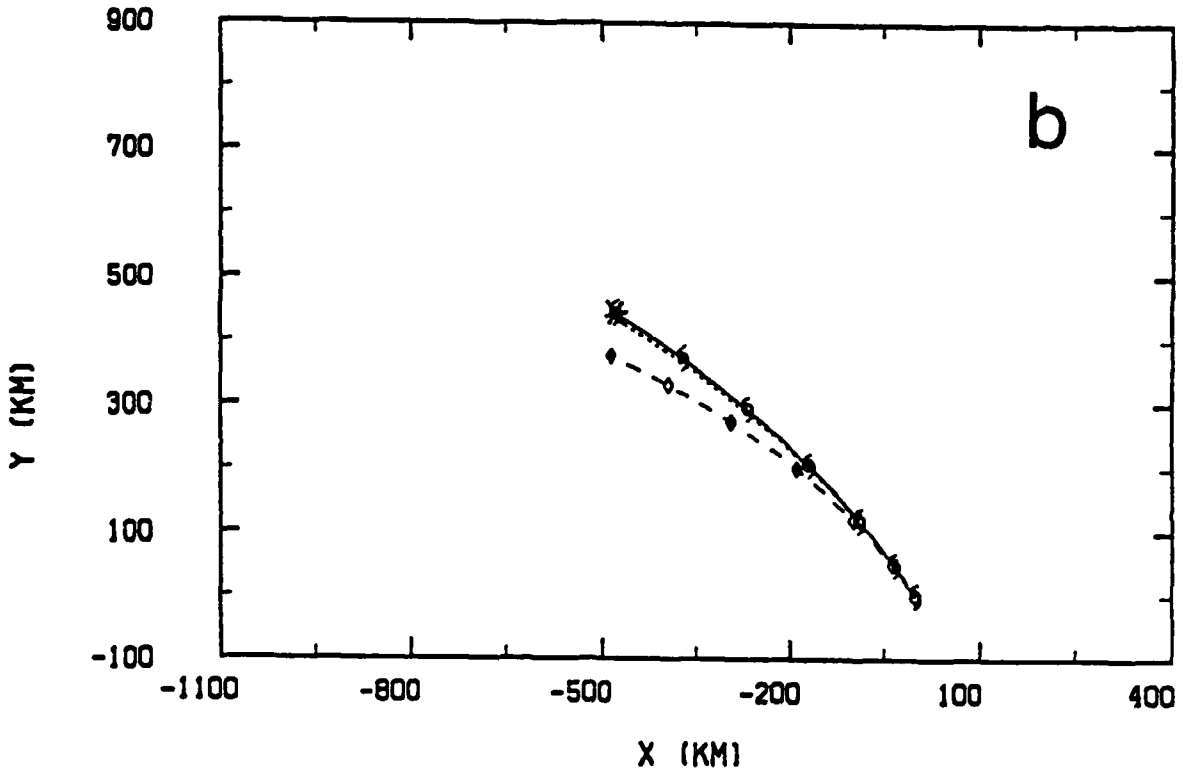

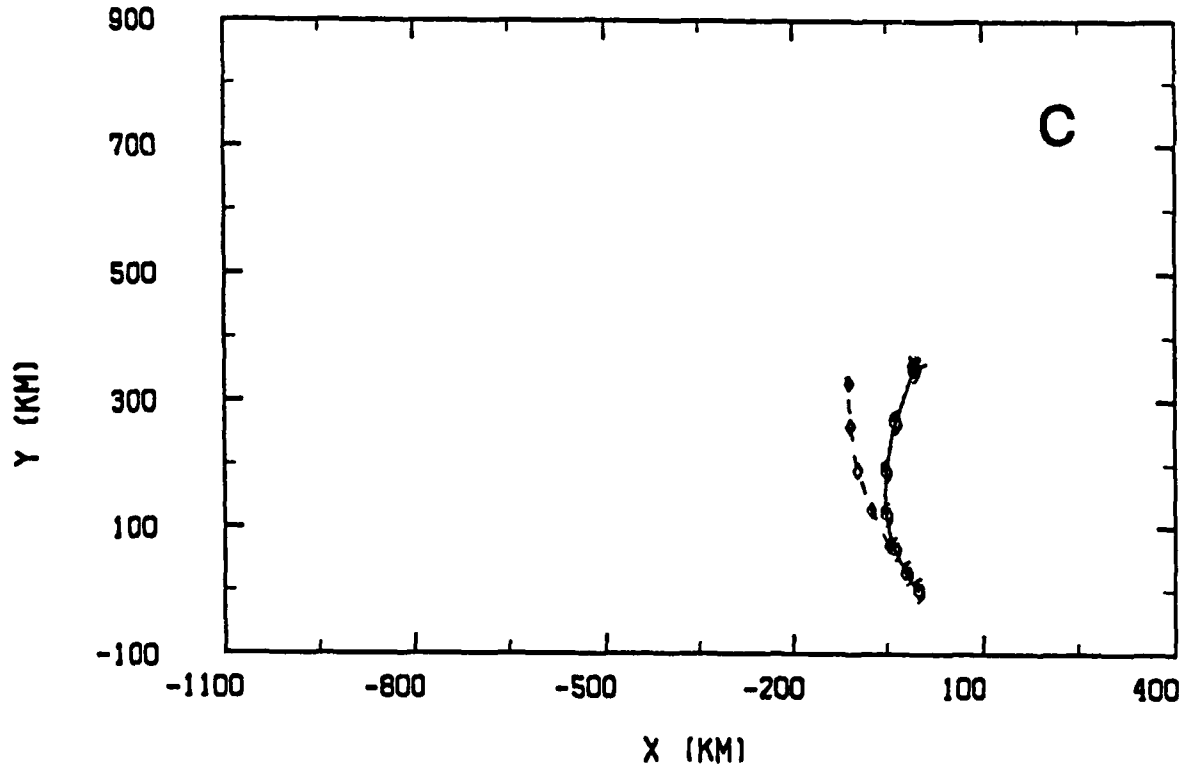

Fig. 7-15. (Continued)

greatest effects for the B1-type vortices that have more intense inner core regions.

The steady-state speed of motion is compared (Fig. 7-16) with the percentage of the streamfunction amplitude that is projected onto the large scales. The nearly 1:1 correspondence indicates that the magnitude of beta drift is directly proportional to the amplitude of the large-scale component of the vortex. This has implications for vortex specification in the operational forecast models.

First, insertion or "bogusing" of a tropical cyclone vortex into a synoptic-scale analysis modifies the large-scale components in the vicinity of the vortex. For example, adequate environmental observations and a good synoptic-scale analysis may actually resolve the large-scale component of the tropical cyclone vortex, especially if this large-scale component vortex is displaced from the cyclone center as illustrated in Fig. 7-11. Thus, the degree of agreement between the large scales in the specified vortex and the actual large scales in the environmental flow analysis could significantly affect the track. If the large scale in the bogus vortex erroneously modifies a good synoptic analysis, the cyclone track would tend to have errors. In summary, it would be desirable to design an insertion procedure that blends the large scales in the bogus vortex smoothly with the large scales in the environmental flow analysis.

The medium scales in the vortex have an important role in the rotation of the asymmetric gyres and the orientation of the ventilation flow. Furthermore, these scales are not rapidly generated through the dynamical process of nonlinear scale interaction (Fig. 7-7). Although more realistic models have mechanisms to modify and create medium-scale features, it is nevertheless important to specify these scales initially so as to promote a correct orientation in

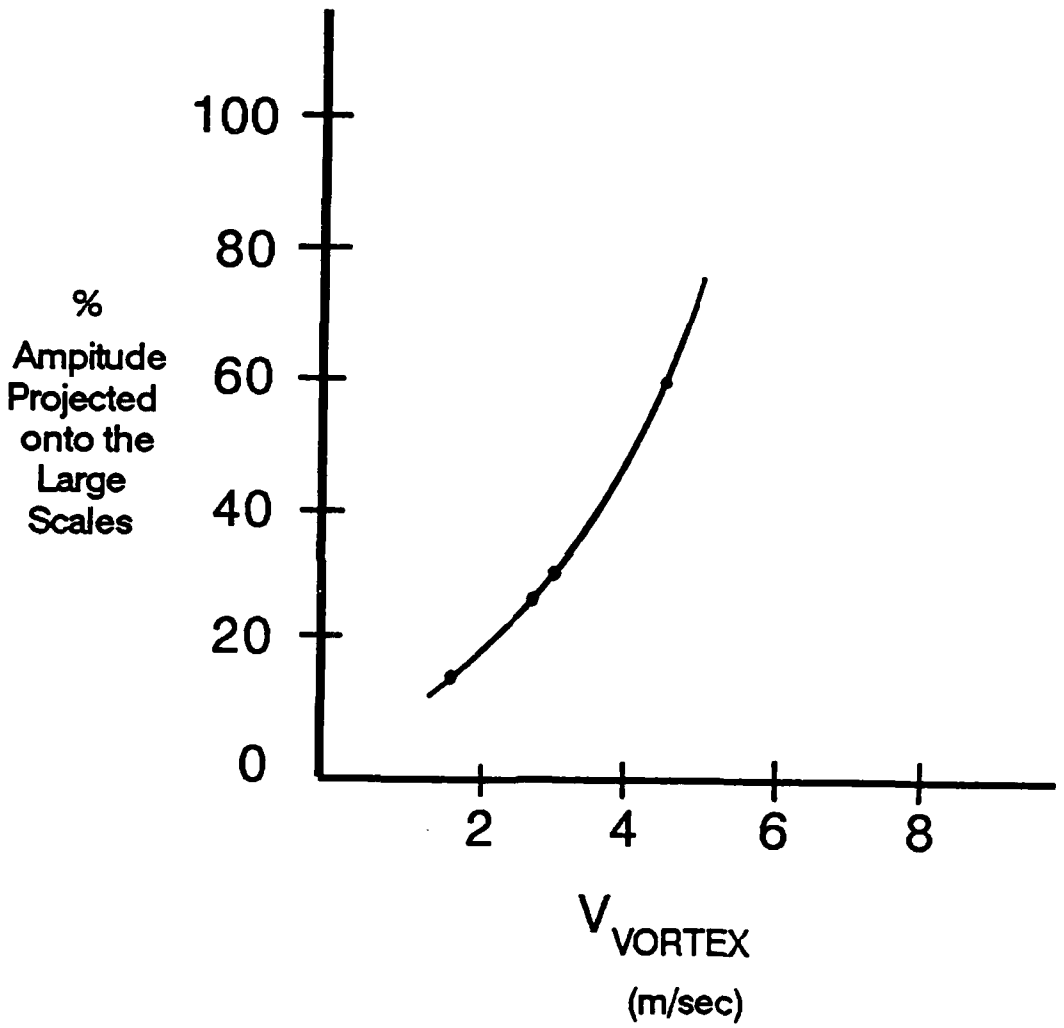

Fig. 7-16. Steady-state speed of motion as a function of the percentage of the total vortex amplitude projected onto the large scales from Table 7-3.

the track forecast and to avoid persistent and long-term track fluctuations.

These results also suggest that most important scales in the vortex that must be resolved by an observation system are on a fairly large scale (e.g., beyond r = 300 km). While this may be advantageous in terms of the number of data points that are required for an accurate specification, the current fixation (pun intended) with the inner-core region in field programs and operations may have diverted attention to the observation of these important scales.

It must be stressed that these results can not be transferred completely to more realistic and complete models. There has been very limited experimentation with baroclinic models (e.g., Hovermale, 1980; Jones, 1977; and Mathur, 1987) for tropical cyclone motion studies. Nevertheless, a common finding is that barotropic dynamics appears to be a dominant factor in the motion of the vortex in the sense that the cyclone tends to move in a steering/beta drift-like manner. Rather than defining the precise problems to be expected in the operational baroclinic models, the purpose of these experiments is to provide procedures for analysis of the motion process and to suggest potential problem areas that require further work.

F. SUMMARY

The symmetric vortex structures used in this research are based on typical values for the tropical cyclone. A 2-D Fourier analysis procedure has been applied to understand how the vortex structure, as it is projected onto various scales of motion, determines the subsequent motion. The scales of motion have been arbitrarily divided into three groups based on the wavelength of the Fourier basis functions ("small," $\lambda < 500$ km; "medium," $500 \leq \lambda \leq 1500$ km; and "large," $\lambda > 1500$ km).

How these scales in the initial conditions contribute to the beta-drift effect has been demonstrated by Fourier filtering to selectively retain or delete different scales. Transfer of energy between wave groups due to nonlinear scale interaction occurs sufficiently slowly in this model that the scale group that is removed in the initial conditions is not restored by 72 h.

The largest scales, which account for a significant fraction of the vortex structure, primarily determine the speed of motion. Furthermore, the speed of motion is proportional to the percentage of the total vortex that projects onto the largest scales. The medium and small scales that contained less energy (a function of the vortex structure parameters) have a significant effect on the direction of motion as they influence the rotation of the large-scale asymmetric gyres.

Application of these results to more complicated forecast models is limited and these experiments are intended mainly for illustration of potential problem areas, and the development of diagnostic procedures. Given these caveats, the most important implications of these tests for dynamical tropical cyclone forecast models is that the initial vortex specification projects energy onto large scales and that these scales significantly affect track prediction. The agreement between the large scales in the bogus vortex and in the environmental analysis needs to be carefully considered.

VIII. SUMMARY AND CONCLUSIONS

The primary purpose of this study is to understand how tropical cyclone motion depends on the structure of the horizontal circulation. This dependence has been examined in the context of the asymmetric and symmetric circulations and the scales of motion in the vortex. Through a series of initial condition and dynamical sensitivity tests, a more thorough description of the nonlinear dynamics of beta drift has been obtained.

A. RESEARCH APPROACH

The dynamical framework of this research is the nondivergent barotropic equation on a beta plane with no basic flow. The model is solved numerically using a highly stable, energy and enstrophy conserving scheme (e.g., Tupaz et al., 1978). A unique aspect of the numerical model is a moving grid procedure that permits very long integrations without requiring extremely large domains. Although the dynamical framework is simple, it does have applicability to tropical cyclone motion as the system contains the processes generally accepted as being first-order effects (e.g., Chan, 1982; Willoughby, 1987): 1) linear Rossby dispersion; and 2) nonlinear advection. The structure dependence is evaluated using an initial-condition sensitivity approach, an analysis of the model tendency equation in terms of the symmetric and asymmetric circulations, and dynamical sensitivity experiments in which the model equation is modified during the integration. In this methodology, the initial vortex is varied in accordance with the observed features of real tropical cyclones. A vortex specification procedure is developed to more systematically control the symmetric

cyclone. For example, the flow inward of r < 300 km can be fixed while varying the vortex beyond r = 300 km.

B. NUMERICAL EFFECTS

The numerical model has been run on the CYBER 205 supercomputer of Fleet Numerical Oceanography Center. This resource allows many experiments to be performed for very large grids (e.g., 201x201 points). In this way, the numerical precision of the model solutions has been more completely established compared to previous studies (e.g., Chan and Williams, 1987). The small space-scale (10-50 km) and short time-scale oscillations in the model track, which appear to be similar to observed oscillations, are shown to be strictly numerical and are related to the number of grid points covering the inner core. Therefore, such oscillations in the model track solution are smoothed to prevent misinterpretations.

Using a radius of maximum wind of 100 km, acceptable results (track noise that did not distort the general path) have been obtained with a grid spacing of 80 km. Thus, high resolution (e.g., Δx = 20 km) is not required to simulate to the larger-scale aspects of the barotropic cyclone vortex.

Domain size has a larger effect on the model tracks than resolution, which is due to the way the lateral boundary conditions influence the development of very large-scale (domain-wide) features. The model configuration is set at Δx = 40 km and 101x101 points to provide a 4000x4000 km domain. Smaller domains cause reductions in the speed of motion in agreement with the experiments of DeMaria (1987).

C. DEPENDENCE ON THE INITIAL SYMMETRIC VORTEX

Four types of initial vortex sensitivity tests have been made to determine the role of the structure of a symmetric vortex in the beta drift: (i) radius of maximum wind (RMW); (ii) flow in the "inner" and "outer" zones; (iii) symmetric

perturbations; and (iv) the "far outer" flow. These experiments not only establish the basic structure sensitivity, but also provides the basis for the dynamical sensitivity tests and for the circulation tendency analysis.

1. Radius of Maximum Wind

The flow in the inner core of the vortex (r < 100 km) has no bearing in beta drift in agreement with other studies (e.g., DeMaria, 1985). It is also shown that increasing the RMW to r = 100 km from a more observationally typical value of r = 50 km (while holding the vortex constant beyond r = 200 km) has no effect on the motion. Thus, the structural influences critical to tropical cyclone motion in this model lie beyond the inner core.

2. Inner/Outer Changes

The radius of 15 m/sec (r_{15}) is set to r = 300 km and the flow inward and outward of r_{15} is varied. This value of r_{15} is used to separate the "inner" flow from the "outer" flow. It is found that the outer flow has the greatest influence on the motion. Specifically, the speed of motion is proportional to the magnitude of the net flow in the r = 300 - 800 km annulus ("outer" strength), whereas changes in the inner region ("inner" strength) have very little influence on the motion. This result points to the importance of the larger-scale component of the vortex structure in tropical cyclone motion. Furthermore, additional tests confirm that the scale dependence is not related to the other vortex quantities. That is, the beta drift is controlled by processes dependent on the physical scales in the vortex or to linear Rossby dispersion that is embodied in the βv term in the model vorticity equation.

3. Symmetric Perturbations

The sense of the symmetric flow in the "critical annulus" of r = 300 - 800 km is related to the long-term turning motions. An anticyclonic (cyclonic) perturbation to

the tangential wind in the critical annulus causes a slow and steady clockwise (counterclockwise) turning away from the track of an unperturbed vortex. This finding suggests: (i) an interaction between the symmetric flow and the source of the motion forcing; and (ii) a relationship between the motion and the net relative angular momentum.

4. Far Outer Flow

Decreases in the symmetric flow beyond r = 800 km, for the case of a vortex with significant flow far from the center, lead to a reduction in the speed of motion. However, the effect is on the order of 10% Thus, the flow in the r = 300 - 800 km annulus is the key to the structure dependence.

D. EVOLUTION OF THE SYMMETRIC AND ASYMMETRIC FLOW

The first use of the symmetric/asymmetric decomposition procedure is to examine how the symmetric (or tangential) wind profile changes during the integration and how the asymmetric flow develops. There are two notable changes in the initially symmetric wind field during the integration: (i) a slight reduction in the maximum wind; and (ii) the formation of an anticyclone beyond r ~ 400 km that lowers the integrated RAM. These changes are shown to be an indirect consequence of how the asymmetric circulation forms.

1. The Asymmetric Flow

The asymmetric circulation after the motion has reached a quasi-steady state is distinguished by: (i) a cyclonic-anticyclonic (wavenumber 1) pair of large-scale (r ~ 500-700 km) gyres; (ii) a nearly uniform "ventilation" flow through the zone of significant symmetric flow (r < 300 km); and (iii) zero flow at the vortex center. The correspondence between the motion of the center and the ventilation flow vector in both direction and magnitude is approximately 95%. Thus, the dominant barotropic dynamics

of tropical cyclone motion is contained in the asymmetric flow. Therefore, the role of vortex structure in the motion process depends on how the structure influences the formation and evolution of the asymmetric flow.

The asymmetric flow tends to zero at the center because the linear forcing that generates the asymmetric flow (βv) approaches zero and because the high inertial stiffness resists distortion of the symmetric inner core. This zero in the asymmetric circulation appears as a set of small cyclonic-anticyclonic gyres when the storm motion is subtracted. The horizontal scale and magnitudes of these "inner-core gyres" are comparable to that found by Marks and Houze (1987) using a similar analysis method in a real tropical cyclone.

2. Circulation Tendency Analysis

The role of the asymmetric flow features in the motion process has been examined using a circulation (vice vorticity) tendency analysis. In this approach, the model equation is expressed in terms of the symmetric and asymmetric components of the streamfunction.

The formation of the asymmetric flow is due to the asymmetric component of the linear term (βv). In other words, the symmetric flow forces the asymmetric flow through Rossby dispersion, which stresses the strong link between the symmetric and asymmetric circulation systems.

An evaluation of the nonlinear advective tendency terms shows that the motion process occurs on two space scales. In the inner core, the advection of asymmetric vorticity (the inner-core gyres) by the symmetric flow is responsible for the movement of the inertially stiff core. On a larger scale ($r > 300$ km), the vortex is moved through the advection of symmetric vorticity (the "vortex") by the asymmetric flow ("ventilation").

A new and important finding is that nonlinear advection opposes the growth of the asymmetric flow relative to the moving center such that during steady-state motion, the cancellation is nearly perfect. This cancellation maintains the asymmetric circulation in a nearly steady state. Furthermore, the tendency analysis reveals that the advection of asymmetric vorticity by the symmetric flow is the principal source of the nonlinear asymmetric flow opposition and the turning motion in the symmetric perturbation vortices.

E. DYNAMICAL SENSITIVITY

Three types of model integrations have been performed to confirm the motion processes suggested by the evolution of the symmetric/asymmetric flow and by the circulation tendency analysis. In the first set, the ratio of nonlinear to linear effects ($|J(\psi,\nabla^2\psi)/\beta v|$) is varied to control the balance between the linearly-induced asymmetric flow forcing and the nonlinear compensation. The second type of model experiments concerns the manner in which nonlinear advection modifies the asymmetric flow. In these experiments, the linear term is set to zero (effectively, $\beta = 0$) and the model is initialized with an asymmetric vortex from a linear solution. In the third set of dynamical sensitivity tests, the nonlinear term is rewritten using the symmetric/asymmetric formulation and the terms related to nonlinear interaction between the symmetric and asymmetric circulations are modified and/or deleted.

1. Balance between Motion and Ventilation Flow Generation

Associated with the wavenumber one, large-scale asymmetric gyres generated by Rossby dispersion is a nearly uniform flow that "ventilates" the inner regions of the vortex. This ventilation flow, together with inner-core processes, moves the vortex through nonlinear advection. As demonstrated by Chan and Williams (1987), the vortex does

not move due to linear processes alone. However, the linear solutions do show that the ventilation flow generation is directly proportional to time for a stationary vortex. Thus, the ventilation flow formation relative to the moving center will be a function of the speed of motion. In other words, a moving vortex resists ventilation flow development by reducing the time at a fixed location for the flow to develop.

The nature of the balance between vortex motion and the ventilation flow formation is controlled by scaling the relative magnitude of the nonlinear to linear terms, because the linear term controls the asymmetric flow and the nonlinear term is primarily responsible for the motion. Four vortices are chosen to illustrate the effects of the flow in the critical annulus and the model integrations with the varying nonlinear-to-linear ratios are used to calculate a curve relating the magnitude of the ventilation flow vector to the speed of motion. These "ventilation flow curves" depend on the flow in the critical annulus and suggest that some vortices may be less stable to changes in the ventilation flow-motion balance.

2. Nonlinear-only Integrations after Initialization with a Linear Solution.

Using a linear solution for the initial conditions provides a vortex that contains both a symmetric and an asymmetric circulation. By then setting the linear term to zero during the integration, the mechanism for ventilation flow formation is eliminated. Thus, the only way to change the asymmetric flow is through nonlinear advection. Although the tendency analysis suggests that the nonlinear term counteracts the linear forcing, ultra-long model integrations (12 days) with only the nonlinear term show that advection does not eliminate the asymmetric circulation

as the motion is persistent even at the end of a 12-day integration.

This type of integration has been performed for a variety of vortices and it is found that the path is similar to that in the full (linear plus nonlinear) integrations. That is, the motion dependence on the outer flow is not changed. For example, a counterclockwise turning vortex turns in the same way in the nonlinear-only experiments. Thus, the turning motions are strictly a nonlinear effect. An examination of the asymmetric streamfunction shows that nonlinear advection acts to destroy the initial large-scale asymmetric gyres and that this weakening process proceeds outward from the inner core. However, a very large scale (~ 1500 km) "background" ventilation flow remains, even after ultra-long integrations, and it is this flow that causes the persistent motion.

3. Modification of the Symmetric/Asymmetric Tendencies

The diagnostic analysis of the model tendency equation, which is expanded in terms of the symmetric and asymmetric circulations, shows that the advection of asymmetric vorticity by the symmetric flow ($-J(\psi_s,\nabla^2\psi_a)$ or AAVS) is responsible for: (i) the rotation of the large-scale gyres; (ii) the motion of the inner-core; and (iii) helps to negate the linearly-induced asymmetric flow generation. The steering-type process of advection of symmetric vorticity (the vortex) by the asymmetric flow ($-J(\psi_a,\nabla^2\psi_s)$ or ASVA) is linked to the motion of the larger-scale vortex.

This diagnostic analysis is extended to a prognostic mode by modifying the nonlinear interaction terms between the symmetric and asymmetric circulations during the model integration. Two types of modification are made: (i) setting AAVS or ASVA to zero; and (ii) adjust the spatial distribution of these terms. When ASVA is set to zero, the

center moves along the same path as in the full model solution, but with reduced speed. This reduced speed demonstrates the magnitude of the inner-core motion process due to AAVS, as this type of advection is the only nonlinear process in this model. When AAVS is set to zero (the only operating advective process is then the steering-type ASVA), the center does not move, even when the initial vortex includes an asymmetric circulation. This surprising result demonstrates the importance of a "coordination" between motion of the larger-scale and vortex and inner core. When the two processes are not properly "phased" (e.g., ASVA = 0), the motion of the center is distorted, particularly when the inner-core process is disturbed.

F. ULTRA-LONG INTEGRATIONS

The moving grid procedure allows ultra-long integrations without resorting to moving nested grids or to extremely large domains. A series of 12-day integrations, which are believed to be the longest ever attempted, shows that all the outer-change vortices in which the inner flow is held constant tend to approach the same common symmetric structure with the same motion vector. This common or quasi-universal structure is referred to the "beta-neutral profile."

The beta-neutral profile is a consequence of the balance between Rossby dispersion, which tends to break the vortex apart (e.g., Flierl, 1977) and the nonlinear, inertia-type resistance that acts to maintain the vortex. When the two processes act over a "long" period of time, a "balanced" profile results that is dependent only on β. In these long integrations, the beta-neutral profile has a net negative integrated RAM in the r = 0 - 2000 km annulus.

G. CONTRIBUTION TO THE MOTION BY DIFFERENT SCALES IN THE INITIAL VORTEX

The final set of model experiments concerns the role of various space scales in the initial vortex. The solution to the linear version of the model is the well-known Rossby dispersion relationship as derived by Chan and Williams (1987). This dispersion relationship states that the phase speed of the waves in the system depends only on wavelength, with longer waves moving faster than the shorter waves. Thus, Rossby wave dispersion and the generation of the wavenumber one asymmetries of a tropical cyclone scale vortex will depend on how much of the spatial variance in the vortex "projects" onto the most dispersive modes. The greater the variance in the largest modes, the greater will be the rate of asymmetric flow generation.

A generalized 2-D Fourier transform procedure (Errico, 1985) is used to calculate the variance spectrum of the axially symmetric vortex and to filter the initial conditions according to space scales. The scales are divided into three groups: (i) "small" ($0 \leq \lambda < 500$ km); (ii) "medium" (500 km $\leq \lambda \leq$ 1500 km); and (iii) "large" ($\lambda >$ 1500 km).

The 1-D spectrum shows little transfer of energy between different 1-D scales during a 72-h integration. However, there is a redistribution of energy between x and y variations within a 1-D scale due to dispersion. When a scale group is deleted, the nonlinear processes are unable to fully restore the removed variance through nonlinear interaction during the integration.

Model runs in which the small, medium and large scales are selectively deleted or retained indicate that the large scales make the greatest contribution to the speed of motion, whereas the small and medium scales have the greatest influence on path. This result further emphasizes

the importance of the large-scale component of the vortex structure.

H. SUMMARY OF STRUCTURE DEPENDENCE

Although the inner-core advective processes are important to moving the center, the intensity of the inner-core flow has very little bearing on the overall track. Initial condition sensitivity experiments, in which the symmetric flow in the "inner" ($r < 300$ km) and "outer" ($r \geq 300$ km) regions are independently varied, demonstrate that the outer structure makes the greatest contribution to the motion. Cyclonic and anticyclonic symmetric perturbations in the "critical" r = 300 - 800 k annulus force long-term (t > 72 h) turning motion in the same sense as the perturbation. This result stresses the importance of the interaction between the symmetric flow and the linearly-induced asymmetric forcing.

The Fourier filtering experiments demonstrate that largest scales control speed of motion and the intermediate scales contribute mostly to the path. Finally, dynamical sensitivity tests suggest that some vortex structures may be more stable with regards to changes in the balance between linear asymmetric forcing and nonlinear compensation.

I. SUMMARY OF NEW FINDINGS REGARDING THE DYNAMICS OF BETA DRIFT

Understanding the role of vortex structure in tropical cyclone motion has required a more detailed analysis of the underlying dynamics of beta drift. A new symmetric/asymmetric decomposition procedure is used as an alternate means of expressing the dynamics. In this system, the vortex is associated the symmetric flow and the interaction of the vortex with the environment is associated with the asymmetric circulation.

A very strong relationship between the asymmetric flow and the movement of the vortex center has been demonstrated.

Thus, the dynamics of beta drift is keyed to the asymmetric flow and the role of structure depends upon how the vortex influences the asymmetric circulation.

The linear term in the model equation (βv) is the source of the asymmetric flow. The nonlinear term ($-J(\psi,\nabla^2\psi)$) moves the vortex through advection of both symmetric and asymmetric vorticity. In the process of moving the vortex, the nonlinear effects act to "balance" the linearly-forced asymmetric circulation and thereby establish quasi-steady motion.

Advection of symmetric vorticity (the "vortex") by the asymmetric flow is a steering-like process that moves the larger scale component ($r > 300$ km) of the vortex. However, the advection of asymmetric vorticity by the symmetric flow is responsible for the motion of the inner core. Dynamical sensitivity tests, in which either the inner-core or larger-scale vortex motion process is disrupted, demonstrate the importance of a correct "phasing" between these two motion effects.

J. APPLICATIONS TO FUTURE THEORETICAL STUDIES AND FORECAST MODELS

There are two essential limitations to this study. The first concerns the model and the second is related to the dynamical scenario. Model extensions to the divergent barotropic and baroclinic framework will improve the physical realism of the model. However, the experiments of Hoke and Anthes (1975), in which divergent and nondivergent barotropic models were used to study beta drift, suggested that the most serious deficiency with the current approach is more in the dynamical situation. Thus, future research with this model should be directed towards considering basic flows on the earth's surface (i.e., relax the beta plane assumption). Another area of experimentation arises from

the long-term integrations. The "beta-neutral profile" is an intiguing concept that needs further development.

The model and dynamical situation used in this research are much simpler than the actual atmosphere and the current suite of operational baroclinic tropical cyclone models. Thus, the implications of these results to these more complete models will depend on the degree to which real cyclones behave in a nondivergent barotropic manner. Nevertheless, there are several important points that should be considered in the development of more sophisticated models. The wide variety of track behaviors exhibited by this simple model leaves open the question of whether the motion process is primarily dynamical or physical. That is, the nonlinear effects included in this model may be the most important. It is possible that the physical processes of convection may simply modify the essentially barotropic dynamics.

High spatial resolution may not be necessary for highly accurate track prediction. The ability of a coarse resolution model to simulate beta drift and the essential structurally-related track effects (i.e., the large-scale vortex) offers a reason for continuing to use "coarse" grid limited-area models and eventually global models. The best dynamical forecast aid in the western North Pacific is still a three-layer, Δx = 205 km model despite competition from a nested grid model and a full physics, baroclinic model (B.J. Williams, Joint Typhoon Warning Center, personal communication).

The consistent dominance of the larger scale aspects of the vortex in the motion process makes the vortex specification problem a particularly difficult one. It is very important to carefully specify the beta-induced wavenumber one asymmetry, because a misrepresentation of this circulation could seriously affect initial speed and

direction of motion. However, it is desirable that the vortex specification not interfere with the larger scales being developed in the vicinity of a cyclone during the model data assimilation.

The large-scale nature of the linearly-induced asymmetric circulation and the nearly perfect relationship between the averaged flow in the r = 0-300 km annulus and the motion of the center indicates that steering is a valid concept. However, the steering flow in this study is generated by the vortex itself. Therefore, it will be very difficult to separate large-scale steering from vortex-generated steering. Even though the steering concept may be useful and dynamically reasonable, these results demonstrate that the structure of the vortex must be accounted for in determining the "steering flow."

The motion of an isolated vortex on a β plane is a conceptually simple, but dynamically complex event involving highly nonlinear processes. The key ingredient to the motion in this situation is the structure of the vortex, both as it interacts with the environment (β here) and as it provides the translation mechanism. It is believed that this research provides new concepts and techniques for analyzing the motion in more complex models. By developing a more complete understanding of the motion process in a series of progressively more complex models, it may eventually be possible to build a forecast model that simulates tropical cyclone motion with far greater "intelligence" and produces more skillful track predictions.

APPENDIX A:

DERIVING THE TANGENTIAL WIND PROFILE AND VORTEX PARAMETERS FROM THE SYMMETRIC STREAMFUNCTION

The vortex structure parameters discussed in Chapter III are derived from the symmetric component $\psi_S(r)$ of the model streamfunction solution. This function is available at the grid points of the cylindrical grid (Fig. 4-1) and the tangential wind $v(r)$ and relative vorticity $\zeta(r)$ are calculated via

$$v(r) = \frac{\partial \psi_S}{\partial r} \quad , \tag{A.1}$$

and

$$\zeta(r) = \frac{1}{r} \frac{\partial (rv(r))}{\partial r} \quad , \tag{A.2}$$

using the derivative routine of the spline-under-tension subprogram ("CURV" in the NCAR Scientific Subroutine Package; SSP) that is used in the symmetric/asymmetric decomposition procedure.

The critical points of the v profile are found by specifying the derivative using the splines at intermediate "subgrid" points between points of the cylindrical grid (radius) and linearly interpolating for the zero at the extrema point. The procedure is illustrated in Fig. A-1. In this example, and as in the symmetric/asymmetric decomposition, the cylindrical grid has Δr = 20 km and the subgrid points have a spacing of 5 km.

The critical points give the maximum wind (intensity), the radius of maximum wind (RMW), the minimum v (maximum anticyclonic velocity in the outer portion of the vortex), and the radius of minimum v. These later quantities were

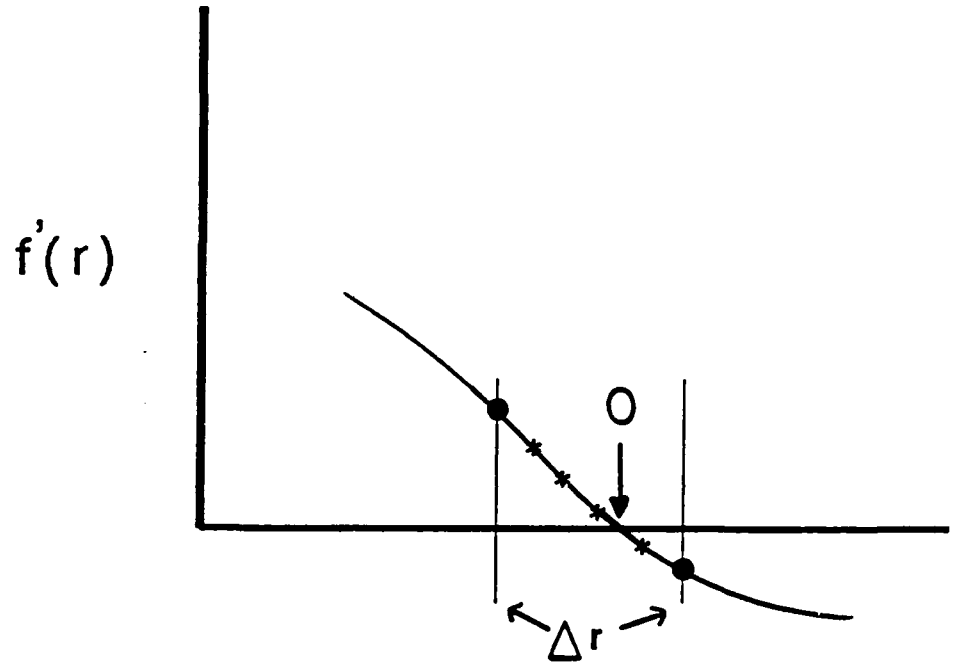

Fig. A-1. Illustration of finding an extrema of a function using the derivative. The large dots indicate the cylindrical grid points (Δr = 20 km) and the asterisks subgrid points (Δr = 5 km). The derivative at the subgrid points is evaluated using a cubic spline and the zero value (the extrema) is found by linear interpolation between subgrid points.

not discussed in the text, but were examined for potential relationships to motion.

The procedure is able to recover the initial intensity and RMW within 1% of the input values. The size radius is calculated in a similar way as the extrema, except that the 15 m/sec value of the function is found rather than the zero of the derivative. The numerical precision of the radius calculation also has an error on the order of 1%.

The inner (3.1), outer strength (3.2), integrated relative angular momentum (3.7), and the inertial stability parameter ($\Gamma = (\zeta + f)(f + 2v/r)$ are also calculated from $v(r)$ on the cylindrical grid using the NCAR SSP routines.

APPENDIX B:

DERIVING THE INITIAL 2-D STREAMFUNCTION FROM AN ANALYTICAL TANGENTIAL WIND PROFILE

Chan and Williams (1987) define the initial streamfunction (ψ) on the model grid by solving the Helmholtz equation (2.4 in Chapter II) for ψ with the forcing function (ζ) specified directly from analytical tangential wind profile (3.3). Although this method involves a minimum of finite differencing, a significant (5%) discrepancy is found between the flow calculated from the initial psi (2.5) and the tangential wind profile. An alternative approach was developed to reduce this discrepancy.

The tangential wind (v_θ) is specified (e.g., the analytical profile) on the 2-D Cartesian model grid and then converted to Cartesian wind components (v_C, u_C) via

$$\begin{aligned} v_C(x,y) &= v_\theta(r) \cos\theta \\ u_C(x,y) &= -v_\theta(r) \sin\theta \quad . \end{aligned} \tag{B.1}$$

The forcing function ($\zeta_{i,j}$) is calculated using the same centered-in-space finite differences as in the model equation in terms of the Cartesian wind components

$$\zeta_{i,j} = \left\{ \frac{v_{C\,i+1,j} - v_{C\,i-1,j}}{2\,\Delta x} \right\} - \left\{ \frac{u_{C\,i,j+1} - v_{C\,i,j-1}}{2\,\Delta y} \right\} , \tag{B.2}$$

where $\Delta x = \Delta y$ (= 40 km in the standard model configuration). Finally, the Helmholtz equation for ψ is solved following the same inversion routine as in the model (for the tendency) to give the initial streamfunction.

This method for calculating the initial vorticity uses more finite difference operations than Chan and Williams

(1987), but it achieves greater finite difference compatibility between the initial ψ and the initial wind. Even though differences between the two approaches are not large, it is desirable to more closely recover the analytical v profile from the numerically-derived streamfunction.

APPENDIX C:

THE MODEL TENDENCY EQUATION IN THE SYMMETRIC/ASYMMETRIC FRAMEWORK

To study the interaction between the symmetric and asymmetric circulations, the model tendency equation is rewritten with respect to these two circulations. The decomposition of the total field (ψ_t) into symmetric (ψ_s) and asymmetric (ψ_a) components is made prior to any calculations with the rewritten equations using the procedures discussed in Chapter IV.

The decomposition is accomplished by

$$f = A(f) + S(f) \quad , \tag{C.1}$$

where the A operator returns the asymmetric component of f and S returns the symmetric component. As discussed in Chapter IV, the decomposition (the A and S operators) is a numerical procedure that precisely decomposes (i.e., the residual $[f - \{A(f)-S(f)\}]$) is very small) the symmetric and asymmetric components.

In the model, the decomposition is applied to the total streamfunction

$$\psi_{t\,i,j} = \psi_{s\,i,j} + \psi_{a\,i,j} \quad , \tag{C.2}$$

where the i,j subscripts in (C.2) denote values on the the model grid. The indices are from i = 1, ... , M and j = 1, ... , N, where M is the number of points in the x or i direction and N is the number of points in the y or j direction.

The model tendency equation for the total streamfunction (as in (2.6) with the i,j indices dropped for convenience) is

$$\nabla^2 \frac{\partial \psi_t}{\partial t} = -J(\psi_t, \nabla^2 \psi_t) + \beta \frac{\partial \psi_t}{\partial x} \quad . \qquad (C.3)$$

Defining the inverse operator of $H(f) = \nabla^2 f$, as H^{-1}, and noting that the Cartesian north-south wind component is $v = \partial\psi/\partial x$ (2.5), the model equation becomes

$$\frac{\partial \psi_t}{\partial t} = H^{-1}(-J(\psi_t, \nabla^2 \psi_t) + H^{-1}(\beta v) \quad , \qquad (C.4)$$

Substituting (C.2) into the nonlinear term of (C.4) yields

$$\begin{aligned} \frac{\partial \psi_t}{\partial t} = {} & H^{-1}(-J(\psi_a, \nabla^2 \psi_s) + H^{-1}(-J(\psi_s, \nabla^2 \psi_a) \\ & \text{(ASVA)} \qquad\qquad \text{(AAVS)} \\ & + H^{-1}(-J(\psi_a, \nabla^2 \psi_a) + H^{-1}(-J(\psi_s, \nabla^2 \psi_s) \\ & \text{(AAVA)} \qquad\qquad \text{(ASVS)} \\ & + H^{-1}(\beta v) \quad . \end{aligned} \qquad (C.5)$$

where ASVA = Advection of Symmetric Vorticity by the Asymmetric flow;

AAVS = Advection of Asymmetric Vorticity by the Symmetric flow;

AAVA = Advection of Asymmetric Vorticity by the Asymmetric flow; and

ASVS = Advection of Symmetric Vorticity by the Symmetric flow.

ASVS is zero by definition, but AAVA is in general nonzero. However, AAVA is numerically an order of magnitude smaller that AAVS, and ASVS is not exactly zero because of finite difference errors. The spatial distribution of ASVS has a $2\Delta x$ checker-board appearance and does not contribute to the dynamical processes, but does introduce noise into the track as noted in the Chapter II.

The remaining tendencies are calculated on the model grid using the model finite difference operators. Furthermore, the tendencies in the model and in the figures are nondimensionalized with a length scale of 10^6 m and a time scale of 10^5 sec as in the model.

To explicitly show how β forces the symmetric and asymmetric circulations, the decomposition (C.1) is applied to βv vice $\beta\partial\psi/\partial x$. This yields a βv tendency field that corresponds directly to the symmetric and asymmetric circulations. The rewritten model equation now becomes,

$$\frac{\partial \psi_t}{\partial t} = H^{-1}(-J(\psi_a,\nabla^2\psi_s) + H^{-1}(-J(\psi_s,\nabla^2\psi_a) + H^{-1}\{\underset{(SB)}{S(\beta v)}\} + H^{-1}\{\underset{(AB)}{A(\beta v)}\}, \qquad (C.6)$$

This equation shows the basic coupling between the symmetric and asymmetric circulations within the vortex, which are: (i) environmental forcing by β (SB and AB); and (ii) internal nonlinear interaction (AAVA and ASVA). A complete analysis of the coupling is given in Chapter IV.

APPENDIX D:
CALCULATING THE MOTION TENDENCY

In Chapter IV, the streamfunction tendency due to the uniform translation of the vortex is removed from various tendency fields to isolate on "relative-to-the-moving-center" changes in the vortex. This "motion" tendency is calculated by first observing that the vorticity change due to constant translation can be expressed as

$$\frac{\partial \zeta}{\partial t} = - \vec{C} \cdot \nabla \zeta \quad , \tag{D.1}$$

where $\vec{C}$ is a uniform velocity vector equal to the motion of the vortex center at a given time. This vector is derived a posteriori from the hourly positions as described below. Converting (D.1) to an equivalent form in terms of the streamfunction ψ gives

$$\nabla^2 \frac{\partial \psi}{\partial t} = - J(\psi_m, \nabla^2 \psi) \quad , \tag{D.2}$$

where ψ_m is a uniformly varying streamfunction whose orientation and gradient are equal to the vortex motion. Although this equation can be applied to either the symmetric or asymmetric circulations, it is generally used for the motion tendency of the symmetric circulation that is associated with the "vortex." The problem in calculating this tendency is finding ψ_m and $\vec{C}$.

The vortex position (ψ center) is saved every hour during a model integration and the motion vector is calculated over 3, 6, 12, 18 and 24 h intervals. These positions are smoothed with a Shuman (1957) smoother-desmoother prior to the motion calculation to eliminate unrepresentative, numerically-induced oscillations (see

Section IV-F). The motion vector is defined to be the 6-h motion vector that is closest to the valid time of the model streamfunction ψ in the calculations in Sec. IV-E. The constant-gradient streamfunction (zero vorticity) is found by solving

$$\nabla^2 \psi_m = 0 \quad , \tag{D.3}$$

with boundary conditions from

$$\frac{\partial \psi_m}{\partial s} = - v_n \quad , \tag{D.4}$$

where n indicates the outward pointing unit vector and increases outward from the edge of the domain, s is distance along the boundary and increases counterclockwise, and v_n is the wind component normal to the domain (in the direction of n).

A finite difference form of (D.4) is integrated counterclockwise starting in the southwest corner (the 1,1 point on the grid or the lower left hand corner) to yield the boundary values of ψ_m. The interior values of the constant-gradient ψ_m are then solved using the same Helmholtz equation inversion routine as in the model.

Given ψ_m and the model ψ solution (either total or the symmetric component), the motion tendency is calculated in the same manner as all the other tendencies in the budget equations.

LIST OF REFERENCES

Adem, J., 1956: A series solution for the barotropic vorticity equation and its application in the study of atmospheric vortices. Tellus, **8**, 364-372.

Alaka, M.A., 1962: The occurrence of dynamic instability in incipient and developing hurricanes. Mon. Wea. Rev., **90**, 49-58.

Anthes, R.A., 1982: Tropical cylones: their evolution, structure and effects. Meteorological Monographs, , Vol. 19, No. 41, American Meteorological Society, Boston, MA, 02018, 208 pp.

_____, and J.E. Hoke, 1975: The effect of horizontal divergence and the latitudinal variation of the Coriolis parameter on the drift of a model hurricane. Mon. Wea. Rev., **103**, 757-763.

Arakawa, A., 1966: Computational design for long-term numerical integrations for the equations of atmospheric motion. J. Comput. Phys., **1**, 119-143.

Bell, G., 1979: Operational forecasting of tropical cyclones: past, present, and future. Australian Metereor. Mag., **27**, 249-258.

Brand, S., C.A. Buenafe and H.D. Hamilton, 1981: Comparison of tropical cyclone motion and environmental steering. Mon. Wea. Rev., **109**, 908-909.

Chan, J.C.-L., 1982: On the physical processes responsible for tropical cyclone motion. Dept. of Atmos. Sci. Paper No. 358, Colorado State University, Ft. Collins Co. 200 pp.

_____, 1984: An observational study of the physical processes responsible for tropical cyclone motion. J. Atmos. Sci., **41**, 1036-1048.

_____, 1986: Supertyphoon Abby -- an example of present track forecast inadequacies. Weather and Forecasting, **1**, 113-126.

_____, and W.M. Gray, 1982: Tropical cyclone movement and surrounding flow relationships. Mon. Wea. Rev., **110**, 1354-1374.

_____, and R.T. Williams, 1987: Analytical and numerical studies of the beta-effect in tropical cyclone motion. Part I: zero mean flow. J. Atmos. Sci., **44**, 1257-1265.

Chang, S. W.-J., and R.V. Madala, 1982: Comments on "Comparison of tropical cyclone motion and environmental steering", Mon. Wea. Rev., **110**, 2070-2071.

DeMaria, M., 1985: Tropical cyclone motion in a nondivergent barotropic model. Mon. Wea. Rev., **113**, 1999-1210.

_____, 1987: Tropical cyclone track prediction with a barotropic spectral model. Mon. Wea. Rev., **115**, 2346-2357.

_____, and J.-J. Biak, 1987: The effect of vortex structure on barotropic hurricane track forecasts. Extended Abstracts, 17th Conference on Hurricanes and Tropical Meteorology, 7-10 April, 1987, Miami, FL, American Meteorological Society, Boston, MA, 02108, 52-54.

Eliassen, A., 1951: Slow thermally or frictionally controlled meridional circulation in a circular vortex. Astrophysica Norvegica, **5**, 19-60.

Elsberry, R.L., 1986: Some issues related to the theory of tropical cyclone motion. Technical Report # NPS 63-86-005, Naval Postgraduate Schoool, Monterey, CA, 23 pp.

_____, 1987: Tropical cyclone motion. Chap. 4 in A Global View of Tropical Cyclones, Univ. Chicago Printing Press, 184 pp.

_____, and M. Fiorino, 1985: Design considerations for an advanced tropical cyclone model. NAVENVPREDRSCHFAC Tech. Rep. TR 85-03, NEPRF, Monterey, CA, 152 pp.

Errico, R.M., 1985: Spectra computed from a limited area grid. Mon. Wea. Rev., **113**, 1554-1562.

_____, and D. Baumhefner, 1987: Predictability experiments using a high-resolution limited-area model. Mon. Wea. Rev., **115**, 488-504.

Ferrel, W., 1859: The motion of fluids and solids relative to the earth's surface. Math. Mon., **1**, 300-307.

Fiorino, M., 1985a: A review of the dynamic tropical cyclone models developed by the U.S. Navy. Appendix F of R.L. Elsberry and M. Fiorino, NAVENVPREDRSCHFAC Tech. Rept. TR 87-03, 152 pp.

_____, 1985b: Operational numerical modeling of tropical cyclone motion. Topic Chairman and Rapporteur Reports, WMO International Workshop on Tropical Cyclones, Bangkok, Thailand, 25 November - 5 Decembert, 1985, World Meteorological Organization Technical Document, WMO/TD-No. 72.

_____, and R.L. Elsberry, 1987: The role of vortex structure in barotropic tropical cyclone motion. Extended Abstracts, 17th Conference on Hurricanes and Tropical Meteorology, 7-10 April, 1987, Miami, FL, American Meteorological Society, Boston, MA, 02108, 55-59.

_____, E.J. Harrison, Jr., and D.G. Marks, 1982: Comparison of the performance of two operational tropical cyclone models. Mon. Wea. Rev., **110**, 651-656.

Flierl, G.R., 1977: The application of linear quasi-geostrophic dynamics to Gulf Stream rings. J. Phys. Oceanogr., **7**, 365-379.

George, J.E., and W.M. Gray, 1976: Tropical cyclone motion and surrounding parameter relationships. J. Appl. Meteor., **15**, 1252-1264.

Gerald, C.F., and P.O. Wheatley, 1984: Applied Numerical Analysis. Addison-Wesley Publishing Company, 579 pp.

Gray, W.M., 1981: Recent advances in tropical cyclone research from rawindsonde composite analysis. WMO Programme in Research in Tropical Meterology Report, World Metereorological Society, Geneva, 407 pp.

Haberman, R., 1983: Elementary applied partial differential equations. Prentice-Hall, Inc., Englewoods Cliffs, NJ, 07632, 533 pp.

Haltiner, G.J., and R.T. Williams, 1980: Numerical prediction and dynamic meteorology. John Wiley and Sons, Inc., New York, NY, 477 pp.

Harrison, E.J., Jr., 1973: Three-dimensional numerical simulations of tropical storms utilizing nested finite grids. J. Atmos. Sci., **30**, 1528-1543.

_____, Jr., 1981: Initial results from the Navy two-way interactive nested tropical cyclone model Mon. Wea. Rev., **109**, 173-177.

_____, and M. Fiorino, 1982: A comprehensive test of the Navy nested tropical cyclone model. Mon. Wea. Rev., **110**, 645-650.

Hodur, R.M., 1987: Evaluation of a regional model with an update cycle. Mon. Wea. Rev., **115**, 2707-2718.

_____, R.M., and S.D. Burk, 1978: The Fleet Numerical Weather Central tropical cyclone model: Comparison of cyclic and one-way interactive boundary conditions. Mon. Wea. Rev., **106**, 1665-1671.

Holland, G.J., 1983: Tropical cyclone motion: Environmental interaction plus a beta effect. J. Atmos. Sci., **40**, 328-342.

Hovermale, J.B., 1980: Dominant factors influencing the accuracy of track forecasts in dynamical hurricane models. Paper presented at the WMO Symposium on Typhoons, Shanghai, China. Oct. 6-11, 1980.

Iwasaki, T., H. Nakano, and M. Sugi, 1987: The performance of a typhoon track prediction model with cumulus parameterization. J. Meteor. Soc. Japan., in press.

Jones, R.W., 1970: Acceleration of hurricane Betsy on 29 August 1965. Ph.D. Dissertation, Dept. of Meteor., Univ. of Oklahoma, 123 pp.

_____, 1977: Vortex motion in a tropical cyclone model. J. Atmos. Sci., **34**, 1518-1527.

Kasahara, A., 1957: The numerical prediction of hurricane movement with the barotropic model. J. Meteor., **14**, 386-402.

_____, 1960: The numerical prediction of hurricane movement with a two-level, baroclinic model. J. Meteor., **17**, 357-370.

Keyser, D., and L.W. Uccellini, 1987: Regional models: emerging research tools for synoptic meteorologists. Bull. Amer. Meteor. Soc., **68**, 306-320.

Kitade, T., 1981: Numerical study of the vortex motion with barotropic models. J. Meteor. Soc. Japan, **59**, 801-807.

Kuo, H.-L., 1969: Motions of vortices and circulating cylinder in shear flow with friction. J. Atmos. Sci., **26**, 390-398.

Marks, F.D., and R.A. Houze, Jr., 1987: Three-dimensional structure of the eyewall of hurricane Norbert as determined from an airborne Doppler radar. Extended Abstracts, 17th Conference on Hurricanes and Tropical Meteorology, 7-10 April, 1987, Miami, FL, American Meteorological Society, Boston, MA, 02108, 347-350.

Mathur, M., 1987: Development of the NMC's high resolution hurricane model. Extended Abstracts, 17th Conference on Hurricanes and Tropical Meteorology, 7-10 April, 1987, Miami, FL, American Meteorological Society, Boston, MA, 02108, 60-63.

McWilliams, J.C., and G.R. Flierl, 1979: On the evolution of isolated nonlinear vortices. J. Phys. Oceanogr., **9**, 1183-1206.

Merrill, R.T., 1982: A comparison of large and small tropical cyclones. Dept. of Atmos. Sci. Paper No. 352, Colo. State Univ., Ft. Collins, CO, 75 pp.

Neumann, C.J., 1979: On the use of deep-layer-mean geopotential height fields in statistical prediction of tropical cyclone motion. Preprints, Sixth Conf. on Prob. and Stat. in Atmos. Sci., 9-12 Oct. 1979, Banff, Canada, American Meteorological Society, Boston, MA, 02108.

Ookochi, Y., 1978: Preliminary test of typhoon forecast with a moving multi-nested grid (MNG). J. Meteor. Soc. Japan, **56**, 571-583.

Riehl, H., 1962: Some relations between wind and thermal structure of steady state hurricanes. J. Atmos. Sci., **30**, 276-287.

Rosmond, T.E., and F.D. Faulkner, 1976: Direct solution of elliptic equations by block cyclic reduction and factorization. Mon. Wea. Rev., **104**, 641-649.

Rossby, C.G., 1939: Relation between variations in the intensity of the zonal circulation of the atmosphere and the displacement of the semi-permanent centers of action. J. Marine Res., **2**, 239-263.

_____, 1948: On the displacement and intensity change of atmospheric vortices. J. Marine. Res., **7**, 175-187.

Shuman, F., 1957: Numerical methods in weather prediction: II. smoothing and filtering. Mon. Wea. Rev., **85**, 357-361.

Sweet, R., 1971: Subroutine POISDD, NCAR Computing Facility, Boulder, CO, 5 pp.

Tojo, S., 1953: The dynamics of a vortex embedded in a constant zonal current. J. of Meteor., **10**, 175-178.

Tupaz, J.B., 1977: A numerical study of barotropic instability of a zonally varying easterly jet. Ph.D. Thesis, Dept. of Meteorology, U.S. Naval Postgraduate School, Monterey, CA, 93943, 107 pp.

_____, R.T. Williams and C.-P. Chang, 1978: A numerical study of barotropic instability in a zonally varying easterly jet. J. Atmos. Sci., **35**, 1265-1280.

Weatherford, C.L., 1985: Typhoon structural variability. Dept. of Atmos. Sci. Paper No. 391, Colorado State University, Ft. Collins, CO, 80523, 77 pp.

Williams, B.J., 1986: Effects of storm-related parameters on the accuracy of the nested tropical cyclone model. M.S. Thesis, Dept. of Meteorology, U.S. Naval Postgraduate School, Monterey, CA, 93943, 108 pp.

Willoughby, H.E., 1987: Tropical cyclone track prediction: some theoretical aspects. Extended Abstracts, 17th Conference on Hurricanes and Tropical Meteorology, 7-10 April, 1987, Miami, FL, American Meteorological Society, Boston, MA, 02108, 262-265.

Yeh, T.-C., 1950: The motion of tropical storms under the influence of a superimposed southerly current. J. Meteor., 7, 108-113.

INITIAL DISTRIBUTION LIST

		No. Copies
1.	Defense Technical Information Center Cameron Station Alexandria, VA 22304-6145	2
2.	Library Code 0142 Naval Postgraduate School Monterey, CA 93943-5002	2
3.	Oceanographer of the Navy U.S. Naval Observatory 34th and Massachusetts Ave. N.W. Washington, D.C. 20390	1
4.	Commander Naval Oceanography Command NSTL Station Bay St. Louis, MS 39522	1
5.	Commanding Officer Fleet Numerical Oceanography Center Monterey, CA 93943-5105	1
6.	Commanding Officer Naval Environmental Prediction Reserach Facility Monterey, CA 93943-5106	1
7.	Chief of Naval Reserach Marine Meteorology Program (Code 112MM) 800 N. Quincy St. Arlington, VA 22217	1
8.	Commanding Officer Naval Eastern Oceanography Center McAdie Bldg. Naval Air Station Norfolk, VA 23511	1
9.	Commanding Officer Naval Western Oceanography Center Box 113 Pearl Harbor, HI 96860	1
10.	Commanding Officer Naval Oceanography Command Center, Guam Box 12 FPO San Francisco, CA 96630	1
11.	Chairman, Oceanography Department United States Naval Academy Annapolis, MD 21402	1
12.	Chairman (Code 63Rd) Department of Meteorology Naval Postgraduate School Monterey, CA 93943-5000	1

13. Prof. R.L. Elsberry (Code 63Es) 5
Department of Meteorology
Naval Postgraduate School
Monterey, CA 93943-5000

14. Prof. R.T. Williams (Code 63Wu) 1
Department of Meteorology
Naval Postgraduate School
Monterey, CA 93943-5000

15. Prof. C.-P. Chang (Code 63Cp) 1
Department of Meteorology
Naval Postgraduate School
Monterey, CA 93943-5000

16. Prof. R. Franke (Code 53Fe) 1
Department of Mathematics
Naval Postgraduate School
Monterey, CA 93943-5000

17. Prof. P. Jacobs (Code 55Jc) 1
Department of Operations Research
Naval Postgraduate School
Monterey, CA 93943-5000

18. Dr. Michael Fiorino 5
Fleet Numerical Oceanography Center
Monterey, CA 93943-5105

19. Mr. Chris Hall 1
British Meteorological Office
Met O 26 Room R207
London Road
Bracknell Berkshire RG12 2SZ
ENGLAND

20. Mr. Daniel Soderman 1
European Centre for Medium Range
Weather Forecasting
Shinfield Park
Reading Berkshire RG2 9AX
ENGLAND

21. Dr. Toshiki Iwasaki 1
c/o Dr. A. Kasahara, AAP
National Center for Atmospheric Reserach
P.O. Box 3000
Boulder, CO 80307-3000

22. Dr. Edward J. Harrison, Jr. 1
3470 Constellation Dr.
Davidsonville, MD 21035

23. Dr. John Fiorino 1
2705 Salem Ct.
Cinnaminson, NJ 08077

24. Dr. Takeo Kitade 1
Numerical Prediction Divison
Japan Meteorological Agency
Otemachi 1-3-4
Chiyodaku
Tokyo
JAPAN 100

25. Dr. Hugh Willoughby 1
Hurricane Research Division/AOML
4301 Rickenbacker Causeway
Miami, FL 33149

26. Dr. Mark DeMaria 1
Hurricane Research Division/AOML
4301 Rickenbacker Causeway
Miami, FL 33149

27. Dr. Johnny C.-L. Chan 1
29-33 Soares Ave.
22/F Flat B
Kowloon
HONG KONG

28. Dr. Thomas Keenan 1
BMRC
GPO Box 1289K
Melbourne Victoria 3001
AUSTRALIA

29. Dr. Tom Warner 1
Department of Meteorology
503 Walker Building
Pennsylvania State University
University Park, PA 16802

30. Dr. William D. Bonner, Director 1
National Meteorological Center
World Weather Building
Washington, DC 20233

31. Dr. Robert Sheets 1
National Hurricane Center
Gables No. 1 Towers - Rm 631
1320 S. Dixie Highway
Coral Gables, FL 33146

32. LCDR Henry Jones 1
Officer in Charge
Naval Oceanography Command Detachment, FLEACTS
FPO Seattle, WA 98770-0051

33. Ms. Angakana Pyombjamsri 1
Meteorology Department
612 Sukhumvit Rd.
Bangkok 10110
THAILAND

34. Prof. William Gray 1
Department of Atmospheric Science
Colorado State University
Ft. Collins, CO

35. Dr. Alan Weinstein 1
ONR
800 N. Quincy
Arlington, VA 22217

36. Dr. Masanori Yamasaki 1
Meteorological Research Institute
1-1 Nagamine, Yatabe
Tsukuba-gun, Ibaraki
JAPAN 305

37. Dr. Jorge G. De Las Alas 1
Dept. of Meteorology and Oceanography
University of the Philippines
Diliman, Quezon City, 3004
PHILIPPINES

38. Dr. Yoshio Kurihara 1
G.F.D.L./NOAA
Princeton University
P.O. BOX 308
Princeton, NJ 08542

39. Dr. Richard A. Anthes, Director 1
National Center for Atmospheric Research
P.O. BOX 3000
Boulder, CO 80307

40. Dr. William M. Frank, Chairman 1
Department of Meteorology
503 Walker Building
Pennsylvania State University
University Park, PA 16802

41. Dr. Mukut Mathur 1
NOAA, National Meteorological Center
W/NMC22, World Weather Building
Room 204
Washington, DC 20233

42. Mr. Lianshou Chen 1
Central Meteorological Observatory
National Meteorological Bureau
Baishiqiaolu No. 46, Western Suburb
Beijing (Peking)
THE PEOPLE'S REPUBLIC OF CHINA

43. Mr. Jerry D. Jarrell 1
Science Applications Inc.
205 Montecito Ave.
Monterey, CA 93940

44. Dr. Enrique Camarillo Cruz 1
Office of the Department
of Geography and Meteorology
Avenida del Observatorio 192
TACUBAYA,
11860 MEXICO
D.F.

45. Prof. Hanliang Jin 1
Shanghai Typhoon Institute
Shanghai Meteorological Bureau
Shanghai
THE PEOPLE'S REPUBLIC OF CHINA

46. Prof. Chenglan Bao 1
Department of Atmospheric Science
Nanjing University
Nanjing, Jiangsu Province
THE PEOPLE'S REPUBLIC OF CHINA

47. Mr. Kas Magari 1
PNG Meteorology Service
P.O. Box 1240
Boroko
PAPUA NEW GUINEA

48. LCDR Brian Williams 1
Operations Department
USS NIMITZ (CVN 68)
FPO Seattle 98780-2820

49. CDR Scott Sandgathe 1
Operations Department/OA Division
USS CARL VINSON
FPO San Francisco 96629

50. Mr. Patrick Harr 1
Fleet Numerical Oceanography Center
Monterey, CA 93943

51. Mr. Charles J. Mauck 1
Fleet Numerical Oceanography Center
Monterey, CA 93943

END

DATE

FILMED

5-88

DTIC